Phenomenology of new physics beyond the Standard Model: signals of dark matter and new gauge bosons at colliders

Özer Özdal

A Thesis
In the Department
of
Physics

Presented in Partial Fulfillment of the Requirements
For the Degree of
Doctor of Philosophy (Physics) at
Concordia University
Montréal, Québec, Canada

25 August 2020

CONCORDIA UNIVERSITY
SCHOOL OF GRADUATE STUDIES

This is to certify that the thesis prepared

By: **Özer Özdal**

Entitled: **Phenomenology of new physics beyond the Standard Model: signals of dark matter and new gauge bosons at colliders**

and submitted in partial fulfillment of the requirements for the degree of

DOCTOR OF PHILOSOPHY (Physics)

complies with the regulations of the University and meets the accepted standards with respect to originality and quality.

Signed by the final Examining Committee:

_____ Chair
Jose Garrido

_____ External Examiner
Sabine Kraml

_____ External to Program
Galia Dafni

_____ Examiner
Alexandre Champagne

_____ Examiner
Panagiotis Vasilopoulos

_____ Thesis Supervisor
Mariana Frank

Approved by _____
Valter Zazubovits
Graduate Program Director

_____ 2020 _____
André Roy, Dean
Faculty of Arts & Science

Abstract

Phenomenology of new physics beyond the Standard Model: signals of dark matter and new gauge bosons at colliders

Özer Özdal, Ph.D.
Concordia University, 2020

In this PhD thesis we investigate various aspects of phenomenology of new physics beyond the Standard Model (SM) in the context of extensions of supersymmetric & non-supersymmetric realisations.

In extensions of supersymmetric realisations, we first study the low scale predictions of the supersymmetric standard model extended by $U(1)_{B-L} \times U(1)_R$ symmetry, obtained from $SO(10)$ breaking via a left-right supersymmetric model, imposing universal boundary conditions. We find that the lightest neutralino or sneutrino emerge as dark matter candidates, with different low scale implications. Secondly, we perform a comprehensive analysis of the secluded UMSSM model, consistent with present experimental constraints. In this model the additional Z' gauge boson can be leptophobic without resorting to gauge kinetic mixing and, thus lowering the LHC bounds on its mass. Thirdly, we test E_6 realisations of a generic $U(1)'$ extended Minimal Supersymmetric Standard Model (UMSSM) against all currently available data, from space to ground experiments, from low to high energies. Large gauge kinetic mixing implies that the Z' boson emerging from the breaking of the additional $U(1)'$ symmetry is rather wide since it decays mainly into WW pairs.

In extensions of non-supersymmetric realisations, we study mass bounds of the W_R gauge boson in generic left-right symmetric models. Assuming that the gauge bosons couple universally to quarks and leptons, we allow different gauge couplings $g_R \neq g_L$ and mass mixing, $V_{CKM}^L \neq V_{CKM}^R$ in the left and right sectors. W_R mass bounds can be considerably

relaxed, while Z_R mass bounds are much more stringent. In addition, we perform a consistent analysis of the alternative left-right symmetric model emerging from E_6 grand unification. We show that the exotic neutrino inherent to this class of models, the scotino, is a viable candidate for dark matter satisfying relic density and direct detection constraints.

To my sister Özge Özdal,
and to my parents Ziyneti Özdal and Nail Özdal,
without whom it was impossible for me to complete my thesis work...

Acknowledgements

This Ph.D thesis is the result of four years of hard working and studying under the inspiring supervision of Professor Mariana Frank at the Physics Department in Concordia University. I would like to take this opportunity to send my sincere greatfulness to my supervisor Prof. Dr. Mariana Frank not only for her patience and kindness throughout this study, which was a great comfort, but also for endless encouragement and support during my stay in Concordia University. Her brilliant supervision and continuous support helped me to finish my work on time. She was always more than a supervisor, there is a lot to say about her but in short she will always remain as a very special person in rest of my career and life.

I would like to express my great appreciation to Professor Benjamin Fuks, Professor Stefano Moretti and Professor Poulose Poulose for their contributions, valuable and constructive suggestions during my Ph.D. I have learned a lot from them about various aspects of our field. I was inspired with their knowledge and enthusiasm in physics.

I would like to express my gratitude to my parents Ziyneti Özdal and Nail Özdal and to my sister Özge Özdal for their endless support, encouragement, motivation, love and trust in me. Without you, I would not be the person I am today. I cannot thank enough to my partner Livia Kathleen Thibeault-Budai for her love and constant support, and for keeping me sane over the past few months. Thank you for being my muse, editor, proofreader and nurse. But most of all, thank you for being my best friend.

There is absolutely no way to express what my officemate Jack Yakup Araz means to me. I have learned a lot from him. Our deep discussions about physics have always inspired me. Also I thank him for taking care of me when I was inebriated at the party and then slept in the bathtub (Yes, that happened!). I am so blessed to have such a great friend in my life. I believe, I will always enjoy his friendship till the end of our lives.

My special thanks go to my former supervisor Associate Professor Cem Salih Ün for his constant moral support, enlightening discussions, useful comments and suggestions. I thank my old ex-friend Kathleen McGarvey-Lechable for her support and fruitful physics discussions in the early stages of my PhD journey. Of course, I cannot forget my buddy, Tyrell Edward Umbach, whom I admire for his intellectual knowledge and enjoy spending time with. Quite frankly, this journey was not possible without my amazing friends, Tuğrul Güner and Özge Güner. I thank them for being always there by my side and for the charm they brought to my life in Montreal. I also thank Diana Rojas-Ciofalo, Yaşar Hiçyılmaz and Onur Benli for making my life in Southampton a lot more exciting and fun.

Finally, I would like to thank MITACS Globalink Research Award for giving me the chance to study at the University of Southampton as a visiting PhD student. I also would like to acknowledge University of Southampton for their hospitality.

Contribution of the Author

The original research study is presented in chapters 3, 4, 5, 6 and 7. The research in chapter 3 is in collaboration with Mariana Frank, and the publication can be found in ref. [1]. M.F. encouraged Ö.Ö. to investigate supersymmetric $\mathrm{U}(1)_{B-L}\times \mathrm{U}(1)_R$ model. M.F. conceived of the presented idea. Ö.Ö. developed the theory and performed the computations. All authors discussed the results and contributed to the final manuscript.

The research in chapter 4 is in collaboration with Yaşar Hiçyılmaz, Mariana Frank and Stefano Moretti. The publication can be found in ref. [2]. M.F. conceived of the presented idea. M.F. and S.M. supervised the project. M.F. and Ö.Ö. developed the theoretical formalism. Ö.Ö. performed the analytic calculations and performed the numerical simulations. Y.H. contributed to the design and implementation of the research. All authors discussed the results and contributed to the final manuscript.

The research in chapter 5 is in collaboration with Yaşar Hiçyılmaz, Mariana Frank and Stefano Moretti. The publication can be found in ref. [3]. S.M. conceived of the presented idea. S.M. and M.F. supervised the project. Y.H. worked out almost all of the technical details, and performed the numerical calculations for the suggested study. Ö.Ö. contributed to technical details and interpretation of the results. All authors provided critical feedback and helped shape the research and manuscript.

The research in chapter 6 is in collaboration with Mariana Frank and Poulose Poulose. The publication can be found in ref. [4]. P.P. and M.F. conceived of the presented idea. P.P. and M.F. encouraged Ö.Ö. to investigate LHC constraints on the W_R mass. Ö.Ö. designed and directed the project. Ö.Ö. also carried out the implementation and performed the calculations. M.F. and Ö.Ö. wrote the manuscript in consultation with P.P.

The research in chapter 7 is in collaboration with Mariana Frank and Benjamin Fuks. The publication can be found in ref. [5]. M.F. and B.J. devised the project, the main

conceptual idea. M.F., B.J. and Ö.Ö. developed the theoretical formalism. B.J. and Ö.Ö. designed the model and the computational framework. Ö.Ö. performed the calculations, made the simulations and performed the analysis. All authors discussed the results and contributed to the final manuscript.

Contents

List of Figures

List of Tables

Chapter 1

Introduction: The Standard Model of Particle Physics

As the main achievement of 20th century, Particle Physics questions of how the fundamental particles interact and how three of four forces are related to each other. These are included in an elegant way in the Standard Model (SM) of particle physics.

1.1 Main Blocks of the Standard Model

In this section, we will explain the SM without giving full details. Detailed reviews and books can be found in the literature [25–27]. The SM is a theory that explains the particles discovered so far and three of the four fundamental forces which are important for interactions of these particles. These three forces are the electromagnetic, strong and weak forces. One of the greatest achievements of the SM is to calculate the properties of particles and their interactions with great precision. In short, the SM is a gauge theory of spin 0, 1/2 and 1 particles based on $SU(3)_C \otimes SU(2)_L \otimes U(1)_Y$ gauge symmetry group with subscripts C, L, Y denoting color, left chirality and weak hypercharge. $SU(2)_L \otimes U(1)_Y$ governs the electroweak interactions and $SU(3)_C$ determines the strong interactions. For each gauge group there are corresponding generators, and each generator has an associated "vector field". These vector fields keep the the Lagrangian invariant under local transformations. For this reason, vector fields, which are carriers of physical forces, are also called "gauge fields".

In the SM, the particles are arranged in two groups, as fermions and bosons. Fermions

are particles having half-integer spin. They obey Fermi-Dirac Statistics. In the SM, fermions are divided into three families of quarks and leptons. These three families are identical to each other, except for their masses. The ordinary matter is made up of the first families, while heavier families are rather unstable and decay to the particles of the first families. Leptons are singlets under $SU(3)_C$. In other words, they do not carry color charge; and hence, they do not participate in strong interactions. They only participate in electro-weak interactions. However, quarks are color triplets. Namely, each quark flavour carries three colors. Since quarks carry both color charge and hyper-charge, they participate both strong and electroweak interactions.

According to solutions of the Dirac equation, we have left and right handed particles. Left handed particles are doublets under $SU(2)_L \otimes U(1)_Y$ symmetry and carry the same hypercharge within the doublet, while right-handed particles are singlets under the same gauge symmetry. In this context, $SU(2)_L \otimes U(1)_Y$ forms a chiral theory, since it distinguishes the left-handed particles from the right-handed ones. On the other hand, bosons are particles with integer spin. They obey Bose-Einstein Statistics and they are force carrier particles. $SU(3)_C$ has 8 generators (3^2 - 1 = 8 generators) which are the gluons (G^a_μ, a=1,2,..,8) of $SU(3)_C$. $SU(2)_L$ has 3 generators (W^a_μ, a=1,2,3 gauge fields) and $U(1)_Y$ has one generator (B_μ gauge field). The latter 4 generators mix to give masses to the $W^\pm$ and Z bosons, which are mediators of the weak interactions and the photon, the mediator of the electromagnetic interactions, remains massless.

$$SU(3)_C \longrightarrow 8 \text{ gauge bosons (Gluons } G^a_\mu)$$

$$SU(2)_L \longrightarrow 3 \text{ gauge bosons } (W^\pm,\ Z)$$

$$U(1)_Y \longrightarrow 1 \text{ gauge boson } (B_\mu)$$

At high energies, these 12 gauge bosons are massless. However at low energies $SU(2)_L \otimes U(1)_Y$ symmetry breaks down to $U(1)_{EM}$ through the spontaneous symmetry breaking mechanism, and the gauge bosons acquire their masses. The mechanism behind this symmetry breaking is called the Higgs Mechanism. Therefore, in order to be a consistent theory, the SM predicts a scalar (spin=0) Higgs boson which was experimentally observed at CERN in July 2012 [28, 29].

1.1.1 Spontaneous Symmetry Breaking

The electroweak part of the SM distinguishes the left-handed and right-handed fermions and hence it forms a chiral theory. The subscript "L" in $SU(2)_L$ indicates that $SU(2)_L$ only interacts with left-handed fermions and is blind to right-handed ones. Therefore, in the formulation of the SM, left-handed fermions reside in $SU(2)_L$ doublets, while right-handed ones are singlets. In the electroweak Lagrangian, it could easily be seen that left-handed and right-handed particles transform differently under $SU(2)_L \otimes U(1)_Y$.

$$\mathcal{L}_{EW} = \overline{\Psi}_R \gamma^\mu D_\mu^{(R)} \Psi_R + \overline{\Psi}_L \gamma^\mu D_\mu^{(L)} \Psi_L \tag{1.1}$$

where

$$D_\mu^{(L)} = \partial_\mu - \frac{ig_L}{2} W_\mu^i \cdot \sigma^i - \frac{ig_Y}{2} B_\mu \tag{1.2}$$

$$D_\mu^{(R)} = \partial_\mu - \frac{ig_Y}{2} B_\mu \tag{1.3}$$

Under $SU(2)_L$ transformations, left-handed particles transform as $\Psi_L \rightarrow \Psi'_L$ where $\Psi'_L = \exp(-\frac{ig_L}{2} W_\mu^i \cdot \sigma^i)\Psi_L$, whereas right-handed particles remain unchanged (i.e. $\Psi_R \rightarrow \Psi'_R = \Psi_R$). This arises from the fact that right-handed fermions do not carry a $SU(2)_L$ charge.

When one writes down the electroweak Lagrangian, one may also consider writing a mass term, $\mathrm{m}\psi\overline{\psi} = \mathrm{m}(\overline{\psi_R}\psi_L + \overline{\psi_L}\psi_R)$, for fermion fields. However, the mass term of fermions includes mixing of the left and right handed fermions. Since left-handed and right-handed fermions transform in different ways under $SU(2)_L \otimes U(1)_Y$, one can easily see that the Lagrangian with such a mass term is not invariant . Therefore, mass terms of fermions in the electroweak Lagrangian are forbidden by $SU(2)_L \otimes U(1)_Y$ symmetry.

$$\mathcal{L}_{EW} = \overline{\Psi}_R \gamma^\mu D_\mu^{(R)} \Psi_R + \overline{\Psi}_L \gamma^\mu D_\mu^{(L)} \Psi_L + \cancel{m(\overline{\Psi}_R \Psi_L + \overline{\Psi}_L \Psi_R)} \tag{1.4}$$

However, experiments show that the fermions are massive. In order to derive fermions masses, a new complex scalar $SU(2)_L$ doublet Higgs field, $\Phi = \begin{pmatrix} \phi_1 \\ \phi_2 \end{pmatrix}$ is introduced with no color

charge. This Higgs complex scalar field interacts with fermions as indicated below in the Yukawa Lagrangian, written only for first families.

$$\mathcal{L}_y = y_d \overline{Q} \Phi d_R + y_R \overline{L} \Phi e_R + y_u \overline{Q} \Phi^c u_R + ... \tag{1.5}$$

where $Q = \begin{pmatrix} u_L \\ d_L \end{pmatrix}$ and $L = \begin{pmatrix} \nu_{e_L} \\ e_L \end{pmatrix}$.

In order to conserve hypercharge in the electroweak interactions, the total hypercharge of each term in the Yukawa Lagrangian must be zero. This is satisfied if the hybercharge of the complex scalar Higgs field is 1. Then it turns out that, according to the Gell-Mann-Nishijima formula ($Q = \tau_3 + Y/2$), the upper component of the complex Higgs doublet has an electric charge of 1 while the lower component is neutral as indicated below where τ_3 stands for the isospin.

$$\Phi = \begin{pmatrix} \phi_1 \\ \phi_2 \end{pmatrix} \begin{matrix} \longrightarrow \tau_3 = 1/2, Y = 1, \text{then Q} = +1 \\ \longrightarrow \tau_3 = -1/2, Y = 1, \text{then Q} = 0 \end{matrix} \longrightarrow \Phi = \begin{pmatrix} \phi^+ \\ \phi^0 \end{pmatrix}. \tag{1.6}$$

Another important feature of the Yukawa Lagrangian is that d-type quarks masses are generated with the interaction of the Higgs field itself, while the masses of the u-type quarks are obtained with the interaction with the conjugate Higgs scalar field. The Higgs field has a non-zero vacuum expectation value (VEV), which induces the mass terms for the fermions. The Higgs potential is introduced in Eq. 1.7 where λ is always positive to satisfy vacuum stability. The Higgs potential has the following form below where two different configurations are possible according to sign of μ^2 as represented in Fig. 1.1.

For the positive values of μ^2, the minimum of the Higgs potential gives zero VEV while the negative value of μ^2 leads to a non-zero VEV.

$$V(\phi) = \frac{1}{2}\mu^2\phi^2 + \frac{1}{4}\lambda\phi^4\,, \tag{1.7}$$

$$\frac{\partial V(\phi)}{\partial \phi} = \phi(\mu^2 + \lambda\phi^2) = 0\,, \tag{1.8}$$

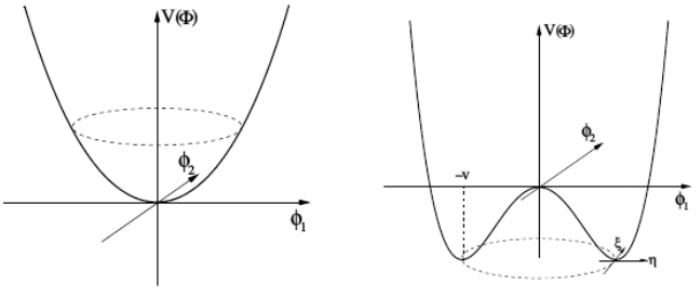

Figure 1.1: Higgs potential before (left) and after (right) spontaneously symmetry breaking.

$$\mu^2 > 0 \longrightarrow v = \langle\phi\rangle = 0\,, \tag{1.9}$$

$$\mu^2 < 0 \longrightarrow v = \langle\phi\rangle = \pm\sqrt{\frac{-\mu^2}{\lambda}}\,. \tag{1.10}$$

Consequently, the Higgs scalar field develops its VEV due to its desire to be at the minimum potential energy. Then, the fermion mass terms, which could not be written in the electroweak Lagrangian, are obtained through spontaneous symmetry breaking. The fact that the gauge bosons of the weak interactions ($W^{\pm}$, Z bosons) are massive and the photon as a mediator of electromagnetic interactions is massless, forces $SU(2)_L \otimes U(1)_Y$ symmetry to break into $U(1)_{EM}$ symmetry. Note that the Higgs field does not carry any color charge; and hence, its non-zero VEV does not break $SU(3)_C$ symmetry. In this sense, gluons remain massless after the electroweak symmetry breaking and $SU(3)_C$ forms an exact symmetry.

Since the Higgs field is described as a doublet and complex scalar, it has four degrees of freedom. After the spontaneous symmetry breaking, three massless Higgs bosons arise in addition to one massive Higgs boson. These massless Higgs bosons which are called "Goldstone Bosons" are swallowed by $W^{\pm}$ and Z bosons and the remaining massive one is generated as the physical state called the Higgs boson.

As fermions acquire their masses via Yukawa interactions, gauge bosons acquire their masses through the gauge interactions. In order to assign gauge bosons masses, the kinetic terms associated with the Higgs field interact in the Lagrangian indicated as follow.

$$\mathcal{L}_{kin} = \frac{1}{2}(D_\mu\Phi)^\dagger(D^\mu\Phi) \tag{1.11}$$

where Φ is given as follows, after it develops VEV.

$$\Phi = \begin{pmatrix} 0 \\ v+h \end{pmatrix} \tag{1.12}$$

While v represents the VEV of the neutral Higgs field, h denotes the perturbative effects around the vacuum expectation value.

1.1.2 Mass Generation of Gauge Bosons

The D_μ in the Equation 1.11 is defined under $SU(2)_L \otimes U(1)$ symmetry as follows

$$D_\mu = \partial_\mu - \frac{ig_L}{2} W_\mu^i \cdot \sigma^i - \frac{ig_Y}{2} B_\mu \tag{1.13}$$

where the covariant derivative for the $SU(2)$ part can be written as

$$W_\mu^i \cdot \sigma^i = W_\mu^1 \cdot \sigma^1 + W_\mu^2 \cdot \sigma^2 + W_\mu^3 \cdot \sigma^3 = \begin{bmatrix} W_\mu^3 & \sqrt{2}W_\mu^+ \\ \sqrt{2}W_\mu^- & -W_\mu^3 \end{bmatrix}. \tag{1.14}$$

After expanding $(D_\mu\Phi)^\dagger(D^\mu\Phi)$ expression, one gets the terms which are arranged in parantheses multiplying v^2, hv and hh, as denoted in Equation 1.15.

$$\begin{aligned}(D_\mu\Phi)^\dagger(D^\mu\Phi) = v^2 &\left(\frac{g_L^2}{2} W_\mu^- W^{\mu+} + \frac{g_L^2}{8} W_\mu^3 W^{\mu 3} - \frac{g_L g_Y}{4} W_\mu^3 B^\mu + \frac{g_Y^2}{8} B_\mu B^\mu\right) \\ + hv &\left(\frac{g_L^2}{\sqrt{2}} W_\mu^- W^{\mu+} + \frac{g_L^2}{2\sqrt{2}} W_\mu^3 W^{\mu 3} - \frac{g_L g_Y}{\sqrt{2}} W_\mu^3 B^\mu + \frac{g_Y^2}{2\sqrt{2}} B_\mu B^\mu\right) \\ + hh &\left(\frac{g_L^2}{2} W_\mu^- W^{\mu+} + \frac{g_L^2}{4} W_\mu^3 W^{\mu 3} - \frac{g_L g_Y}{2} W_\mu^3 B^\mu + \frac{g_Y^2}{4} B_\mu B^\mu\right),\end{aligned} \tag{1.15}$$

where W_μ^+ and W_μ^- are defined as, respectively

$$W_\mu^+ = \frac{1}{\sqrt{2}}(W_1 - iW_2) \qquad W_\mu^- = \frac{1}{\sqrt{2}}(W_1 + iW_2) \tag{1.16}$$

It turns out that the terms in the v^2 parantheses in Equation 1.15 are the mass terms of weak gauge bosons. These bosons acquire their masses depending on the magnitude of the coupling constant g. The first term represents the mass term of W^- and W^+ bosons. Nevertheless, the mass of Z boson cannot be obtained from the second, third and the fourth terms since both W^3_μ and B_μ fields both contribute to the mass of Z boson. Therefore, the mass of Z boson can be acquired only after diagonalising the second, third and the fourth terms.

$$\frac{1}{2}\begin{pmatrix} W^3_\mu & B_\mu \end{pmatrix}\begin{pmatrix} g_L^2 & -g_L g_Y \\ g_L g_Y & g_Y^2 \end{pmatrix}\begin{pmatrix} W^3_\mu \\ B_\mu \end{pmatrix} = \begin{pmatrix} A_\mu & Z_\mu \end{pmatrix}\begin{pmatrix} a & 0 \\ 0 & b \end{pmatrix}\begin{pmatrix} A_\mu \\ Z_\mu \end{pmatrix}. \tag{1.17}$$

Then, A_μ, Z_μ, W_μ and B_μ can be obtained as follows

$$W^3_\mu = \cos\theta A_\mu - \sin\theta Z_\mu \quad B_\mu = -\sin\theta A_\mu + \cos\theta Z_\mu$$

$$Z_\mu = -\sin\theta W^3_\mu + \cos\theta B_\mu \quad A_\mu = \cos\theta W^3_\mu + \sin\theta B_\mu\,, \tag{1.18}$$

where θ is called the "Weinberg angle" and responsible for the mixing. It is represented in the following way

$$\sin\theta = \frac{g_Y}{\sqrt{g_Y^2 + g_L^2}} \quad \cos\theta = \frac{g_L}{\sqrt{g_Y^2 + g_L^2}} \tag{1.19}$$

Then, one can obtain the following expression in which the mass terms of W^+, W^- and Z bosons can be easily seen.

$$(D_\mu\Phi)^\dagger(D^\mu\Phi) = \frac{1}{2}v^2\left[\left(\frac{g_L^2}{2}W^-_\mu W^{\mu+}\right) + (g_L^2 + g_Y^2)Z_\mu Z^\mu\right] + ... \tag{1.20}$$

In Eq. 1.20, the masses of W^- and W^+ bosons depend only on the constant g_L whereas the mass of Z boson depends on both the constants g_L and g_Y. After the diagonalisation process, the mass of the field A is obtained to be zero which represents to the massless photon. With all these physical states of gauge fields, the kinetic part of the Higgs Lagrangian vacuum takes the following form

$$\frac{g_L^2 v^2}{4}W^{\mu+}W_{\mu-} + \frac{1}{2}\frac{(g_L^2 + g_Y^2)}{4}Z^\mu Z_\mu + 0A^\mu A_\mu \tag{1.21}$$

and the predictions for the tree level physical masses of gauge bosons are

$$M_W = \frac{g_L v}{2}, \qquad M_Z = \frac{gv}{2} = \frac{M_W}{\cos\theta_W}, \qquad M_A = 0\,, \tag{1.22}$$

where g = $\sqrt{g_L^2 + g_Y^2}$ and the photon (A_μ) remains massless. The numerical values of $W^\pm$ and Z boson masses are approximately calculated to be $M_{W^\pm} \approx 78$ GeV and $M_Z \approx 89$ GeV. When the loop corrections are included, they add to the prediction of tree-level calculation by roughly 2 GeV, and these estimates achieve to a complete agreement with the observed masses.

$$M_W = 80.398 \pm 0.025 \text{ GeV}, \qquad M_Z = 91.1876 \pm 0.0021 \text{ GeV}\,. \tag{1.23}$$

1.2 Challenges of the Standard Model

Although the SM is consistent with experimental results in almost all predictions, it is still far from being a complete theory due to numerous unexplained arbitrary parameters and unexplained phenomena. Some of the problems of the SM are summarized as follows:

Gauge Hierarchy Problem: In the SM, a doublet Higgs field is introduced to generate masses for weak gauge bosons and fermions. When the Higgs boson mass is calculated at tree level, its mass is obtained to be around electroweak scale. Besides that, the Higgs boson mass must remain stable in a theoretical consistent model. However, quantum corrections from each particle that couples directly or indirectly to the Higgs field yield very large contributions to Higgs boson mass. This is known as "Gauge Hierarchy Problem". This problem will be analysed in more detail in subsection 1.2.1.

Neutrino Masses and Mixings: Right-handed neutrinos have not been observed experimentally thus and they are not included in the SM. Therefore, left-handed neutrinos cannot acquire their masses even after the electroweak symmetry breaking since the mass term contains both left and right-handed spinors. Even though neutrino masses are predicted to be much lighter compared to the other fermions, the experimental measurements indicate that the neutrinos must have mass.

Baryon Asymmetry Problem: The SM cannot explain the dominance of matter

with respect to anti-matter. There is some convincing evidence that the amounts of matter and anti-matter should be equal at high energies as the solution of Dirac equation described. However, as the temperature decreases after the Big Bang, this symmetry is somehow broken. As a result, we live in a matter dominated universe. The source of this asymmetry can be explained with the CP violation, which was firstly observed in neutral Kaon meson. However, the amount of CP violation in the SM is not sufficient to generate the observed baryon asymmetry in the universe.

Dark Matter: Based on the cosmological observations, the Standard Model can only explain about 4% of the universe. This observation states that 23% of the energy density of the universe must consist of dark matter which does not interact via electromagnetic interactions. In the SM, there is no suitable candidate particle for dark matter, which is proposed to interact weakly with Standard Model particles.

Family Problem: All observed matter is made up of only the first family (ν_e, e^-, u, d). However, the existence of two other families (ν_μ, μ^-, c, s) and (ν_τ, τ^-, t, b) has been proved by experiments. The second and third families are just heavier copies of the first family and they eventually decay into the first family particles, and do not play any role in generating the existent matter. Hence, the SM has no a proper explanation to the question of why the second and third families of quarks and leptons exist in the universe.

Fermion Masses: It seems that Higgs mechanism can precisely explain the fermion masses. However, the value of the fermion masses is proportional to the Yukawa coupling, which describes the strength of the interaction of Higgs boson and fermions. Yet these couplings cannot be determined in the SM and are expressed as free parameters in the theory.

Gauge Symmetry Problem: The mathematical framework of the SM is a direct product of three gauge groups $SU(3)_C \otimes SU(2)_L \otimes U(1)_Y$ with their different corresponding arbitrary gauge couplings. However, the SM does not provide any deep explanation to understand the origin of the SM gauge symmetry. In addition, there is no understanding for the parity violating chiral feature of electroweak part of the SM. Moreover, since the hypercharges of fermions under the corresponding gauge group are assigned to obtain the correct electric charge of each fermion, they are completely arbitrary quantum numbers in the SM.

Electrical Charge Quantization: The Standard Model has no explanation to the question of why the electric charges of particles are always quantized as multiples of $e/3$ to

form neutral atoms and stabilize the matter.

Gauge Coupling Unification: According to the Standard Model, gauge couplings corresponding to three fundamental forces do not unify at any energy scale. However, at high energies,, only one single symmetry group and the corresponding gauge coupling is proposed, included in Grand Unified Theories (GUT). Since the SM is a valid theory at low scales, the corresponding grand unified theory has the SM as a subgroup, and the breaking mechanism can enlighten the origin of the SM gauge groups. On the other hand, in other extended models such as supersymmetry, the gauge couplings unify at Grand Unification Scale ($M_{GUT} \approx 10^{16}$ GeV) and it provides a strong motivation for supersymmetric (SUSY) GUTs.

1.2.1 Gauge Hierarchy Problem

As summarized briefly above, one of the most significant problems of the SM is known as the "Gauge Hierarchy Problem". This arises from the contributions to the Higgs boson mass resulting from quantum corrections, when we take the loop level corrections into account. Every particle that interacts with the Higgs field generates very large contributions to its mass. If there is no other accepted theory between the Plank scale and electroweak scale, the Planck scale can be taken as the cut-off scale (Λ_{UV}). In this way, radiative corrections to the Higgs boson mass squared have scale of 10^{38} GeV^2. Those quantum corrections depend on Yukawa couplings, the self interaction coupling of Higgs boson and gauge boson couplings as represented in Fig. 1.2. These contributions diverge quadratically depending on the cut-off scale as indicated in Eq. 1.24.

$$m_h^2 = m_0^2 + \frac{1}{16\pi^2}\left(\frac{3}{4}g_1^2 + \frac{9}{4}g_2^2 + 3\lambda_h - 12\lambda_t^2\right)\wedge_{\mathrm{UV}}^2 , \tag{1.24}$$

where λ_h, λ_t, g_2, and g_1 are the Higgs quartic, top Yukawa, $SU(2)_L$, and hypercharge gauge couplings, respectively. Here m_0 is the bare Higgs mass parameter that appears in the Lagrangian prior to renormalization, and m_h is the renormalized quadratic term which determines the value of the physical Higgs mass. Contributions to Higgs boson mass are much larger than Higgs boson's own mass. The amount of required for fine-tuning the Higgs mass to its measured value and to cancel quantum corrections in SM is temendous. In the SM, quadratic divergences occur only in the Higgs sector because fermions and bosons have chiral and gauge symmetries respectively to protect their own masses, and they depend on the cut-off scale (Λ_{UV}) logarithmically. However, the Higgs boson mass is not preserved by any

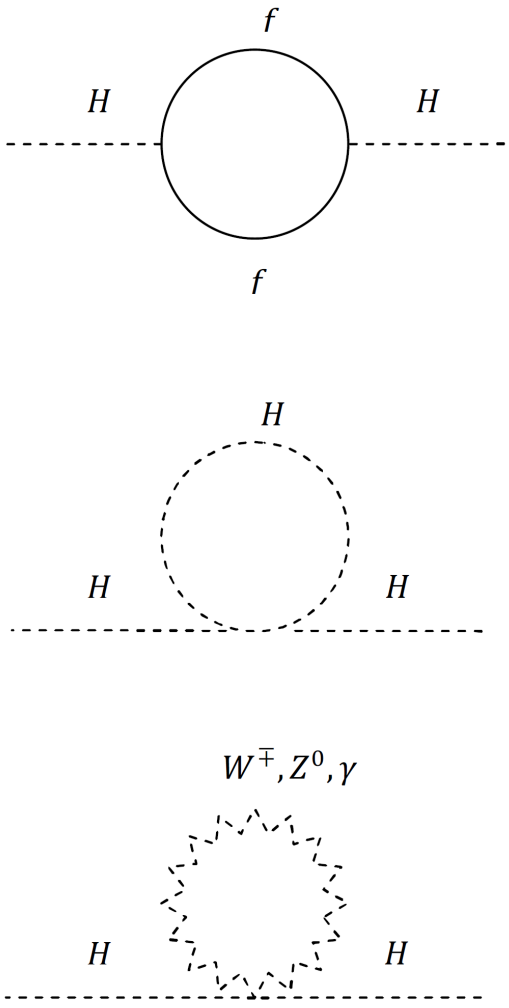

Figure 1.2: Quantum corrections to Higgs mass after interacting with fermions, with itself (top) and gauge bosons (bottom) respectively.

symmetry.

As indicated in Eq. 1.24, bosonic and fermionic loops give contributions with different sign. Therefore, in supersymmetry (SUSY) these contributions can cancel in an elegant way by defining a fermionic partner for each boson and vice versa as illustrated in Fig. 1.3. In order to cancel the contributions in Eq. 1.24 resulting from the fermion loop, the coupling of the fermion loop and the coupling of the corresponding bosonic superpartner must be equal. In addition to that, the higgsino which is the fermionic superpartner of Higgs boson, counters the Higgs contribution in Eq. 1.24. In order to cancel this contribution, two Higgs bosons are required in the theory. As we will discuss further in subsection 2.2.1, two Higgs doublets must indeed exist in SUSY because of the holomorphy of the superpotential. Therefore, all

ultraviolet divergences can be naively cancelled in SUSY.

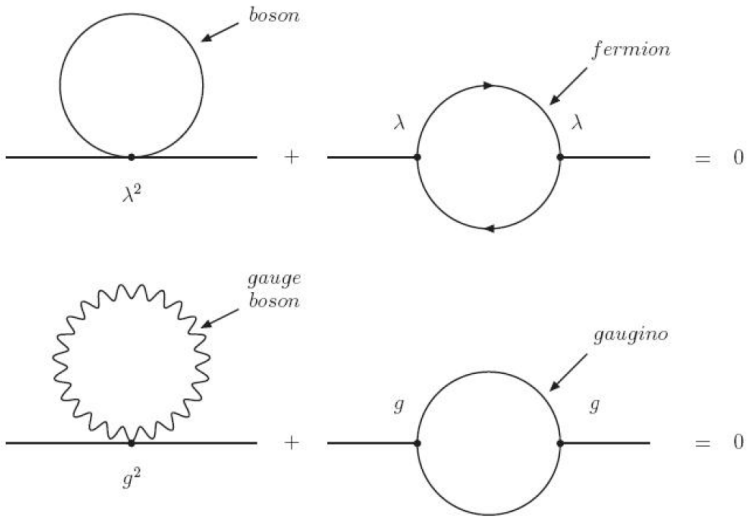

Figure 1.3: Supersymmetry (SUSY) defines a superpartner to each particle to cancel quadratic quantum corrections to the Higgs mass.

1.3 New Physics Hunter: Extended Summary of the Thesis

The aim of this thesis is to investigate various aspects of phenomenology of new physics beyond the Standard Model (SM) in the context of extensions of supersymmetric & non-supersymmetric realisations. The thesis is organized as follows.

In chapter 2, we introduce the motivation for Minimal Supersymmetric Standard Model (MSSM) and briefly discuss its field content and interactions. We conclude with the shortcomings of MSSM which lead us to explore the models discussed in chapter 3, chapter 4 and chapter 5. The detailed analysis on the mass spectrum and Higgs boson decays is presented in the supersymmetric standard model extended by $U(1)_{\rm B-L}$ symmetry (BLSSM) [30, 31].

In chapter 3, we study the low scale predictions of the supersymmetric standard model extended by $U(1)_{B-L} \times U(1)_R$ symmetry, obtained from $SO(10)$ breaking via a left-right supersymmetric model, imposing universal boundary conditions [1]. Two singlet Higgs fields are responsible for the radiative $U(1)_{B-L} \times U(1)_R$ symmetry breaking, and a singlet fermion S is introduced to generate neutrino masses through an inverse seesaw mechanism.

The lightest neutralino or sneutrino emerge as dark matter candidates, with different low scale implications. We find that the composition of the neutralino lightest supersymmetric particle (LSP) changes considerably depending on the neutralino LSP mass, from roughly half $U(1)_R$ bino, half minimal supersymmetric model (MSSM) bino, to a singlet higgsino, or completely dominated by the MSSM higgsino. The sneutrino LSP is statistically much less likely, and when it occurs it is a 50-50 mixture of right-handed sneutrino and the scalar $\tilde{S}$. Most of the solutions consistent with the relic density constraint survive the XENON 1T exclusion curve for both LSP cases. We compare the two scenarios, investigate parameter space points and find consistency with the muon anomalous magnetic moment only at the edge of a 2σ deviation from the measured value. However, we find that the sneutrino LSP solutions could be ruled out completely by the strict reinforcement of the recent Z' mass bounds. We finally discuss collider prospects for testing the model.

In chapter 4, we perform a comprehensive analysis of the secluded UMSSM model, consistent with present experimental constraints [2]. We find that in this model the additional Z' gauge boson can be leptophobic without resorting to gauge kinetic mixing and, consequently, also d-quark-phobic, thus lowering the LHC bounds on its mass. The model can accommodate very light singlinos as DM candidates, consistent with present day cosmological and collider constraints. Light charginos and neutralinos are responsible for muon anomalous magnetic predictions within 1σ of the measured experimental value. Finally, we look at the possibility that a lighter Z', expected to decay mainly into chargino pairs and followed by the decay into lepton pairs, could be observed at 27 TeV.

In chapter 5, we test E_6 realisations of a generic $U(1)'$ extended Minimal Supersymmetric Standard Model (UMSSM), parametrised in terms of the mixing angle pertaining to the new $U(1)'$ sector, θ_{E_6}, against all currently available data, from space to ground experiments, from low to high energies [3]. We find that experimental constraints are very restrictive and indicate that large gauge kinetic mixing and $\theta_{E_6} \approx -\pi/3$ are required within this theoretical construct to achieve compliance with current data. The consequences are twofold. On the one hand, large gauge kinetic mixing implies that the Z' boson emerging from the breaking of the additional $U(1)'$ symmetry is rather wide since it decays mainly into WW pairs. On the other hand, the preferred θ_{E_6} value calls for a rather specific E_6 breaking pattern different from those commonly studied. We finally delineate potential signatures of the emerging UMSSM scenario in both Large Hadron Collider (LHC) and in Dark Matter (DM) experiments.

In chapter 6, we study mass bounds of the W_R gauge boson in generic left-right symmetric models [4]. Assuming that the gauge bosons couple universally to quarks and leptons, we allow different gauge couplings $g_R \neq g_L$ and mass mixing, $V^L_{CKM} \neq V^R_{CKM}$ in the left and right sectors. Imposing constraints from collider experiments and K^0, B_d, B_s physics, we investigate scenarios where W_R is lighter, or heavier than the right handed neutrino ν_R. In these scenarios, W_R mass bounds can be considerably relaxed, while Z_R mass bounds are much more stringent. In the case where $M_{W_R} \leq M_{\nu_R}$, the experimental constraints come from $W_R \to tb$ and $W_R \to jj$ channels, while if $M_{W_R} \geq M_{\nu_R}$, the dominant constraints come from $W_R \to \ell\ell jj$. The observed (expected) limits in the two-dimensional (M_{W_R}, M_{ν_R}) mass plane excluded at 95% confidence level extend to approximately M_{W_R}= 3.1 (3.3) TeV in the ee channel and 3.3 (3.4) TeV in the ($\mu\mu$) channel, for a large range of right-handed neutrino masses up to M_{ν_R}= 2.1 (2.1) TeV in the ee channel and 2.6 (2.5) in the ($\mu\mu$) channel, representing a significant relaxation of the mass bounds.

In chapter 7, we perform a consistent analysis of the alternative left-right symmetric model emerging from E_6 grand unification [5]. We include a large set of theoretical and experimental constraints, with a particular emphasis on dark matter observables and collider signals. We show that the exotic neutrino inherent to this class of models, the scotino, is a viable candidate for dark matter satisfying relic density and direct detection constraints. This has strong implications on the scotino mass restricting it to lie in a narrow window, as well as on the spectrum of Higgs bosons, rendering it predictable, with a few light scalar, pseudoscalar and charged states. Moreover, we also show that the extra charged W' gauge boson can be light, and investigate the most promising signals at the future high-luminosity upgrade of the LHC. Our findings show that the most optimistic cosmologically-favoured scenarios should be observable at 5σ, whilst others could leave visible hints provided the background is under good control at the systematical level.

In chapter 8, we conclud the predictions of supersymmetric & non-supersymmetric realisations, and discuss briefly directions for future research.

Chapter 2

Minimal Supersymmetric Extention of the Standard Model

In this section, we describe the basics of the Minimal Supersymmetric Standard Model (MSSM) without going into all the details. Detailed reviews and books can be found in the literature [32–48].

2.1 Motivation

The "Gauge Hierarchy Problem" of the Standard Model is the most important problem regarding the Higgs mass stabilization. Supersymmetry (SUSY) suggests an elegant solution for Gauge Hierarchy Problem by relating bosonic and fermionic degrees of freedom of particles. In Supersymmetry a cancellation of the quadratic corrections to the Higgs mass is obtained by introducing a boson partner for each fermion and a fermion partner for each boson, which are called superpartners. For this purpose, SUSY requires a transformation, so-called a supersymmetric transformation, which turns a bosonic state into a fermionic state and vice versa. Therefore, SUSY can be simply described as a symmetry that provides a connection between fermions and bosons. The idea of a symmetry between bosons and fermions has been introduced in two-dimensional string theory. Later, in 1974, Wess and Zumino constructed the first four dimensional supersymmetric field theory. SUSY generators represented by $\widehat{Q}$ are constructed in such a way that, when they act upon a bosonic state, they transform it to a fermionic one and vice versa.

$$\widehat{Q}|\text{Fermion}\rangle = |\text{Boson}\rangle, \qquad \widehat{Q}|\text{Boson}\rangle = |\text{Fermion}\rangle\,. \tag{2.1}$$

Since SUSY operators $\widehat{Q}$ alter only the spin of the particles by $1/2$ unit, all quantum numbers of the particles and superpartners are exactly the same except for their spin. Interestingly, two successive SUSY transformations end with the initial state, but they shift the field in spacetime. In this context, SUSY is the only known symmetry that also relates the internal symmetries to the spacetime symmetries.

2.2 SUSY Formalism

In the Wess-Zumino model, the SUSY algebra is not closed off-shell. As we stated before, SUSY requires the number of bosonic and fermionic degrees of freedom to be equal in supermultiplets. As a Weyl spinor has two complex components, it contains four degree of freedom. However, in the case of on-shell fields, the equation of motion imposes two constraints which reduce the number of degree of freedom to two. Since a complex scalar field has two degrees of freedom, the number of fermionic and bosonic degrees of freedom match on-shell. However, off-shell fields do not have to satisfy the equation of motion and so the number of bosonic and fermionic degrees of freedom do not match. Therefore, SUSY algebra only closes on-shell when there is a single complex scalar field and one Weyl spinor in the theory.

SUSY can be rendered a symmetry also in the off-shell cases by adding scalar an "auxiliary field" denoted by F . Such a field provides two more bosonic off-shell degree of freedom. On the other hand, it does not have a kinetic term. F has to be zero on-shell in a model which is invariant under SUSY transformations. The degrees of freedom of the fields are listed in Table 2.1.

	On-shell	Off-shell
Φ	2	2
Ψ	2	4
F	0	2

Table 2.1: Number of bosonic and fermionic degrees of freedom in the chiral Lagrangian.

In order to get the field F to have no on-shell degrees of freedom, the equation of motion for this field is written as $F^* = F = 0$. Since the simplest real term depending on F

and F^* is FF^*, the Lagrangian takes the form as represented in Eq 2.2

$$\mathcal{L} = \partial_\mu \Phi^* \partial^\mu \Phi + \Psi^\dagger i\overline{\sigma}^\mu \partial_\mu \Psi \, . + FF^* \tag{2.2}$$

Despite of being a scalar field, dimension of field F is 2, that is, $[F] = 2$.

$$[\Phi] = 1 \qquad [\Psi] = 3/2 \qquad [F] = 2 \tag{2.3}$$

After adding the F field in our theory, the variation of each field can be represented as follows:

$$\delta\Phi = \epsilon\Psi \tag{2.4}$$

$$\delta\Psi = -i\sigma^\mu(i\sigma^2\epsilon^*)\partial_\mu\Phi + F\epsilon \tag{2.5}$$

$$\delta F = -i\epsilon^\dagger\overline{\sigma}^\mu\partial_\mu\Psi \, . \tag{2.6}$$

In order to have a interacting supersymmetric theory, one also has to deal with supersymmetric gauge theories. If we consider $U(1)$ free gauge theory, the superpartner of the photon field A_μ will be a left-chiral Weyl spinor denoted by λ and called "photino". Therefore, the summation of the kinetic terms for the photon and the photino constitutes the gauge Lagrangian represented in Eq. 2.7

$$\mathcal{L} = -\frac{1}{4}F_{\mu\nu}F^{\mu\nu} + \lambda^\dagger i\overline{\sigma}^\mu\partial_\mu\lambda \tag{2.7}$$

where transformations of the fields are described as follows

$$\delta A^\mu = \epsilon^\dagger\overline{\sigma}^\mu\lambda + \lambda^\dagger\overline{\sigma}^\mu\epsilon \tag{2.8}$$

$$\delta\lambda = \frac{i}{2}F_{\mu\nu}\sigma^\mu\overline{\sigma}^\nu\epsilon \tag{2.9}$$

$$\delta\lambda^\dagger = -\frac{i}{2}F_{\mu\nu}\epsilon^\dagger\overline{\sigma}^\nu\sigma^\mu \tag{2.10}$$

However, here again the algebra does not close off-shell. In case of on-shell, A_μ has two degrees of freedom as two transverse polarization states and the photino, represented as a left-chiral Weyl fermion, has two degrees of freedom on-shell. Nevertheless, when off-shell, a vector field A_μ has three degrees of freedom whereas a left-chiral Weyl fermion has four. Therefore, one has to add one extra bosonic degree of freedom in the form of a real scalar field which is conventionally denoted by D as indicated in Table 2.2.

	On-shell	Off-shell
A	2	3
λ	2	4
D	0	1

Table 2.2: Number of bosonic and fermionic degrees of freedom in the $U(1)$ gauge Lagrangian.

In order to guarantee that the field D has no on-shell degrees of freedom, the equation of motion for this field is written as $D = 0$. Like the auxiliary field F, dimension of the D field is also 2. Therefore, following term is added to the Lagrangian.

$$\mathcal{L}_{aux} = \frac{1}{2}D^2\,. \tag{2.11}$$

$$\mathcal{L} = \mathcal{L}_{gauge} + \mathcal{L}_{aux} = -\frac{1}{4}F_{\mu\nu}F^{\mu\nu} + \lambda^\dagger i\overline{\sigma}^\mu\partial_\mu\lambda + \frac{1}{2}D^2\,. \tag{2.12}$$

The variations of the fields after adding the D real scalar field are defined as follows:

$$\delta A^\mu = \epsilon^\dagger\overline{\sigma}^\mu\lambda + \lambda^\dagger\overline{\sigma}^\mu\epsilon\,. \tag{2.13}$$

$$\delta\lambda = \frac{i}{2}F_{\mu\nu}\sigma^\mu\overline{\sigma}^\nu\epsilon + D\epsilon\,. \tag{2.14}$$

$$\delta D = -i\epsilon^\dagger\overline{\sigma}^\mu\partial_\mu\lambda + i(\partial_\mu\lambda)^\dagger\overline{\sigma}^\mu\epsilon\,. \tag{2.15}$$

In the light of success of the special relativity, any kind of relativistic model of elementary particles should be constructed in a way that guarantees the Lorentz invariance. In this sense,

the Lagrangian and relevant operators must be consistent with the relativistic transformations of the fields. In the SM, the internal symmetries and Lorentz symmetry are not connected to each other. On the other hand, the connection between SUSY and Lorentz symmetry can be understood within the graded Lie algebra of Poincare group, in which the Poincare group generators are extended with anti-commuting operators.

The symmetry group of four-dimensional spacetime, $SL(2,C)$ is isomorphic to $SU(2)\otimes SU(2)$ which transforms differently under Lorentz transformations. Hence the spinor representation of $SL(2,C)$ should be formed by two Weyl spinors, one of which is indicated with dotted indices, while the other with the undotted ones. If one extends the Poincare algebra with the generators that transform these dotted and undotted spinors, the commutation and anti-commutation rules can be obtained as

$$\{Q_\alpha, Q_\beta\} = \{\overline{Q}_{\dot{\alpha}}, \overline{Q}_{\dot{\beta}}\} = 0\,, \tag{2.16}$$

$$\{Q^i_\alpha, \overline{Q}^j_{\dot{\beta}}\} = 2\delta^{ij}(\sigma^\mu)_{\alpha\dot{\beta}}P_\mu\,, \tag{2.17}$$

$$[P_\mu, Q^i_\alpha] = [P_\mu, \overline{Q}^i_{\dot{\alpha}}] = 0\,, \tag{2.18}$$

$$[Q^i_\alpha, M_{\mu\nu}] = \frac{1}{2}(\sigma^{\mu\nu})^\beta_\alpha Q^i_\beta\,, \tag{2.19}$$

$$[\overline{Q}^i_{\dot{\alpha}}, M_{\mu\nu}] = -\frac{1}{2}Q^i_{\dot{\beta}}(\overline{\sigma}^{\mu\nu})^{\dot{\beta}}_{\dot{\alpha}}\,, \tag{2.20}$$

where P_μ represent the generators of translations and $M_{\mu\nu}$ stand for the generators of Lorentz transformations while the spinorial indices are $\alpha, \dot{\alpha}, \beta, \dot{\beta} = 1, 2$, and the space-time indices are denoted by $\mu, \nu = 0, .., 3$ and $i, j = 1, 2, .., N$. If we apply the commutation rules given in Eqs.(2.19 and 2.20) for $M_{1,2} = J_3$, it is seen that the generators Q and $\overline{Q}$ respectively raise and lower the spin by $1/2$ when they act on to the particle state, and this is basically the definition of the SUSY transformations.

This extended algebra which provides a useful opportunity to combine statistics of particles of integer and half-integer spin by enlarging space-time symmetries is called "Super-Poincare Algebra". In this thesis, we consider only unextended $N = 1$ supersymmetry

which corresponds to one spinor of charge Q_α and its conjugate $\overline{Q}_{\dot{\alpha}}$ in order to deal with minimal particle content and to avoid the renormalizability problems in the extended SUSY models.

Despite of the fact that left handed and right handed fermions are indicated by doublets and singlets, respectively in SM, particles in SUSY can be represented in irreducible particle states, so called "supermultiplets" , where each supermultiplet contains both fermionic and bosonic states with the condition that the fermionic and bosonic degrees of freedom of each supermultiplet must be equal to each other.

$$n_F = n_B \,, \tag{2.21}$$

where the fermionic and bosonic degrees of freedom in the supermultiplet are represented as n_F and n_B, respectively. In order to construct the SUSY correctly, there are two types of supermultiplets where each fundamental particle of SM exists with its corresponding superpartner.

Chiral (Matter) Supermultiplets : A chiral supermultiplet consists of a two component chiral Weyl fermion and its corresponding superpartner as a complex scalar field. Since a two component spinor has two degrees of freedom on-shell, its corresponding superpartner must be a complex scalar field to satisfy the equality of number of degrees of freedom in supermultiplets. Chiral supermultiplets classify fermions whose left-handed parts transform differently than the right-handed parts under $SU(2)_L \otimes U(1)_Y$, as well as Higgs bosons and their fermionic superpartners, the higgsinos. Since there must be one chirality in the SUSY, instead of introducing right handed particles, conjugates of the right handed particles and corresponding right handed superpartners are included in supermultiplets.

Gauge (Vector) Supermultiplets : Vector bosons (spin 1) of SM and their fermionic (spin 1/2) superpartners are combined in one supermultiplet so-called "gauge (vector) supermultiplets". In order to conserve the equality of number of fermionic and bosonic degrees of freedom, the superpartner of the massless spin 1 vector boson must be a massless two component spin 1/2 Weyl spinor.

2.2.1 Field Content

Since MSSM shares the same gauge group $SU(3)_C \otimes SU(2)_L \otimes U(1)_Y$ with the SM, it is the simplest supersymmetric extension of the SM. Each gauge field and each fermion is replaced by a vector supermultiplet and a chiral supermultiplet, respectively. Therefore, MSSM has a minimal number of superpartners and their interactions. Since there is a corresponding superpartner for each SM particle, MSSM doubles the number of particles of the SM. Also, while the SM has one Higgs doublet, for the reason explained below, there is an extra doublet Higgs field in MSSM as demonstrated in Eq. 2.22. In the SM while d-type quark masses are gained by complex scalar Higgs field itself, the charge conjugate of the Higgs field is introduced to acquire masses to the u-type quarks. However, the holomorphic feature of the superpotential strictly prohibits any field and complex conjugate of that field to exist in the superpotential simultaneously. Since introducing complex conjugate of Higgs field is not allowed in superpotential, one Higgs doublet is not enough to give mass to all particles as it is in SM. Because of the fact that Yukawa interaction terms can be obtained only from superpotential, a second doublet Higgs field is required in the MSSM as represented in Eq. 2.22. In order to conserve hypercharge, the second Higgs doublet (H_d) is introduced by assigning it -1 hypercharge ($Y_{H_u} = +1$ and $Y_{H_d} = -1$).

$$H_u = \begin{pmatrix} H_u^+ \\ H_u^0 \end{pmatrix} \qquad H_d = \begin{pmatrix} H_d^0 \\ H_d^- \end{pmatrix} \tag{2.22}$$

The superpotential for MSSM is now written as

$$\hat{W} = \mu \hat{H}_u \cdot \hat{H}_d + h_u \hat{Q} \cdot \hat{H}_u \hat{u}_R^c + h_d \hat{Q} \cdot \hat{H}_d \hat{d}_R^c + h_e \hat{L} \cdot \hat{H}_d \hat{e}_R^c \,, \tag{2.23}$$

where H_u, H_d, Q, L, u_R^c, d_R^c, e_R^c denote the superfields and h_u, h_d, h_e stand for dimensionless Yukawa couplings. The dot product in the superpotential can be expressed using the anti-symmetric parameter $\epsilon^{\alpha\beta}$ such as $\mu \hat{H}_u \cdot \hat{H}_d = \mu \epsilon^{\alpha\beta} (H_u)_\alpha (H_d)_\beta$. Instead of the antisymmetric parameter $\epsilon^{\alpha\beta}$, $\mu \hat{H}_u \cdot \hat{H}_d = \mu \hat{H}_u^T (i\sigma_2) \hat{H}_d$ can be used as an alternative notation.

2.2.2 SUSY Breaking

Supercharges commute with the momentum operator as indicated in Eq. 2.24. So, when supercharges act on a state, the eigenvalue of $P^\mu P_\mu$ remains unchanged as in the follow-

ing.

$$[P_\mu, Q_\alpha] = 0\,, \tag{2.24}$$

$$P^\mu P_\mu |\Psi\rangle = m^2 |\Psi\rangle \tag{2.25}$$

$$Q_\alpha |\Psi\rangle = m^2 |\Psi\rangle\,. \tag{2.26}$$

Therefore, all the particles in the same supermultiplet have the same mass. However, if the bosonic partner of electron, so the-called selectron, was as light as the electron, this would mean that we would have seen it by now. Since selectrons are bosons, they are not restricted by Pauli-Exclusion Principle. Therefore, all selectron could be located in the ground state and this would be totally disaster. Fortunately, this kind of particle degeneracy does not exist in nature.

SUSY can be broken by adding some terms to the Lagrangian which are not invariant under SUSY transformations. These SUSY breaking interactions cancel divergences, property which is the main motivation of SUSY. Therefore, only softly-broken terms are included into the Lagrangian as in Eq. 2.27 in order to maintain main motivation of SUSY.

$$\begin{aligned}
\mathcal{L}_{\cancel{\text{SUSY}}} = &-\frac{1}{2}(M_1 \widetilde{B}\widetilde{B} + M_2 \widetilde{W}\widetilde{W} + M_3 \widetilde{g}\widetilde{g}) + \text{h.c.} \\
&-m_{H_u}^2 H_u^\dagger H_u - m_{H_d}^2 H_d^\dagger H_d - (b H_u H_d + \text{h.c.}) \\
&-m_Q^2 \widetilde{q}^\dagger \widetilde{q} - m_L^2 \widetilde{l}^\dagger \widetilde{l} - m_u^2 \widetilde{u}_R^\dagger \widetilde{u}_R - m_d^2 \widetilde{d}_R^\dagger \widetilde{d}_R - m_e^2 \widetilde{e}_R^\dagger \widetilde{e}_R \\
&-(A_u \widetilde{u}_R \widetilde{q} H_u + A_d \widetilde{d}_R \widetilde{q} H_d + A_e \widetilde{e}_R \widetilde{l} H_d)\,.
\end{aligned} \tag{2.27}$$

In order to break supersymmetry, spontaneous symmetry breaking (SSB) can also be used as discussed in the SM. In case of SSB, charges that generate the symmetry do not annihilate the ground state.

$$Q|0\rangle \neq 0\,. \tag{2.28}$$

In SUSY, supercharges Q_1 and Q_2 do not annihilate the ground state. Then, a non-zero VEV of the Hamiltonian is obtained.

$$\langle 0|H|0\rangle > 0\,. \tag{2.29}$$

In free space, the kinetic energy part of the Hamiltonian can be taken as zero which leaves only the potential energy part. Since the scalar field is the only field that has non-zero VEV, we can construct

$$\langle 0|V(\phi)|0\rangle > 0 \tag{2.30}$$

The auxiliary fields yield the potential energy as in the following.

$$V(\phi_i) = F_i F_i^\dagger + \frac{1}{2}D^2\,, \tag{2.31}$$

where $F_i = \frac{\partial W}{\partial \phi_i}$ and $D = q_i\phi_i^\dagger\phi_i - \xi$ for Abelian gauge theories. In this case, a term ξD, so-called Fayet-Illiopoulos term, is included into the Lagrangian. This term is important for D-type SUSY breaking. However, gauge invariance prevents the existence of a Fayet-Illiopoulos term for non-Abelian theories and a D^aD^a term is included to the Lagrangian, where $D^a = g\phi_i^\dagger T^a\phi_i$.

2.2.3 R-parity

In addition to conservation of hypercharge, baryon and lepton number are also conserved in Eq. 2.23. However, it is possible to add some gauge invariant extra terms to superpotential as represented in Eq. 2.32. Even though these terms conserve hypercharge, and they are not restricted by gauge invariance and renormalization, the extra terms in Eq. 2.32 violate baryon and lepton number conservation.

$$\hat{W}' = \mu'\hat{L}\cdot\hat{H}_u + \lambda_1\hat{L}\cdot\hat{L}\hat{e}_R^c + \lambda_2\hat{L}\cdot\hat{Q}\hat{d}_R^c + \lambda_3\hat{u}_R^c\hat{d}_R^c\hat{d}_R^c\,, \tag{2.32}$$

where the lepton numbers are $L = +1$ for $\hat{L}_i$, $L = -1$ for $\hat{e}_R^c$ and $L = 0$ for all other super-multiplets and $B = +1/3$ for $\hat{Q}_i$, $B = -1/3$ for $\hat{u}_R^c, \hat{d}_R^c$ and $B = 0$ for all others. Therefore, the first three terms in Eq. 2.32 violate conservation of lepton number by 1 unit and the last term in Eq. 2.32 violates the conservation of baryon number by 1 unit. However, baryon and lepton number violating processes have not been observed in experiments. Besides, if these violating terms are allowed, then the proton, which constitutes the matter, decays rapidly. Proton decay through $\tilde{s}_R^*$ interaction is represented in Fig. 2.1. Therefore, a new symmetry so-called "R-parity" is introduced to prohibit rapid proton decays and to make it a stable particle. R-parity is defined by introducing opposite R-parity numbers to the scalar and

fermion components of a chiral superfield as follows:

$$P_R = (-1)^{3B+L+2S}\,, \tag{2.33}$$

where B, S and L denote baryon number, spin and lepton number, respectively.

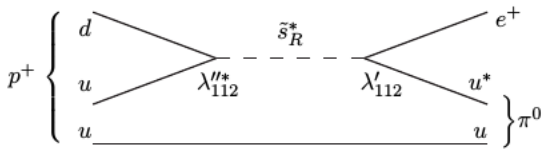

Figure 2.1: Proton decays via R-parity violating $\tilde{s}^*_R$ interactions.

R-parity introduces opposite R-parity numbers to the scalar and fermion components of a chiral superfield due to the spin dependence as (-1)^{2S}. Considering the dependence on the baryon and lepton numbers, all SM particles and Higgs bosons have $P_R = +1$ while all superpartners have $P_R = -1$. Since this new symmetry is not conserved in Eq 2.32, these R-parity violating interactions interactions become strictly prohibited and the proton keeps its stability safely. R-parity brings two significant consequences that I remark upon below

• Since the initial state in the LHC experiments involve only the SM particles ($P_R = +1$), the conservation of R-parity allows only the processes with final states including an even number of superpartners ($P_R = -1$).

• In the decay chain of a superpartner, the lightest supersymmetric particle (LSP) which cannot decay into a SM particle in the final state due to the conservation of R-parity must be a stable particle. Therefore, at least one sparticle must exist as LSP in the final state. If the LSP is neutral, it could be evaluated as a candidate for non-baryonic dark matter candidate.

2.3 The Shortcomings of MSSM

Since sparticles are not observed in experiments at the same energy level as their corresponding SM particles, SUSY indeed is a broken symmetry. In order to cancel one loop radiative corrections from the top quark, the corresponding top squark mass should be around 1 TeV. Therefore, the soft SUSY breaking scale must be above the electroweak scale. Although this rescaling creates gauge hierarchy problem one more time, the required fine-tuning is not so

much. In this way, MSSM reduces gauge hierarchy problem of SM to the “little hierarchy problem".

One of the most important problems of the MSSM is the μ problem. The bi-linear mixing of the MSSM Higgs doublets are parmetrized by the μ-term in the superpotential, and this term is crucial in the electroweak symmetry breaking (EWSB). In this context, the EWSB condition can determine the value of μ-term up to its sign. Despite its connection to the EWSB, the μ-term can be at any scale, since it preserves SUSY. This is called μ-problem in MSSM. More explicitly, the Z boson mass can be written as a function of the SUSY scale MSSM parameters defined at SUSY scale beyond tree level as seen in Eq. 2.34.

$$\frac{M_Z^2}{2} = \frac{M_{H_d^2} + \sum_d - (M_{H_u^2} + \sum_u) \tan\beta^2}{\tan\beta^2 - 1} - \mu^2 \,, \tag{2.34}$$

where $\sum_{u,d}$ are loop corrections at the SUSY scale. The fine tuning measure can be defined as in Eq. 2.35.

$$\mathrm{FT} = \Delta_{\mathrm{EW}} = \mathrm{max_i} \left| \frac{\mathrm{C_i}}{\mathrm{M_Z^2/2}} \right| \,, \tag{2.35}$$

where the coefficients C_i are defined as

$$C_{M_{H_d}} = \frac{M_{H_d}^2}{\tan^2\beta - 1}, \qquad C_{\sum_d} = \frac{\mathrm{max}(\sum_{\mathrm{d}})}{\tan^2\beta - 1}$$

$$C_{M_{H_u}} = \frac{M_{H_u}^2 \tan^2\beta}{\tan^2\beta - 1}, \qquad C_{\sum_u} = \frac{-\mathrm{max}(\sum_{\mathrm{u}}) \tan^2\beta}{\tan^2\beta - 1}$$

$$C_\mu = -\mu^2 \,. \tag{2.36}$$

In other words, the fine tuning measures the maximum contribution relative to the squared Z-mass/2 [49, 50]. If one of these single contributions is large, the other contributions have to be “fine-tuned" to compensate.

Electroweak breaking in the MSSM requires substantial fine-tuning, mainly due to the smallness of the tree-level Higgs quartic coupling. Hence the fine tuning is efficiently reduced in supersymmetric models with larger tree-level Higgs quartic coupling, and this happens naturally when the breaking of SUSY occurs at a low scale. [51–57].

Chapter 3

Supersymmetric $\mathrm{U}(1)_{B-L}\times\ \mathrm{U}(1)_R$ model (BLRSSM)

3.1 Introduction

The discovery of the SM-like Higgs boson, while completing the particle content of the Standard Model (SM), has not slowed down the search for new physics. As it stands, the SM may be viable over a certain energy range, but is incomplete, since it fails to explain properties such as the hierarchy problem, neutrino masses, cosmological inflation, and dark matter. As well, a Higgs mass of 125 GeV presents a problem for the SM (*e.g.*, electroweak vacuum instability), and for most of its extensions. Thus constructing and studying viable alternatives, models which aim to solve some of the outstanding problems in SM, are both justified and necessary. Out of these, supersymmetry presents a compelling solution to the hierarchy problem and a clear one for dark matter. However, in its minimal incarnation, the minimal supersymmetric model (MSSM), it shares some of its outstanding problems with the SM.

Some of these issues may be resolved in models with extended gauge groups. In these models, additional D-term contributions to the Higgs mass matrices weaken considerably MSSM mass limits [58–60]. Depending on the models studied, these models can also resolve additional problems of MSSM. For instance, models with left-right symmetry [61] can yield neutrino masses via the seesaw mechanism [62–64].

In [65], an extended supersymmetric model based on $SU(3)_C \times SU(2)_L \times U(1)_R \times$

$U(1)_{B-L}$ was proposed. The model can be embedded in $SO(10)$ SUSY-GUT, much like the left-right supersymmetric model, and generate a new seesaw mechanism for neutrino masses. The factor $U(1)_R$ can be thought off as remnant of a more complete $SU(2)_R$. Unlike the left-right supersymmetric model, which requires Higgs triplet representations with vacuum expectation values (VEV) $v_R \sim 10^{15}$ GeV for obtaining neutrino masses and gauge unification, the symmetry in this model can be broken by singlet Higgs bosons (thought of as remnants of a doublet representation in left-right models), with VEVs in the TeV range, while still allowing for gauge coupling unification. In [65], the smallness of neutrino masses was explained as based on an inverse seesaw mechanism. The general features of the TeV scale soft-supersymmetry breaking parameters were explored in [66], outlining conditions for models with intermediate scales obtained from breaking $SO(10)$. The Higgs sector of the model was further explored, showing that a larger mass than that predicted by MSSM can be obtained. The parameter space was further explored in [67], where benchmarks, branching ratios, as well as lepton violation constraints were analyzed.

In this work, we concentrate on investigating, discriminating, and restricting the parameter space of the model using dark matter studies. We include up-to-date constraints on the spectrum coming from the Higgs signal strengths and mass data, and including LHC restrictions on squark and gluino masses, constraints on flavor parameters from the B sector, as well as recent lower limits on the Z' mass. Assuming universal scalar and gaugino masses, we show that the lightest supersymmetric particle (LSP) can be the sneutrino (which is different from the usual in this scenario, being a mixture of the right sneutrino and a gauge singlet fermion introduced to generate the inverse seesaw mechanism); or the lightest neutralino (which is favored to be a mixture of the two $U(1)$ binos). Relic density and indirect dark matter detection severely restrict the parameter space, as indeed does the recent limit on the Z' mass [6]. Within the parameter space allowed by dark matter limits, we analyze the consequences on sparticle spectra, the neutral Higgs sector and on the anomalous magnetic moment of the muon, which shows more than 3 σ [68] discrepancy with the SM prediction. Finally we investigate the possibilities of testing the model at the LHC.

Our work is organized as follows. We provide a brief description of the model in Sec. 6.2, capitalizing on more complete descriptions which have appeared previously. In Sec. 7.3 we describe in detail the parameters of the model and constraints imposed on them. Dark matter phenomenology is explored in Sec. 3.4, for both neutralino LSP 3.4.1 and sneutrino LSP 3.4.2. We then look at the consequences of our findings and compare the two scenarios in Sec. 3.5, for the sparticle spectrum, the Higgs sector 3.5.1 and the anomalous magnetic

moment of the muon 3.5.2, and show that imposing the Z' strict mass limits basically rules out the sneutrino DM solutions in 3.5.3. We discuss possibilities for detection in Sec. 7.6. We leave some relevant formulas for the Appendix.

3.2 Model Description

In this section, we describe the supersymmetric model under investigation briefly. This model, based on $SU(3)_c \times SU(2)_L \times U(1)_R \times U(1)_{B-L}$ (thereafter referred to as the BLRSSM) was first introduced in [65] and further studied in [66, 67, 69]. The model emerges from breaking of supersymmetric $SO(10)$ to the SM through the following intermediary steps,

$$SO(10) \to SU(3)_C \times SU(2)_L \times SU(2)_R \times U(1)_{B-L} \to SU(3)_C \times SU(2)_L \times U(1)_R \times U(1)_{B-L}$$
$$\to SU(3)_C \times SU(2)_L \times U(1)_Y.$$

The advantages of this model are

- It is obtained by breaking of SO(10) through a left-right symmetric model, thus inheriting some of its attractive features [61, 70];
- It is able to explain neutrino masses by the inverse seesaw mechanism [65];
- It preserves gauge coupling unification of the MSSM, even when the breaking scale in the last step is of the order of the electroweak scale [66];
- It resolves the MSSM Higgs mass problem by yielding larger Higgs masses through additional D-terms in the soft-breaking potential, without resorting to heavy particles [66];
- It could yield signals differentiating it from MSSM, which may lie in different regions of SUSY parameter space;
- It could provide different dark matter candidates and phenomenology, which in turn informs the study of direct and indirect searches.

The particle content of the model contains, in addition to the SM particles:

1. In the fermionic/matter sector, an additional (right-handed) neutrino N_i^c, required for anomaly cancellation, and an additional singlet fermion S, needed for generating

neutrino masses. Both these fermions come in 3 families and are accompanied by their scalar partners;

2. In the bosonic/Higgs sector, two new Higgs fields, $\mathcal{X}_R$ and $\overline{\mathcal{X}}_R$, remnants of $SU(2)_R$ doublets, needed to break $U(1)_R \times U(1)_{B-L} \to U(1)_Y$, and their fermionic partners;

3. In the gauge sector, an additional neutral gauge field, Z', which emerges from the mixing of the neutral gauge fields of $SU(2)_L, U(1)_R$ and $U(1)_{B-L}$, (W^0, B_R, B_{B-L}), and its fermionic partner.

In a sense, the model described here is minimal: however it requires an extra $\mathcal{Z}_2$ matter parity to avoid breaking of R-parity [67].

The superpotential in this model is described by

$$\begin{aligned} W &= \mu H_u H_d + Y_u^{ij} Q_i H_u u_j^c - Y_d^{ij} Q_i H_d d_j^c - Y_e^{ij} L_i H_d e_j^c \\ &+ Y_\nu^{ij} L_i H_u N_i^c + Y_s^{ij} N_i^c \mathcal{X}_R S - \mu_R \overline{\mathcal{X}}_R \mathcal{X}_R + \mu_S S S \,, \end{aligned} \tag{3.1}$$

where the first line of Eq.(4.1) contains the usual terms of the MSSM, while the second line includes the additional interactions from the right-handed neutrino N_i^c and the singlet Higgs fields $\overline{\mathcal{X}}_R$, $\mathcal{X}_R$ with -1/2 and +1/2 $B-L$, and +1/2 and -1/2 R charges, respectively. The first term of the second line in superpotential describes the Yukawa interactions between neutrinos, and Y_ν^{ij} is the Yukawa coupling associated with these interactions. In a similar manner, Y_s^{ij} represents the Yukawa coupling among N_i^c, $\mathcal{X}_R$ and S. Moreover, μ_R is similar to μ' term of the $B-L$ extension of supersymmetric model (BLSSM) and stands for bilinear mixing between $\mathcal{X}_R$ and $\overline{\mathcal{X}}_R$ fields. Note that there is also a μ_S term to generate non-zero neutrino masses with inverse seesaw mechanism, and as customary, it is restricted to have a low value, as it cannot give important contributions to any other sector except for neutrinos. Contrary to BLSSM [31, 71, 72], where neutrinos have Majorana mass terms, N_i^c fields interact with $\mathcal{X}_R$ and S through $Y_s^{ij} N_i^c \mathcal{X}_R S$ term, and lead to SM-singlet pseudo-Dirac mass eigenstates. Besides, the interaction of the $SU(2)_L$ singlet Higgs fields $\mathcal{X}_R$, S and N_i^c yield a significant contribution to the masses of the extra Higgs bosons. Implementing the inverse seesaw mechanism into model allows Y_ν^{ij} and Y_s^{ij} to be at the order of unity. Hence, the contribution from the right-handed neutrino sector to the Higgs boson cannot be neglected and yields a different low scale phenomenology from MSSM and BLSSM with inverse seesaw mechanism [73–75].

The soft-breaking Lagrangian terms in the model are

$$\begin{aligned}
-\mathcal{L}_{SB,W} &= -B_\mu(H_u^0 H_d^0 - H_d^- H_u^+) - B_{\mu_R}\mathcal{X}_R\overline{\mathcal{X}}_R + A_u(\tilde{u}^\star_{R,i}\tilde{u}_{L,j}H_u^0 - \tilde{u}^\star_{R,i}\tilde{d}_{L,j}H_u^+) \\
&+ A_d(\tilde{d}^\star_{R,i}\tilde{d}_{L,j}H_d^0 - \tilde{d}^\star_{R,i}\tilde{u}_{L,j}H_d^-) + A_e(\tilde{e}^\star_{R,i}\tilde{e}_{L,j}H_d^0 - \tilde{e}^\star_{R,i}\tilde{\nu}_{L,j}H_d^-) \\
&+ A_\nu(\tilde{\nu}^\star_{R,i}\tilde{\nu}_{L,j}H_u^0 - \tilde{e}^\star_{R,i}\tilde{\nu}_{L,j}H_u^-) + A_{s,ij}\mathcal{X}_R\tilde{\nu}_{R,i}\tilde{S} + \text{h.c.}\,, \\
-\mathcal{L}_{SB,\phi} &= m^2_{\mathcal{X}_R}|\mathcal{X}_R|^2 + m^2_{\overline{\mathcal{X}}_R}|\overline{\mathcal{X}}_R|^2 + m^2_{H_d}(|H_d^0|^2 + |H_d^-|^2) + m^2_{H_u}(|H_u^0|^2 + |H_u^+|^2) \\
&+ m^2_{q,ij}(\tilde{d}^\star_{L,i}\tilde{d}_{L,j} + \tilde{u}^\star_{L,i}\tilde{u}_{L,j}) + m^2_{d,ij}\tilde{d}^\star_{R,i}\tilde{d}_{R,j} + m^2_{u,ij}\tilde{u}^\star_{R,i}\tilde{u}_{R,j} \\
&+ m^2_{l,ij}(\tilde{e}^\star_{L,i}\tilde{e}_{L,j} + \tilde{\nu}^\star_{L,i}\tilde{\nu}_{L,j}) + m^2_{e,ij}\tilde{e}^\star_{R,i}\tilde{e}_{R,j} + m^2_{\nu,ij}\tilde{\nu}^\star_{R,i}\tilde{\nu}_{R,j} + m^2_{s,ij}\tilde{S}^\star_i\tilde{S}_j \\
-\mathcal{L}_{SB,\lambda} &= \frac{1}{2}\left(M_1\lambda_B^2 + M_2\lambda_W^2 + M_3\lambda_g^2 + 2M_{B_R}\lambda_B\lambda_R + \text{h.c.}\right)\,,
\end{aligned} \tag{3.2}$$

which contain triple scalar interactions, scalar masses and masses for the gauginos of all gauge groups, denoted by λ's.

The $U(1)_R \times U(1)_{B-L}$ symmetry is broken spontaneously to $U(1)_Y$ by the vacuum expectation values (VEVs) of $\mathcal{X}_R$ and $\overline{\mathcal{X}}_R$

$$\langle\mathcal{X}_R\rangle = \frac{v_{\mathcal{X}_R}}{\sqrt{2}}\,, \qquad \langle\overline{\mathcal{X}}_R\rangle = \frac{v_{\overline{\mathcal{X}}_R}}{\sqrt{2}}\,, \tag{3.3}$$

while $SU(2)_L \times U(1)_Y$ is broken further to $U(1)_{EM}$ by the VEVs of the Higgs doublets

$$\langle H_d^0\rangle = \frac{v_d}{\sqrt{2}}\,, \qquad \langle H_u^0\rangle = \frac{v_u}{\sqrt{2}}\,. \tag{3.4}$$

We denote $v_R^2 = v^2_{\mathcal{X}_R} + v^2_{\overline{\mathcal{X}}_R}$ and $\tan\beta_R = \dfrac{v_{\mathcal{X}_R}}{v_{\overline{\mathcal{X}}_R}}$, in analogy with $v^2 = v_d^2 + v_u^2$, $\tan\beta = \dfrac{v_u}{v_d}$. The spectrum for this model, including particle masses, neutrino seesaw, mixing of gauge bosons and the neutralino sector has been discussed before [69], and we do not repeat it here. In what follows we concentrate on scanning the model parameters first by imposing Higgs sector, particle masses and other low energy restrictions, and then looking for dark matter candidates and resolution of the anomalous magnetic moment of the muon, thus restricting the parameter space to region where these conditions are satisfied.

3.3 Scanning Procedure and Experimental Constraints

We proceed to analyze the model by scanning the fundamental parameter space of BLRSSM. We use SPheno 3.3.3 package [76, 77] obtained from the model implementation in Sarah

Parameter	Scanned range	Parameter	Scanned range
m_0	$[0., 3.]$ TeV	v_R	$[6.5, 20.]$ TeV
$M_{1/2}$	$[0., 3.]$ TeV	$diag(Y_\nu^{ij})$	$[0.001, 0.99]$
A_0/m_0	$[-3., 3.]$	$diag(Y_s^{ij})$	$[0.001, 0.99]$
$\tan\beta$	$[0., 60.]$	sign of μ	positive
$\tan\beta_R$	$[1., 1.2]$	sign of μ_R	positive or negative

Table 3.1: Scanned parameter space.

4.6.0 [78, 79]. This package employs renormalization group equations (RGEs), modified by the inverse seesaw mechanism to evolve Yukawa and gauge couplings from $M_{\rm GUT}$ to the weak scale, where $M_{\rm GUT}$ is determined by the requirement of gauge coupling unification. We do not strictly enforce the solutions to unify at $M_{\rm GUT}$, since a few percent deviation is allowed due to unknown GUT-scale threshold corrections [80]. $M_{\rm GUT}$ is thus dynamically determined by the requirement of gauge unification, that is $g_L = g_R = g_{B-L} \approx g_3$, with subindices denoting the gauge couplings associated with $SU(2)_L, SU(2)_R, U(1)_{B-L}$ and $SU(3)_C$ respectively. With boundary conditions determined at $M_{\rm GUT}$, all the soft supersymmetry breaking (SSB) parameters along with the gauge and Yukawa couplings are evolved to the weak scale.

We performed random scans over the parameter space, as illustrated in Table 3.1, imposing universal boundary conditions for scalar and gaugino masses. We comment briefly first on the parameters chosen, and then on the constraints included. Here m_0 corresponds the mass terms for all scalars, and $M_{1/2}$ represents the mass terms for all gauginos, including the ones associated with the $U(1)_{B-L}$ and $U(1)_R$ gauge groups. In setting the ranges for the free parameters, we scan scalar and gaugino SSB mass terms between 0–3 TeV, regions which yield sparticle masses at the low scale, especially the LSP.

Here A_0 is the trilinear scalar interaction coupling coefficient, and we adjusted its range to avoid charge and/or color breaking minima, which translates into $|A_0| \lesssim 3m_0$ [81, 82]. Also, $\tan\beta$ is the ratio of vacuum expectation values of the MSSM Higgs doublets v_u/v_d, while $\tan\beta_R$ which denotes the ratio of vacuum expectation values of $v_{\chi_R}/v_{\overline{\chi}_R}$, is also free parameter in this model. Practically however, $\tan\beta_R$ is required to be close to 1, in order to prevent large D-term contributions to the sfermion masses and to avoid tachyonic solutions. The VEV v_R represents the vacuum expectation value which breaks extra $U(1)_{B-L} \times U(1)_R$ symmetry. Since the breaking scale of the extra symmetry plays a crucial role in determining the Z' mass, the gauge boson associated with $U(1)_{B-L} \times U(1)_R$ symmetry, we scan v_R

Observable	Constraints	Ref.	Observable	Constraints	Ref.
m_{h_1}	$[122, 128]$ GeV	[29]	$m_{\widetilde{t}_1}$	$\geqslant 730$ GeV	[87]
$m_{\widetilde{g}}$	> 1.75 TeV	[87]	$m_{\chi_1^\pm}$	$\geqslant 103.5$ GeV	[87]
$m_{\widetilde{\tau}_1}$	$\geqslant 105$ GeV	[87]	$m_{\widetilde{b}_1}$	$\geqslant 222$ GeV	[87]
$m_{\widetilde{q}}$	$\geqslant 1400$ GeV	[87]	$m_{\widetilde{\tau}_1}$	> 81 GeV	[87]
$m_{\widetilde{e}_1}$	> 107 GeV	[87]	$m_{\widetilde{\mu}_1}$	> 94 GeV	[87]
$\chi^2(\hat{\mu})$	≤ 2.3	-	$\mathrm{BR}(B_s^0 \to \mu^+\mu^-)$	$[1.1, 6.4] \times 10^{-9}$	[88]
$\frac{\mathrm{BR}(B \to \tau\nu_\tau)}{\mathrm{BR}_{SM}(B \to \tau\nu_\tau)}$	$[0.15, 2.41]$	[89]	$\mathrm{BR}(B^0 \to X_s\gamma)$	$[2.99, 3.87] \times 10^{-4}$	[90]
$m_{Z'}$	> 3.5 TeV	[6]	$\Omega_{DM}h^2$	[0.09-0.14]	[91, 92]

Table 3.2: Current experimental bounds imposed on the scan for consistent solutions.

between 6.5 and 20 TeV to obtain Z' boson masses consistent with the current experimental bounds.

The parameter μ is the bilinear mixing of the MSSM doublet Higgs fields, while μ_R is the bilinear mixing of the $SU(2)_R$ remnants Higgs fields, which are singlet under $SU(2)_L$ symmetry. The values of μ and μ_R can be determined by the radiative electroweak symmetry breaking (REWSB) but their signs cannot; thus, only their signs remain as free parameters. Since the model contributions to muon anomalous magnetic moment are related to the sign of $\mu M_{1/2}$, we scan over positive μ values, but we accept both negative and positive solutions of μ_R, while requiring solutions consistent with experimental predictions, and favoring solutions which improve upon the SM predictions for the muon $g-2$ factor. The superpotential of the model also includes a μ_S parameter, which yields non-zero neutrino masses via the inverse seesaw mechanism. However, μ_S is constrained to be small, so that it cannot effect any supersymmetric particle masses or decays. We also fixed the top quark mass to its central value ($m_t = 173.3$ GeV) [83] in our scan. The Higgs boson mass is very sensitive to the top quark mass, and small changes in its value can shift Higgs boson mass by 1-2 GeV [84, 85], although it does not significantly affect sparticle masses [86]. Hence, we scan both $\mathrm{diag}(Y_\nu^{ij})$ and $\mathrm{diag}(Y_s^{ij})$ between 0.001–0.99, though the inverse seesaw mechanism prefers values of order 1.

In scanning the parameter space, we use the interface which employs Metropolis-Hasting algorithm described in [93]. All collected data points satisfy the requirement of REWSB. After collecting the data, we impose current experimental mass bounds on all the

sparticles and SM-like Higgs boson as highlighted in Table 3.2. Although we restrict the SM-like Higgs boson to lie between 122-128 GeV with 3 GeV uncertainty, we also employed HiggsBounds 4.3.1 package [94] to compare our Higgs sector predictions with the experimental cross section limits from the LHC, and we require agreement with Higgs boson decay signal strengths at tree level, $h \to WW^\star$, $h \to ZZ^\star$ and $h \to b\bar{b}$. Thus using the mass-centered χ^2, and selecting the parametrization for the Higgs mass uncertainty as "box" we employed HiggsSignals 1.4.0 package [95] and bounded the solutions which yield total $\chi^2(\hat{\mu}) \leqslant 2.3$. Another constraint comes from rare B-decay processes, $B_s \to \mu^+\mu^-$ [88], $b \to s\gamma$ [90] and $B_u \to \tau\nu_\tau$ [89]. The B-meson decay into a muon pairs, in particular, constrains the parameter space since there the SM predictions are consistent with the experimental measurements. The supersymmetric contributions are proportional to $(\tan\beta)^6/m_{A_i}^4$ and constrained to be small. Hence, m_{A_i} has to be heavy enough ($m_{A_i} \sim$ TeV) to suppress the supersymmetric contributions for large $\tan\beta$ values. In addition to these limitations, dark matter observations severely restrict the parameter space, requiring the LSP to be stable and electric and color neutral, which excludes a significant portion of parameter space where stau is the LSP. We concentrate on two different data sets, one with the neutralino being the LSP, and one where sneutrino is the LSP, and we shall distinguish these two scenarios throughout our investigations. We employ micrOMEGAs 4.3.1 package [96] and tag the solutions which yield consistent relic density within 20% uncertainty range provided from WMAP data [91, 92] as specified in Table 3.2. Apart from relic abundance constraint, we do not impose any restriction from the dark matter experiments. All the experimental restrictions mentioned above are listed in Table 3.2.

3.4 Dark matter phenomenology

For either neutralino or sneutrino to be viable candidates for dark matter, they must yield the correct level of relic abundance for thermal dark matter production in the early Universe, determined very precisely as the amount of non-baryonic dark matter in the energy-matter of the Universe, $\Omega_{DM}h^2 = 0.1199 \pm 0.0027$ [11], with Ω_{DM} being the energy density of the dark matter with respect to the critical energy density of the universe, and h the reduced Hubble parameter.

In addition, as the lack of any dark matter signals in either direct or indirect dark matter detection experiments confront our theoretical expectations, these must satisfy in-

creasingly severe constraints from experiments. The interaction of dark matter with detector nuclear matter can be spin-dependent or spin-independent. The spin-dependent scattering can only happen for odd-numbered nucleons in the nucleus of the detector material, while in spin-independent (scalar) scattering, the coherent scattering of all the nucleons in the nucleus with the DM are added in phase. Consequently, in direct detection experiments, the experimental sensitivity to spin-independent (SI) scattering is much larger than the sensitivity to spin-dependent scattering, and thus we shall concentrate on the former.

We proceed as follows. First, we analyze the consequences of having the lightest neutralino as the dark matter candidate. Using the results in the previous sections, we explore the parameter space of the model which is consistent with this assumption. We follow in the next subsection with the parameter restrictions for sneutrino dark matter.

3.4.1 Neutralino Dark Matter

In this subsection, we concentrate on analyzing the consequences on the mass spectrum of the BLRSSM obtained by scanning over the parameter space given in Table 3.1 where lightest neutralino ($\widetilde{\chi}_1^0$) is always the LSP, and highlight the solutions compatible with the constraints showed in Table 3.2. We start with Fig. 3.1 which displays the allowed parameter regions, with plots in $m_0 - M_{1/2}$, $m_0 - A_0/m_0$ and $M_{1/2} - \tan\beta$ planes. Throughout the graphs, all points satisfy REWSB. Blue points satisfy all experimental mass bounds, signal strengths of SM-like Higgs boson and rare B-decay constraints given in Table 3.2. Red points obey the above mentioned constraints, as well as relic density bounds, $0.09 \leq \Omega_{DM}h^2 \leq 0.14$. The $m_0 - M_{1/2}$ plane shows that solutions for $M_{1/2} \lesssim 800$ GeV are excluded by the constraints in Table 3.2, and the requirement of consistent relic density (red points) excludes a significant portion of the LHC allowed region (blue points). For $M_{1/2} \sim 1$ TeV, m_0 is bounded between 2–3 TeV, and low m_0 values can survive for larger $M_{1/2}$. On the other hand, the $m_0 - A_0/m_0$ panel shows that the regions with larger m_0 values prefer positive values of the trilinear scalar interaction strength A_0, while almost all solutions with consistent relic density have positive A_0 parameter. Unlike the $B - L$ Supersymmetric Standard Model (BLSSM) [31], where negative A_0 solutions for $m_0 \geq 1$ TeV do not satisfy REWSB, here all LSP constraints can be fulfilled for this portion of parameter space, while only the relic density constraint imposes positivity of A_0. The $M_{1/2} - \tan\beta$ plot indicates that it is possible to find solutions with $0.09 \leq \Omega_{DM}h^2 \leq 0.14$ only for large $\tan\beta$ values, $40 \leq \tan\beta \leq 60$, although it is easier to satisfy LHC limitations for low $\tan\beta$ values.

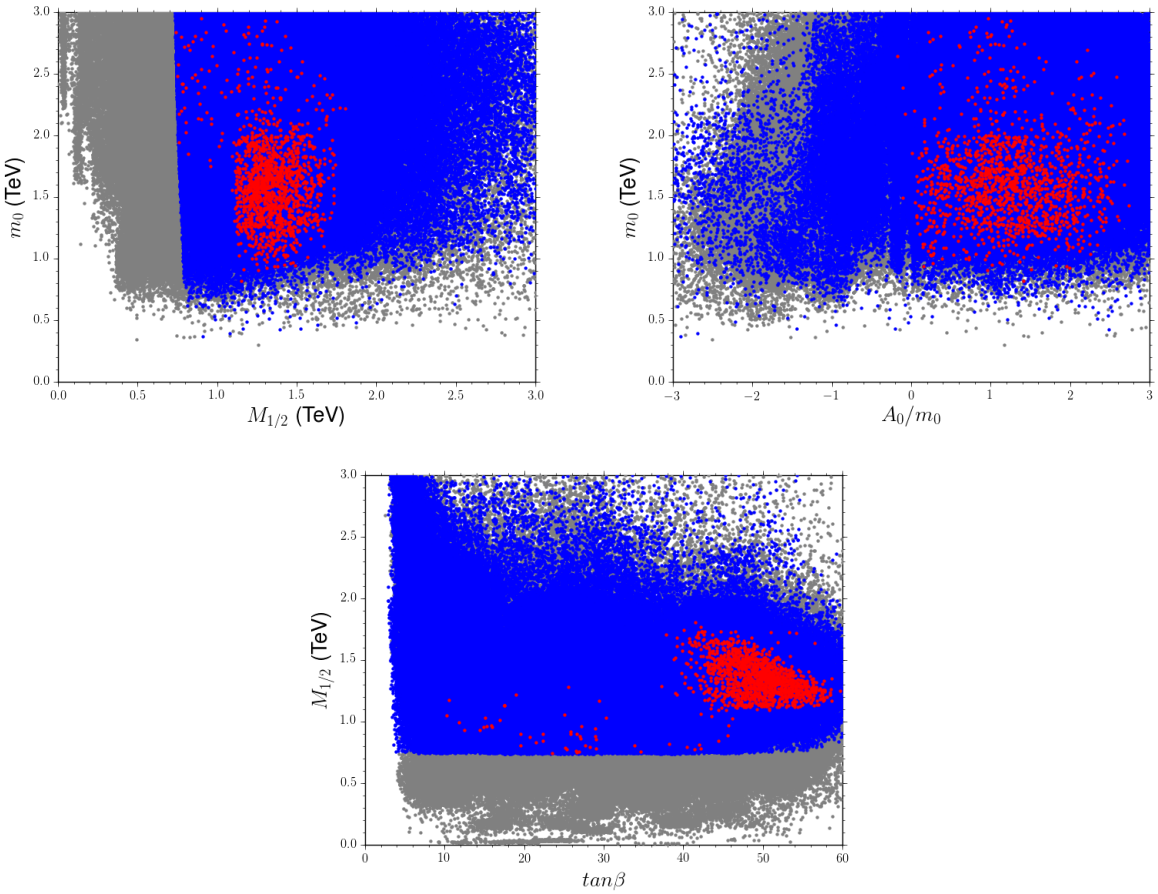

Figure 3.1: Parameter scans for neutralino LSP scenario. (Left) m_0 vs $M_{1/2}$, (center) m_0 vs A_0/m_0 and (right) $M_{1/2}$ vs $\tan\beta$. All points are consistent with REWSB and neutralino LSP. Blue points satisfy all the experimental limits listed in Table 3.2. Red points form a subset of blue, and represent solutions consistent with the relic density constraint.

In Fig. 3.2, we show specific results for the determination of sparticle mass spectrum, with plots in (top left) $m_{\widetilde{t}_1} - m_{\widetilde{\chi}_1^0}$, (top right) $m_{\widetilde{b}_1} - m_{\widetilde{\chi}_1^0}$, (bottom left) $m_{\widetilde{\chi}_1^\pm} - m_{\widetilde{\chi}_1^0}$ and (bottom right) $m_{\widetilde{\tau}_1} - m_{\widetilde{\chi}_1^0}$ planes. The color coding is the same as Fig. 3.1. Furthermore, the mass region in which the two masses are degenerate is displayed as a solid green line. We note that the LSP neutralino solutions consistent with the relic density bound can be obtained only when 300 GeV $\leq m_{\widetilde{\chi}_1^0} \leq$ 800 GeV. As can be seen from $m_{\widetilde{t}_1} - m_{\widetilde{\chi}_1^0}$ and $m_{\widetilde{b}_1} - m_{\widetilde{\chi}_1^0}$ planes, we find that stop and sbottom masses have to be at least $\sim$ 1.5 TeV and 2 TeV respectively to fulfill all the restrictions. Even though it is possible to find light stop solutions ($m_{\widetilde{t}_1} \leq 1$ TeV) when 340 GeV $\leq m_{\widetilde{\chi}_1^0} \leq$ 550 GeV, the relic density condition is not satisfied for these solutions. Moreover, unlike the results of BLSSM [31] where the lightest chargino masses are always above 600 GeV, here the $m_{\widetilde{\chi}_1^\pm} - m_{\widetilde{\chi}_1^0}$ plot shows that there is a region of parameter space where lightest chargino solutions is nearly degenerate with the lightest neutralino when 300 GeV $\leq m_{\widetilde{\chi}_1^0} \leq$ 500 GeV. These solutions correspond to the case where the lightest chargino decays into the neutralino LSP and $W/W^\star$ boson ($\widetilde{\chi}_1^\pm \to \widetilde{\chi}_1^0 + W^\pm(W^{\star\pm})$), and the branching ratio for this channel is almost 1. On the bottom right panel, the $m_{\widetilde{\tau}_1} - m_{\widetilde{\chi}_1^0}$ plane illustrates the stau mass along with the LSP neutralino mass. There is a parameter space around $m_{\widetilde{\chi}_1^0} \sim$ 600 GeV, where stau mass is almost degenerate with the LSP neutralino and becomes the next to lightest supersymmetric particle (NLSP), but also for a region of the parameter space, the stau can be much heavier than the neutralino LSP. The lightest stau NLSP solutions compatible with the relic density constraint occur around 500 GeV. One can choose one of these solutions and study relevant neutralino annihilation processes mediated by a light stau [97].

The bottom plots in Fig. 3.2, show our results for the sparticle spectrum for the gluino and sneutrinos, with the plots in $m_{\widetilde{q}} - m_{\widetilde{g}}$, (where $\widetilde{q}$ represents squarks from the first two families), and $m_{\widetilde{\nu}_1} - m_{\widetilde{\chi}_1^0}$ planes. The $m_{\widetilde{q}} - m_{\widetilde{g}}$ plane shows that squarks masses for the first two families and gluino masses should be heavier than 2.2 TeV but lighter than 4 TeV (orange points). Although the relic density condition and the current ATLAS experimental limit [98] strictly constrain the crucial portion of the parameter space, most of the solutions are consistent with this experimental exclusion. Finally, the $m_{\widetilde{\nu}_1} - m_{\widetilde{\chi}_1^0}$ plane reveals that it is hard to find solutions with sneutrino as the supersymmetric NLSP if we require consistency with the relic density bound, and the lightest sneutrino solutions satisfying all bounds can be obtained at around 1 TeV.

Note that the graphs contain also information on the composition of the neutralino LSP. As can be seen from gluino vs squarks panel, light blue points, which represent the

mixed neutralino LSP solutions consistent with the relic density bounds, are mostly found under the yellow curve (the excluded region). However, orange points representing mixtures of R-bino and $B-L$ bino (gauginos of $U(1)_R$ and $U(1)_{B-L}$, respectively) as well as green and black points which stand for $\widetilde{H}$-like and $\widetilde{H}_R$-like neutralino LSPs respectively are mostly located within the 1 sigma error of the yellow line.

To continue the investigation of the neutralino LSP composition, in Fig. 3.3 we plot the correlation between the neutralino mass and gaugino and higgsino mass ratios with (top left) M_4/M_1, (top right) M_1/μ, (bottom left) M_2/μ, and (bottom right) μ_R - μ, for correct relic density. The color coding is the same as Fig. 3.1. According to the $M_4/M_1 - m_{\widetilde{\chi}_1^0}$ plane, there must be a clear relation between the $B-L$ bino $\widetilde{B}$ and $\widetilde{B}_R$ masses so that the ratio of $\widetilde{B}_R/\widetilde{B}$ should be at around ~ 1.8, decreasing slightly when the neutralino LSP mass increases. The next two plots compare the bino-higgsino (top right) and wino-higgsino (bottom left) masses, respectively, by looking at their mass ratio. In the top right plot, almost all solutions satisfying LHC collider bounds, and *all* solutions satisfying relic density constraints have $M_1/\mu \lesssim 1$, that is the bino is lighter than the higgsino mass parameter. The left bottom plane shows that, despite allowing for light higgsinos, the wino is mostly lighter than the higgsino over all the parameter space where relic density bounds are satisfied. The $\mu_R - \mu$ plot (bottom right) shows that solutions prefer positive μ_R to the negative ones, and μ_R can take values in a large range between 500 GeV–7 TeV while the relic density bound can only be fulfilled with the low μ values. As can be seen from $\mu_R - \mu$ plane, the relic density constraint can be satisfied mostly when $\mu \lesssim 0.5$ TeV and 0.7 TeV $\lesssim \mu \lesssim 1.5$ TeV.

The neutralino LSP content consistent with all constraints (including relic density) is as follows: its mass is constrained as 300 GeV $\lesssim m_{\widetilde{\chi}_1^0} \lesssim$ 500 GeV, and for those parameter points, the neutralino LSP content is a $\widetilde{B}_R$-ino, $\widetilde{H}$-ino and $\widetilde{B}$-ino mixture, in this region the wino masses are heavier than the higgsino masses for solutions consistent with the relic density bound. Since $M_1/\mu \lesssim 1$, the bino mixes more than the higgsinos to form the LSP neutralino. In the region 500 GeV $\lesssim m_{\widetilde{\chi}_1^0} \lesssim$ 800 GeV, the LPS neutralino is about $60\%\widetilde{B}_R - 40\%\widetilde{B}$ admixture, consistent also with the top left plot in Fig. 3.4.

In Fig. 3.4 we present results specific to dark matter phenomenology, plotting the relic density and spin-independent cross section as a function of the lightest neutralino mass. In addition, we plot the correlation between the lightest pseudoscalar and the third lightest neutral Higgs boson h_3, to highlight the fact that dark matter annihilation proceeds through these two funnels. We show (top left) $\Omega_{DM}h^2 - m_{\widetilde{\chi}_1^0}$, (top right) $\sigma^{SI}_{nucleon} - m_{\widetilde{\chi}_1^0}$, (bottom left)

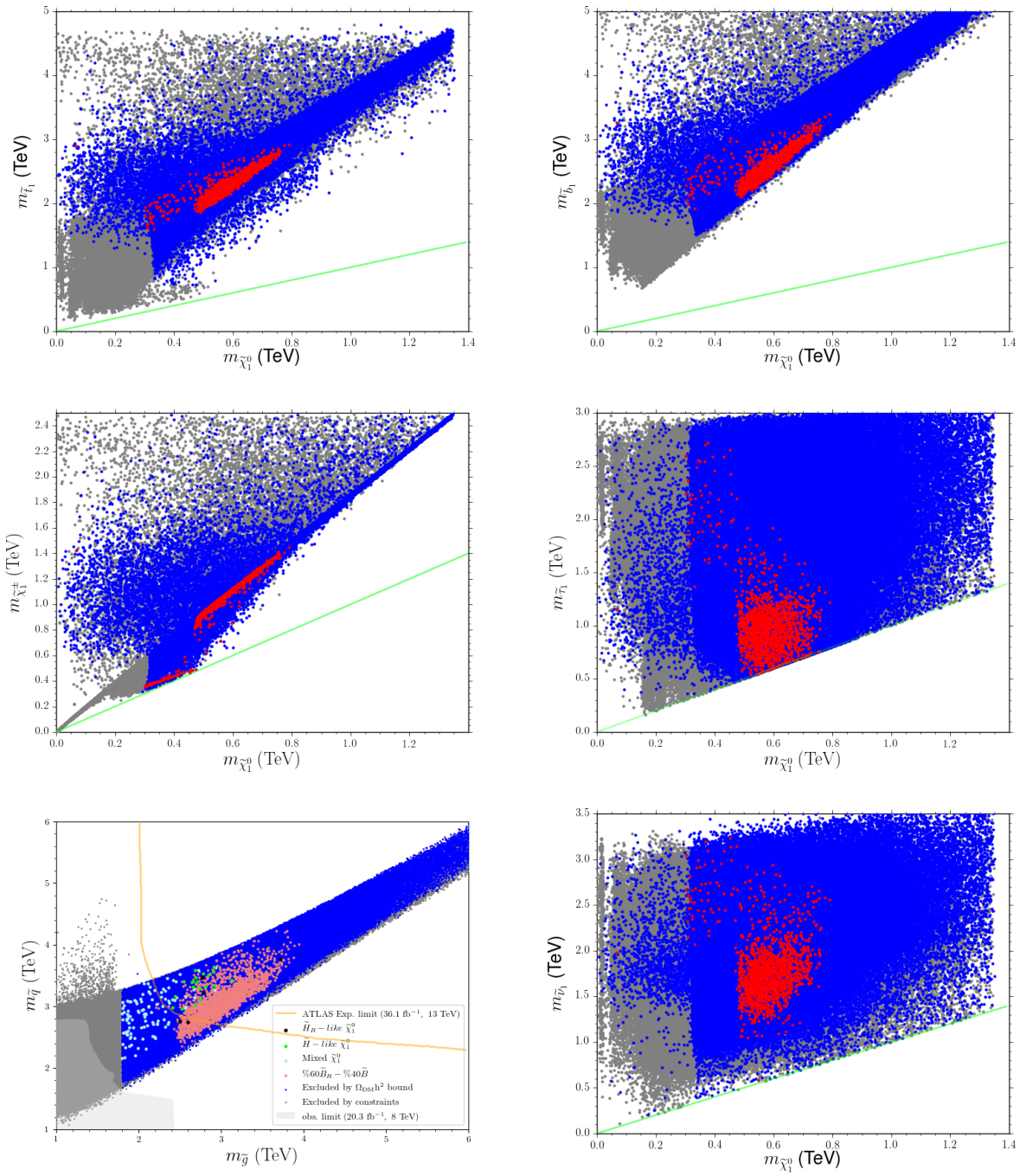

Figure 3.2: Plots in (top left) $m_{\tilde{t}_1} - m_{\tilde{\chi}_1^0}$, (top right) $m_{\tilde{b}_1} - m_{\tilde{\chi}_1^0}$, (middle left) $m_{\tilde{\chi}_1^\pm} - m_{\tilde{\chi}_1^0}$, (middle right) $m_{\tilde{\tau}_1} - m_{\tilde{\chi}_1^0}$, (bottom left) $m_{\tilde{q}} - m_{\tilde{g}}$, and (bottom right) $m_{\tilde{\nu}_1} - m_{\tilde{\chi}_1^0}$ planes. The color coding is the same as Fig. 3.1. In the bottom left panel, the color coding represents the neutralino composition as indicated in the insert. The solid line in each plane indicates the degenerate mass region.

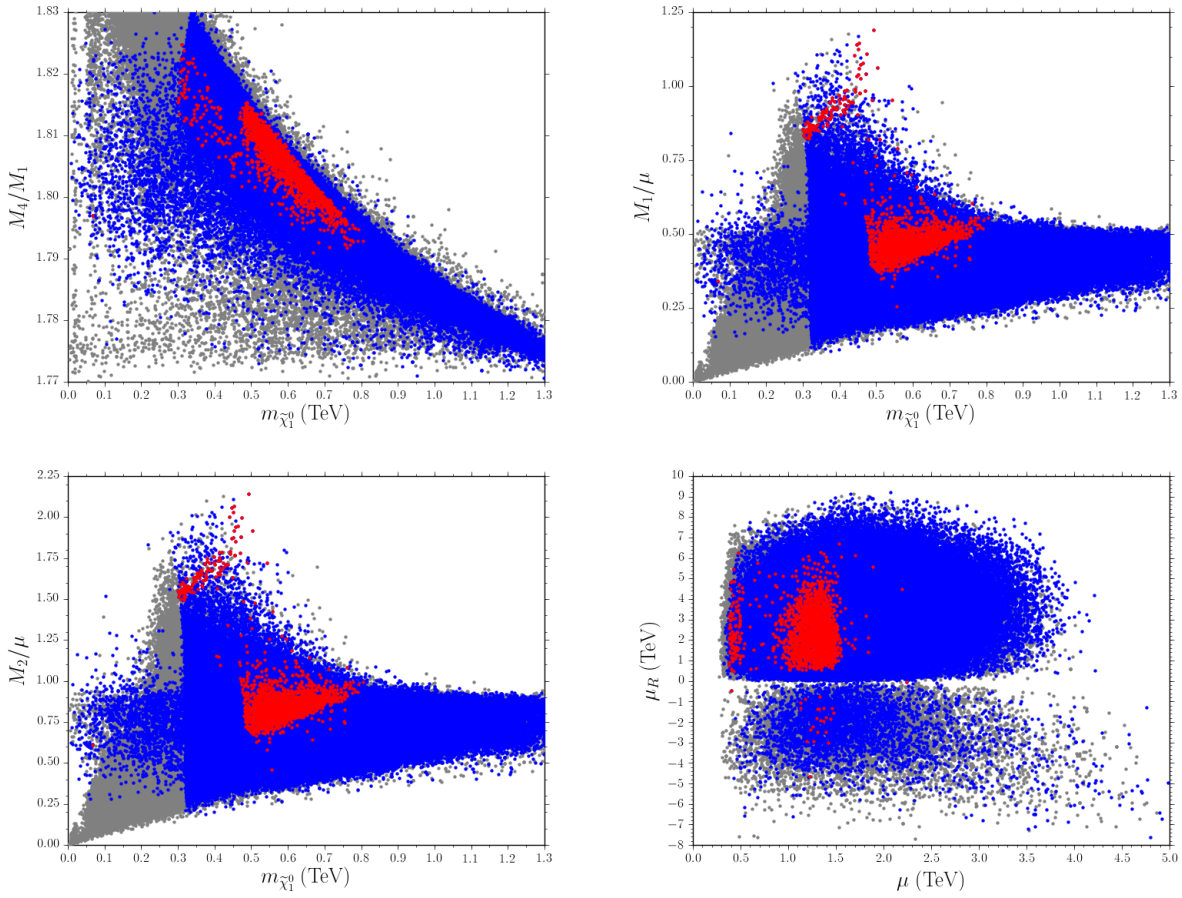

Figure 3.3: Plots for the neutralino LSP mass and mass ratios: (top left) M_4/M_1, (top right) M_1/μ, (bottom left) M_2/μ, and (bottom right) μ_R - μ correlations. The color coding is the same as Fig. 3.1.

$m_{A_1} - m_{\widetilde{\chi}_1^0}$, and (bottom right) $m_{h_3} - m_{A_1}$ plots. In the top left and top right plane color coding is indicated in the insert, while for the bottom plots the color coding is the same as Fig. 3.3. The top left plot confirms our previous results on the content of LSP neutralino between 500 – 800 GeV is composed of 60% $\widetilde{B}_R$-ino and 40% $\widetilde{B}$-ino, whereas when 300 GeV $\lesssim m_{\widetilde{\chi}_1^0} \lesssim$ 500 GeV, its content is shared among $\widetilde{B}_R$-ino, $\widetilde{H}$-ino and $\widetilde{B}$-ino . The top left plot shows the dependence of the relic density, and the right plot shows the dependence of the spin-independent proton and neutron cross section, with neutralino LSP mass. The solid green line represents the current exclusion limit for XENON1T experiment [99] while yellow and green shaded regions represent solutions within $\pm 1\sigma, \pm 2\sigma$ errors respectively. As can be seen from the graph, most solutions consistent with the relic density constraint can be found below the XENON1T exclusion bound, specifically between 10^{-10} pb – 10^{-11} pb. Hence they can be detected by the next generation DM detectors such as XENONnT [100], LZ and DARWIN [101]. Note that we also have a substantial amount of solutions consistent with the relic density above XENON1T exclusion limit. These solutions correspond to the region where 300 GeV $\lesssim m_{\widetilde{\chi}_1^0} \lesssim$ 500 GeV and where the LSP content is either completely $\widetilde{H}$-ino or the mixture of $\widetilde{B}_R$-ino, $\widetilde{H}$-ino and $\widetilde{B}$-ino. Thus all solutions surviving consistency with both the current XENON1T exclusion limit and the relic density constraint consist of LSP neutralinos with 500 GeV $\lesssim m_{\widetilde{\chi}_1^0} \lesssim$ 800 GeV, and with 60% $\widetilde{B}_R$ and 40% $\widetilde{B}$ admixture. Finally, the $m_{A_1} - m_{\widetilde{\chi}_1^0}$ and $m_{h_3} - m_{A_1}$ plots indicate the funnel channels for the LSP neutralino. The solid green line displays the degenerate mass region for the lightest CP-odd Higgs boson and the LSP neutralino, while the yellow shadowed region indicates solutions with $m_{A_1} = 2m_{\widetilde{\chi}_1^0}$, within 8% error. As can be seen from the graph, the lightest CP-odd Higgs boson, or the neutral h_3 Higgs boson can annihilate into two LSP neutralinos when 450 GeV $\lesssim m_{\widetilde{\chi}_1^0} \lesssim$ 800 GeV. Solutions consistent with the relic density constraint can be found when A_1 is degenerate with h_3, with mass between 1 and 3 TeV. In this energy scale A_1 and h_3 provide the main funnel channels of this model. Apart from these, we have also verified the relation of the relic density with the IceCube confidence level exclusion and the neutrino flux, and all neutralino LSP solutions surviving relic and cross section bounds are within 1% confidence level of the experimental result.

3.4.2 Sneutrino Dark Matter

The BLRSSM contains, in addition to the three left sneutrinos, six additional singlet states, three right sneutrinos and three $\widetilde{S}$, the scalar partners of S. The latter two provide candidates

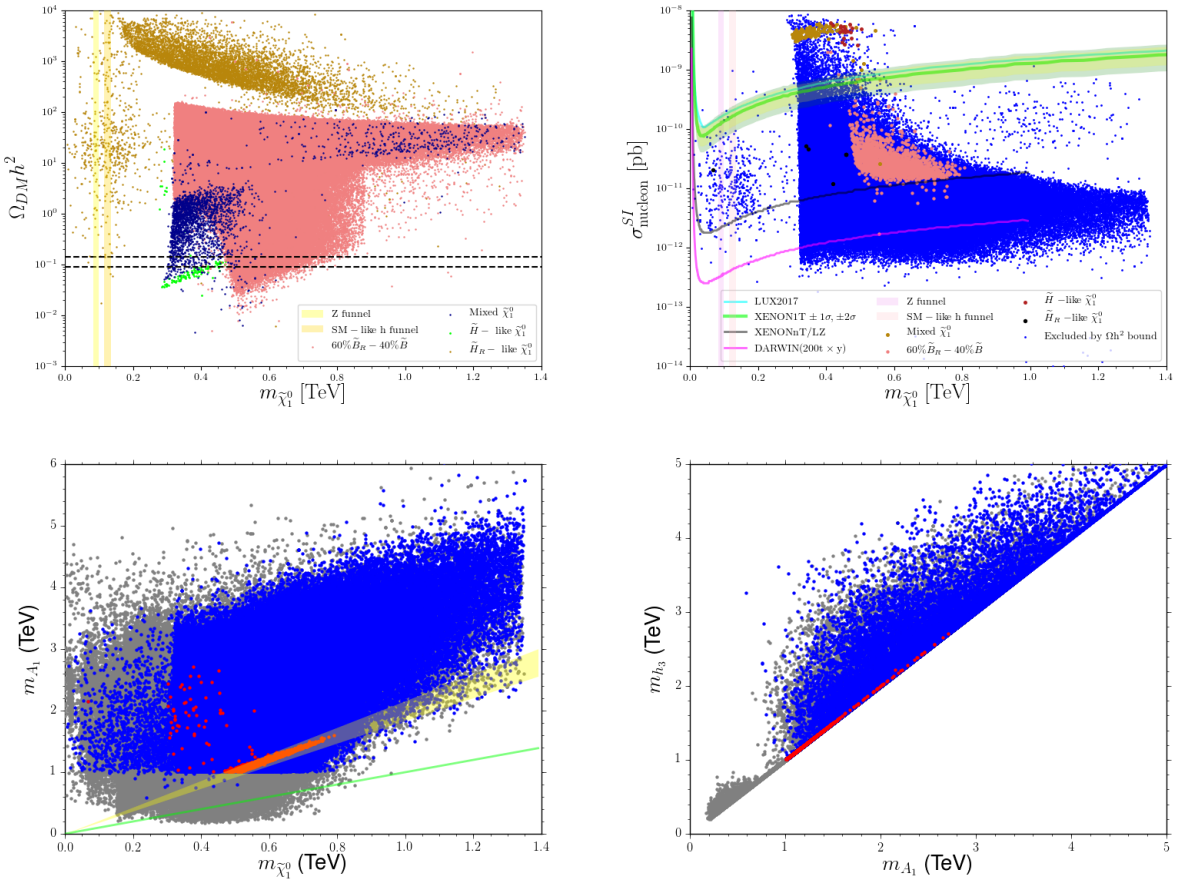

Figure 3.4: Dependence of: (top left) relic density and (top right) spin independent cross section with nuclei on $m_{\widetilde{\chi}_1^0}$, (bottom left) the lightest pseudoscalar Higgs mass on $m_{\widetilde{\chi}_1^0}$ planes, and (bottom right) the degeneracy between the lightest pseudoscalar mass and the third lightest neutral Higgs boson. Both of these provide the funnel channel for the LSP neutralino annihilation. All points except the dark blue ones are consistent with all constraints as in Table 3.2, while the dark blue ones violate the relic constraints only. The color coding in the $m_{\widetilde{\chi}_1^0} - m_{A_1}$ plot is the same as in Fig. 3.1. The solid line shows the degenerate mass region in these plots. In addition, the shaded region represents A_1 funnel solutions where $m_{A_1} = 2m_{\widetilde{\chi}_1^0}$ within 8% error.

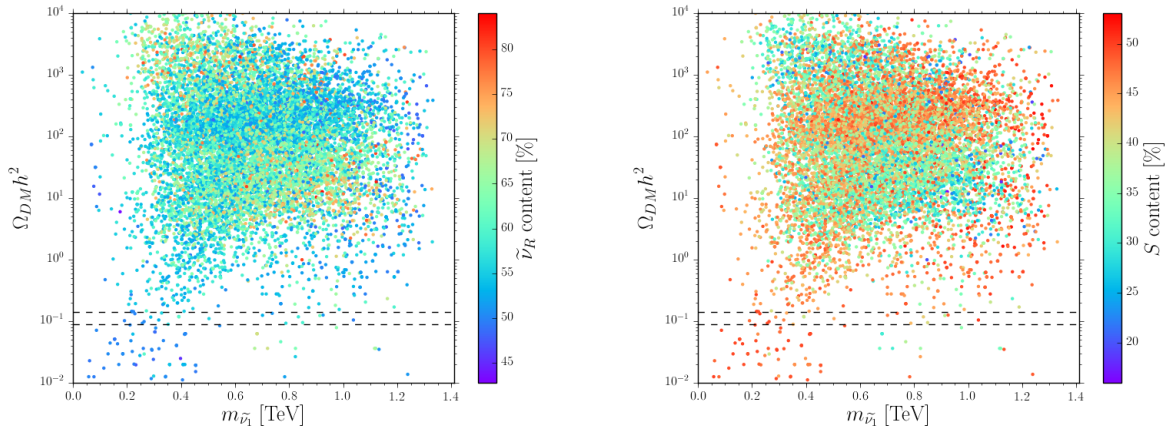

Figure 3.5: Dependence of the relic density $\Omega_{DM}h^2$ on the lightest sneutrino mass $m_{\widetilde{\nu}_1}$, showing the right sneutrino composition (left panel) and $\widetilde{S}$ composition (right panel). All points are consistent with REWSB, LHC bounds, B-physics constraint and sneutrino LSP, while only the points between the two dashed lines satisfy relic density constraints.

for sneutrino dark matter, as they do not suffer from too large annihilation cross section (thus small relic density) from interacting through Z or W bosons. Sneutrinos thus provide alternative candidates for dark matter in this model, and we analyze their consequences in this subsection. In the left and right panels of Fig. 3.5 we show the dependence of the relic density $\Omega_{DM}h^2$ as a function of the lightest scalar neutrino mass. The color bars in the right side of each plot indicate the right-handed sneutrino and the $\widetilde{S}$ content, respectively. As can be seen from the plot, even though it is possible to find sneutrino LSP solutions for almost all values of $m_{\widetilde{\nu}_1}$ between 0–1400 GeV, requiring consistency with the relic density bound constraints LSP sneutrinos to be between 200–400 GeV. Thus the indication would be that sneutrino LSP case allows lighter LSP masses compared to the neutralino LSP scenario. The right-handed content of the sneutrino LSP solutions changes between 45%-80%, while $\widetilde{S}$ composition varies between 20%-52%. Imposing relic density bounds, the mixed sneutrino LSP is about 50-50 % between right-handed and $\widetilde{S}$. Thus the scalar partner of S, introduced for neutrino seesaw, plays a crucial role in the sneutrino LSP composition.

In Fig. 3.6 we analyze the dependence of the nucleon spin-independent cross section, σ_p^{SI} for both the proton (left panel) and neutron (right panel). The color coding is the same as Fig. 3.1 and also indicated in the legend of the plots. The plots show the relation for the spin independent cross section for proton and neutron respectively. We note that both dark matter constraints (the relic density and σ_p^{SI}) severely restrict the parameter space where the sneutrino is the LSP in this model.

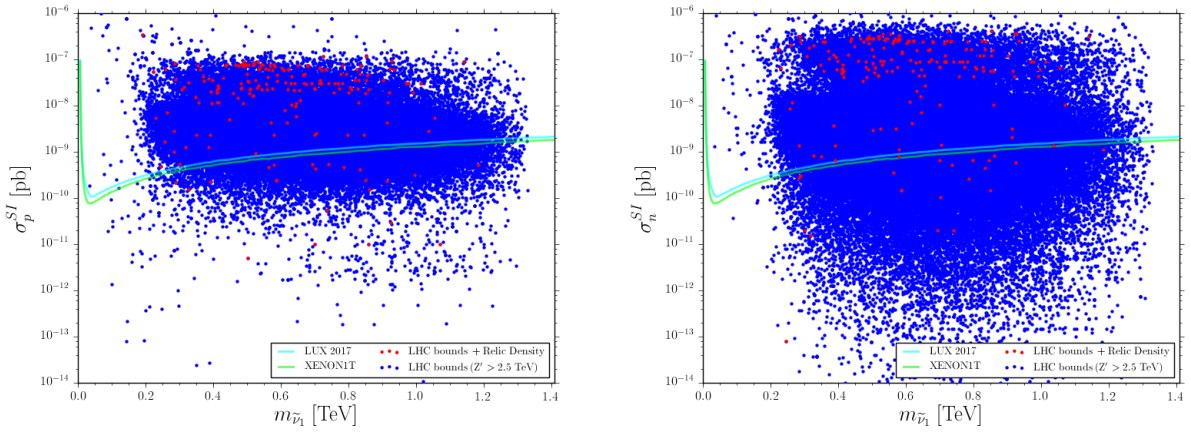

Figure 3.6: Dependence of the spin independent cross section for the proton σ_p^{SI} (left) and neutron σ_n^{SI} (right) as a function on the sneutrino LSP mass $m_{\widetilde{\nu}_1}$. All points are consistent with REWSB and sneutrino LSP. The color coding in each plane is the same as Fig. 3.1.

3.5 Comparison of the two Dark Matter scenarios

In the previous section, we analyzed DM phenomenology for both neutralino LSP and sneutrino LSP scenarios in BLRSSM. As discussed in detail, BLRSSM provides quite different mass spectrum for two distinct variants of LSP, and these relatively two different mass spectra change the low scale DM phenomenology in important manner. While we found sneutrino LSP scenario to be highly constrained and statistically unlikely, there are a few parameter points that survive universal boundary conditions, so in this section, we compare results for the two different LSP scenarios. In Fig. 3.7 we plot in the $\mu - \mu_R$ and $\tan\beta - M_2/\mu$ dependence. Dark blue points satisfy the mass bounds and constraints from the rare B-decays for the neutralino LSP solutions. Red points form a subset of dark blue, and represent neutralino LSP solutions which satisfy the relic density constraint. Light blue solutions are consistent with the mass bounds and the constraints from the rare B-decays for sneutrino LSP solutions, while yellow points form a subset of light blue, and represent sneutrino LSP solutions consistent with the relic density constraint.

The $\mu - \mu_R$ plots compare the higgsino sectors of our model. We note that while the neutralino LSP solution can allow values of μ_R between 0–9 TeV, sneutrino LSP solutions prefer low μ_R values, mainly between 0–4 TeV for positive μ_R. Even this range becomes narrow, around 1.5 TeV, for lighter higgsinos. For the sneutrino LSP solutions, μ_R values favor the region between 4–7 TeV when $\mu < 1.5$ TeV. On the right panel, the $\tan\beta - M_2/\mu$ plane shows the relative wino and higgsino mass ranges for the two LSP scenarios.

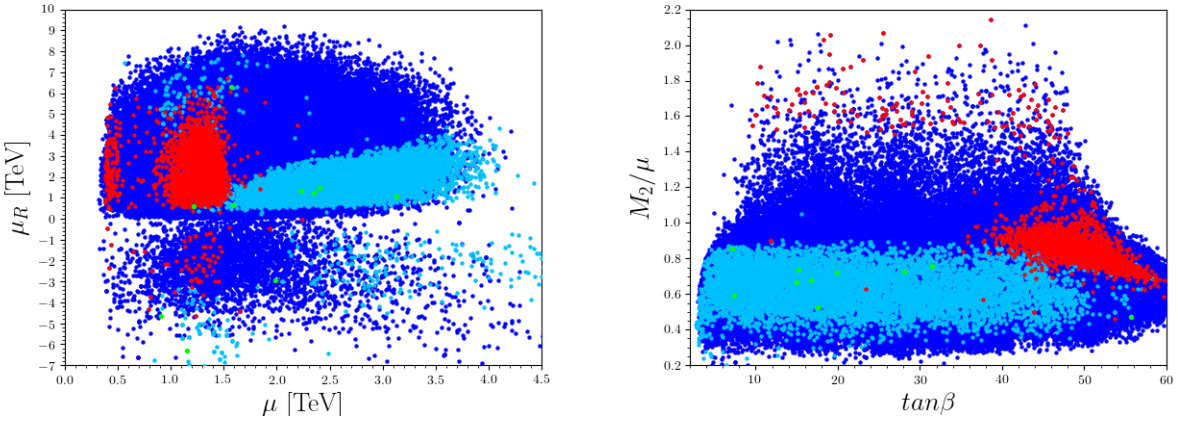

Figure 3.7: Dependence of higgsino parameters μ_R and μ (left), and of M_2/μ of $\tan\beta$ (right). All points are consistent with mass bounds, B-physics bounds, HiggsBounds and HiggsSignals. Dark blue points displays neutralino LSP solutions whereas light blue ones stand for sneutrino LSP solutions. Red points represent the neutralino LSP solution, while green ones stand for sneutrino LSP solutions, consistent in addition, with the relic density bound.

From the plots, we conclude that for sneutrino LSP, $M_2/\mu \lesssim 1$ and the wino is always lighter than the higgsino over all the parameter space. For the neutralino LSP case, the higgsinos can be lighter or heavier than winos. Also, $\tan\beta$ values for sneutrino LSP solutions are found anywhere in the 0–50 range, and solutions consistent with the relic density constraint can be obtained for either $M_2/\mu \lesssim 1$ or $M_2/\mu \gtrsim 1$. Requiring consistency with the relic density bound solutions with $M_2/\mu \gtrsim 1$ correspond to neutralino LSP, and $\tan\beta$ values lie in the 10–50 range. Requiring compatibility with the relic density bound, further constrains the region $M_2/\mu \lesssim 1$ to correspond to $\widetilde{B} - \widetilde{B}_R$ dominated neutralino LSP solution, where $\tan\beta$ should be between 40–60.

In general the model clearly favors solutions with neutralino LSP to those with sneutrino LSP.

3.5.1 The neutral Higgs sector

The choice of LSP affects the heavier states in the Higgs Sector of BLRSSM. For both neutralino and sneutrino LSP solutions, the lightest neutral Higgs boson can be lighter than 150 GeV. Fig. 3.8 shows the results for the values of Higgs masses for both LSP cases with plots for m_{h_2} relative to m_{h_1} (left) and m_{A_1} dependence of $\tan\beta$ (right), where A_1 is the

lightest pseudoscalar. The color coding is described in the legend of these planes. The left plot shows that while the two lightest neutral Higgs bosons can be degenerate when the LSP is neutralino, degenerate solutions cannot be obtained for the sneutrino LSP, where the second lightest Higgs boson mass is between 150–700 GeV. This phenomenon can be explained as due the contributions obtained from different elements of CP-even Higgs mass matrix. When $m_{h_2} > 150$ GeV, the dominant contribution comes from the m^2_{RR} element of CP-even Higgs mass matrix, corresponding to singlet Higgs fields associated with $U(1)_R \times U(1)_{B-L}$. Thus there h_2 is mostly a singlet Higgs boson. The off-diagonal term m^2_{LR} which provides essential mixing between the two sectors becomes important when $m_{h_2} < 150$ GeV. For the sneutrino LSP solutions, the Yukawa coupling Y_s is constrained to be small (as the sneutrino LSP mass is generated mostly through this term), unlike when the LSP is the neutralino. The Y_s coupling then imposes lighter h_2 masses, mostly generated by the singlet Higgs field $\mathcal{X}_R$. The other Higgs bosons can be quite heavy. This is seen also in the right-hand side of Fig. 3.8, where we plot the dependence of the mass of the lightest pseudoscalar Higgs boson A_1 (degenerate with h_3), with $\tan\beta$. As before, the region in $\tan\beta \sim$ 40-60 represents the mixed binos neutralino LSP solutions, while for $\tan\beta < 40$, regions with larger (smaller) A_1 mass correspond to sneutrino (neutralino) LSP. Thus second lightest Higgs boson is a singlet in both scenarios, but, while the sneutrino LSP scenario favors the 150-700 GeV mass range, for the neutralino LSP solutions the second lightest Higgs boson mass can be much heavier than 700 GeV.

3.5.2 The muon anomalous magnetic moment

The experimental results for the muon anomalous magnetic moment pioneered by the BNL E821 experiment [102, 103] have been improved with the updated results from FNAL E989 [104] and J-PARC E34 [105] experiments. However, the SM prediction for the muon anomalous magnetic moment [106], $a_\mu = (g-2)_\mu/2$, indicates a 3.5σ deviation from the experimental results,

$$\Delta a_\mu = a_\mu^{\text{exp}} - a_\mu^{\text{SM}} = (28.7 \pm 8.0) \times 10^{-10} (1\sigma) \tag{3.5}$$

The SM prediction is limited in precision by the evaluation of hadronic vacuum polarization contributions. Calculations exist for the lowest contributions, evaluated using perturbative QCD and experimental cross section data involving e^+e^- annihilation into hadrons. However, the large discrepancy has motivated possible explanations within new physics scenarios.

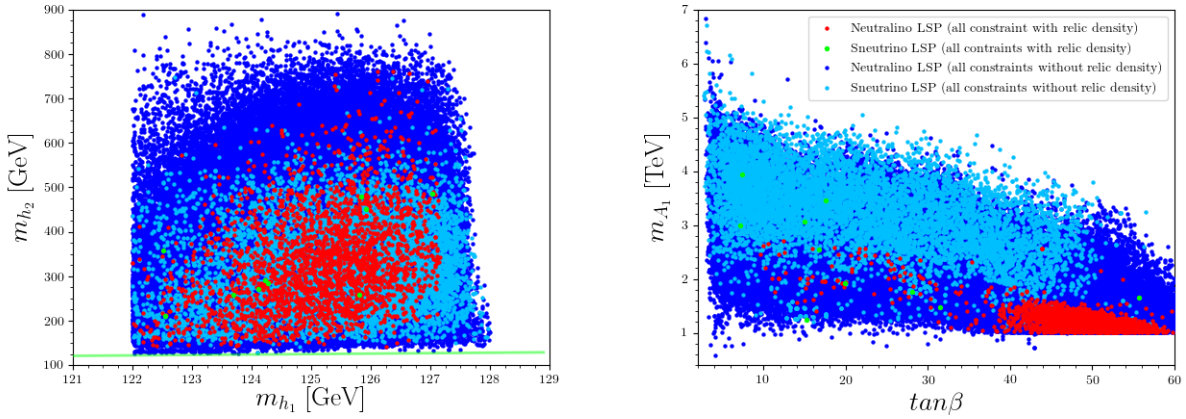

Figure 3.8: Dependence of m_{h_2} and m_{h_1} (left) and dependence of m_{A_1} on $\tan\beta$ (right). The color coding is as follows. Dark blue and light blue points represent neutralino LSP and sneutrino LSP solutions respectively, and they both satisfy all experimental bounds illustrated in Table 3.2, except for the relic density bound. In addition, red and green solutions form a subset of dark blue and light blue respectively, and they both represent solutions consistent with the constraints in Table 3.2, including the relic density bound. In addition, the solid green line shows the degenerate mass region where $m_{h_1} = m_{h_2}$.

In MSSM, if one of the smuons and bino or wino soft masses can be sufficiently light, supersymmetry can ameliorate this discrepancy. However, if the model is required to obey universality conditions at $M_{\rm GUT}$, obtaining the correct Higgs boson mass is the greatest challenge to explaining the muon $g-2$ anomaly. We can expect better results from the BLRSSM model since it includes inverse seesaw mechanism and an extra gauge sector. The effect of inverse seesaw mechanism can be read through RGE for the smuons. As can be seen from the last two terms of Eq. (A.7), the Yukawa coupling Y_ν helps decrease the smuon masses at low scales, as compared to models without inverse seesaw. A similar effect can be read through the RGE of μ Eq. (A.1) and sneutrinos Eq. (A.6). The presence of another free Yukawa coupling Y_s in addition to Y_ν contributes to evolving light sneutrino masses to the low scale via RGE as can be seen from the Eq. (A.6).

Here we investigate the effects on the muon $g-2$ anomaly for both sneutrino and neutralino LSP cases. Fig. 3.9 displays the correlations between muon a_μ and the relevant free parameters in m_0, $M_{1/2}$, $\tan\beta$ and μ. The color coding is the same as Fig. 3.8 except that we do not impose the relic density constraint. In addition, the shadowed regions show 1, 2 and 3 σ deviations between the calculated contribution to muon $g-2$ factor and its experimental value. The top left side plot shows that Δa_μ favors low values for m_0 (light scalar masses). Similarly light gaugino masses (light electroweakinos) are also required to decrease

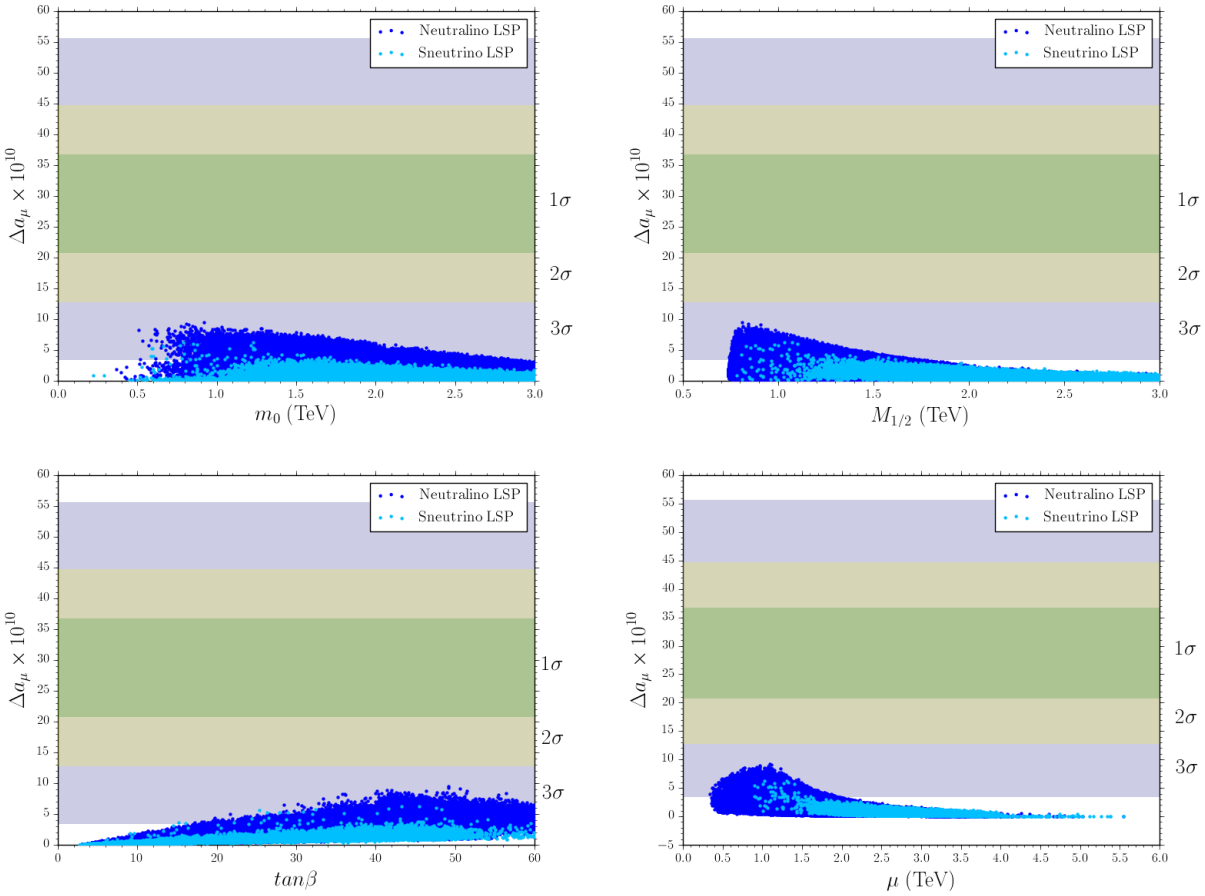

Figure 3.9: Δa_μ dependence of m_0 (top left) , $M_{1/2}$ (top right), $\tan\beta$ (bottom left) and μ (bottom right). The color coding is the same as Fig. 3.8, except that the relic density bound is not implemented. In addition, the shadowed regions show 1 σ, 2 σ and 3 σ differences between the theoretical contribution to muon $g-2$ factor and its experimental value.

the Δa_μ discrepancy, as seen from the top right handed plot. The need of light scalars and electroweakinos agrees with large $\tan\beta$ values (bottom left panel). Finally, the Δa_μ depends sensitively on the μ parameter, as in MSSM, and here the contribution to the muon $g-2$ factor drops sharply for $\mu > 1.5$ TeV. This is due to one loop contributions effects, where, as the μ term increases, the contributions where the higgsinos run in the loop are suppressed, while bino-smuon loop is left as only effective contributing diagram. However, as the bino masses cannot be as low as $\tilde{B}_R$ masses, the contribution from this channel is insufficient. And thus, against expectations, the inverse seesaw mechanism cannot sufficiently enhance muon Δa_μ within universality conditions, and the corrections hardly reach the 2σ region.

3.5.3 Z' mass constraints

To highlight the differences between the two scenarios, we kept the model as general as possible and did not impose the latest Z' mass bounds so far. In this subsection, we include an investigation of implications of the constraints imposed on the Z' mass by a recent new study at ATLAS [6], requiring an increase in the lower bound for the BLRSSM model to $M_{Z'} > 3.9\,(3.6)$ TeV in the $ee(\mu\mu)$ channels. One must be careful when applying these bounds. First, the experiment assumes non-supersymmetric models, and thus a case where Z' does not decay to supersymmetric particles, which will modify its total decay width and thus branching ratios. Second, the parameter choice and unification scale is different from ours: the choice depends on symmetry breaking scales and assumed multiplet composition of the GUT parent. With this note of caution, we explore the parameter space here.

First, we show some of the decay rates of the Z' boson in BLRSSM. Fig. 3.10 displays some of the important decay channels of Z' where $BR(Z' \to ll) = BR(Z' \to ee) + BR(Z' \to \mu\mu) + BR(Z' \to \tau\tau) + BR(Z' \to \nu\nu)$, $BR(Z' \to \widetilde{ll})$, $BR(Z' \to qq)$ and $BR(Z' \to \widetilde{\chi}\widetilde{\chi})$, all plots as a function of $m_{Z'}$. Throughout, all points are consistent with LHC, B-physics bounds, HiggsBounds and HiggsSignals. Dark blue points show neutralino LSP solutions whereas light blue ones stand for sneutrino LSP solutions.

The top left panel in Fig. 3.10 exhibits the branching ratio of Z' into lepton pairs while the top right panel shows the branching for the supersymmetric partners in the same channel. As can be seen from top left plane, the branching ratio of Z' into all leptons (e^+e^-, $\mu^+\mu^-$, $\tau^+\tau^-$ and their neutrinos). changes between $25\% - 37\%$ while its decays into their supersymmetric partners, sleptons, are low, in the range of 0% and 16%. It is interesting to note that these models, unlike E_6-derived models containing an extra $U(1)'$ gauge group, are not likely to be leptophobic as the branching ratio into leptons is significant throughout the parameter space investigated. The bottom panels of Fig. 3.10 show the branching ratio into quarks (left) and into neutralinos and/or charginos (right). As usual, the largest branching ratio obtained is hadronic (40%-62%), which, though significant, is not as large as for $U(1)'$ models [107], which will likely adversely affect the Z' production cross section. The decay into two charginos or neutralinos occurs above their mass threshold and is very small throughout the whole parameter space (0%-8%). So it appears that the decay of the Z' boson is fairly consistent with a non-supersymmetric scenario. Based on this, we shall investigate the effects of setting the mass lower bound to be $m_{Z'} > 3.5$ TeV throughout our analyses.

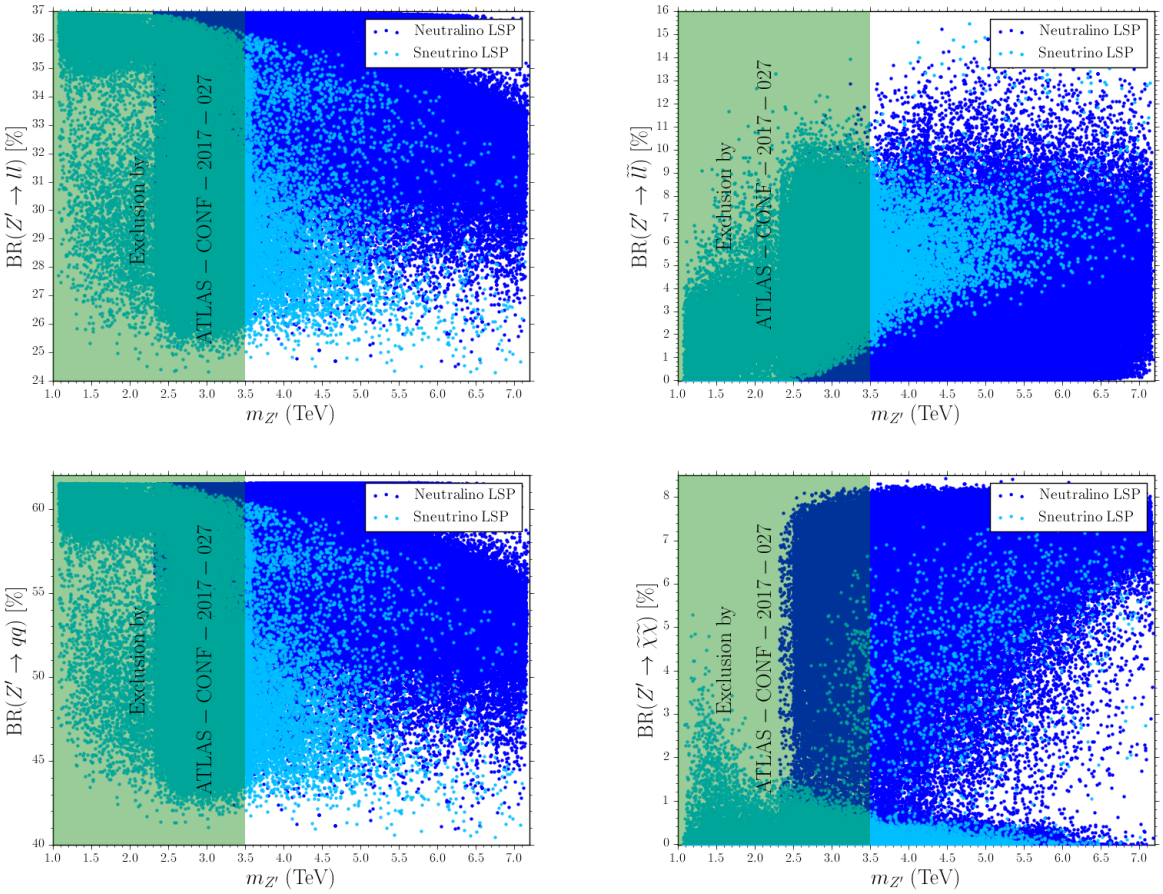

Figure 3.10: Branching ratios of Z' in BLRSSM. (Top left): $BR(Z' \to ll(ee + \mu\mu + \tau\tau$ and their neutrinos)); (top right) $BR(Z' \to \widetilde{l}\widetilde{l})$, (bottom left) $BR(Z' \to q\bar{q})$ and (bottom right) $BR(Z' \to \widetilde{\chi}\widetilde{\chi})$. Neutralino LSP points are represented in dark blue, sneutrino LSP points in light blue. The solutions excluded by [6] are in the shaded green region.

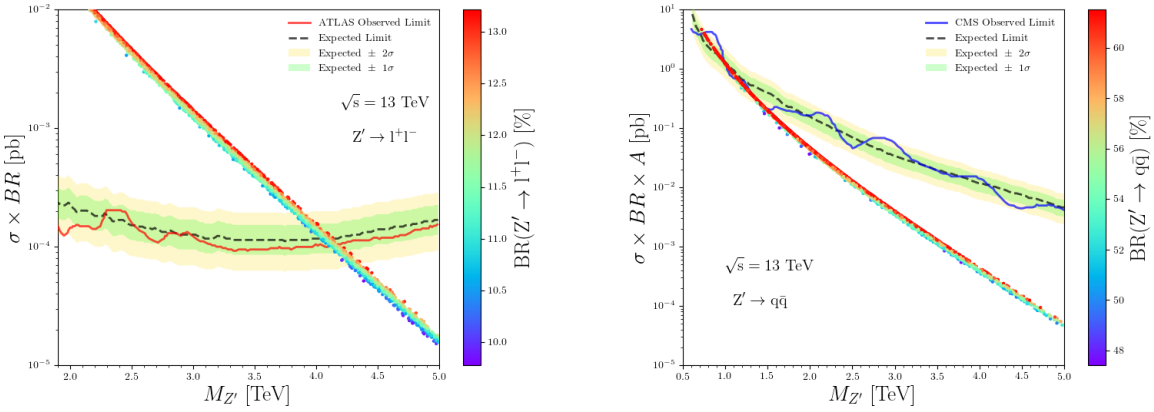

Figure 3.11: Cross sections times branching ratios of Z' in BLRSSM. (Left): $\sigma(pp \to Z') \times BR(Z' \to ll(ee + \mu\mu))$; (right) $\sigma(pp \to Z') \times BR(Z' \to q\bar{q})$, with branching ratios values only shown in the right-sided panels. The experimental results from by ATLAS [6] (left) and CMS [7] (right), are shown as red curves, with 1σ deviation shaded in green and 2σ deviation shaded in yellow.

Next, we analyze the likelihood of observing the Z' in hadronic or leptonic decays. In Fig. 3.10 we plot the production cross section $\sigma(pp \to Z')$ followed by the decay into leptons ($e^+e^- + \mu^+\mu^-$ only, as in the ATLAS [6] results), on the left hand side, and the same production cross section, followed by the decay into $q\bar{q}$ pairs (excluding top quarks), on the right. We indicate the branching ratios explicitly on the panels at the right-hand side, and compare both results with the experimental curves obtained by ATLAS [6] and CMS [7]. Although the dominant decay modes of Z' are into $q\bar{q}$ pairs, the leptonic decays are the most limiting and, in this very much constrained model, the limits on the Z' mass turn out to be closer to 3.75 TeV (at 2σ). Clearly, the model parameters are quite close to this limit, and Z' should be observed with only a small increase in luminosity. For the three benchmarks chosen in Sec. 7.6, in Table 3.3, we chose the mass of Z' to be close to the experimental limit. The values for $\sigma(pp \to Z') \times BR(Z' \to ll(ee + \mu\mu))$ are just below the experimental limits, but again, an increase of luminosity of a factor of 2-5 will either show a peak in the curve, or rule this scenario out.

3.6 Collider Signals and Dark Matter Detection

With the constraints on Z' mass from the previous subsection, we revisit the plots for the spin independent cross section for proton and neutron respectively. While in the Fig. 3.6,

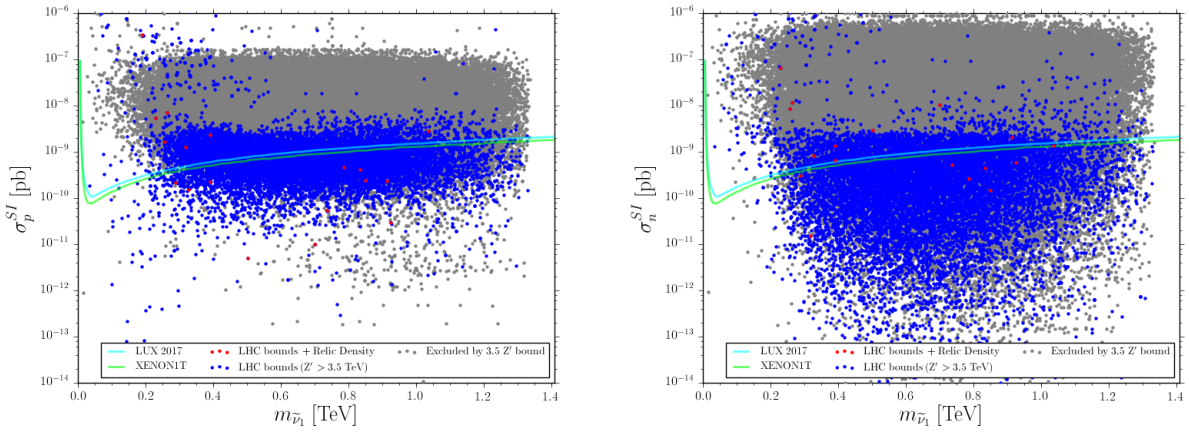

Figure 3.12: Dependence of the spin independent cross section for the proton σ_p^{SI} (left) and neutron σ_n^{SI} (right) as a function on the sneutrino LSP mass $m_{\tilde{\nu}_1}$, for , $m_{Z'} \geq 3.5$ TeV. All points are consistent with REWSB and sneutrino LSP. The color coding in each plane is the same as Fig. 3.1.

we considered $m_{Z'} \geq 2.5$ TeV, and the spin-independent proton (or neutron) cross sections for sneutrino LSP solutions were satisfied with XENON1T experimental exclusion limit, imposing the new Z' mass limit excludes most of the parameter space for sneutrino LSP solutions, as shown in Fig. 3.12. Specifically, of about 10^6 scanned parameter points only 18 solutions compatible with the relic density bound are found, and only 10 of them can survive XENON1T experimental exclusion limit. Imposing Z' mass constraints, the sneutrino LSP scenario thus emerges as extremely constrained and, realistically, ruled out. However, the neutralino LSP scenario is unaffected by the Z' mass limits and survives direct detection constraints, as in Fig. 3.4.

In addition to *direct detection*, DM searches also attempt to identify visible products resulting from DM interactions, focusing on searching for SM particles produced by the decay or annihilation of DM. These are *indirect searches*, and the advantages of these are the large amounts of available DM, while the challenges are that the DM interacts weakly with SM particles, so the rate of production of these particles is expected to be small. In our model, R-parity is exact and the DM is stable, however DM can annihilate into leptons, hadrons and W^+W^- pairs. We plot, in Fig. 3.13, left top panel, the annihilation cross section of DM as a function of the LSP neutralino mass, and compare it with the constraints from $\mu^+\mu^-$ (pink dotted line), $\tau^+\tau^-$ (yellow dotted line), W^+W^- (green dotted line), and $b\bar{b}$ (black dotted line), derived from the combined analysis from Fermi-LAT experiment [8][1]. As

[1]Comparably strong limits come also from AMS-02 [108] and the cosmic microwave background.

before, the regions in red satisfy all constraints, including for relic density, and they lie below the exclusion curves. The dominant annihilation decays of DM are into $b\bar{b}$ and $\tau^+\tau^-$, and in Table 3.3, we give branching ratios for the specific benchmarks chosen. Since solutions consistent with the relic density (the red points) are close to the Fermi-LAT experimental curves, we included these in the annihilation cross section plot. However, for both neutrino flux and muon flux (bottom panels), our results are small compared to experimental Fermi-LAT results [8]. Specifically, our values for neutrino flux are changing between 10^6 – 10^{10} km^2/year, while experimental results for neutrino flux are between 10^{10} – 10^{14} km^2/year [109]. Similarly, our values for the muon flux are between 10^{-2} – 10^3 km^2/year, while experimental results for muon flux are between 10^2 – 10^5 km^2/year [110]. Finally, we show the photon flux result (top right panel), which changes between 10^{-14} – 10^{-22} km^2/year, and which is tiny and does not explain the γ-ray excess from the galactic centre (GC) detected by Fermi-LAT, for photons between 20 MeV and 300 GeV. We include exact values for the fluxes for our benchmarks in Table 3.3.

Lastly, we would like to analyze the production and decays for this scenario at the LHC. We choose benchmarks from the parameter scan results which satisfy all experimental bounds, including the relic density constraint and XENON1T exclusion limits, and favor light neutralino LSP solutions as the only ones surviving all constraints. We proceed by exporting the BLRSSM to the UFO format [111] and use MG5_aMC@NLO framework version 2.5.5 [112] to simulate hard-scattering LHC collisions and evaluate the cross sections for various signals. For the calculation of cross sections, we select three benchmarks with different features, which could showcase different features of the model for detection at the LHC.

The first benchmark, benchmark 1 has $H_{\widetilde{R}}$-like neutralino LSP. (Even though parameter scans allow Higgsino-like and higgsino-binos mixed LSP neutralino solutions between 300-500 GeV, no benchmark in this range can be found as these states are completely excluded by the XENON1T exclusion limit.) We thus select benchmarks with mixed $\widetilde{B}_R - \widetilde{B}$ content. For benchmarks 2-3, BR($\widetilde{\chi}_2^0 \to \widetilde{\chi}_1^0 h_1$) and BR($\widetilde{\chi}_1^\pm \to \widetilde{\chi}_1^0 W^\pm$) are almost unity. Sparticle masses are similar in both cases, with the exception of the lightest chargino, which is heavier for benchmark 3. Also, for benchmark 3, BR($\widetilde{\tau}_1 \to \tau_1 \widetilde{\chi}_1^0$) ~ 1 while this is much smaller for benchmark 2. Note that benchmarks satisfy all the constraints, including the IceCube22 [113] exclusion. Our results are shown in Table 3.3.

Even though LSP neutralino mass is quite light (428 GeV) for benchmark 1, we find

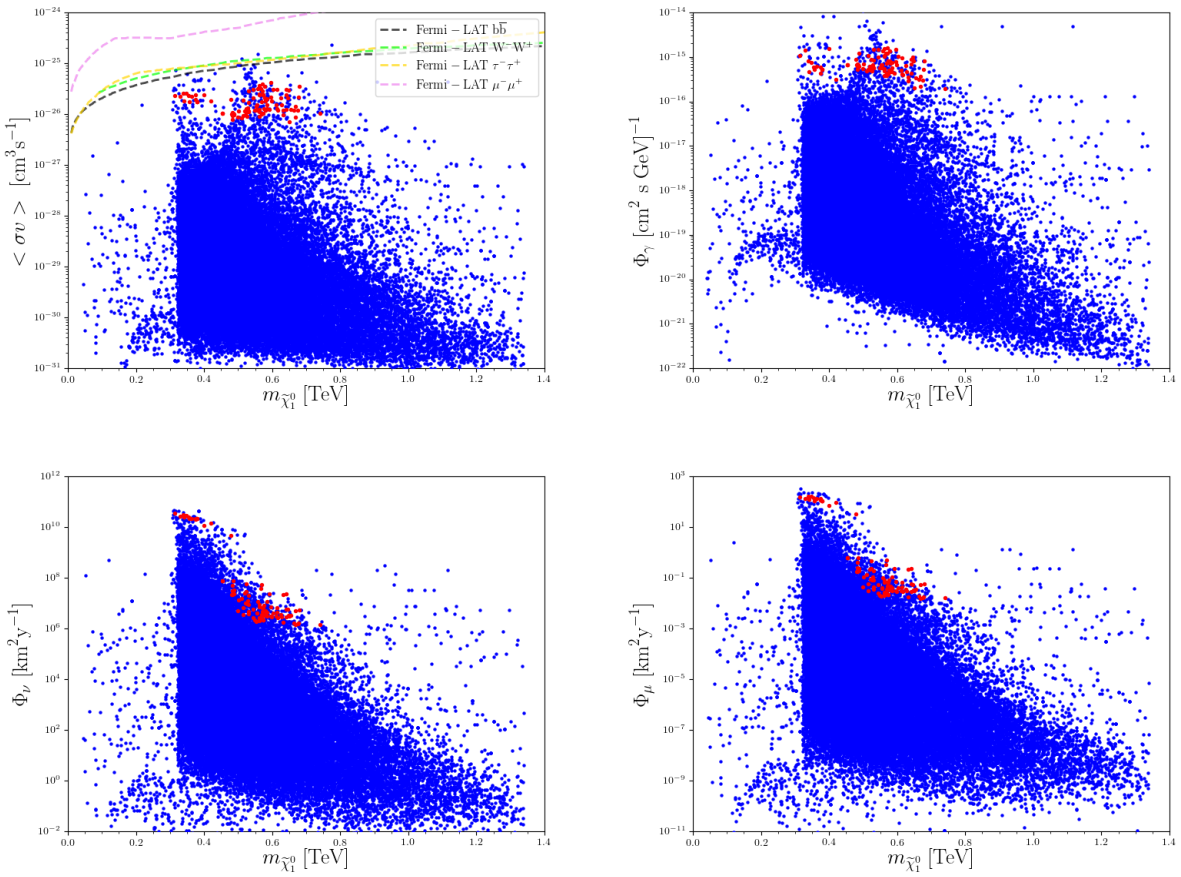

Figure 3.13: (Top left): Annihilation cross section of DM as a function of the LSP neutralino mass, and compare it with the constraints from $\mu^+\mu^-$ (pink dotted line), $\tau^+\tau^-$ (yellow dotted line), W^+W^- (green dotted line), and $b\bar{b}$ (black dotted line), derived from the combined analysis from Fermi-LAT experiment [8]; (top right): Photon flux as a function of the LSP neutralino mass; (bottom left): Neutrino flux as a function of the LSP neutralino mass; (bottom right): Muon flux as a function of the LSP neutralino mass. As before, the regions in red satisfy all constraints, including relic density.

that both chargino-chargino and neutralino-chargino production cross sections are quite low, due to the fact that the neutralino is mostly $\widetilde{H}_R$-like. For the other benchmarks, with neutralino contents of mixed binos, the second lightest neutralino and chargino masses are degenerate. We estimated the cross sections for chargino/neutralinos and stau production as being the most promising. The highest cross-section values for chargino-chargino production and chargino-neutralino production are obtained for benchmark 2 whose neutralino and chargino masses are 470 GeV and 767 GeV, respectively. As can be seen from the Table 3.3, chargino-chargino production and neutralino-chargino production cross sections are 7.03 $\times 10^{-1}$ fb and 1.27 fb, respectively. The cross-section values decrease in benchmark 3 (with respect to benchmark 2) when neutralino and chargino masses are 506 GeV and 954 GeV (versus 470 and 767 GeV), respectively. For all benchmarks, Z' masses are above 4 TeV, consistent with the latest ATLAS result, but very close to the exclusion limit, as discussed in the previous subsection, 3.5.3. Note that gluino masses are about 2.5 TeV for all benchmarks, making gluino results testable at the HL-LHC or by the next generation colliders [114, 115].

Including all the constraints, we conclude that production of supersymmetric particles in BLRSSM fall below detector sensitivity. Especially because the final signals will have even lower production cross sections, as they will be suppressed by branching ratios of chargino/neutralinos to missing energy + leptons. A way to improve our results is to relax some or most universality constraints, and looking for effective cuts which would enhance the signal over the background. We shall return to this in a future work.

	Benchmark 1	Benchmark 2	Benchmark 3
m_0 [GeV]	2916	1831	2073
$M_{1/2}$ [GeV]	1159	1092	1166
$\tan\beta$	55.9	45.3	58.6
$\tan\beta_R$	1.15	1.19	1.06
A_0 [GeV]	-16.56	826	1652
$< v_R >$ [GeV]	11321	11711	12969
$Y_\nu \quad (M_{\rm SUSY})$	0.18	2.11×10^{-3}	0.25
$Y_s \quad (M_{\rm SUSY})$	0.41	0.62	0.49
μ [GeV]	1246	787	1305
μ_R [GeV]	434	1144	3817
$m_{\widetilde{\chi}_1^0}$ [GeV]	**428** ($\widetilde{H}_R$-like)	**470** (mixed $\widetilde{B}_R - \widetilde{B}$)	**506** (mixed $\widetilde{B}_R - \widetilde{B}$)
$m_{\widetilde{\chi}_2^0}$ [GeV]	**958**	**768**	**954**
$m_{\widetilde{\chi}_1^\pm}$ [GeV]	**507**	**767**	**954**
m_{h_2} [GeV]	428	380	224
m_{h_3} [GeV]	1158	1018	1013
m_{A_1} [GeV]	1175	1020	1017
$m_{\widetilde{t}_1}$ [GeV]	2455	1977	2209
$m_{\widetilde{b}_1}$ [GeV]	2778	2279	2458
$m_{\widetilde{\tau}_1}$ [GeV]	1790	1332	1064
$m_{\widetilde{\nu}_1}$ [GeV]	2638	2036	1858
$m_{Z'}$ [GeV]	4046	4182	4632
$m_{\widetilde{g}}$ [GeV]	2671	2473	2634
$\sigma(pp \to \widetilde{\chi}_1^\pm \widetilde{\chi}_2^0)$ [fb]	1.25×10^{-3}	1.27	7.29×10^{-1}
$\sigma(pp \to \widetilde{\chi}_1^+ \widetilde{\chi}_1^-)$ [fb]	3.9×10^{-1}	7.03×10^{-1}	3.47×10^{-1}
$\sigma(pp \to \widetilde{\tau}_1 \widetilde{\tau}_1)$ [fb]	4.50×10^{-4}	2.05×10^{-3}	3.46×10^{-3}
BR($\widetilde{\chi}_2^0 \to \widetilde{\chi}_1^0 h_1$)	-	0.94	0.89
BR($\widetilde{\chi}_1^\pm \to \widetilde{\chi}_1^0 W^\pm$)	-	0.99	0.99
BR($\widetilde{\tau}_1 \to \tau_1 \widetilde{\chi}_1^0$)	-	0.51	0.99
$\sigma(pp \to Z' \to q\bar{q})$ [fb]	5.75×10^{-1}	4.24×10^{-1}	1.61×10^{-1}
$\sigma(pp \to Z' \to e^+e^- + \mu^+\mu^-)$ [fb]	1.31×10^{-1}	9.67×10^{-2}	3.68×10^{-2}
BR($Z' \to e^+e^- + \mu^+\mu^-$)	0.12	0.12	0.12
BR($Z' \to e^+e^- + \mu^+\mu^- + \tau^+\tau^-$)	0.18	0.18	0.18
BR($Z' \to \nu\bar{\nu}$)	0.16	0.16	0.15
BR($Z' \to q\bar{q}$)	0.56	0.56	0.55
BR($Z' \to l\bar{l}$)	4.01×10^{-4}	3.54×10^{-3}	2.07×10^{-2}
BR($Z' \to \widetilde{q}\widetilde{q}$)	-	1.79×10^{-4}	1.38×10^{-4}
BR($Z' \to \widetilde{\chi}\widetilde{\chi}$)	7.64×10^{-2}	8.06×10^{-2}	7.33×10^{-2}
Ωh^2	0.1369	0.0978	0.0958
$\sigma^{SI}_{\rm nucleon}$ [pb]	1.60×10^{-11}	1.80×10^{-10}	2.43×10^{-11}
$\sigma^{SD}_{\rm p}$ [pb]	4.68×10^{-8}	1.12×10^{-6}	6.72×10^{-8}
$\sigma^{SD}_{\rm n}$ [pb]	4.31×10^{-8}	9.15×10^{-7}	6.38×10^{-8}
Icecube22 Exclusion CL [%]	1.15×10^{-2}	0.65	3×10^{-2}
$< \sigma v >$ [cm$^3 s^{-1}$]	2.12×10^{-26}	1.33×10^{-26}	3.07×10^{-26}
Φ_ν[km$^2 y^{-1}$]	2.39×10^{6}	1.70×10^{8}	6.97×10^{6}
Φ_μ[km$^2 y^{-1}$]	2.28×10^{-2}	1.37	6.16×10^{-2}
Φ_γ[cm^2 s GeV]$^{-1}$	9.25×10^{-16}	8.42×10^{-16}	1.85×10^{-15}
Annihilation modes			
$\widetilde{\chi}_1^0\widetilde{\chi}_1^0 \to b\bar{b}$	76%	74%	75%
$\widetilde{\chi}_1^0\widetilde{\chi}_1^0 \to \tau^+\tau^-$	23%	20%	24%
$\widetilde{\chi}_1^0\widetilde{\chi}_1^0 \to h_1 Z$	-	6%	-

Table 3.3: Benchmarks for BLRSSM with relevant cross-sections and branching ratios. We include relevant information on the Z' boson and dark matter. In bold, the lightest chargino and the two lightest neutralino states. Missing entries represent values smaller than 10^{-4}.

Chapter 4

Leptophobic Z' bosons in the secluded $U(1)'$ model

4.1 Introduction

With the discovery of the Higgs boson, the last piece of the Standard Model (SM) construction was fit into place. Furthermore, almost all SM predictions have been confirmed by experimental results, even precision tests involving higher order perturbative Electroweak (EW) and Quantum Chromodynamics (QCD) effects. However, as it stands, the SM cannot be the final theory and the quest for physics Beyond the SM (BSM) is very much alive. Among the many proposed BSM scenarios, Supersymmetry (SUSY) appears to be one of the most popular ones, since it provides elegant solutions to the SM drawbacks, such as the stabilization of the EW scale under radiative corrections, an explanation for the baryon asymmetry of the Universe and for the presence of Dark Matter (DM) in it. However, the minimal version of SUSY, the Minimal Supersymmetric SM (MSSM), provides no explanation for the μ problem [116–119]. The μ parameter, the so-called higgsino mass term, is expected to be at the SUSY-breaking scale but, for successful EW symmetry breaking, its value should be at the scale of the latter. Adding a $U(1)'$ gauge symmetry to the MSSM, one solves this problem by replacing the μ parameter of the MSSM with an effective one, generated dynamically by the Vacuum Expectation Value (VEV) of the singlet Higgs field responsible for breaking $U(1)'$. Furthermore, the additional $U(1)'$ symmetry is able to generate neutrino masses by allowing right-handed neutrinos into the superpotential and can account for either Majorana- [120] or Dirac-type neutrinos [121].

Normally, it is expected that both EW and $U(1)'$ symmetry breaking are achieved through soft-breaking parameters, which would imply that the mass of the gauge boson associated with $U(1)'$, a Z', would be of the same order as the EW scale [122–124]. This conflicts with experimental measurements at the Large Hadron Collider (LHC) [9], though, which impose a lower bound on the Z' mass, from the Drell-Yan (DY) channel, i.e., di-lepton hadro-production, of $\mathcal{O}(4)$ TeV or more. The most natural solution to this inconsistency is that the VEV of the singlet Higgs field is large compared to the EW scale, $\mathcal{O}(1-10)$ TeV, pushing the SUSY scale very high and rendering it mostly unobservable at the present LHC. Alternatively, it was observed that fine-tuning the kinetic mixing between the two $U(1)$ groups could yield Z' bosons which do not decay directly into lepton pairs [125]. Corresponding Z' gauge boson masses are then limited by its di-jet decays, whose bounds are much weaker in comparsions to DY ones [10]. Various aspects of the additional gauge boson and its phenomenological implications have been also studied within non-SUSY and SUSY frameworks [126–136].

An alternative is represented by a $U(1)'$ model where the SUSY-breaking scale and Z' mass are disjoint: the former is close to the EW scale while a large value for the latter can be generated by the VEVs of additional Higgs fields (S_1, S_2, S_3, so-called secluded singlets) which are charged under the $U(1)'$ group but couple weakly to the SM fields [137]. This BSM scenario is known as the *secluded* $U(1)'$ model, a realization of the generic class of $U(1)'$-extended MSSMs (UMSSMs). It allows for both explicit and spontaneous CP symmetry breaking and is able to account for baryogenesis [138]. Differences between this UMSSM scenario and the MSSM would likely reveal themselves in the nature of DM, as in the extended scenario several additional singlinos as well as sneutrinos could be viable candidates for it [139].

In a nutshell, the secluded $U(1)'$ model extends the MSSM by an additional Abelian group, to $SU(3)_c \otimes SU(2)_L \otimes U(1)_Y \otimes U(1)'$, and by four Higgs singlets (three in addition to the one needed to break $U(1)'$, to ensure a $Z'-Z$ mass hierarchy). Exotics with Yukawa couplings to a singlet Higgs field must be introduced to ensure the theory is anomaly free. However, despite the presence of these couplings, one can assume their masses to be at the Grand Unification Theory (GUT) scale and thus neglect them in TeV scale phenomenology[1]. (Note, however, that they have been studied extensively in [140].) Previous studies of this secluded $U(1)'$ model exist, but none consistent with present experimental data on the discovered Higgs boson mass and signal strengths or with Z' gauge boson mass bounds. In this work,

[1]Furthermore, their charges are such that they do not mix with ordinary matter.

we revisit this BSM scenario in detail, with particular interest in addressing the unresolved problems of UMSSMs, by providing light Z' masses yet compatible with current bounds, an acceptable $(g-2)_\mu$ value and DM relic density plus the viable existence of light SUSY particles, altogether providing one with new distinguishing signals of this BSM realization in LHC experiments.

In showing all this, we shall prove first that, in such a $U(1)'$ secluded model, leptophobia can be achieved easily and without gauge kinetic mixing between the Z and Z', so that a light Z' gauge boson can survive all experimental constraints in presence of finite width effects. Furthermore, we shall show that this BSM scenario can predict corrections to $(g-2)_\mu$ within 1σ of the experimentally observed value. Finally, we will also find that, in our UMSSM realization, the Lightest SUSY Particle (LSP), for a large region of its parameter space, is a singlino consistent with all DM constraints accompanied by very light charginos and neutralinos, with masses of $\mathcal{O}(100)$ GeV, in turn consistent with collider limits, into which a Z' can then decay yielding sizable signals at the LHC.

Our work is organized as follows. In the next section, Sec. 6.2, we provide a description of the secluded $U(1)'$ model, with particular emphasis on the gauge and neutralino sectors, i.e., where differences with respect to the MSSM will manifest themselves. We describe the implementation of this BSM scenario, including the free parameters and the constraints imposed on these, in Sec. 7.3. Then, we explain the implications emerging from a wide scan of its parameter space for Z' physics at colliders, in Sec. 6.5, and onto the DM candidate in relic density and direct detection experiments, in Sec. 4.5. Furthermore, in presence of all such constraints on the mass and coupling spectrum of the model, we analyze the consequences for the muon anomalous magnetic moment in Sec. 4.6. We further study the possibility of observing a light Z' boson via chargino/neutralino decays at the High-Luminosity LHC (HL-LHC) and High-Energy LHC (HE-LHC) in Sec. 4.7.

4.2 The secluded $U(1)'$ Model

In this section, we review the secluded $U(1)'$, known also as the secluded UMSSM. In addition to the MSSM superfields, the model has three right-handed neutrino superfields $\hat{N}_i^c$ and four

scalar singlets $\hat{S}$, $\hat{S}_1$, $\hat{S}_2$ and $\hat{S}_3$. The superpotential in this model is described by

$$\begin{aligned} W &= Y_u^{ij}\hat{Q}_i\hat{H}_u\hat{u}_j^c - Y_d^{ij}\hat{Q}_i\hat{H}_d\hat{d}_j^c - Y_e^{ij}\hat{L}_i\hat{H}_d\hat{e}_j^c \\ &+ Y_\nu^{ij}\hat{L}_i\hat{H}_u\hat{N}_i^c + \lambda\hat{H}_u\hat{H}_d\hat{S} + \frac{\kappa}{3}\hat{S}_1\hat{S}_2\hat{S}_3 + \sum_{n=1}^{n_\varphi} h_\varphi^i S\varphi_i\overline{\varphi}_j + \sum_{n=1}^{n_\Upsilon} h_\Upsilon^i S\Upsilon_i\overline{\Upsilon}_j, \end{aligned} \tag{4.1}$$

where the first line of Eq. 4.1 contains the usual terms of the MSSM while the second line includes the additional interactions of right-handed neutrinos $\hat{N}_i^c$ (assumed to be Dirac fields here) and $\hat{H}_u$, as well as the singlet superfields $\hat{S}$, $\hat{S}_1$, $\hat{S}_2$ and $\hat{S}_3$, and where Υ_i and φ_i are the exotics, which, as explained above, are assumed to be heavy and decoupled from the low energy spectrum. The effective μ term is generated dynamically as $\mu = \lambda\langle S\rangle$. The scalar potential includes the F-term, given by

$$\begin{aligned} V_F = &\lambda^2(|H_u|^2|H_d|^2 + |S|^2|H_u|^2 + |S|^2|H_d|^2) \\ &+ \kappa^2(|S_1|^2|S_2|^2 + |S_2|^2|S_3|^2 + |S_3|^2|S_1|^2)\,, \end{aligned} \tag{4.2}$$

while the D-term scalar potential is

$$\begin{aligned} V_D = &\frac{g_1^2+g_2^2}{8}(|H_d|^2 - |H_u|^2)^2 \\ &+ \frac{1}{2}g'^2\left(Q_S|S|^2 + Q_{H_u}|H_u|^2 + Q_{H_d}|H_d|^2 + \sum_{n=1}^{3} Q_{S_i}|S_i|^2\right)^2, \end{aligned} \tag{4.3}$$

where g_1, g_2 and g' are the coupling constants for the $U(1)_Y$, $SU(2)_L$ and $U(1)'$ gauge groups while Q_ϕ is the $U(1)'$ charge of the field ϕ. Finally, the potential includes the SUSY-breaking soft terms,

$$\begin{aligned} V_{\text{soft}} &= m_{H_u}^2|H_u|^2 + m_{H_d}^2|H_d|^2 + m_S^2|S|^2 + \sum_{n=1}^{3} m_{S_i}^2|S_i|^2 - (A_\lambda\lambda S H_u H_d + A_\kappa\kappa S_1S_2S_3 + h.c) \\ &+ (m_{SS_1}^2 SS_1 + m_{SS_2}^2 SS_2 + m_{S_1S_2}^2 S_1^\dagger S_2 + h.c.). \end{aligned} \tag{4.4}$$

In Table 4.1 we give the complete list of the fields in the model, together with their spin, number of generations and charge assignments under the extended gauge group. The secluded $U(1)'$ charge assignments and anomaly cancellation conditions allow for some freedom in the choice of the $U(1)'$ charges, absent in other $U(1)'$ models. In general, the $U(1)'$ change

SF	Spin 0	Spin $\frac{1}{2}$	Generations	$U(1)_Y \otimes SU(2)_L \otimes SU(3)_C \otimes U(1)'$
$\hat{q}$	$\tilde{q}$	q	3	$(\frac{1}{6}, \mathbf{2}, \mathbf{3}, Q'_q)$
$\hat{l}$	$\tilde{l}$	l	3	$(-\frac{1}{2}, \mathbf{2}, \mathbf{1}, Q'_\ell)$
$\hat{H}_d$	H_d	$\tilde{H}_d$	1	$(-\frac{1}{2}, \mathbf{2}, \mathbf{1}, Q'_{H_d})$
$\hat{H}_u$	H_u	$\tilde{H}_u$	1	$(\frac{1}{2}, \mathbf{2}, \mathbf{1}, Q'_{H_u})$
$\hat{d}$	$\tilde{d}^*_R$	d^*_R	3	$(\frac{1}{3}, \mathbf{1}, \overline{\mathbf{3}}, Q'_d$
$\hat{u}$	$\tilde{u}^*_R$	u^*_R	3	$(-\frac{2}{3}, \mathbf{1}, \overline{\mathbf{3}}, Q'_u)$
$\hat{e}$	$\tilde{e}^*_R$	e^*_R	3	$(1, \mathbf{1}, \mathbf{1}, Q'_e)$
$\hat{v}_R$	$\tilde{\nu}^*_R$	ν^*_R	3	$(0, \mathbf{1}, \mathbf{1}, Q'_v)$
$\hat{S}$	S	$\tilde{S}$	1	$(0, \mathbf{1}, \mathbf{1}, Q'_s)$
$\hat{S}_1$	S_1	$\tilde{S}_1$	1	$(0, \mathbf{1}, \mathbf{1}, Q'_{s_1})$
$\hat{S}_2$	S_2	$\tilde{S}_2$	1	$(0, \mathbf{1}, \mathbf{1}, Q'_{s_2})$
$\hat{S}_3$	S_3	$\tilde{S}_3$	1	$(0, \mathbf{1}, \mathbf{1}, Q'_{s_3})$
$\hat{\varphi}$	$\tilde{\varphi}$	φ	3	$(Y_\varphi, \mathbf{1}, \mathbf{1}, Q'_\varphi)$
$\hat{\overline{\varphi}}$	$\tilde{\overline{\varphi}}$	$\overline{\varphi}$	3	$(Y_{\overline{\varphi}}, \mathbf{1}, \mathbf{1}, Q_{\overline{\varphi}'})$
$\hat{\Upsilon}$	$\tilde{\Upsilon}$	Υ	2	$(Y_\Upsilon, \mathbf{1}, \mathbf{1}, Q'_\Upsilon)$
$\hat{\overline{\Upsilon}}$	$\tilde{\overline{\Upsilon}}$	$\overline{\Upsilon}$	2	$(Y_{\overline{\Upsilon}}, \mathbf{1}, \mathbf{1}, Q_{\overline{\Upsilon}'})$

Table 4.1: Superfield configuration in the secluded UMSSM.

assignments can be chosen as follows:

$$
\begin{aligned}
Q_Q = \alpha, \qquad Q_{H_u} = \beta, \qquad Q_S = \gamma, \qquad Q_\ell = -3\alpha + \frac{\gamma}{3}, \\
Q_{H_d} = -\beta - \gamma, \qquad Q_u = -\alpha - \beta, \qquad Q_d = -Q_Q - Q_{H_d} = -\alpha + \beta + \gamma, \\
Q_e = -Q_\ell - Q_{H_d} = 3\alpha + \beta + \frac{2\gamma}{3}, \qquad Q_N = -Q_\ell - Q_{H_u} = 3\alpha - \beta - \frac{\gamma}{3}, \\
Q_{S_1} = Q_{S_3} = \delta, \qquad Q_{S_2} = -2Q_{S_1} = -2Q_{S_3} = -2\delta.
\end{aligned} \tag{4.5}
$$

Here, $Q_{H_d} = 0$ dictates $\gamma = -\beta$. From the conditions above we can choose, for simplicity, $Q_e = Q_\ell$. The leptophobic condition $Q_\ell = Q_e = 0$ requires $\alpha = -\frac{\beta}{9}$, so that the leptophobia condition can be achieved without resorting to kinetic mixing between the two $U(1)$ groups[2]. Thus, Eq. 4.5 can be rewritten in terms of α and δ only as:

$$
\begin{aligned}
Q_Q = \alpha, \qquad Q_{H_u} = -9\alpha, \qquad Q_S = 9\alpha, \qquad Q_\ell = 0, \qquad Q_{H_d} = 0, \\
Q_u = 8\alpha, \qquad Q_d = -\alpha, \qquad Q_e = 0, \qquad Q_N = 9\alpha, \\
Q_{S_1} = Q_{S_3} = \delta, \qquad Q_{S_2} = -2Q_{S_1} = -2Q_{S_3} = -2\delta.
\end{aligned} \tag{4.6}
$$

[2]This is unlike models where the $U(1)'$ charges are derived from the mixing of, e.g., θ_{E_6} angles [3].

After the spontaneous breaking of the extended gauge symmetry group down to electromagnetism (EM), the $W^{\pm}, Z$ and Z' bosons acquire masses while the photon remains massless. At tree level, the squared masses of the Z and Z' bosons are given by

$$\begin{aligned} M_Z^2 &= \frac{g_1^2+g_2^2}{2}\left(\langle H_u^0\rangle^2+\langle H_d^0\rangle^2\right), \\ M_{Z'}^2 &= g'^2\left(Q_S\langle S\rangle^2+Q_{H_u}\langle H_u^0\rangle^2+Q_{H_d}\langle H_d^0\rangle^2+\sum_{n=1}^{3}Q_{S_i}\langle S_i\rangle^2\right), \end{aligned} \tag{4.7}$$

where $H_d^0 \equiv \frac{v_d}{\sqrt{2}}$ and $H_u^0 \equiv \frac{v_u}{\sqrt{2}}$ stand for the neutral components of the down-type and up-type Higgs fields H_d and H_u.

While the chargino sector is unaltered, the neutralino sector of the secluded $U(1)'$ model includes five additional fermion fields: the $U(1)'$ gauge fermion $\widetilde{Z}'$ and four singlinos $\widetilde{S}$, $\widetilde{S}_1$, $\widetilde{S}_2$, $\widetilde{S}_3$, in total, nine neutralino states $\widetilde{\chi}_i^0$ $(i=1,\ldots,9)$ [137]:

$$\widetilde{\chi}_i^0 = \sum_a \mathcal{N}_{ia}^0 \widetilde{G}_a\,, \tag{4.8}$$

where the mixing matrix $\mathcal{N}_{ia}^0$ connects the gauge-basis neutral fermion states to the physical-basis neutralinos $\widetilde{\chi}_i^0$. The neutralino masses $M_{\widetilde{\chi}_i^0}$ are obtained through the diagonalization $\mathcal{N}^0\mathcal{M}\mathcal{N}^{0\,T} = \text{Diag}\left\{M_{\widetilde{\chi}_1^0},\,\ldots,\,M_{\widetilde{\chi}_9^0}\right\}$. The 9×9 neutral fermion mass matrix is

$$\mathcal{M} = \begin{pmatrix} M_{\tilde{Z}} & 0 & -M_{\tilde{Z}\tilde{H}_d} & M_{\tilde{Z}\tilde{H}_u} & 0 & M_{\tilde{Z}\tilde{Z}'} & 0 & 0 & 0 \\ 0 & M_{\tilde{W}} & M_{\tilde{W}\tilde{H}_d} & -M_{\tilde{W}\tilde{H}_u} & 0 & 0 & 0 & 0 & 0 \\ -M_{\tilde{Z}\tilde{H}_d} & M_{\tilde{W}\tilde{H}_d} & 0 & -\mu & -\mu_{H_u} & \mu'_{H_d} & 0 & 0 & 0 \\ M_{\tilde{Z}\tilde{H}_u} & -M_{\tilde{W}\tilde{H}_u} & -\mu & 0 & -\mu_{H_d} & \mu'_{H_u} & 0 & 0 & 0 \\ 0 & 0 & -\mu_{H_u} & -\mu_{H_d} & 0 & \mu'_S & 0 & 0 & 0 \\ M_{\tilde{Z}\tilde{Z}'} & 0 & \mu'_{H_d} & \mu'_{H_u} & \mu'_S & M_{\tilde{Z}'} & \mu'_{S_1} & \mu'_{S_2} & \mu'_{S_3} \\ 0 & 0 & 0 & 0 & 0 & \mu'_{S_1} & 0 & -\frac{\kappa v_3}{3\sqrt{2}} & -\frac{\kappa v_2}{3\sqrt{2}} \\ 0 & 0 & 0 & 0 & 0 & \mu'_{S_2} & -\frac{\kappa v_3}{3\sqrt{2}} & 0 & -\frac{\kappa v_1}{3\sqrt{2}} \\ 0 & 0 & 0 & 0 & 0 & \mu'_{S_3} & -\frac{\kappa v_2}{3\sqrt{2}} & -\frac{\kappa v_1}{3\sqrt{2}} & 0 \end{pmatrix}, \tag{4.9}$$

(4.10)

where the lightest eigenvalue is the DM candidate. In the neutralino mass matrix, the mass

mixing terms are defined in terms of $\tan\beta = \frac{v_d}{v_u}, \langle S \rangle = \frac{v_S}{\sqrt{2}}$ and $\langle S_i \rangle = \frac{v_i}{\sqrt{2}}$ $(i = 1, 2, 3)$, as

$$\begin{aligned} M_{\widetilde{Z}\,\widetilde{H}_d} &= M_Z \sin\theta_W \cos\beta\,, \quad M_{\widetilde{Z}\,\widetilde{H}_u} = M_Z \sin\theta_W \sin\beta\,, \\ M_{\widetilde{W}\,\widetilde{H}_d} &= M_Z \cos\theta_W \cos\beta\,, \quad M_{\widetilde{W}\,\widetilde{H}_u} = M_Z \cos\theta_W \sin\beta\,, \end{aligned} \tag{4.11}$$

where μ_i, μ'_j stand for the effective couplings in each sector, given in terms of h_s or g', the coupling constant of $U(1)'$, as

$$\begin{aligned} \mu_{H_d} &= h_s \frac{v_d}{\sqrt{2}}\,, \quad \mu_{H_u} = h_s \frac{v_u}{\sqrt{2}}\,, \quad \mu'_{H_d} = g' Q_{H_d} v_d, \\ \mu'_{H_u} &= g' Q_{H_u} v_u\,, \quad \mu'_S = g' Q_S v_S\,, \quad \mu'_{S_i} = g' Q_{S_i} v_i\,. \end{aligned} \tag{4.12}$$

4.3 Computational Setup

Following the development of the model as in Sec. 6.2, to enable our analysis and impose constraints coming from experimental data, we implement the model within a computational framework. We have then made use of SARAH (version 4.13.0) [78, 79, 141] to generate CalcHep [142] model files and a UFO [111] version of the model [143], so that we could employ MicrOMEGAs (version 5.0.9) [144] for the computation of the predictions relevant for our dark matter study, MG5aMC (version 2.7.2) [112] for generating the hard-scattering event samples necessary for our collider study, and SPheno (version 4.0.4) [76, 77] package for spectrum analysis. We make use of HiggsBounds [94] to constrain the possibility of BSM Higgs bosons detection at colliders and HiggsSignals [95] to test the signal strengths of the SM-like Higgs state. During the numerical analysis performed in this work, we have used the PySLHA 3.2.4 package [145] to read the input values for the model parameters that we encode under the SLHA format [146], and to integrate the various employed programmes into a single framework.

Using our interfacing and following the Metropolis-Hastings technique, we performed a random scan over the parameter space, illustrated in Table 7.2, where we restrict ourselves only to universal boundary conditions. Here m_0 denotes the Spontaneous Symmetry Breaking (SSB) mass term for all the scalars while $M_{1/2}$ stands for the SSB mass terms for the gauginos including the one associated with the U(1)$'$ gauge group. As before, $\tan\beta$ is the ratio of VEVs of the MSSM Higgs doublets, A_0 is the SSB trilinear scalar interacting term, λ is the

Parameter	Scanned range	Parameter	Scanned range
m_0	$[0., 3.]$ TeV	v_S	$[0.97, 15.8]$ TeV
$M_{1/2}$	$[0., 3.]$ TeV	v_1	$[1.6, 15.]$ TeV
$\tan\beta$	$[1., 55.]$	v_2	$[0.8, 11.2]$ TeV
$A_0/m0$	$[-3., 3.]$ GeV	v_3	$[1.6., 15.]$ TeV
λ	$[3. \times 10^{-2}, 0.6]$	κ	$[0.3, 2.65]$
A_λ	$[1.8, 7.5]$ TeV	A_κ	$[-8.3, -0.2]$ TeV
$Y_\nu^{ij}, (i = j)$	$[1 \times 10^{-8}, 1 \times 10^{-7}]$	$Y_\nu^{ij}, (i \neq j)$	0.

Table 4.2: Scanning range of parameter space of the secluded $U(1)'$ model.

coupling associated with the interaction of the $\hat{H}_u$, $\hat{H}_d$ and $\hat{S}$ fields while κ is the coupling of the interaction of the $\hat{S}_1$, $\hat{S}_2$ and $\hat{S}_3$ fields. Trilinear couplings for λ and κ are defined as $A_\lambda\lambda$ and $A_\kappa\kappa$, respectively, at the SUSY scale. Here, Y_ν^{ij} is the Yukawa coupling of the term $\hat{L}_i\hat{H}_u\hat{N}_i^c$ and we vary only the diagonal elements in the range of 1×10^{-8} – 1×10^{-7} while setting the off-diagonal elements to zero.

We followed [147] where a simple method for analyzing the impact of precision EW data above and below the Z peak on flavor-conserving heavy new physics is implemented. There, the corrections to all leptonic data can be converted into oblique corrections to the vector boson propagators and condensed into seven parameters. Numerical fits for the new physics parameters are included and the method is applied to generic Z' gauge bosons highlighting parameter combinations most strongly constrained. The authors report the 99% Confidence Level (CL) iso-contours of bounds on $M_{Z'}/g'$ for a set of Z''s. Their constraints depend only on the leptonic and Higgs $U(1)'$ charges, Q_{H_u}, Q_{H_d}, Q_ℓ, Q_e, and the assumption that their arbitrary overall normalization is fixed, $Q_{H_u}^2 + Q_{H_u}^2 + Q_\ell^2 + Q_e^2 = 2$. Given that we fix $Q_\ell = Q_e = Q_{H_d} = 0$, the Z' gauge boson in our model cannot be considered as one of the given set of Z''s, so that the bounds on $M_{Z'}/g'$ given by [147] are not applicable in a straightforward way. Therefore, we require a 2σ (i.e. 95% CL) agreement with EW precision observables, parametrized through the oblique parameters S, T, U [148–151]. The constraints

from the latter are included by evaluating

$$\chi^2_{\rm STM} = X^T C^{-1} X\,, \tag{4.13}$$

with $X^T = (S-\hat{S}, T-\hat{T}, U-\hat{U})$. The observed parameters deviations are given by [152]

$$\hat{S} = 0.05, \qquad \hat{T} = 0.09, \qquad \hat{U} = 0.01, \tag{4.14}$$

where the unhatted quantities denote the model predictions. The covariance matrix is [152]

$$\mathbf{C}_{ij} = \begin{bmatrix} 0.0121 & 0.0129 & -0.0071 \\ 0.0129 & 0.0169 & -0.0119 \\ -0.0071 & -0.0119 & 0.0121 \end{bmatrix}.$$

We then require $\chi^2_{\rm STU} \leq 8.025$, corresponding to a maximal 2σ deviation given the 3 degrees of freedom.

4.4 Gauge boson mass constraints

After imposing the constraints from the previous section, we turn our attention to gauge bosons. From the SSB of the $SU(2)_L \otimes U(1)_Y \otimes U(1)'$ symmetry, the gauge bosons Z and Z' mix to form physical mass eigenstates. The $Z - Z'$ mixing mass matrix is

$$\mathbf{M_Z^2} \;=\; \begin{pmatrix} M^2_{ZZ} & M^2_{ZZ'} \\ M^2_{ZZ'} & M^2_{Z'Z'} \end{pmatrix}. \tag{4.15}$$

As the mixing between the Z and Z' bosons is very small, to a good approximation, these are good physical states, with masses given in Eq. 4.7. Following the methodology described in the previous section, we scan the parameter space imposing constraints on SUSY particles, rare B-meson decays and oblique parameters so that the SM Z gauge boson properties are consistent with experimental data, as indicated in Table 6.1. In the following, we analyze the properties of the gauge sector for all scenarios accepted in our scanning procedure. In Fig. 4.1, we depict the relations between the parameters $M_{Z'}$, $g'_{\rm SUSY}$, Q_Q, the ratio of $M_{Z'}/g'_{\rm SUSY}$ and $\chi^2_{\rm STU}$. Here, $g'_{\rm SUSY}$ is the coupling constant for the $U(1)'$ group at the SUSY-breaking scale. The color bar of the upper panels shows the $\chi^2_{\rm STU}$ values for solutions with $\chi^2_{\rm STU} \leq 8.025$ while the color bar of the left bottom panel represents the gauge coupling $g'_{\rm SUSY}$. According

Observable	Constraints	Ref.	Observable	Constraints	Ref.
m_{h_1}	$[122, 128]$ GeV	[29]	$m_{\widetilde{t}_1}$	$\geqslant 730$ GeV	[153]
$m_{\widetilde{g}}$	> 1.75 TeV	[153]	$m_{\chi_1^\pm}$	$\geqslant 103.5$ GeV	[153]
$m_{\widetilde{\tau}_1}$	$\geqslant 105$ GeV	[153]	$m_{\widetilde{b}_1}$	$\geqslant 222$ GeV	[153]
$m_{\widetilde{q}}$	$\geqslant 1400$ GeV	[153]	$m_{\widetilde{\tau}_1}$	> 81 GeV	[153]
$m_{\widetilde{e}_1}$	> 107 GeV	[153]	$m_{\widetilde{\mu}_1}$	> 94 GeV	[153]
$\chi^2_{\rm STU}$	≤ 8.025	-	$\mathrm{BR}(B_s^0 \to \mu^+\mu^-)$	$[1.1, 6.4] \times 10^{-9}$	[88]
$\dfrac{\mathrm{BR}(B \to \tau\nu_\tau)}{\mathrm{BR}_{SM}(B \to \tau\nu_\tau)}$	$[0.15, 2.41]$	[89]	$\mathrm{BR}(B^0 \to X_s\gamma)$	$[2.99, 3.87] \times 10^{-4}$	[90]

Table 4.3: Current experimental and theoretical bounds used to determine consistent solutions in our scans.

to the top left panel of Fig. 4.1, the ratio $M_{Z'}/g'_{\rm SUSY}$ can be as low as 2.2 TeV when the charge Q_Q is small (i.e., $[1. - 3.] \times 10^{-2}$) while the bound on $M_{Z'}/g'_{\rm SUSY}$ tends to increase up to 8 TeV for larger Q_Q values (i.e., 1×10^{-1}). Further, the top right and bottom left panel of Fig. 4.1 shows that light Z' solutions consistent with the constraints given in Table 6.1 can be found to lie around 1.5 TeV. For heavier Z' masses, the range for the ratio $M_{Z'}/g'_{\rm SUSY}$ opens up to a larger interval. As seen from the bottom panels of the figure, the lowest bound on the ratio $M_{Z'}/g'_{\rm SUSY}$ can be fulfilled at 2117 GeV when $M_{Z'} = 1388$ GeV, the corresponding gauge coupling being $g'_{\rm SUSY} \simeq 0.66$, $Q_Q = 1.11 \times 10^{-2}$ and $\chi^2_{\rm STU} = 2.64$. The lowest bound on $M_{Z'}/g'_{\rm SUSY}$ increases drastically, up to 15.7 TeV, when $g'_{\rm SUSY}$ has its minimum value 0.25, $M_{Z'} = 3940$ GeV and $\chi^2_{\rm STU} = 6.01$.

In Fig. 7.1 top left panel, we present the comparison of $\sigma(pp \to Z') \times \mathrm{BR}(Z' \to \ell\ell)$ vs $M_{Z'}$ consistent with the ATLAS data of [9], scanning through the whole parameter space and displaying the values of $\mathrm{BR}(Z' \to \ell\ell)$ in different color codes. The experimental constraints are the same as in Fig. 4.1 except that we relax the $\chi^2_{\rm STU}$ value, since we want to plot the branching ratios (BR) also for light Z' solutions which are excluded by the $\chi^2_{\rm STU}$ bound. Since we fix $Q_\ell = Q_e = 0$, the Z' state does not couple to $\ell\ell$. However, the small mass mixing $Z - Z'$ still allows the Z' to decay into $\ell\ell$ states, but only with BRs of 0.01% for $M_{Z'} \simeq 600$ GeV while the BR decreases drastically for heavier Z' masses. The ATLAS observed limit on the fiducial cross section times BR ranges from 3.6 (13.1) fb at 250 GeV to about 0.014 (0.018) fb at 6 TeV for a zero (10%) relative width signal in the combined di-lepton channel [9]. Therefore, our results imply a lower limit of ~ 700 GeV at the 95%

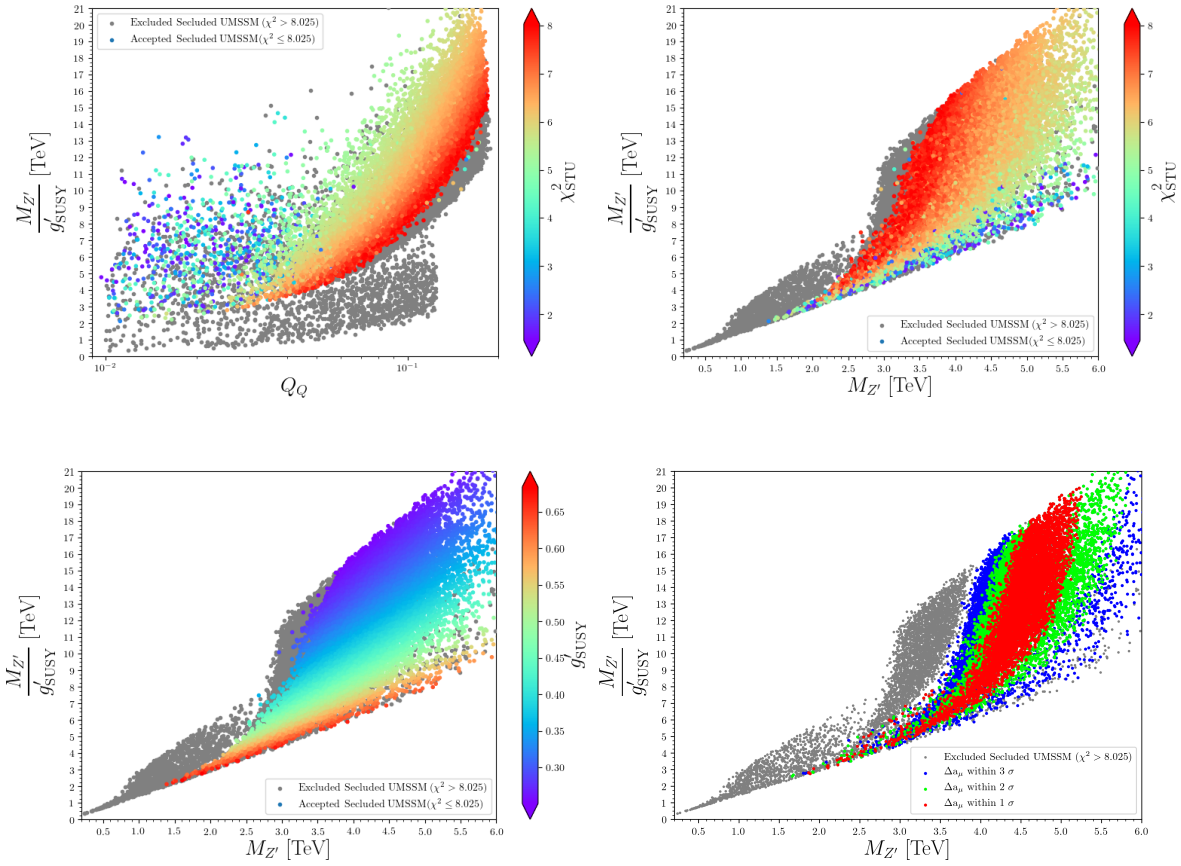

Figure 4.1: The effect of oblique parameters and $(g-2)_\mu$ experimental bounds on the ratio $M_{Z'}/g'$.

CL on $M_{Z'}$ for the Z' boson in the combined di-lepton channel. In the top right panel of Fig. 7.1 we compare the CMS high-mass di-jet yield from Ref. [10] with our predictions for $\sigma(pp \to Z') \times \text{BR}(Z' \to q\bar{q})$, obtained after scanning the secluded UMSSM parameters as described in Table 7.2 and imposing the constraints of Table 6.1. For the sake of consistency with the experimental analysis, the $\sigma \times \text{BR}$ rate is multiplied by an acceptance factor $A = 0.5$ and the fraction of $Z' \to t\bar{t}$ events is not included in the calculation.

These results are similar to those found in Z' models which employ gauge kinetic mixing to achieve leptophobia. However, there are some differences. One is that, while in these other scenarios the di-jet BR of the Z' cannot be lowered below 36%, in the secluded UMSSM it can be lowered to 5%. Another important aspect is that the model is also d-quark-phobic (the BR of Z' to d-type quarks is only about 1.4%). This is a direct consequence of different $U(1)'$ charge assignments. Leptophobia and d-quark-phobia have thus further lowered the bound on the Z' mass by lowering its production cross section. Also, we benefit from new experimental acceptance ($A = 0.5$ with the new data at $\mathcal{L} = 137$ fb^{-1} [10], compared to $A = 0.6$ at $\mathcal{L} = 27$ fb^{-1} and 36 fb^{-1} [154]). From the top right panel of Fig. 7.1, one learns that the computed $\sigma \times \text{BR}$ is always below the CMS exclusion limits [10, 154] in the range 1.5 TeV $< M_{Z'} <$ 6 TeV at the 95% CL, with the exception of a tiny region around $M_{Z'} \simeq 2.3$ TeV. One can, therefore, conclude that much lighter Z' bosons consistent with the constraints given in Table 6.1 could be allowed by data when leptophobic secluded UMSSM realizations, such as the one introduced in section 6.2, are considered. In the middle left panel, we check the ratio $\Gamma(Z')/M_{Z'}$ to assure that the Narrow Width Approximation (NWA) can be used consistently while in the middle right panel we investigate the variation of the Z' mass limit with the Q_Q charge, $Q_Q = \alpha$, the free parameter for the matter fields in the secluded $U(1)'$ group. As seen from the color bar in the middle left panel, the Z' is quite narrow for the solutions found while the color bar of the middle right panel indicates that also the α parameter should be quite small (less than $\alpha < 2 \times 10^{-1}$). Moreover, one can see the correlation between α and $\Gamma(Z')/M_{Z'}$. When α is increased, the $\Gamma(Z')/M_{Z'}$ ratio also increases and approaches the CMS observed limits. As seen from the bottom left panel of Fig. 7.1, $M_{Z'}/g'$ ratios below ~ 3 TeV require a decay width smaller than 1% and a Q_Q value smaller than $\sim 2 \times 10^{-2}$. Finally, the bottom right panel of Fig. 7.1 shows the relation between various Z' masses and the $U(1)'$ charges for the S_1, S_2 and S_3 secluded singlets, where we set $Q_{S_1} = Q_{S_3} = -Q_{S_2}/2 = \delta$ for simplicity. Solutions with lighter Z' masses necessitate smaller δ values while δ values increase for heavier Z' masses. This relation can be understood via Eq. 4.7.

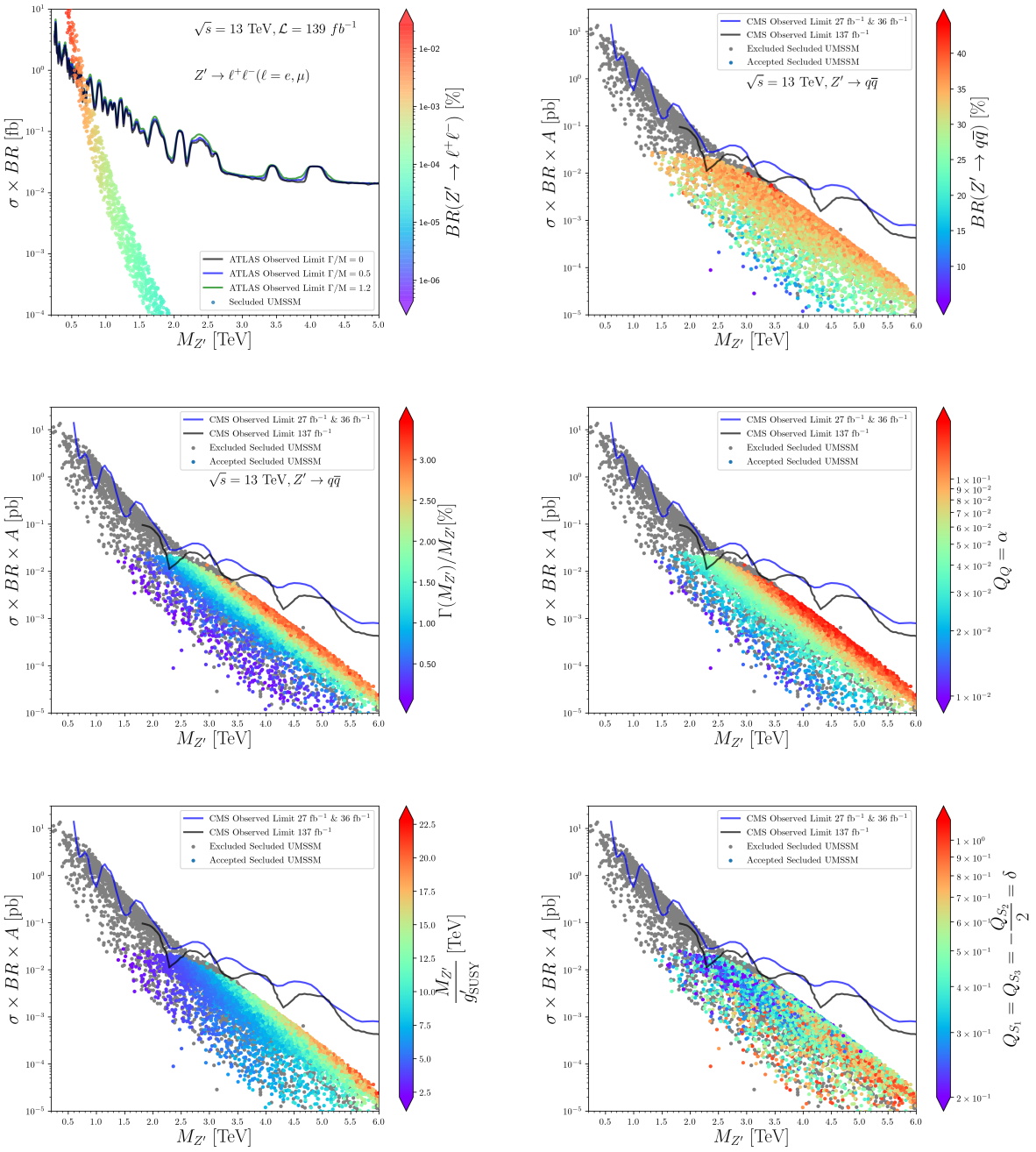

Figure 4.2: Leptophobic Z' mass limits ($Q_\ell = Q_e = 0$). We investigate the Z' production cross section multiplied by the di-lepton and di-jet BR (and by the acceptance $A = 0.5$ for the latter), respectively. We compare theoretical predictions of the secluded UMSSM to the bounds obtained by the ATLAS [9] and CMS [10] collaborations.

4.5 Dark Matter

In this section, we analyze the model parameters which survive cosmological bounds from the DM experiments. We investigate the constraints on the model arising from requiring the lightest neutralino to be a viable DM candidate, with properties compatible with current cosmological data. First, we demand that the predicted relic density agrees within 20% (to conservatively allow for uncertainties on the predictions) with the recent Planck results, $\Omega_{DM}h^2 = 0.12$ [11, 12]. We calculate, for all points returned by our scanning procedure in Table 7.2 that are in addition compatible with current experimental bounds given in Table 6.1, the associated DM relic density. We present our results in Fig. 4.3.

In all the subfigures, the relic density is plotted as a function of the mass of the lightest neutralino, denoted by $M_{\tilde{\chi}_1^0}$. As seen from the panels, solutions consistent with the relic density constraint emerge for almost all values of $M_{\tilde{\chi}_1^0}$ depending on the $\tilde{\chi}_1^0$ composition, which is given in the following basis: $(\tilde{B}', \tilde{B}, \tilde{W}, \tilde{H}_u, \tilde{H}_d, \tilde{S}, \tilde{S}_1, \tilde{S}_2, \tilde{S}_3)$. The color bar of the top left panel of Fig. 4.3 shows the $\tilde{S}$ content, as we are particularly interested in singlinos as non-MSSM LSP candidates. One can learn from this panel that the relic density observed by the Planck collaboration can be accommodated by $\tilde{S}$-like $\tilde{\chi}_1^0$'s lying roughly in the [25, 300] GeV window, region largely disallowed for MSSM neutralinos. Once the lightest neutralino spectrum becomes heavier, the contribution of the combination of $\tilde{S}_1$, $\tilde{S}_2$ and $\tilde{S}_3$ singlets increases, so as to become dominant for $M_{\tilde{\chi}_1^0}$ heavier than 400 GeV, as seen from the upper right panel of Fig. 4.3. In the middle left panel, we focus on the combined contribution of all singlinos, that is, $\tilde{S}$, $\tilde{S}_1$, $\tilde{S}_2$ and $\tilde{S}_3$. As seen from the panel, singlino-like LSP solutions largely dominate the parameter space. The middle right panel shows the higgsino-like neutralino content. As observed from the panel, the relic density is at the scale of 10^{-3} for higgsino-like neutralino with $M_{\tilde{\chi}_1^0} \sim 100$ GeV, but it increases dramatically for heavier higgsino-like neutralino masses. As in the MSSM, the relic density observed by the Planck collaboration can be accommodated by higgsino-like solutions at roughly ~ 1 TeV. Since TeV scale neutralino solutions are naturally less appealing from a collider point of view and we want to pay particular attention to singlino LSP scenarios, we did not increase the scanned neutralino mass range beyond 1 TeV. Although potentially viable scenarios could be obtained for even heavier neutralinos (in particularly, for winos), for the purpose of this work, we ignore this regime throughout. The bottom left panel of Fig. 4.3 represents the bino composition of the lightest neutralino. Note that only solutions with bino contribution larger than 20% are represented in the panel. Although there are some bino dominated $\tilde{\chi}_1^0$ solutions in our spectrum, their

corresponding relic density mostly tends to lie in the [10, 100] range. An important fact is that the lightest bino-like solutions can be obtained near 300 GeV. Bino contributions start to decrease, yielding lower values of the relic density, and giving a maximum 50% contribution, when the relic density constraint is satisfied and $M_{\tilde{\chi}_1^0} \sim 400$ GeV. The other $\sim 50\%$ contributions to mostly bino-like solutions consistent with the relic density constraint mainly come from higgsinos and winos, both of which contribute more significantly for heavier $\tilde{\chi}_1^0$ masses, up to roughly 850 GeV, where we can classify the DM as mixed neutralino states. We summarize the various lightest neutralino DM compositions in the bottom right panel of Fig. 4.3. As seen from this panel, bino dominated neutralino solutions cannot be good candidates for DM since they do not satisfy the relic density constraints. Viable mixed (mostly bino and higgsino) neutralino DM solutions can be found with a mass lying in the 400–800 GeV range. When the spectrum is heavier, i.e., with a lightest neutralino $M_{\tilde{\chi}_1^0} \in [0.8\text{–}1.0]$ TeV, the relic density as observed by the Planck collaboration can be accommodated by higgsino or singlino dominated solutions. It should be noted that $\tilde{B}'$ contributions are no more than 5% in the whole parameter space. Given that we mostly focus on small Q_Q values, this leads to small couplings with the gaugino $\tilde{B}'$ associated with the $U(1)'$ gauge group, so relatively small $\tilde{B}'$ contributions are expected.

Finally, we depict, in Fig. 4.4, the constraints coming from direct detection experiments. The top panels show the spin-independent cross section for the nucleon as a function of the mass of the lightest neutralino. Note that the results for spin-independent cross sections for proton and neutron are almost the same. Therefore, we denoted it as $\sigma_{\rm SI}^{\rm nucleon}$ and normalised it to the present-day relic density. The top left plane shows how the spin-independent cross section for the nucleon depends on the composition of the lightest neutralino for solutions which survive all the constraints given in Table 6.1. Blue solutions in the top right panel refer to all solutions represented in the top left plane whilst all the other colors are subsets of blue and represent solutions consistent with the relic density constraint in addition to the ones in Table 6.1. The black line indicates the limits from the Xenon 1T [155] with the region above the curve being excluded. In addition, the blue and red lines show the prospects for XENON nT and DARWIN [101] collaborations, respectively. As seen from the top left plane, almost all singlino solutions survive the results of the Xenon 1T experiment [155] while some portion of higgsino and bino dominated solutions are excluded. Another important feature is that all mixed neutralino solutions are strictly excluded by Xenon 1T. Once we compare our solutions consistent with the relic density bound to the result of Xenon 1T, a large fraction of higgsino dominated solutions consistent with the former are excluded

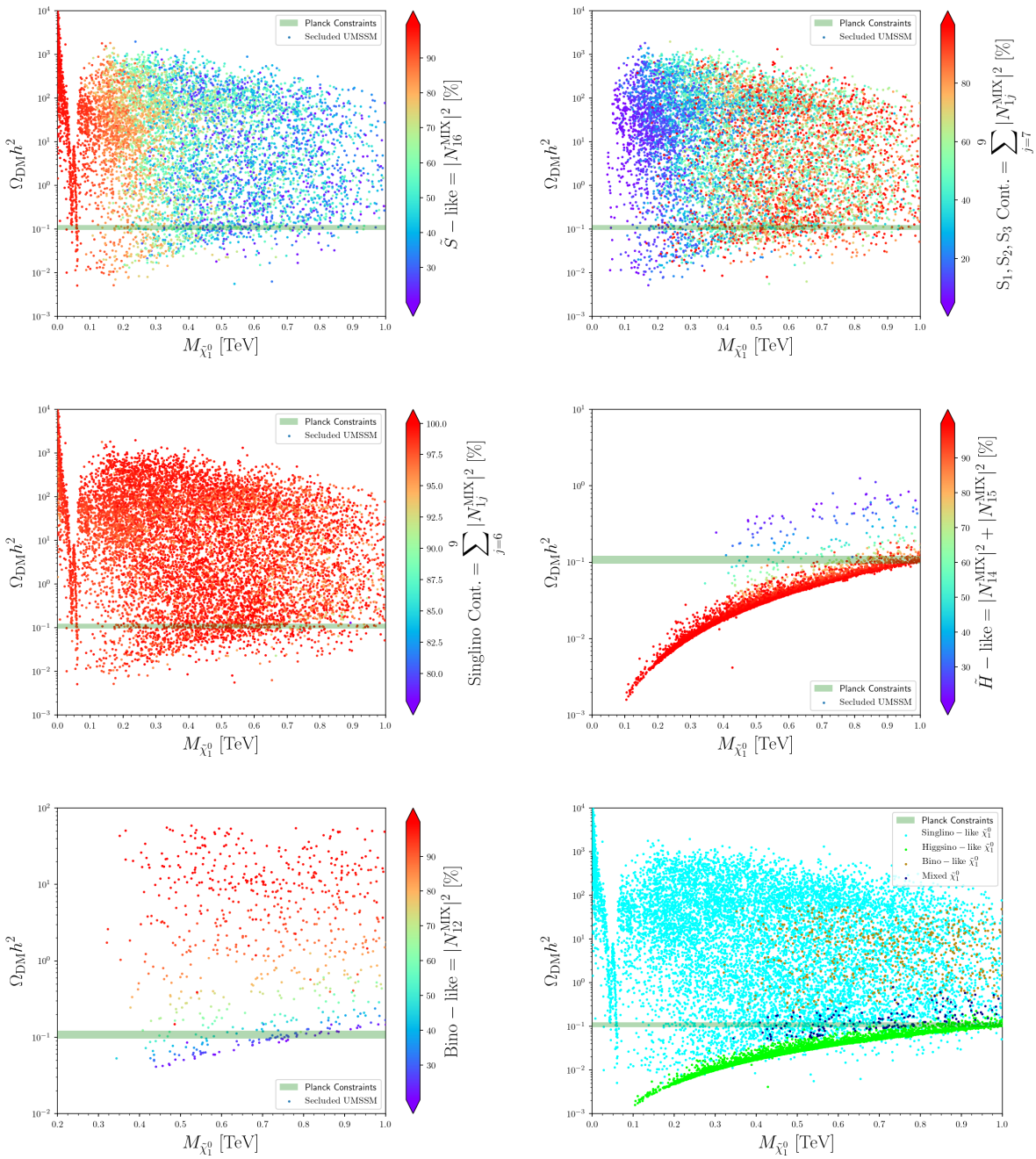

Figure 4.3: Relic density predictions for secluded UMSSM scenarios satisfying all the constraints imposed during our scan and compatible with Z' bounds from the LHC, indicating the dependence on the mass of the lightest neutralino. In each panel of the figure, we analyze the composition of the LSP for different parameter regions. The horizontal green band in all panels indicates the measured value of the relic density, consistent at 2σ with the Planck experiment [11, 12].

by the latter as seen from the top right figure. In contrast, singlino DM solutions consistent with the relic density bound are always below the excluded region by Xenon 1T and can be probed by the next generation of DM experiments such as Xenon nT and Darwin.

Whilst we have demonstrated that the singlino-type lightest neutralino could be a viable DM candidate from the point of view of the relic density and direct detection bounds, at the same time it is important to verify that DM indirect detection bounds are also satisfied. In the bottom panels of Fig. 4.4, we present the value of the total DM annihilation cross section at zero velocity as a function of the lightest LSP neutralino mass for all scanned scenarios satisfying the Z' boson limits from the LHC. Configurations for which the relic density is found in agreement with Planck data are shown along with their higgsino, singlino and mixed compositions in the bottom right panel, whilst any other setup returned by the scan is shown in light sky-blue and tagged as "Main Constraints", referring to those given in Table 6.1. In our predictions, we rescaled also the DM annihilation cross section to its present-day density. We compare our predictions to the latest bounds derived from the Fermi-LAT data [23, 156]. We depict, as a yellow area, the parameter space region that is found out to be excluded. The bottom panel of Fig. 4.4 indicates that, unlike relic density and direct detection bounds, which impose strong constraints on the model parameters, indirect detection experiments are easily satisfied for a large portion of the parameter space. Most singlino DM scenarios naturally feature an annihilation cross section that is at least 3 or 4 orders of magnitude too small to leave any potentially visible signal in Fermi-LAT data. Therefore, singlino DM solutions are unaffected by current indirect detection limits and will potentially stay so for some time by virtue of their correspondingly small annihilation cross sections. In contrast, the annihilation cross sections of higgsino and mixed neutralino solutions are about 10^{-26} cm^3 s^{-1}, hence, they are more likely to be probed by Fermi-LAT when the precision of the annihilation cross section measurement will be improved.

4.6 Muon anomalous magnetic moment

The measurement of the muon anomalous magnetic moment exhibits an intriguing discrepancy between the value found from the E821 experiment at BNL [68] and the value predicted by the SM. Adding uncertainties, the deviations amount to 3.5 σ [153, 157] while recent

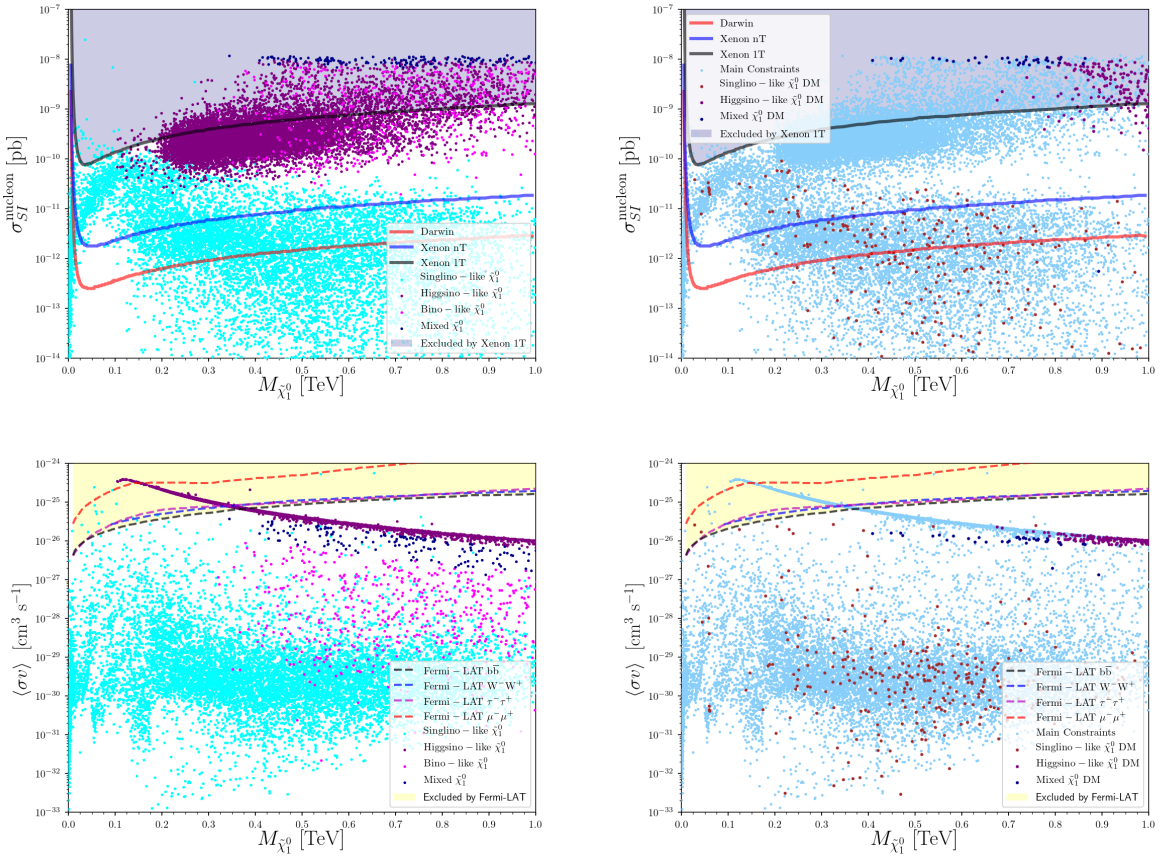

Figure 4.4: DM direct and indirect detection constraints on the parameter space on the secluded UMSSM model. The top panels show the constraints from the spin-independent cross section for the nucleon while the bottom panels show the corresponding annihilation cross sections.

theory predictions for a_μ find values as large as 4.1σ,

$$\Delta a_\mu \equiv a_\mu^{\rm exp} - \Delta a_\mu \equiv a_\mu^{\rm SM} = 268(63)(43) \cdot 10^{-11}.$$

Several models have been constructed and dedicated entirely to explain this discrepancy. Conversely, whether the discrepancy is real or not[3], it has been used as a test of how well BSM scenarios perform.

In the secluded UMSSM, loop diagrams with additional neutralinos and sleptons as well as with (right) sneutrinos and charginos provide additional contributions to the $(g-2)_\mu$ observable. We present the results of our analysis in Fig. 4.5, where we show solutions consistent with the muon anomalous magnetic moment within 1σ of the experimental value. Here, we indicate the model solutions over the following planes: $(M_{\tilde{\chi}_1^\pm}, M_{\tilde{\chi}_1^0})$ (top left); $(M_{\tilde{\chi}_1^\pm}, M_{\tilde{\chi}_2^0})$ (top right); $(M_{\tilde{\chi}_1^\pm}, M_{\tilde{\chi}_3^0})$ (bottom left) and $(M_{\tilde{\nu}_1}, M_{\tilde{\tau}_1})$ (bottom right). When the lightest neutralino is singlino, the second and the third lightest ones are higgsino-like, rather light and almost degenerate in mass. The main contribution to the muon anomalous magnetic moment comes from these two heavier states as well as (albeit more marginally) from the lightest (right) sneutrino and (through slepton-mixing) stau states, in the appropriate diagrammatic combinations. As seen from the figure, a large portion of the solutions satisfies the Δa_μ bound within 1σ. The grey region below the black curve represents the parameter space ruled out by ATLAS searches [13, 14], close to which most solutions are found.

4.7 Z' signal at colliders

In this section, we investigate the observability of a secluded UMSSM scenario with light Z' masses at LHC. To choose correct benchmarks, we first compare the range of chargino and neutralino masses with restrictions from the ATLAS searches for chargino/neutralino states [13, 14]. We make use of SModelS (version 1.2.2) [158–161] in order to calculate the upper limit on the chargino-neutralino cross sections based on ATLAS-SUSY-2019-08 [13] and ATLAS-SUSY-2018-32 [14] implemented and validated with the SModelS authors. Fig. 4.6 showcases our results in terms of the lightest chargino and neutralino masses, as functions of the ratio between our calculated cross sections versus the upper limit on the chargino-neutralino cross sections. We exclude all solutions with signal strength value exceeding 1.

[3]Leading order hadronic vacuum polarization contributions represent the main limitation of theoretical calculations of non-perturbative low-energy QCD behavior.

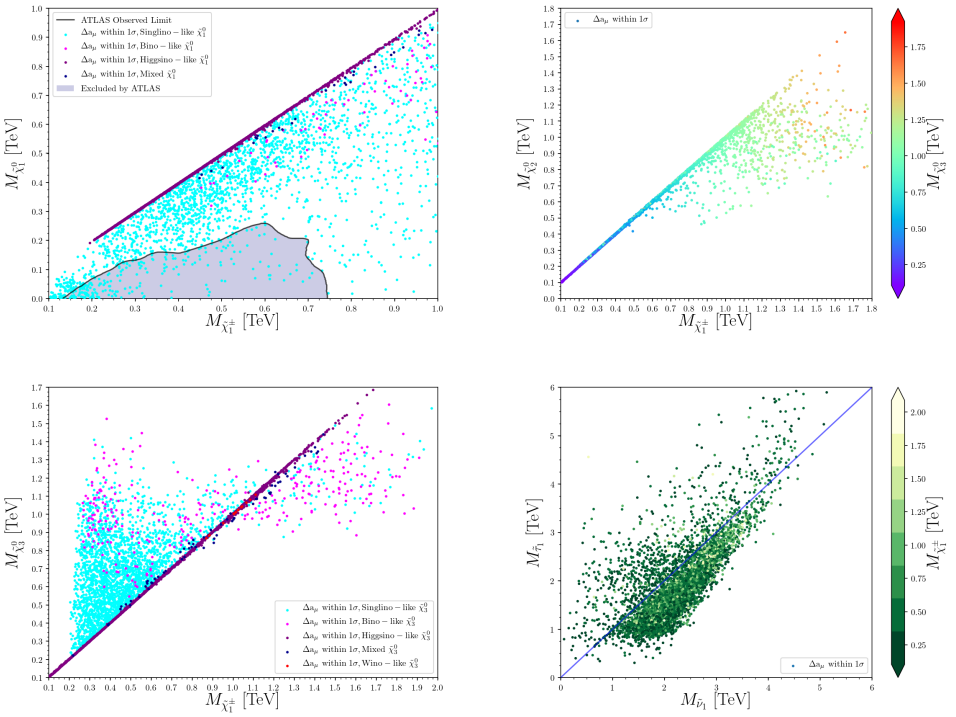

Figure 4.5: Parameter regions of chargino, neutralino, (right) sneutrino and stau masses consistent with Δa_μ within 1σ. We show the following mass mappings: (top left) lightest chargino versus lightest neutralino; (top right) lightest chargino versus second lightest neutralino; (bottom left) lightest chargino versus third lightest neutralino; (bottom right) lightest (right) sneutrino versus lightest stau. The grey region is ruled out by ATLAS searches for chargino-neutralino states [13, 14]. The model solutions to the $(g-2)_\mu$ discrepancy are dominated by the neutralino (higgsino-like)-slepton and chargino-sneutrino loop contributions, where, in particular, the contributing neutralinos and charginos are light yet consistent with all experimental constraints.

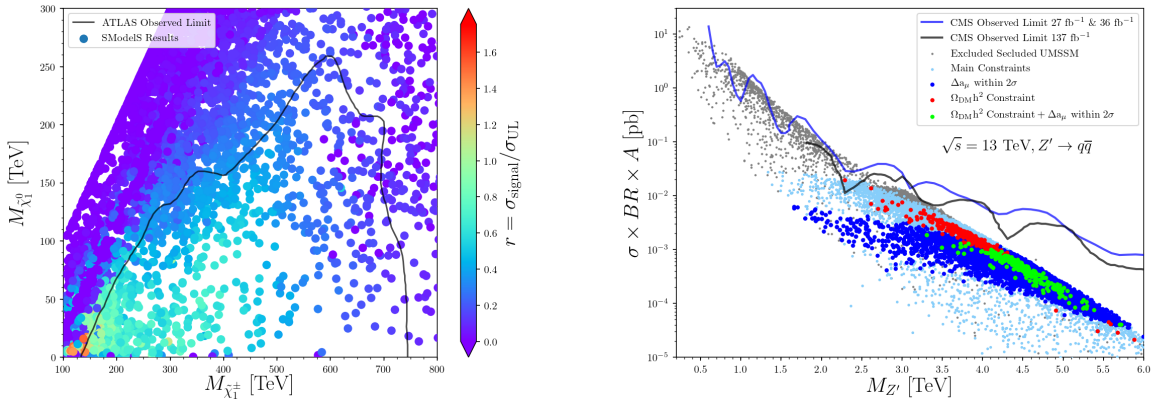

Figure 4.6: (Left) Neutralino-chargino mass limits in secluded UMSSM. The black curve represents mass limits from ATLAS [13, 14], while our analysis rules out only points which exceed the upper limits on the chargino-neutralino cross sections, as indicated on the right-side color bar (which gives our predicted cross section measured against the limits from ATLAS). (Right) Z' production cross sections multiplied by the di-jet BRs (and by the acceptance $A = 0.5$).

This plot is complementary to the one shown in Fig. 4.5 top left panel, with the grey region in that plot corresponding to the area below the curve. While in the former plot we indicate muon $g-2$ values consistent with experiment, here we explore neutralino and chargino masses constrained by bounds given in Table 6.1, with the aim to choose benchmarks compatible with allowed EW-ino masses. Our plot indicates, however, that the parameter space allowed by this model is less restrictive than the one in the ATLAS analysis. We rule out some points for low chargino-neutralino masses (in red, lower left-hand corner) but allow the purple-blue points in the upper right-hand corner. Of particular interest is a region specific to this model, which allows singlino masses $\lesssim 50$ GeV and chargino masses $\lesssim 350$ GeV, region ruled out for neutralinos and charginos in the MSSM. We shall concentrate our analysis in this parameter region.

Scanning over the whole range of allowed Z' mass values, we find that consistency with ATLAS production and di-lepton decay results allows $M_{Z'}$ to be quite light. However, for the parameter space to satisfy both DM and muon anomalous magnetic moment constraints to at least 2σ, the Z' mass must be $M_{Z'} \gtrsim \mathcal{O}(3)$ TeV as seen from the right plane of figure 4.6. To highlight the model characteristics, we chose two benchmarks, **BM I** and **BM II**. The first benchmark is consistent with all constraints, including relic density, and satisfies the bounds on the $g-2$ factor of the muon at 1σ. The second benchmark satisfies the same constraints, except that we relax requirements on consistency with the anomalous magnetic

[GeV]	m_0	$M_{1/2}$	A_0	v_S	$v_{S_1} = v_{S_2} = v_{S_3}$
BM I	942	2821	662	2421	5401
BM II	1722	2568	-1092	2282	6935

	$\tan\beta$	λ	A_λ	κ	A_κ	α	δ	Y_v^{ij}
BM I	11.9	2.04×10^{-1}	3469	1.81	-4781	4.48×10^{-2}	4.44×10^{-1}	1.63×10^{-8}
BM II	20.1	9.70×10^{-2}	3051	6.73×10^{-1}	-3910	4.44×10^{-2}	4.00×10^{-1}	6.71×10^{-8}

Table 4.4: Set values for the free secluded UMSSM parameters defining our benchmark scenarios **BM I** and **BM II**. Here, m_0 is the universal scalar mass and $M_{1/2}$ the gaugino mass.

[GeV]	$M_{Z'}$	$M_{H_1^0}$	$M_{H_2^0}$	$M_{H_3^0}$	$M_{H_4^0}$	$M_{H_5^0}$	$M_{H_6^0}$	$M_{A_1^0}$	$M_{A_2^0}$	$M_{H_1^\pm}$
BM I	3307	126	332	2559	3405	3535	4148	3405	5066	3407
BM II	2291	123	394	758	2474	3138	3332	3138	3580	3139

[GeV]	$M_{\tilde{\chi}_1^0}$	$M_{\tilde{\chi}_2^0}$	$M_{\tilde{\chi}_3^0}$	$M_{\tilde{\chi}_4^0}$	$M_{\tilde{\chi}_5^0}$	$M_{\tilde{\chi}_6^0}$	$M_{\tilde{\chi}_7^0}$	$M_{\tilde{\chi}_8^0}$	$M_{\tilde{\chi}_9^0}$	$M_{\tilde{\chi}_1^\pm}$	$M_{\tilde{\chi}_2^\pm}$
BM I	45	358	363	1247	2295	2321	3595	4106	4590	359	2321
BM II	44	160	165	1100	1133	2122	2201	2325	3025	162	2121

Table 4.5: Particle spectrum of **BM I** and **BM II**: bosons (top) and fermions (bottom). All masses are given in GeV.

moment of the muon. We list the values of the relevant free parameters in the model in Table 4.4 and the corresponding mass values for the fermions and bosons in the model in Table 4.5.

While scanning over the parameter space consistent with all constraints, we were unable to find any allowed parameter space for which $M_{Z'} < 3.3$ TeV (**BM I**). Relaxing the imposed constraints on the anomalous magnetic moment of the muon completely (for **BM II**), while requiring agreement with the measured relic density, still poses rigid constraints on the parameter space, but allows a lower $M_{Z'} \sim 2.3$ TeV. The relevant predictions for **BM I** and **BM II** for the DM and $(g-2)_\mu$ observables discussed in the above sections are shown in Table 7.5. To test the signal coming from production and decay of the leptophobic Z' boson, we use its decay into supersymmetric particles, here into chargino pairs, followed by the decay into lepton pairs or jets plus missing energy[4]. The decay of the lightest chargino yielding lepton or jet final states is into $\tilde{\chi}_1^\pm \to \tilde{\chi}_1^0 W^\pm$ and we choose points for which this

[4]The decay into chargino pairs is not the only one yielding the required di-lepton (or jets) + missing E_T signal, but it dominates other intermediate steps by a few orders of magnitude.

BR is almost 1, as shown in Table 7.6. In the same table, we show predictions for the LHC phenomenology of our two benchmark scenarios, including the production cross sections at a centre-of-mass energy $\sqrt{s} = 13, 14, 27$ and 100 TeV, plus the dominant BRs of the Z'. For both scenarios, Z' boson production is small enough relatively to the LHC limits at a centre-of-mass energy of 13 TeV. The cross section is about 0.016 fb for **BM I** and 0.1889 fb for **BM II** after accounting for the Z' boson decaying into electron and muon pairs through two chargino states. Consequently this makes the Z' signal difficult to observe, even with more luminosity at a centre-of-mass energy of 13 TeV.

The Z' production cross section is therefore about 0.33 fb for **BM I** and 3.82 fb for **BM II** at 13 TeV, after accounting for the Z′ bosons decaying into all SM fermions (quarks + leptons) via two chargino states, giving rise to a multi-jet plus missing energy signature. The latter is also typically expected from supersymmetric squark/gluino production and decay, so that the results of SUSY searches in the multi-jet plus missing energy mode could be reinterpreted to constrain the secluded UMSSM. We therefore recast these results from [162–165] with MadAnalysis 5. However, such a rate is far beyond the reach of typical multi-jet plus missing transverse momentum searches at the LHC, as confirmed by reinterpreting and extrapolating the results of the CMS search in [164] and the results of the ATLAS search in [162, 163, 165] targeting superpartner production and decay in the jets plus missing transverse momentum mode to integrated luminosity of 3 ab^{-1} with MadAnalysis 5. Consequently, this makes the Z' signal difficult to observe in di-jet final states, even with more luminosity. We therefore focus on Z' signals that instead involve di-leptons in the final state at a centre-of-mass energy of 14 TeV and 27 TeV.

The study of [125] provides a prescription for finding leptophobic Z' bosons at the center-of-mass energy $\sqrt{s} = 14$ TeV and 3 ab^{-1} of luminosity in the di-lepton channel. The signal process consists of the resonant production of a chargino pair, followed by the decay of each chargino into a charged lepton and missing energy,

$$pp \to Z' \to \tilde{\chi}_1^{\pm}\tilde{\chi}_1^{\mp} \to \ell^+\ell^- + \not{E}_T. \tag{4.16}$$

We followed the same procedure and carried out a full Monte Carlo (MC) event simulation at the LHC, for a center-of-mass energy $\sqrt{s} = 14$ TeV and applied the cuts as in [125]. The production cross section of Z' boson is 17.1 fb for **BM I** and 146.1 fb for **BM II** for a center-of-mass energy $\sqrt{s} = 14$ TeV as given in Table 7.6. We have made use of SARAH to generate a UFO [111] version of the model, so that we could employ MG5_aMC (ver-

sion 2.7.2) [112] for generating the hard-scattering signal event samples necessary for our collider study. These events, obtained by convoluting the hard-scattering matrix elements with the leading-order set of NNPDF 3.1 parton densities [166], were subsequently matched with PYTHIA 8 (version 8.244) [167] parton showering and hadronisation algorithms, plus we simulated the typical response of an LHC detector by means of the DELPHES 3 [168] programme (version 3.4.2) employing the SNOWMASS parameterization [169, 170] that relies on the anti-k_T algorithm [171] with a radius parameter $R = 0.6$ as implemented into FASTJET [172] (version 3.3.3) for event reconstruction. We have employed MADANALYSIS 5 [173] (version 1.8.23) and normalized our results to an integrated luminosity of 3 ab^{-1} for the collider analysis.

We select events featuring two well-separated muons and veto the presence of jets, by requiring

$$N^{\ell} = 2, \qquad \Delta R(\ell_1, \ell_2) > 2.5, \qquad N^{j} = 0. \tag{4.17}$$

The transverse momenta of the two leptons and the missing transverse energy are required to fulfill

$$p_T(\ell_1) > 300 \text{ GeV}, \qquad p_T(\ell_2) > 200 \text{ GeV}, \qquad \not{E}_T > 100 \text{ GeV}. \tag{4.18}$$

To investigate the observability of the two benchmarks at the HL-LHC, we use of two standard significance parameters, labelled as s and Z_A (the Asimov significance), defined as:

$$s = \frac{S}{\sqrt{B+\sigma_B^2}}\,, \tag{4.19}$$

$$Z_A = \sqrt{2\left((S+B)\ln\left[\frac{(S+B)(S+\sigma_B^2)}{B^2+(S+B)\sigma_B^2}\right] - \frac{B^2}{\sigma_B^2}\ln\left[1+\frac{\sigma_B^2 S}{B(B+\sigma_B^2)}\right]\right)}\,, \tag{4.20}$$

where S is the number of signal events, B of background events and σ_B is the standard deviation of background events.

The corresponding cutflows are shown in Table 4.8, where we give our original and final number of signal events, and the ones surviving each cut, shown in the left-handed column. We assume that we would get the same cut efficiency of the background as in [125]. One can see that the significance of the benchmarks at 14 TeV and with integrated luminosity 3 ab^{-1} is very small, making it unlikely to be observed, even at the HL-LHC. Therefore, we extend the analysis of our benchmark scenarios at 27 TeV, and in Table 4.8, we give our original and final number of signal events in parentheses. We estimate the number of background events at 27 TeV by using a boost factor calculated from the dominant background channel,

	$\Omega_{\rm DM}h^2$	$\sigma_{\rm SI}^{\rm proton}$ [pb]	$\sigma_{\rm SI}^{\rm neutron}$ [pb]	$\langle\sigma v\rangle$ [cm^{3}s^{-1}]	$\Delta a_\mu \times 10^{10}$
BM I	0.131	1.84×10^{-13}	1.89×10^{-13}	5.58×10^{-29}	36.4 (within 1σ)
BM II	0.124	2.21×10^{-11}	2.26×10^{-11}	8.17×10^{-29}	173.4 (outside 3σ)

Table 4.6: Predictions for the **BM I** and **BM II** scenarios, of the observables discussed in our dark matter analysis.

	$\sigma(pp\to Z')$				BR($Z'\to\tilde\chi_1^\pm\tilde\chi_1^\mp$)	BR($Z'\to jj$)	BR($\tilde\chi_1^\pm\to\tilde\chi_1^0W^\pm$)
	13 TeV	14 TeV	27 TeV	100 TeV			
BM I	12.09	17.1	169.3	2474	0.059	0.309	0.99
BM II	113.7	146.1	862.2	8638	0.066	0.340	1.0

Table 4.7: Z' production cross section at $\sqrt{s} = 13, 14, 27$ and 100 TeV and branching ratios for the **BM I** and **BM II** scenarios, relevant for the associated LHC phenomenology.

the di-boson production. While **BM I** remains below the 3σ minimum significance required for a positive identification, the **BM II** significance rises above 3σ at $\sqrt{s} = 27$ TeV and integrated luminosity 3 ab^{-1}, making this benchmark promising at the HE-LHC. That this indeed so is seen in Fig. 4.7, where we plot significance curves for s and Z_A at $\sqrt{s} = 27$ TeV, for both **BM I** and **BM II**, as a function of the total integrated luminosity $\mathcal{L}$. While **BM I** would be observable at high integrated luminosity 3 ab^{-1} at 3σ under only the most optimistic scenario, in which we assume small systematic errors ($\Delta_{\rm syst} = 5\%$), **BM II** shows promise for observability even for larger systematic errors, $\Delta_{\rm syst} = 20\%$. Of course, we stress that, while **BM II** is promising, it was obtained by relaxing the condition that the model satisfies $(g-2)_\mu$ to (1-2)σ.

Step	Requirements	**BM I**	**BM II**
0	Initial	71 (92)	726 (3854)
1	$N^{\ell} = 2$	45 (61)	386 (2310)
2	Electron Veto	13 (18)	115 (712)
3	$\lvert\eta^{\ell}\rvert < 1.5$	13 (18)	112 (685)
4	$I^{\mu}_{\rm rel} < 0.15$	13 (18)	107 (663)
5	$\Delta R(\ell_1, \ell_2) > 2.5$	11 (18)	107 (662)
6	$N^{j} = 0$	11 (18)	60 (330)
7	$p_T(\ell_1) > 300$ GeV	6 (18)	17 (107)
8	$p_T(\ell_2) > 200$ GeV	2 (17)	6 (36)
9	$\not{E}_T > 100$ GeV	2 (15)	4 (25)
s	$(\Delta_{\rm syst} = 20\%)$	0.53 (2.33)	1.09 (3.89)
Z_A	$(\Delta_{\rm syst} = 20\%)$	0.51 (2.03)	0.99 (3.16)

Table 4.8: Events surviving after each cut (as given in the left column) and significance of **BM I** and **BM II** at 14 (27) TeV and integrated luminosity 3 ab^{-1}.

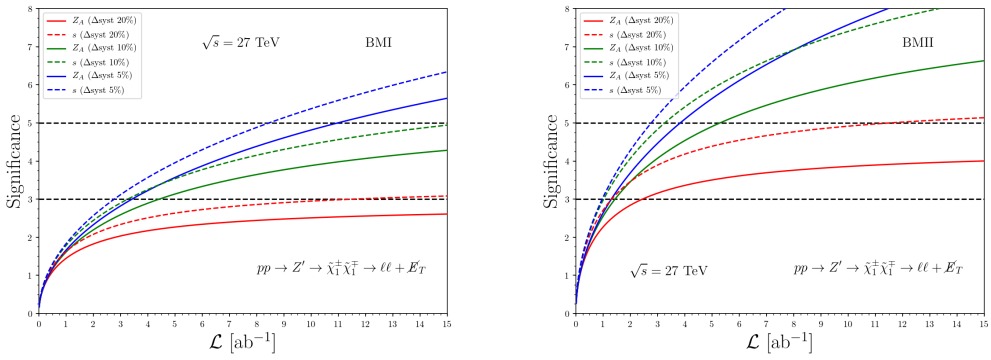

Figure 4.7: Significance of benchmarks **BM I** (left panel) and **BM II** (right panel) at $\sqrt{s} = 27$ TeV, as a function of the luminosity $\mathcal{L}$. In each panel we plot the usual significance s and the Asimov significance Z_A. Different curves are obtained assuming different systematic errors, as indicated in the upper left-hand panel.

Chapter 5

E_6 Motivated UMSSM Confronts Experimental Data

5.1 Introduction

After the observation of a Standard Model (SM)-like Higgs boson by ATLAS [28] and CMS [29] in 2012, almost all ongoing and planned observational or collider experiments have been concentrating on searching for New Physics (NP). Undoubtedly, Supersymmetry (SUSY) is one of the most studied NP theories at these experiments, since it has remarkable advantages. In SUSY theories, the stability problem of the hierarchy between the Electro-Weak (EW) and Planck scales is solved by introducing new particles, differing by half a spin unit from the SM ones, thereby onsetting a natural cancellation between otherwise divergent boson and fermion loops in a Higgs mass or self-coupling. Furthermore, since it relates the latter to the strength of the gauge boson couplings, SUSY predicts a naturally light Higgs boson in its spectrum, indeed compatible with the discovered 125 GeV Higgs boson. Also, SUSY is able to generate dynamically the Higgs potential required for EW Symmetry Breaking (EWSB), which is instead enforced by hand in the SM. Finally, another significant motivation for SUSY is the natural Weakly Interacting Massive Particle (WIMP) candidate predicted in order to solve the DM puzzle, in the form of the Lightest Supersymmetric Particle (LSP).

Though SUSY also has the key property of enabling gauge coupling unification, this requires rather light stops (the counterpart of the SM top quark chiral states), though, at odds with the fact that a 125 GeV SM–like Higgs boson requires such stops to be rather

heavy within the Minimal Supersymmetric Standard Model (MSSM), which is the simplest SUSY extension of the SM, thereby creating an unpleasant fine tuning problem. Another phenomenological flaw of the MSSM is that, in the case of universal soft-breaking terms and the lightest neutralino as a DM candidate, the constraints from colliders, astrophysics and rare decays have a significant impact on the parameter space of the MSSM [174], such that the MSSM, in its constrained (or universal) version, is almost ruled out under these circumstances [175]. Moreover, the MSSM has some theoretical drawbacks too, such as the so-called μ problem and massless neutrinos. The aforementioned flaws of the MSSM are motivations for non-minimal SUSY scenarios [48].

Among these, UMSSMs, which have been broadly worked upon the literature, are quite popular [122, 139, 176–196]. In the SUSY framework, these models can dynamically generate the μ term at the EW scale [117, 197, 198] while even the non-SUSY versions of these are able to provide solutions for DM [199–202], the muon anomaly [203] and baryon leptogenesis [204, 205]. The right-handed neutrinos are also allowed in the superpotential to build a see-saw mechanism for neutrino masses if the extra $U(1)$ symmetry arises from the breaking pattern of the E_6 symmetry [206]. Moreover, such E_6 motivated UMSSMs meet the anomaly cancellation conditions by heavy chiral states in the fundamental **27** representation.

Since there is an extra gauge boson, so-called Z' boson, as well as new SUSY particles in their spectrum, UMSSM have a richer collider phenomenology than the MSSM. Promising signals for a Z' state at the LHC would emerge from searches for heavy resonances decaying into a pair of SM particles in Drell-Yan (DY) channels. The most stringent lower bound on the Z' mass has been set by ATLAS in the di-lepton channel as 4.5 TeV for an E_6 motivated ψ model [9]. Such heavy resonance searches rely upon the analysis of the narrow Breit-Wigner (BW) line shape. In the case of the Z' boson with large decay width $\Gamma(Z')$ this analysis becomes inappropriate because the signal appears as a broad shoulder spreading over the SM background instead of a narrow BW shape [207]. Furthermore, the emerging shape can be affected by a large (and often negative) interference between the broad signal and SM background. However, there are alternative experimental approaches for wide Z' resonances in the literature [208]. In these circumstances, the stringent experimental bounds on the Z' mass could be relaxed for a Z' boson with a large width $\Gamma(Z')$.

This large Z' width can be obtained in several Beyond the SM (BSM) scenarios when the Z' state additionally decays into exotic particles or the couplings to the fermion families are different. In an E_6 motivated UMSSM, through these channels, $\Gamma(Z')$ could be as large

as 5% of the Z' mass [209]. However, other decay channels could come into play, such as WW and/or hZ (where h is the SM–like Higgs boson), could have large partial widths in the presence of kinetic mixing between two $U(1)$ gauge groups. With this in mind, we study in this work an E_6 motivated UMSSM in a framework where such two $U(1)$ groups kinetically mix so as to, on the one hand, enable one to find only very specific such models compatible with all current experimental data and, on the other hand, generate a wide Z' which in turn allows for Z' masses significantly lower than the aforementioned limits, These could onset signals probing such constructs, at both the LHC and DM experiments.

The outline of the paper is the following. We will briefly introduce E_6 motivated UMSSMs in Section **??**. After summarising our scanning procedure and enforcing experimental constraints in Section 5.3, we present our results over the surviving parameter space and discuss the corresponding particle mass spectrum in Section 5.4, including discussing DM implications.

5.2 Model Description

In addition to the MSSM symmetry content, the UMSSM includes an extra Abelian group, which we indicate as $U(1)'$. The most attractive scenario, which extends the MSSM gauge structure with an extra $U(1)'$ symmetry, can be realised by breaking the exceptional group E_6, an example of a possible Grand Unified Theory (GUT) [122, 177–184, 190–196, 210, 211], as follows:

$$E_6 \to SO(10) \times U(1)_\psi \to SU(5) \times U(1)_\chi \times U(1)_\psi \to G_{\rm MSSM} \times U(1)', \tag{5.1}$$

where $G_{\rm MSSM} = SU(3)_c \times SU(2)_L \times U(1)_Y$ is the MSSM gauge group and $U(1)'$ can be expressed as a general mixing of $U(1)_\psi$ and $U(1)_\chi$ as

$$U(1)' = \cos\theta_{E_6} U(1)_\chi - \sin\theta_{E_6} U(1)_\psi. \tag{5.2}$$

In this scenario, the cancellation of gauge anomalies is ensured by an anomaly free E_6 theory, which includes additional chiral supermultiplets. These additional chiral supermultiplets are assumed to be very heavy and embedded in the fundamental **27**-dimensional

representations of E_6, which constitute the particle spectrum of this scenario alongside the MSSM states and an additional singlet Higgs field $\hat{S}$ [210]. The Vacuum Expectation Value (VEV) of S is responsible for the breaking of the $U(1)'$ symmetry. Furthermore, E_6 scenarios are also encouraging candidates for extra $U(1)'$ models since they may arise from superstring theories [212]. Moreover, E_6 theories generally allow one to include see-saw mechanisms for neutrino mass and mixing generation because of the presence of the right-handed neutrino in their **27** representations [213]. In this study, we assume that the right-handed neutrino does not affect the low energy implications and set its Yukawa coupling to zero.

One can neglect the superpotential terms with the additional chiral supermultiplets as these exotic fields do not interact with the MSSM fields directly, their effects in the sparticle spectrum being quite suppressed by their masses. In this case, the UMSSM superpotential can be given as

$$W = Y_u \hat{Q} \hat{H}_u \hat{U} + Y_d \hat{Q} \hat{H}_d \hat{D} + Y_e \hat{L} \hat{H}_d \hat{E} + h_s \hat{S} \hat{H}_d \hat{H}_u, \tag{5.3}$$

where $\hat{Q}$ and $\hat{L}$ denote the left-handed chiral superfields for the quarks and leptons while $\hat{U}$, $\hat{D}$ and $\hat{E}$ stand for the right-handed chiral superfields of u-type quarks, d-type quarks and leptons, respectively. Here, H_u and H_d are the MSSM Higgs doublets and $Y_{u,d,e}$ are their Yukawa couplings to the matter fields. The corresponding Soft-SUSY Breaking (SSB) Lagrangian can be written as

$$\begin{aligned} -\mathcal{L}_{\cancel{\text{SUSY}}} &= m_{\tilde{Q}}^2 |\tilde{Q}|^2 + m_{\tilde{U}}^2 |\tilde{U}|^2 + m_{\tilde{D}}^2 |\tilde{D}|^2 + m_{\tilde{E}}^2 |\tilde{E}|^2 + m_{\tilde{L}}^2 |\tilde{L}|^2 \\ &+ m_{H_u}^2 |H_u|^2 + m_{H_d}^2 |H_d|^2 + m_S^2 |S|^2 + \textstyle\sum_a M_a \lambda_a \lambda_a \\ &+ \left(A_S Y_S S H_u \cdot H_d + A_t Y_t \tilde{U}^c \tilde{Q} \cdot H_u + A_b Y_b \tilde{D}^c \tilde{Q} \cdot H_d + A_\tau Y_b \tilde{L}^c \tilde{e} \cdot H_d + h.c. \right), \end{aligned} \tag{5.4}$$

where $m_{\tilde{Q}}$, $m_{\tilde{U}}$, $m_{\tilde{D}}$, $m_{\tilde{E}}$, $m_{\tilde{L}}$,m_{H_u}, m_{H_d} and $m_{\tilde{S}}$ are the mass matrices of the scalar particles identified with the subindices, while $M_a \equiv M_1, M_2, M_3, M_4$ stand for the gaugino masses. Further, A_S, A_t, A_b and A_τ are the trilinear scalar interaction couplings. In Eq. (5.3), the MSSM bilinear mixing term $\mu H_d H_u$ is automatically forbidden by the extra $U(1)'$ symmetry and it is instead induced by the VEV of S as $\mu = h_S v_S/\sqrt{2}$, where $v_S \equiv \langle S \rangle$. Employing Eqs. (5.3) and (5.4), the Higgs potential can be obtained as

$$V^{\text{tree}} = V_F^{\text{tree}} + V_D^{\text{tree}} + V_{\cancel{\text{SUSY}}}^{\text{tree}} \tag{5.5}$$

with

$$
\begin{aligned}
V_F^{\text{tree}} &= |h_s|^2 \left[|H_u H_d|^2 + |S|^2 \left(|H_u|^2 + |H_d|^2\right)\right], \\
V_D^{\text{tree}} &= \frac{g_1^2}{8}\left(|H_u|^2 + |H_d|^2\right)^2 + \frac{g_2^2}{2}\left(|H_u|^2|H_d|^2 - |H_u H_d|^2\right) \\
&\quad + \frac{g'^2}{2}\left(Q_{H_u}|H_u|^2 + Q_{H_d}|H_d|^2 + Q_S|S|^2\right), \\
V_{\cancel{\text{SUSY}}}^{\text{tree}} &= m_{H_u}^2|H_u|^2 + m_{H_d}^2|H_d|^2 + m_S^2|S|^2 + \left(A_s h_s S H_u H_d + h.c.\right),
\end{aligned}
\tag{5.6}
$$

which yields the following tree-level mass for the lightest CP-even Higgs boson mass:

$$
m_h^2 = M_Z^2 \cos^2 2\beta + \left(v_u^2 + v_d^2\right)\left[\frac{h_S^2 \sin^2 2\beta}{2} + g'^2\left(Q_{H_u}\cos^2\beta + Q_{H_d}\sin^2\beta\right)\right]. \tag{5.7}
$$

All MSSM superfields and $\hat{S}$ are charged under the $U(1)_\psi$ and $U(1)_\chi$ symmetries and the charge configuration for any $U(1)'$ model can be obtained from the mixing of $U(1)_\psi$ and $U(1)_\chi$, which is quantified by the mixing angle θ_{E_6}, through the equation provided in the caption to Table 5.1.

Model	$\hat{Q}$	$\hat{U}^c$	$\hat{D}^c$	$\hat{L}$	$\hat{E}^c$	$\hat{H}_d$	$\hat{H}_u$	$\hat{S}$
$2\sqrt{6}\ U(1)_\psi$	1	1	1	1	1	-2	-2	4
$2\sqrt{10}\ U(1)_\chi$	-1	-1	3	3	-1	-2	2	0

Table 5.1: Charge assignments for E_6 fields satisfying $Q_i = Q_i^\chi \cos\theta_{E_6} - Q_i^\psi \sin\theta_{E_6}$.

In addition to the singlet S and its superpartner, the UMSSM also includes a new vector boson Z' and its supersymmetric partner $\tilde{B}'$ introduced by the $U(1)'$ symmetry. After the breaking of the $SU(2) \times U(1)_Y \times U(1)'$ symmetry spontaneously, Z and Z' mix to form physical mass eigenstates, so that the $Z - Z'$ mass matrix is as follows

$$
\mathbf{M_Z^2} = \begin{pmatrix} M_{ZZ}^2 & M_{ZZ'}^2 \\ M_{ZZ'}^2 & M_{Z'Z'}^2 \end{pmatrix} = \begin{pmatrix} 2g_1^2 \sum_i t_{3i}^2 \left|\langle\phi_i\rangle\right|^2 & 2g_1 g' \sum_i t_{3i} Q_i \left|\langle\phi_i\rangle\right|^2 \\ 2g_1 g' \sum_i t_{3i} Q_i \left|\langle\phi_i\rangle\right|^2 & 2g'^2 \sum_i Q_i^2 \left|\langle\phi_i\rangle\right|^2 \end{pmatrix}, \tag{5.8}
$$

where t_{3i} is the weak isospin of the Higgs doublets or singlet while the $|\langle\phi_i\rangle|$'s stand for their VEVs. The matrix in Eq. (5.8) can be diagonalised by an orthogonal rotation and the mixing angle $\alpha_{ZZ'}$ can be written as

$$
\tan 2\alpha_{ZZ'} = \frac{2M_{ZZ'}^2}{M_{Z'Z'}^2 - M_{ZZ}^2}. \tag{5.9}
$$

The physical mass states of Z and Z' are given by

$$M^2_{Z,Z'} = \frac{1}{2}\left[M^2_{ZZ} + M^2_{Z'Z'} \mp \sqrt{(M^2_{ZZ} - M^2_{Z'Z'})^2 + 4M^4_{ZZ'}}\right] . \tag{5.10}$$

Besides mass mixing, the theories with two Abelian gauge groups also allow for the existence of a gauge kinetic mixing term which is consistent with the $U(1)_Y$ and $U(1)'$ symmetries [127, 214, 215]:

$$\mathcal{L}_{\text{kin}} \supset -\frac{\kappa}{2}\hat{B}^{\mu\nu}\hat{Z}'_{\mu\nu} , \tag{5.11}$$

where $\hat{B}^{\mu\nu}$ and $\hat{Z}'_{\mu\nu}$ are the field strength tensors of $U(1)_Y$ and $U(1)'$, while κ stands for the kinetic mixing parameter. The mixing factor can be generated at loop level by Renormalisation Group Equation (RGE) running while no such term appears at tree level [128]. In order to attach a physical meaning to the kinetic part of the Lagrangian, we need to remove the non-diagonal coupling of $\hat{B}^{\mu\nu}$ and $\hat{Z}'_{\mu\nu}$ by a two dimensional rotation:

$$\begin{pmatrix} \hat{B}_\mu \\ \hat{Z}'_\mu \end{pmatrix} = \begin{pmatrix} 1 & -\frac{\kappa}{\sqrt{1-\kappa^2}} \\ 0 & \frac{1}{\sqrt{1-\kappa^2}} \end{pmatrix} \begin{pmatrix} B_\mu \\ Z'_\mu \end{pmatrix} , \tag{5.12}$$

where $\hat{B}_\mu$ and $\hat{Z}'_\mu$ are original $U(1)_Y$ and $U(1)'$ gauge fields with off-diagonal kinetic terms while B_μ and Z'_μ do not posses such terms. Due to the transformation in Eq. (5.12), a non-zero κ has a considerable effects on the Z' sector of the UMSSM. One of these is that the rotation matrix which diagonalises the mass matrix in Eq. (5.8) is modified. Therefore, the mixing angle in Eq. (5.9) can be rewritten in terms of κ [215]:

$$\tan 2\alpha_{ZZ'} = \frac{-2\cos\chi(M^2_{ZZ'} + M^2_{ZZ}\hat{s}_W \sin\chi)}{M^2_{Z'Z'} - M^2_{ZZ}\cos^2\chi + M^2_{ZZ}\hat{s}^2_W \sin^2\chi + 2M^2_{ZZ'}\hat{s}_W \sin\chi} , \tag{5.13}$$

where $\sin\chi = \kappa$ and $\cos\chi = \sqrt{1-\kappa^2}$ [1]. Note that the impact of κ can be negligible only if $M_Z \ll M_{Z'}$ and $\kappa \ll 1$. The $|\alpha_{ZZ'}|$ value is strongly bounded by EW Precision Tests (EWPTs) to be less than a few times 10^{-3}. In models with kinetic mixing (e.g., in leptophobic Z' models), this limit could be relaxed but does not exceed significantly the $\mathcal{O}(10^{-3})$ ballpark [123]. The kinetic mixing also affects the interactions of the Z' boson with fermions. After applying the rotation in Eq. (5.12), the Lagrangian term which shows

[1] In this notation, generally used to express kinetic mixing factor, χ is called the kinetic mixing angle.

Z-fermion and Z'-fermion interaction can be written as [127]:

$$\mathcal{L}_{\text{int}} = -\bar{\psi}_i \gamma^\mu \left[g_y Y_i B_\mu + (g_p Q_i + g_{yp} Y_i) Z'_\mu \right] \psi_i \,, \tag{5.14}$$

where g_y, g_p and g_{yp} are the redefined gauge coupling matrix elements after absorbing the rotation in Eq. (5.12) and they can be written in terms of original diagonal gauge couplings and the kinetic mixing parameter κ:

$$\begin{aligned} g_y &= \frac{g_{YY} g_{EE} - g_{YE} g_{EY}}{\sqrt{g_{EE}^2 + g_{EY}^2}} &&= g_1, \\ g_{yp} &= \frac{g_{YY} g_{EY} + g_{YE} g_{EE}}{\sqrt{g_{EE}^2 + g_{EY}^2}} &&= \frac{-\kappa g_1}{\sqrt{1-\kappa^2}}, \\ g_p &= \sqrt{g_{EE}^2 + g_{EY}^2} &&= \frac{g'}{\sqrt{1-\kappa^2}}, \end{aligned} \tag{5.15}$$

where g_{YY}, g_{EE}, g_{EY} and g_{YE} are the elements of non-diagonal gauge matrix obtained by absorbing the rotation in Eq. (5.12) [216]:

$$G = \begin{pmatrix} g_{YY} & g_{YE} \\ g_{EY} & g_{EE} \end{pmatrix} . \tag{5.16}$$

It is important to notice that parts of the mass mixing matrix in Eq. (5.8) change in the case of kinetic mixing and the off-diagonal g_{EY} and g_{YE} enter in $M_{ZZ'}$ as well.

As seen from Eqs. (5.14)–(5.15), the kinetic mixing results in a shift in the $U(1)'$ charges of the chiral superfields, which define the couplings of the Z' boson with fermions:

$$Q_i^{eff} = Q_i - \kappa \frac{g_1}{g'} Y_i \,. \tag{5.17}$$

Since the anomaly cancellation conditions for Q_i and Y_i in E_6 models stabilises the theory, this new effective charge configuration is also anomaly free. Moreover, if one makes a special choice in the (κ, Q_i) space, the Z' boson can be exactly leptophobic [125, 128, 129].

Compared to the MSSM, the UMSSM has a richer gaugino sector which consists of six neutralinos. Their masses and mixing can be given in the $(\tilde{B}', \tilde{B}, \tilde{W}, \tilde{h}_u, \tilde{h}_d, \tilde{S})$ basis as

follows:

$$\mathcal{M}_{\tilde{\chi}^0} = \begin{pmatrix} M_1' & 0 & 0 & g'Q_{H_d}v_d & g'Q_{H_u}v_u & g'Q_S v_S \\ 0 & M_1 & 0 & -\frac{1}{\sqrt{2}}g_1 v_d & \frac{1}{\sqrt{2}}g_1 v_u & 0 \\ 0 & 0 & M_2 & \frac{1}{\sqrt{2}}g_2 v_d & -\frac{1}{\sqrt{2}}g_2 v_u & 0 \\ g'Q_{H_d}v_d & -\frac{1}{\sqrt{2}}g_1 v_d & \frac{1}{\sqrt{2}}g_2 v_d & 0 & -\frac{1}{\sqrt{2}}h_s v_u & -\frac{1}{\sqrt{2}}h_s v_u \\ g'Q_{H_u}v_u & \frac{1}{\sqrt{2}}g_1 v_u & -\frac{1}{\sqrt{2}}g_2 v_u & -\frac{1}{\sqrt{2}}h_s v_S & 0 & -\frac{1}{\sqrt{2}}h_s v_d \\ g'Q_S v_S & 0 & 0 & -\frac{1}{\sqrt{2}}h_s v_u & -\frac{1}{\sqrt{2}}h_s v_d & 0 \end{pmatrix}, \quad (5.18)$$

where M_1' is the SSB mass of $\tilde{B}'$ and the first row and column encode the mixing of $\tilde{B}'$ with the other neutralinos. Since the UMSSM does not have any new charged bosons, the chargino sector remains the same as that in the MSSM. Besides the neutralino sector, the sfermion mass sector also has extra contributions from the D-terms specific to the UMSSM. The diagonal terms of the sfermion mass matrix are modified by

$$\Delta_{\tilde{f}} = \frac{1}{2}g'Q_{\tilde{f}}(Q_{H_u}v_u^2 + Q_{H_d}v_d^2 + Q_S v_S^2), \quad (5.19)$$

where $\tilde{f}$ refers to sfermion flavours. It can be noticed that all neutralino and sfermion masses also depend on κ in the presence of kinetic mixing due to Eqs. (5.15) and (5.17) [217].

5.3 Scanning Procedure and Experimental Constraints

In our parameter space scans, we have employed the SPheno (version 4.0.0) package [76] obtained with `SARAH` (version 4.11.0) [78]. In this code, all gauge and Yukawa couplings in the UMSSM are evolved from the EW scale to the GUT scale that is assigned by the condition of gauge coupling unification, described as $g_1 = g_2 = g'$. (Notice that g_3 is allowed to have a small deviation from the unification condition, since it has the largest threshold corrections at the GUT scale [218].) After that, the whole mass spectrum is calculated by evaluating all SSB parameters along with gauge and Yukawa couplings back to the EW scale. These bottom-up and top-down processes are realised by running the RGEs and the latter also requires boundary conditions given at $M_{\rm GUT}$ scale. In the numerical analysis of our work, we have performed random scans over the following parameter space of the UMSSM:

Parameter	Scanned range	Parameter	Scanned range
m_0	$[0., 3.]$ TeV	h_s	$[0., 0.7]$
$M_{1,4}/M_3$	$[-15., 15.]$ TeV	v_S	$[1., 15.]$ TeV
M_3	$[0., 3.]$ TeV	A_s	$[-5., 5.]$ TeV
M_2/M_3	$[-5., 5.]$ TeV	θ_{E_6}	$[-\pi/2, \pi/2]$
$\tan\beta$	$[1., 50.]$	κ	$[-0.5, 0.5]$
A_0	$[-5., -5.]$ TeV		

Table 5.2: Scanned parameter space.

where m_0 is the universal SSB mass term for the matter scalars while M_1, M_2, M_3, M_4 are the SSB mass terms of the gauginos associated with the $U(1)_Y$, $SU(2)_L$ and $SU(3)_c$ and $U(1)'$ symmetry groups, respectively. Besides, A_0 is the SSB trilinear coupling and $\tan\beta$ is the ratio of the VEVs of the MSSM Higgs doublets. A_s is the SSB interaction between the S, H_u and H_d fields. In addition, as mentioned previously, θ_{E_6} and κ are the $Z - Z'$ mass mixing angle and gauge kinetic mixing parameter. Finally, we also vary the Yukawa coupling h_s and v_S (the VEV of S) which is responsible for the breaking of the $U(1)'$ symmetry.

In order to scan the parameter space efficiently, we use the Metropolis-Hasting algorithm [93]. After data collection, we implement Higgs boson and sparticle mass bounds [29, 153] as well as constraints from Branching Ratios (BRs) of B-decays such as BR($B \to X_s\gamma$) [90], BR($B_s \to \mu^+\mu^-$) [88] and BR($B_u \to \tau\nu_\tau$) [89]. We also require that the predicted relic density of the neutralino LSP agrees within 20% (to conservatively allow for uncertainties on the predictions) with the recent Wilkinson Microwave Anisotropy Probe (WMAP) [219] and Planck results, $\Omega_{\rm CDM}h^2 = 0.12$ [11, 12]. The relic density of the LSP and scattering cross sections for direct detection experiments are calculated with MicrOMEGAs (version 5.0.9) [220]. The experimental constraints can be summarised as follows:

$$
\begin{aligned}
&m_h = 123 - 127 \text{ GeV} (\text{and SM} - \text{like couplings}),\\
&m_{\tilde{g}} \geq 1.8 \text{ TeV},\\
&0.8 \times 10^{-9} \leq \text{BR}(B_s \to \mu^+\mu^-) \leq 6.2 \times 10^{-9} \ (2\sigma \text{ tolerance}),\\
&m_{\tilde{\chi}_1^0} \geq 103.5 \text{ GeV},\\
&m_{\tilde{\tau}} \geq 105 \text{ GeV},\\
&2.99 \times 10^{-4} \leq \text{BR}(B \to X_s\gamma) \leq 3.87 \times 10^{-4} \ (2\sigma \text{ tolerance}),\\
&0.15 \leq \frac{\text{BR}(B_u \to \tau\nu_\tau)_{\text{UMSSM}}}{\text{BR}(B_u \to \tau\nu_\tau)_{\text{SM}}} \leq 2.41 \ (3\sigma \text{ tolerance}),\\
&0.0913 \leq \Omega_{\text{CDM}}h^2 \leq 0.1363 \ (5\sigma \text{ tolerance}).
\end{aligned}
\tag{5.20}
$$

As discussed in the previous section, the kinetic mixing affects the $Z - Z'$ mixing matrix and adds new terms related to the off-diagonal gauge matrix elements g_{EY} and g_{YE} into the mixing term $M_{ZZ'}$. Furthermore, the mixing angle could be enhanced near or beyond the EWPT bounds. The main reason is that the new $M_{ZZ'}$ element includes the term with proportional to $g_{EY}Q_S^2v_S^2$. Therefore, one must take a specific g_{EY} range if one wants to avoid violating the EWPT limits for $\alpha_{ZZ'}$. In our analysis, we allow this range as $g_{EY} \sim \mathcal{O}(10^{-3})$ to obtain a large (but compatible with EWPTs) $\alpha_{ZZ'}$, as $\Gamma(Z' \to WW)$ and $\Gamma(Z' \to Zh)$ are very sensitive to this coupling. In order to account for EWPTs, we have parameterised the latter through the EW oblique parameters S, T and U that are obtained from the SPheno output [148–152].

In the case that $\Gamma(Z')/M_{Z'}$ is large[2], the LHC limits on the Z' boson mass and couplings, which are produced under the assumption of Narrow Width Approximation (NWA), cannot be applied, as interference effects are not negligible [222, 223]. Therefore, here, we define the Z' Signal (S) as the difference between $\sigma(pp \to \gamma, Z, Z' \to ll)$ and the SM Background (B) $\sigma(pp \to \gamma, Z \to ll)$, where $l = e, \mu$. The corresponding cross section values have been calculated by using MG5_aMC (version 2.6.6) [112] along with the leading-order set of NNPDF 2.3 parton densities [224].

The following list summarises the relation between colours and constraints imposed in our forthcoming plots.

- Grey: Radiative EWSB (REWSB) and neutralino LSP.

[2]Notice that we have put a bound on the total width of the Z' boson, $\Gamma(Z') \lesssim M_{Z'}/2$, so as to avoid unphysical resonance behaviours [221].

- Red: The subset of grey plus Higgs boson mass and coupling constraints, SUSY particle mass bounds and EWPT requirements.
- Green: The subset of red plus B-physics constraints.
- Blue: The subset of green plus WMAP constraints on the relic abundance of the neutralino LSP (within 5σ).
- Black: The subset of blue plus exclusion limits at the LHC from Z' direct searches via $pp \to Z' \to ll$ and $pp \to Z' \to WW$.

We further discuss the application of these limits in the next section. We ignore here $(g-2)_\mu$ constraints, as we can anticipate that the corresponding predictions in our E_6 inspired UMSSM are consistent with the SM, due to the fact that the relevant slepton and sneutrino masses are rather heavy and so is the Z' mass.

5.4 Mass Spectrum and Dark matter

This section will start by presenting our results for the Z' mass and coupling bounds (in a large $\Gamma(Z')$ scenario) and how these can be related to the fundamental charges of an E_6 inspired UMSSM, then, upon introducing the LHC constraints affecting the SUSY sector, it will move on to discuss the DM phenomenology in astrophysical conditions.

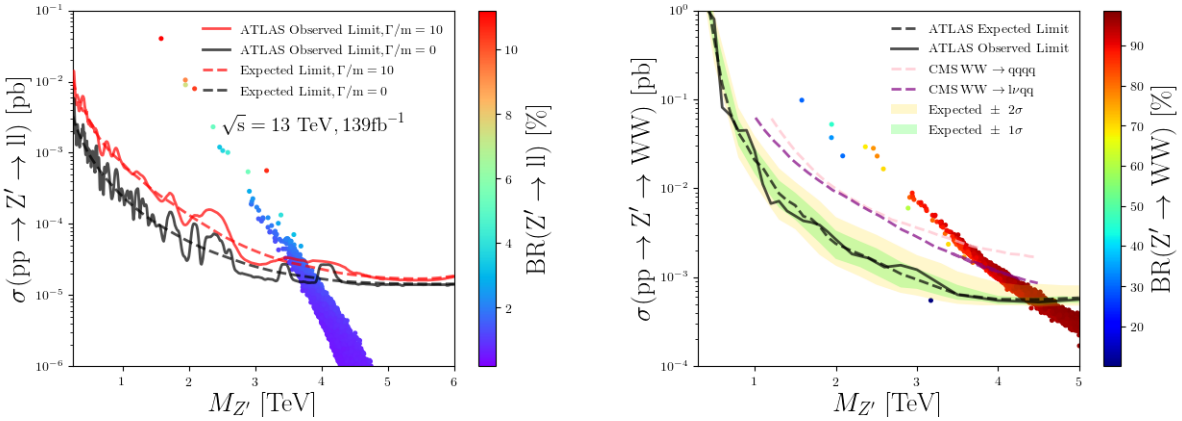

Figure 5.1: The Z' boson mass limits on $\sigma(pp \to Z' \to ll)$ vs $M_{Z'}$ (left panel) and $\sigma(pp \to Z' \to WW)$ vs $M_{Z'}$ (right panel). The experimental exclusion curves obtained by the ATLAS [9, 15] and CMS [16, 17] collaborations are showed against the results of our scan colour coded in terms of the relevant Z' BR.

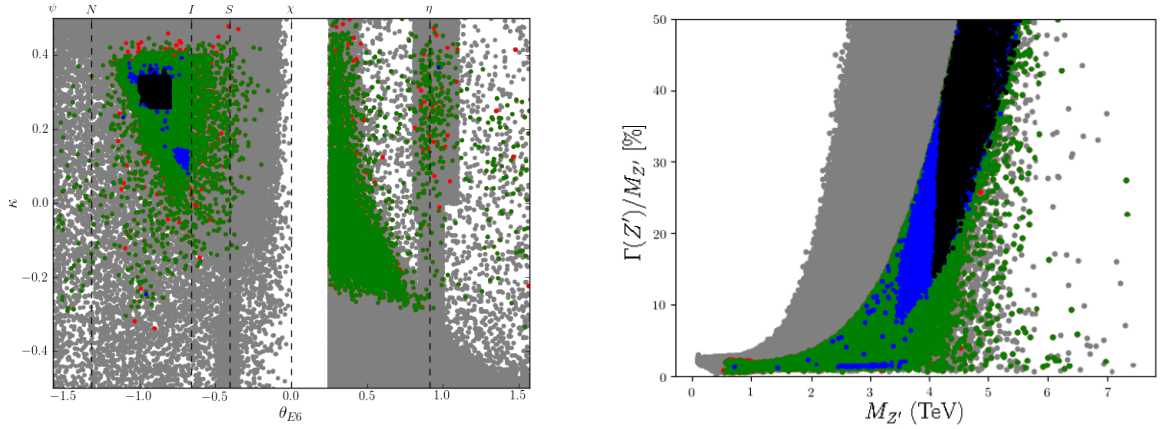

Figure 5.2: The gauge kinetic mixing parameter κ versus $U(1)'$ charge mixing angle θ_{E_6} (left panel) and the Z' width-to-mass ratio $\Gamma(Z')/M_{Z'}$ vs the Z' mass $M_{Z'}$ (right panel). Our colour convention is as listed at the end of Section 5.3. The vertical dashed lines in the left panel corresponds to well-known E_6 realisation with defined θ_{E_6} choices.

Fig. 5.1 shows the comparison of the experimental limits on the Z' boson mass and cross section (hence some coupling combinations) as obtained from direct searches in the processes $pp \to ll$ at $\mathcal{L} = 137$ fb^{-1} [9] and $pp \to WW$ at $\mathcal{L} = 36$ fb^{-1} [15–17]. All points plotted here satisfy all constraints that are coded "Blue" in the previous section while the actual colours display the BR of the related Z' boson decay channel. According to our results, in the left panel, we find that the Z' boson mass cannot be smaller than 3.5 TeV in the light of the ATLAS dilepton results [9]. Indeed, it is thanks to the gauge kinetic mixing effects on the $U(1)'$ charges and the negative interference onset by the wide Z' with the SM background that we are able to obtain this lower limit, as the ATLAS results [9] reported a lower limit at 4.5 TeV (e.g., for an E_6 based ψ model). Furthermore, as can be seen from the right panel, the ATLAS results on the $Z' \to WW$ channel [15], when taken within 2σ, put a lower Z' mass limit at $M_{Z'} \gtrsim 4$ TeV. This lower bound is somewhat relaxed by some CMS results also shown in the same plot, down to 3.5 TeV. In the reminder of this work, therefore, we use the Z' boson mass allowed by all Z' direct searches in the dilepton and diboson channels as being $M_{Z'} \gtrsim 4$ TeV.

In Fig. 5.2 we present our results in plots showing the gauge kinetic mixing parameter versus the $U(1)'$ charge mixing angle, i.e., on the plane (θ_{E_6}, κ) (left panel), and the Z' boson mass versus the ratio of its total decay width over the former, i.e., on the plane $(M_{Z'}, \Gamma(Z')/M_{Z'})$ (right panel). The former plot shows that the parameter space of the θ_{E_6} mixing angle, which also defines the effective charge of $U(1)'$, is constrained severely when

we apply all limits mentioned in Section 5.3. We see that θ_{E_6} values are found in the interval $[-1, -0.8]$ radians while the corresponding κ values are found in $[0.2, 0.4]$. We notice that such solutions do not accumulate against any of the most studied E_6 realisations, known as ψ, N, I, S, χ and η [153]. The latter plot indeed makes the point that wide Z' states are required to evade LHC limits from Z' direct searches, with values of the width being no less than 15% or so of the mass. The right panel shows that $\Gamma(Z')/M_{Z'}$ can drastically increase with large $M_{Z'}$. This is due to the fact that the decay width $\Gamma(Z' \to WW)$ is proportional to $(M_{Z'}^5/M_W^4)$ as well as $\sin^2\alpha_{ZZ'}$ [225]. (Recall that the "Black" points here include the constraints drawn from the previous figure.)

The solutions in the (θ_{E_6}, κ) region which we have just seen have special $U(1)'$ effective charge configurations, are presented in Fig. 5.3. Herein, we show such charges, as given in Eq. (5.17), for left and right chiral fermions by visualising our scan points over the planes (Q_Q^{eff}, Q_U^{eff}), (Q_Q^{eff}, Q_U^{eff}) and (Q_L^{eff}, Q_E^{eff}). As seen from the top left and right panels, when we take all experimental constrains into consideration ("Black" points), the family universal effective $U(1)'$ charges for left handed (Q_Q^{eff}) quarks are always very small, with the right handed up-type (Q_U^{eff}) quark charges smaller than those of the right handed down-type (Q_D^{eff}) ones. As for leptons, it is the left handed (Q_L^{eff}) charges which are generally larger than the right handed ones (Q_E^{eff}) (as shown in the bottom left panel of the figure). This pattern builds up the distribution of fermionic BRs seen in the bottom right panel of the figure, as the partial decay width of the Z' into fermions f, $\Gamma(Z' \to ff)$, is proportional to $M_{Z'}(Q_{\rm left}^{eff\,2} + Q_{\rm right}^{eff\,2})$ [209]. However, such a BR$(Z' \to XX)$ distribution is actually dominated by $Z' \to WW$ decays over most of the $M_{Z'}$ range (with the companion $Z' \to Zh$ channel always subleading), given that, for large Z' masses, as mentioned, $\Gamma(Z' \to WW)$ is proportional to $M_{Z'}^5/M_W^4$, hence the rapid rise up to 98% with increasing $M_{Z'}$, particularly so from 4 TeV onwards (notice that these decay distributions have been produced by the "Blue" points appearing in the other panels). It is thus not surprising that the most constraining search for the Z' of E_6 inspired UMSSM scenarios is the diboson one, rather than the dilepton one (limitedly to the case of its SM decay channels).

We now move on now to study the other two sectors of our $U(1)'$ construct, namely, the spectrum of Higgs and SUSY particle masses. A selection of these is presented in Fig. 5.4 with plots over the following mass combinations (clockwise): $(m_{\tilde{b}}, m_{\tilde{t}})$, $(m_{\tilde{g}}, m_{\tilde{\chi}_1^0})$, $(m_{\tilde{\chi}_1^0}, m_A)$ and $(m_{\tilde{\nu}}, m_{\tilde{\tau}})$. The colour coding is the same as the one listed at the end of Section 5.3. As seen from the top left and right panels of the figure, the SUSY mass spectrum of the allowed parameter region (i.e., the "Black" points) is quite heavy with the lower limit on

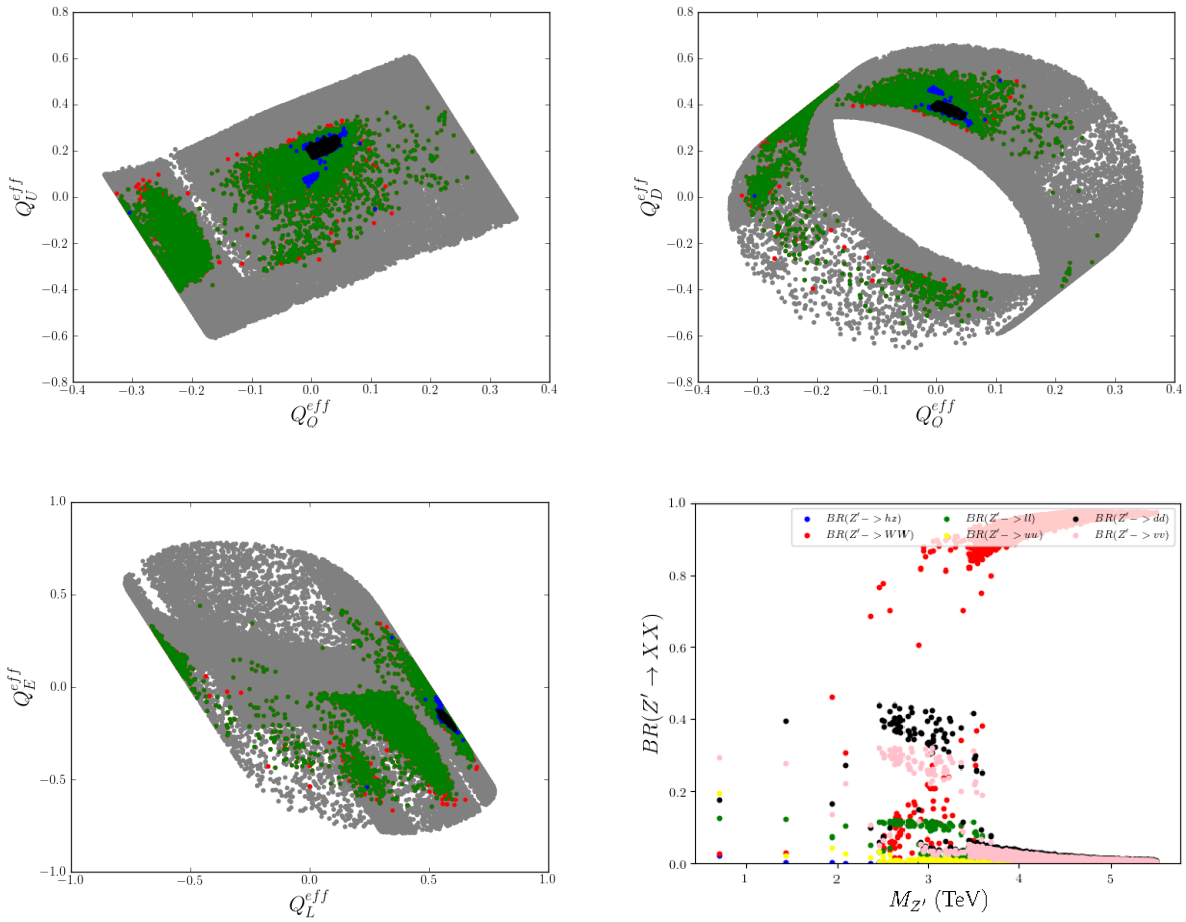

Figure 5.3: The distributions of the effective $U(1)'$ charges for quarks and leptons over the following planes: (Q_Q^{eff}, Q_U^{eff}) (top left), (Q_L^{eff}, Q_E^{eff}) (top right), and (Q_Q^{eff}, Q_D^{eff}) (bottom left). In the bottom right plot we show the BRs of the Z' for different decay channels, $\mathrm{BR}(Z' \to XX)$ as a function on $M_{Z'}$, where XX represents a SM two-body final state. Our colour convention is as listed at the end of Section 5.3 and the bottom right panel contains only the "Blue" points in the other panels.

stop, sbottom and gluino masses of about 4 TeV. The reason for the large sfermions mass arises from the fact that the contributions of the $U(1)'$ sector to such masses are proportional to v_S^2, which also determines the mass of the Z'. Therefore, the experimental limits on the Z' mass in Fig. 5.1 in turn drive those on the sfermion masses. The bottom left panel shows that the LSP (neutralino) mass should be 0.8 TeV $\lesssim m_{\tilde{\chi}_1^0} \lesssim$ 1.7 TeV (the extremes of the "Black" point distribution). In this plot, the solid red line shows the points with $m_A = 2m_{\tilde{\chi}_1^0}$, condition onsetting the dominant resonant DM annihilation via A mediation, so that very few solutions (to WMAP data) are found below it. As for the stau masses, see bottom right frame, these are larger than the sneutrino ones (again, see the "Black" points), both well in the TeV range. In summary, both the Higgs and SUSY (beyond the LSP) mass spectrum is rather heavy, thus explaining the notable absence of non-SM decay channels for the Z', as already seen.

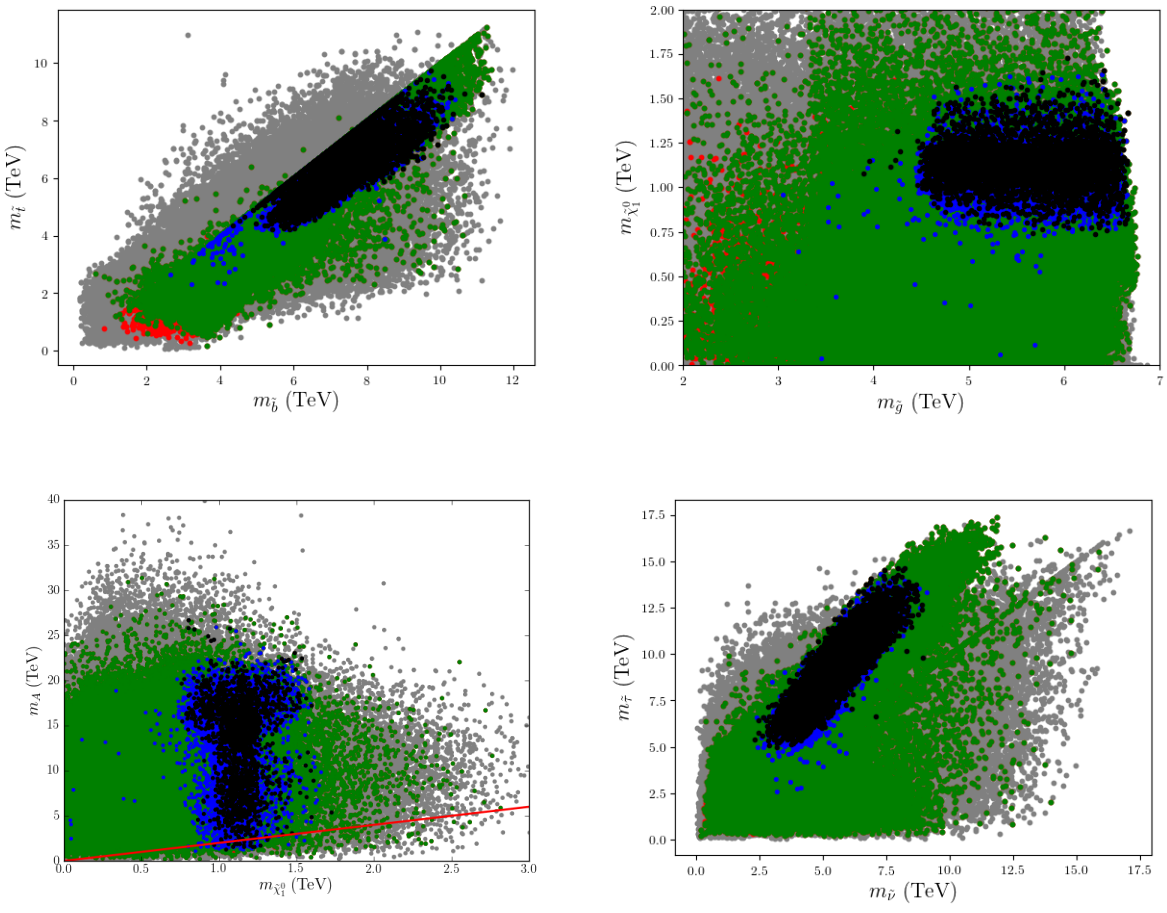

Figure 5.4: The mass spectrum of Higgs and SUSY states over the following planes: $(m_{\tilde{b}}, m_{\tilde{t}})$ (top left), $(m_{\tilde{g}}, m_{\tilde{\chi}_1^0})$ (top right), $(m_{\tilde{\chi}_1^0}, m_A)$ (bottom left) and $(m_{\tilde{\nu}}, m_{\tilde{\tau}})$ (bottom right). Our colour convention is as listed at the end of Section 5.3.

In Fig. 5.5 we illustrate the neutralino and chargino mass spectrum, also in relation to the effective μ parameter, μ_{eff}, using plots over the following parameter combinations ($\tilde{S}$ being the singlino): $(\mu_{eff}, m_{\tilde{S}})$, $(m_{\tilde{\chi}_1^0}, m_{\tilde{\chi}_1^\pm})$, $(m_{\tilde{\chi}_2^0}, m_{\tilde{\chi}_0^3})$ and $(m_{\tilde{\chi}_2^0}, m_{\tilde{\chi}_1^\pm})$. (The colour coding is the same as in Fig. 5.2.) Herein, (the diagonal) dot-dashed red lines indicate regions in which the displayed parameters are degenerate in value. The top left panel shows that the LSP, the neutralino DM candidate, is higgsino-like or singlino-like since the other gauginos that contribute to the neutralino mass matrix are heavier and decouple (see below). The higgsino-like DM mass can be 1 TeV $\lesssim m_{\tilde{\chi}_1^0} \lesssim$ 1.2 TeV while the singlino-like DM mass can cover a wider range, 0.8 TeV $\lesssim m_{\tilde{\chi}_1^0} \lesssim$ 1.7 TeV. Further, as can be seen from the top right panel, the lightest chargino and LSP are largely degenerate in mass (typically, within a few hundred GeV) in the region of the higgsino-like DM mass and the chargino mass can reach 3 TeV. These solutions favour the chargino-neutralino coannihilation channels which reduce the relic abundance of the LSP, such that the latter can be consistent with the WMAP bounds. (This region also yields the A resonant solutions, $m_A = 2m_{\tilde{\chi}_1^0}$, as seen from the bottom left panel of Fig. 5.4.) The bottom left panel illustrates the point that, for higgsino-like DM, the mass gap between the second and third lightest neutralino can be of order TeV, though there is also a region with significant mass degeneracy. Then, as seen from the bottom right panel, the lightest chargino and second lightest neutralino are extremely degenerate in mass for all allowed solutions ("Black" points). Altogether, this means that EW associated production of mass degenerate charginos $\tilde{\chi}_1^\pm$ and neutralinos $\tilde{\chi}_2^0$ where $\tilde{\chi}_1^\pm \to W\tilde{\chi}_1^0$ and $\tilde{\chi}_2^0 \to h\tilde{\chi}_1^0$ is possible for both type of higgsino- and singlino-like LSP. However, it must be said that EW production of mass degenerate neutralinos cannot be possible because of the heavy sleptons shown in the bottom right panel of Fig. 5.4. Hence, a potentially interesting new production and decay mode emerges in the -ino sector, $pp \to \tilde{\chi}_2^0\tilde{\chi}_3^0 \to (h/Z)(h/Z)\tilde{\chi}_1^0\tilde{\chi}_1^0$, which could be probed at the High Luminosity LHC (HL-LHC).

Before closing, we investigate how cosmological bounds from relic density and from DM experiments impact our solutions. Fig. 5.6 shows that our relic density predictions for singlino LSP (left panel) and higgsino LSP (right panel) as the DM candidate. The color bars show the singlino (left panel) and higgsino (right panel) compositions of LSP. (Notice that the population of points used in this plot correspond to the "Green" points listed at the end of Section 5.3, i.e., meaning that all experimental constraints, except for DM itself and the Z' mass and coupling limits, are applied.) The dark shaded areas between the horizontal lines show where the "Black" points are in this figure. The dot-dashed(solid) lines indicate the WMAP bounds on the relic density of the DM candidate within a $5\sigma(1\sigma)$ uncertainty. The

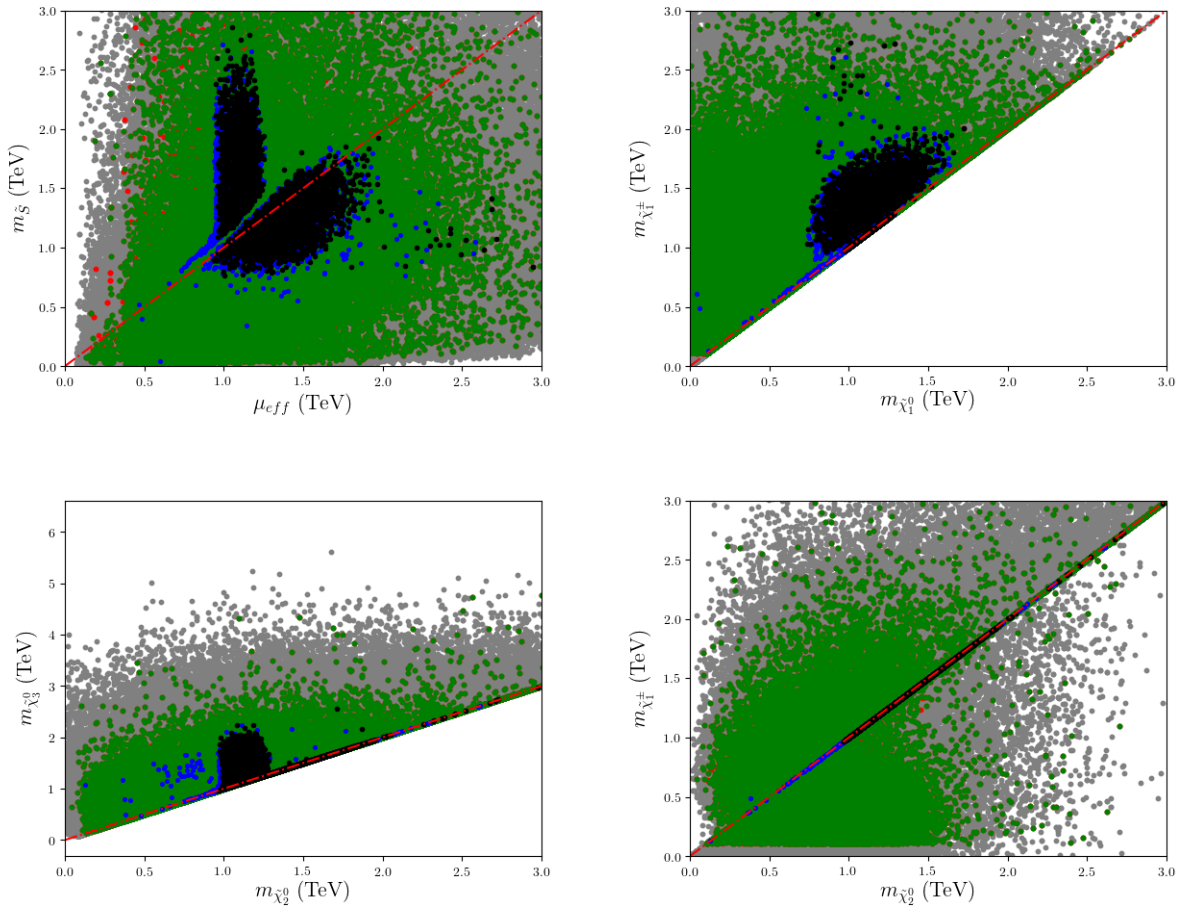

Figure 5.5: The mass spectrum of chargino and neutralino states over the following planes: $(\mu_{eff}, m_{\tilde{S}})$ (top left), $(m_{\tilde{\chi}_1^0}, m_{\tilde{\chi}_1^\pm})$ (top right), $(m_{\tilde{\chi}_2^0}, m_{\tilde{\chi}_0^3})$ (bottom left) and $(m_{\tilde{\chi}_2^0}, m_{\tilde{\chi}_1^\pm})$ (bottom right). Our colour convention is as listed at the end of Section 5.3.

region within the dot-dashed lines covers also the recent Planck bounds [12]. Altogether, the figure points to a singlino-like DM being generally more consistent with all relic density data available, though the higgsino-like one is also viable, albeit in a narrower region of parameter space, with the two solutions overlapping each other.

In Fig. 5.7 we depict the DM-neutron Spin-Independent (SI, left panel) and Spin-Dependent (SD, right panel) scattering cross sections as functions of the WIMP candidate mass, i.e., that of the neutralino LSP. The color codes are indicated in the legend of the panels. Here, all points satisfy all the experimental constraints used in this work, i.e., they correspond to the "Black" points as described at the end of Section 5.3. We represent solutions with $|Z_{16}^{\tilde{\chi}}|^2 > 0.6$ as singlino-like $\tilde{\chi}_1^0$ and show them in dark cyan colour. Likewise, solutions with $|Z_{14}^{\tilde{\chi}}|^2 + |Z_{15}^{\tilde{\chi}}|^2 > 0.6$ are represented as higgsino-like $\tilde{\chi}_1^0$ and they are coded with red

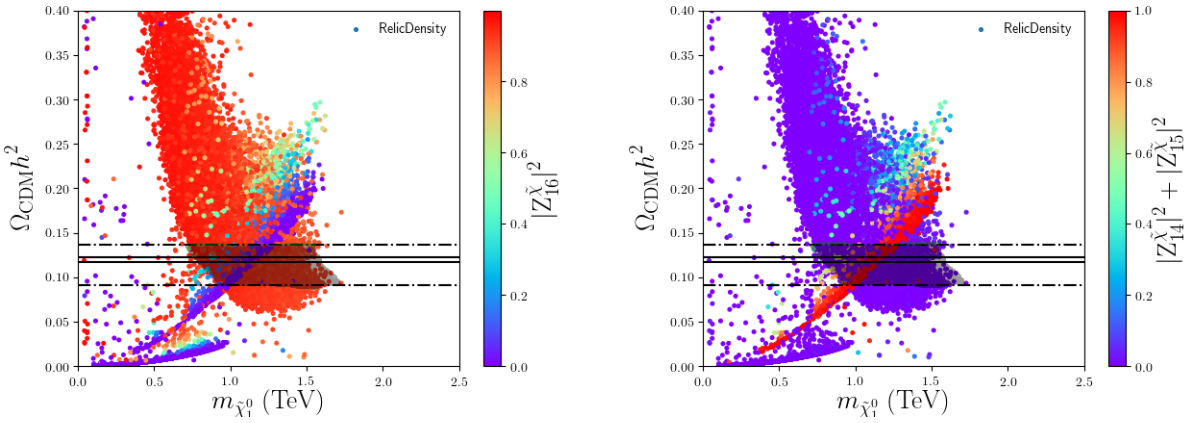

Figure 5.6: Relic density predictions for singlino-like (left) and higgsino-like (right) DM as a function of the mass of the neutralino LSP. The colour bars show the composition of the LSP. The meaning of the horizontal lines is explained in the text.

colour. In the left panel, the solid(dashed) lines indicate the upper limits coming from current(future) SI direct detection experiments. The black, brown and purple solid lines show XENON1T [155], PandaX-II [226] and LUX [227] upper limits for the SI $\tilde{\chi}_1^0$ - n cross section, respectively, while the green and blue dashed lines illustrate the prospects of the XENONnT and DARWIN for future experiments [101], respectively. As seen from this panel, all our points are presently consistent with all experimental constraints yet certain DM solutions can be probed by the next generation of experiments. In the right panel, the black, green and purple solid lines show XENON1T [228], PandaX-II [229] and LUX [230] upper limits for the SD $\tilde{\chi}_1^0$ - n cross section, respectively. As seen from this plot, all solutions are consistent with current experimental results, for both singlino- and higgsino-like DM.

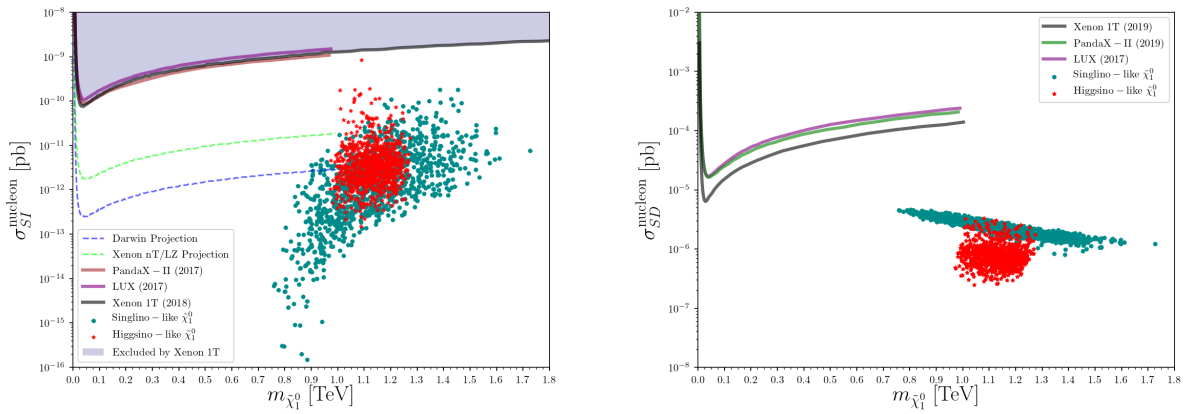

Figure 5.7: DM-neutron SI (left) and SD (right) scattering cross section as a function of the mass of the WIMP candidate (neutralino LSP). The colour bars show the composition of the LSP. Limits from current (solid) and future (dashed) experiments are also shown.

Chapter 6

Relaxing LHC constraints on the W_R mass

6.1 Introduction

The discovery of the Higgs boson at the LHC, while providing the missing ingredient of the Standard Model (SM), has intensified the search for physics beyond it. Though there is a marked lack of non-standard signals at colliders, the existence of neutrino masses is a definite sign of beyond the SM. Using only left-handed neutrinos and the standard Higgs doublet representation of the SM, massive neutrinos appear only from higher dimension operators acting at the Planck scale. While by no means the only solution, left-right symmetric models (LRSMs) [231–233] provide a natural explanation for neutrino masses without resorting to higher scales. Based on the $SU(2)_L \otimes SU(2)_R \otimes U(1)_{B-L}$, these models restore parity symmetry, which is conserved at high energy, and spontaneously broken at some energy scale connected to the $SU(2)_R$ breaking scale [234]. That is, LRSMs provide a renormalizable framework where left- and right-handed fields are treated the same way: they are doublets under $SU(2)$. Small neutrino masses are induced by heavy (and most often, Majorana) right-handed neutrinos through the phenomena known as the seesaw mechanism [62, 235]. Within the framework described here both Type I and Type II seesaw mechanisms can be naturally imbedded in the model.

In addition, LRSMs gauge the anomaly-free $B - L$ (B - baryon, L - lepton, number) symmetry, and replace the physically meaningless hypercharge Y by the $B - L$ quantum

number in the definition of charge

$$Q = T_{3L} + T_{3R} + \frac{B-L}{2},$$

with T_3 the third component of isospin. In some LRSMs, CP-violating phases are connected with the right-handed quark system, and the smallness of the CP violation in the quark sector is related to the suppression of the $V + A$ currents and the large right-handed gauge boson mass [236, 237]. These models also provide a solution to the strong CP violation problem. In LRSMs, the strong CP parameter $\Theta \to -\Theta$ under parity, and thus $\Theta = 0$ at tree level, with small non-zero contributions arising at two loop level only [238]. The LRSMs are constrained at low energies by flavor-violating mixing and decays, by CP observables, and, more recently, by increasingly restrictive collider limits on new particle (additional gauge or Higgs bosons) masses.

In making any specific predictions, there are several sources of uncertainty in the model. One comes from the precise nature of the additional Higgs bosons needed to break the symmetry to the SM one. Higgs triplets are favored by the seesaw mechanisms, and yield Majorana neutrinos. Alternatively, additional left- and right- handed doublet Higgs representations yield Dirac neutrino masses. Another source of uncertainty comes from the right-handed quark mixing matrix, similar to that of the left-handed quark Cabibbo-Kobayashi-Maskawa (CKM) mixing. Two scenarios of left-right models have been most often considered: manifest and pseudo-manifest left-right symmetry. Manifest left-right symmetry, assumes no spontaneous CP violation, *i.e.* all Higgs vacuum expectation values (VEVs) are real. The quark mass matrices are Hermitian, and the left- and right-handed quark mixings become identical, up to a sign uncertainty of the elements from negative quark masses [239, 240]. Pseudo-manifest left-right symmetry assumes that the CP violation comes entirely from spontaneous symmetry breaking of the vacuum and all Yukawa couplings are real [241, 242]. The quark mass matrices are complex and symmetric, and the right-handed quark mixing is related to the complex conjugate of the CKM matrix multiplied by additional CP phases. However, studies of the left-right symmetric model with more general structures, where no *a priory* assumptions on masses and mixing in the right sector are made, also exist in the literature [243–245].

Another source of uncertainty comes from the gauge coupling constant in the right-handed sector. It is commonly assumed that left-right symmetry imposes $g_L = g_R$. If breaking of $SU(2)_R \otimes U(1)_{B-L}$ occurs at a high scale, at that scale $g_L = g_R$, but below

that, the couplings g_L and g_R could evolve differently, and would be different at low energy scales.

Bounds on extra particle masses depend strongly on the above assumptions, in particular on the size of the right-handed gauge coupling and/or the right-handed CKM matrix elements, and none more so than the charged gauge boson W_R. This boson is interesting for several reasons. First, regardless of the other details of the spectrum of left-right models, discovery of a charged gauge boson will be an indication of the presence of an additional $SU(2)$ symmetry group, and if testing its decay products would indicate that it is right-handed, this will be an unambiguous signal for left-right symmetry[1]. Second, the LHC has significantly improved searches for W_R bosons, and the limits on their masses are becoming more stringent. A previous work considered implications for the single W_R production, $pp \to W_R t$ at the LHC, showing that significant signals above the background are possible, if we relax equality between gauge couplings and of CKM matrices in left and right sectors [245].

Extensive analyses performed indicate problems with both manifest and pseudo-manifest scenarios [246]. In the manifest LRSM, there are more minimization conditions than the number of VEVs, thus the model suffers from a fine-tuning problem. In the pseudo-manifest LRSM, the decoupling limit yields either a model with light left-handed triplet Higgs, (already excluded by the ρ parameter), or a two Higgs doublet model (excluded due to large tree level flavor-changing neutral currents). It seems that a better way to proceed would be to keep the parameter space of the model as general as possible, but impose all constraints from collider searches and from flavor and CP bounds from low-energy phenomenology.

In light of recent experimental measurements and interpretations restricting W_R and Z_R boson masses, we re-consider the scenarios assumed in the analyses, and recast the results using an unrestricted LRSM. For example, considering the CMS analysis, the effect of $g_R < g_L$ can reduce the production cross section, thus bringing down the lower limit obtained on M_{W_R}. This analysis is timely, as more precise analyses are expected to emerge from the Run II at the LHC in the next year or so.

We first discuss the relevant parameters of the model and their relations to the masses and couplings of the states involved, and then look for suitable parameter choices that can make an impact on the search channel, at the same time ensuring that all constraints, including those from the flavour sector are satisfied. We also demonstrate that in suitably chosen parameter space regions, it is possible to have other decay channels open up, resulting in a

[1]Unlike the discovery of a Z' which can indicate the presence of any variety of additional $U(1)'$ groups.

reduction of the branching ratio to the collider signal channel.

Our work is organized as follows: In Section 6.2, we briefly describe the left-right symmetric model with an emphasis on the gauge sector. After we summarize the experimental mass bounds on W_R, ν_R and doubly charged Higgs bosons in Section 6.3, we explain the model implementation and the experimental constraints employed in our analysis in Section 7.3. We analyze two separate cases, $M_{W_R} < M_{\nu_R}$, $M_{W_R} > M_{\nu_R}$, and then present our results on $W_R - \nu_R$ mass exclusion limits in Section 6.5.

6.2 The Left-Right Symmetric Model

The framework of the model is based on the gauge group $SU(3)_c \otimes SU(2)_L \otimes SU(2)_R \otimes U(1)_{B-L}$. We extend the Standard Model gauge symmetry, first by introducing the $SU(2)_R$ symmetry, then by gauging the $B-L$ quantum number. Both left- and right-handed fermions are doublets under the extended $SU(3)_c \otimes SU(2)_L \otimes SU(2)_R \otimes U(1)_{B-L}$ gauge group. The quantum numbers of the particles under $SU(2)_L \otimes SU(2)_R \otimes U(1)_{B-L}$ are:

$$L_{Li} = \begin{pmatrix} \nu_L \\ \ell_L \end{pmatrix}_i \sim (\mathbf{2}, \mathbf{1}, -\mathbf{1}), \quad L_{Ri} = \begin{pmatrix} \nu_R \\ \ell_R \end{pmatrix}_i \sim (\mathbf{1}, \mathbf{2}, -\mathbf{1}), \qquad \text{for the leptons, and} \tag{6.1}$$

$$Q_{Li} = \begin{pmatrix} u_L \\ d_L \end{pmatrix}_i \sim (\mathbf{2}, \mathbf{1}, \mathbf{1/3}), \quad Q_{Ri} = \begin{pmatrix} u_R \\ d_R \end{pmatrix}_i \sim (\mathbf{1}, \mathbf{2}, \mathbf{1/3}), \qquad \text{for the quarks,} \tag{6.2}$$

where $i = 1, 2, 3$ are generation indices. The subscripts L and R are associated with the projection operators $P_{L,R} = \frac{1}{2}(1 \mp \gamma_5)$. The electroweak symmetry is broken by the bi-doublet Higgs field

$$\Phi \equiv \begin{pmatrix} \phi_1^0 & \phi_2^+ \\ \phi_1^- & \phi_2^0 \end{pmatrix} \sim (\mathbf{2}, \mathbf{2}, \mathbf{0}). \tag{6.3}$$

In addition, to break the $SU(2)_R \otimes U(1)_{B-L}$ gauge symmetry and to provide Majorana mass terms for neutrinos (the right-handed neutrino is automatically included in the right-handed

lepton doublet), we introduce the Higgs triplets

$$\Delta_L \equiv \begin{pmatrix} \delta_L^+/\sqrt{2} & \delta_L^{++} \\ \delta_L^0 & -\delta_L^+/\sqrt{2} \end{pmatrix} \sim (\mathbf{3},\mathbf{1},\mathbf{2})\,, \quad \Delta_R \equiv \begin{pmatrix} \delta_R^+/\sqrt{2} & \delta_R^{++} \\ \delta_R^0 & -\delta_R^+/\sqrt{2} \end{pmatrix} \sim (\mathbf{1},\mathbf{3},\mathbf{2})\,. \tag{6.4}$$

While only Δ_R is needed for symmetry breaking, Δ_L is included to preserve left-right symmetry. After symmetry breaking, the most general vacuum is

$$\langle\Phi\rangle = \begin{pmatrix} \kappa_1/\sqrt{2} & 0 \\ 0 & \kappa_2 e^{i\alpha}/\sqrt{2} \end{pmatrix}, \quad \langle\Delta_L\rangle = \begin{pmatrix} 0 & 0 \\ v_L e^{i\theta_L}/\sqrt{2} & 0 \end{pmatrix}, \quad \langle\Delta_R\rangle = \begin{pmatrix} 0 & 0 \\ v_R/\sqrt{2} & 0 \end{pmatrix}. \tag{6.5}$$

We define the ratio $\tan\beta = \dfrac{\kappa_1}{\kappa_2}$. The Lagrangian density for this model contains kinetic, Yukawa terms and potential terms:

$$\mathcal{L}_{\rm LRSM} = \mathcal{L}_{\rm kin} + \mathcal{L}_Y - V(\Phi,\Delta_L,\Delta_R)\,. \tag{6.6}$$

The kinetic term is

$$\begin{aligned} L_{\rm kin} &= i\sum \bar\psi\gamma^\mu D_\mu\psi = \bar L_L\gamma^\mu\left(i\partial_\mu + g_L\frac{\vec\tau}{2}\cdot\vec W_{L\mu} - \frac{g_{B-L}}{2}B_\mu\right)L_L \\ &+ \bar L_R\gamma^\mu\left(i\partial_\mu + g_R\frac{\vec\tau}{2}\cdot\vec W_{R\mu} - \frac{g_{B-L}}{2}B_\mu\right)L_R \\ &+ \bar Q_L\gamma^\mu\left(i\partial_\mu + g_L\frac{\vec\tau}{2}\cdot\vec W_{L\mu} + \frac{g_{B-L}}{6}B_\mu\right)Q_L \\ &+ \bar Q_R\gamma^\mu\left(i\partial_\mu + g_R\frac{\vec\tau}{2}\cdot\vec W_{R\mu} + \frac{g_{B-L}}{6}B_\mu\right)Q_R\,, \end{aligned} \tag{6.7}$$

where we introduce the gauge fields, $\vec W_{L,R}$ and B corresponding to $SU(2)_{L,R}$ and $U(1)_{B-L}$. The next term in the Eq. (6.6) is the Yukawa interaction for quarks and leptons

$$\begin{aligned} \mathcal{L}_Y &= -\Big[Y_{L_L}\bar L_L\Phi L_R + \tilde Y_{L_R}\bar L_R\Phi L_L + Y_{Q_L}\bar Q_L\tilde\Phi Q_R + \tilde Y_{Q_R}\bar Q_R\tilde\Phi Q_L + h_L^{ij}\overline{L}^c_{L_i}i\tau_2\Delta_L L_{L_j} \\ &+ h_R^{ij}\overline{L}^c_{R_i}i\tau_2\Delta_R L_{R_j} + \text{h.c.}\Big]\,, \end{aligned} \tag{6.8}$$

where for leptons $Y_{L_{L,R}}$, $\tilde Y_{L_{L,R}}$ and for quarks $Y_{Q_{L,R}}$, $\tilde Y_{Q_{L,R}}$ are 3×3 diagonal complex matrices, h_L^{ij} and h_R^{ij} are 3×3 complex symmetric Yukawa matrices and $\tilde\Phi = \tau_2\Phi^\star\tau_2$. Finally, the last term in the Lagrangian in Eq. (6.6) is the scalar potential for the bidoublet Φ and triplet

$\Delta_{L,R}$ Higgs fields, and is given by

$$
\begin{aligned}
V(\phi,\Delta_L,\Delta_R) &= -\mu_1^2\left(\mathrm{Tr}\left[\Phi^\dagger\Phi\right]\right)-\mu_2^2\left(\mathrm{Tr}\left[\tilde{\Phi}\Phi^\dagger\right]+\left(\mathrm{Tr}\left[\tilde{\Phi}^\dagger\Phi\right]\right)\right)\\
&- \mu_3^2\left(\mathrm{Tr}\left[\Delta_L\Delta_L^\dagger\right]+\mathrm{Tr}\left[\Delta_R\Delta_R^\dagger\right]\right)+\lambda_1\left(\left(\mathrm{Tr}\left[\Phi\Phi^\dagger\right]\right)^2\right)\\
&+ \lambda_2\left(\left(\mathrm{Tr}\left[\tilde{\Phi}\Phi^\dagger\right]\right)^2+\left(\mathrm{Tr}\left[\tilde{\Phi}^\dagger\Phi\right]\right)^2\right)+\lambda_3\left(\mathrm{Tr}\left[\tilde{\Phi}\Phi^\dagger\right]\mathrm{Tr}\left[\tilde{\Phi}^\dagger\Phi\right]\right)\\
&+ \lambda_4\left(\mathrm{Tr}\left[\Phi\Phi^\dagger\right]\left(\mathrm{Tr}\left[\tilde{\Phi}\Phi^\dagger\right]+\mathrm{Tr}\left[\tilde{\Phi}^\dagger\Phi\right]\right)\right)\\
&+ \rho_1\left(\left(\mathrm{Tr}\left[\Delta_L\Delta_L^\dagger\right]\right)^2+\left(\mathrm{Tr}\left[\Delta_R\Delta_R^\dagger\right]\right)^2\right)\\
&+ \rho_2\left(\mathrm{Tr}\left[\Delta_L\Delta_L\right]\mathrm{Tr}\left[\Delta_L^\dagger\Delta_L^\dagger\right]+\mathrm{Tr}\left[\Delta_R\Delta_R\right]\mathrm{Tr}\left[\Delta_R^\dagger\Delta_R^\dagger\right]\right)\\
&+ \rho_3\left(\mathrm{Tr}\left[\Delta_L\Delta_L^\dagger\right]\mathrm{Tr}\left[\Delta_R\Delta_R^\dagger\right]\right)\\
&+ \rho_4\left(\mathrm{Tr}\left[\Delta_L\Delta_L\right]\mathrm{Tr}\left[\Delta_R^\dagger\Delta_R^\dagger\right]+\mathrm{Tr}\left[\Delta_L^\dagger\Delta_L^\dagger\right]\mathrm{Tr}\left[\Delta_R\Delta_R\right]\right)\\
&+ \alpha_1\mathrm{Tr}\left[\Phi\Phi^\dagger\right]\left(\mathrm{Tr}\left[\Delta_L\Delta_L^\dagger\right]+\mathrm{Tr}\left[\Delta_R\Delta_R^\dagger\right]\right)\\
&+ \alpha_2\left(\mathrm{Tr}\left[\Phi\tilde{\Phi}^\dagger\right]\mathrm{Tr}\left[\Delta_R\Delta_R^\dagger\right]+\mathrm{Tr}\left[\Phi^\dagger\tilde{\Phi}\right]\mathrm{Tr}\left[\Delta_L\Delta_L^\dagger\right]\right)\\
&+ \alpha_2^*\left(\mathrm{Tr}\left[\Phi^\dagger\tilde{\Phi}\right]\mathrm{Tr}\left[\Delta_R\Delta_R^\dagger\right]+\mathrm{Tr}\left[\tilde{\Phi}^\dagger\Phi\right]\mathrm{Tr}\left[\Delta_L\Delta_L^\dagger\right]\right)\\
&+ \alpha_3\left(\mathrm{Tr}\left[\Phi\Phi^\dagger\Delta_L\Delta_L^\dagger\right]+\mathrm{Tr}\left[\Phi^\dagger\Phi\Delta_R\Delta_R^\dagger\right]\right)\\
&+ \beta_1\left(\mathrm{Tr}\left[\Phi\Delta_R\Phi^\dagger\Delta_L^\dagger\right]+\mathrm{Tr}\left[\Phi^\dagger\Delta_L\Phi\Delta_R^\dagger\right]\right)\\
&+ \beta_2\left(\mathrm{Tr}\left[\tilde{\Phi}\Delta_R\Phi^\dagger\Delta_L^\dagger\right]+\mathrm{Tr}\left[\tilde{\Phi}^\dagger\Delta_L\Phi\Delta_R^\dagger\right]\right)\\
&+ \beta_3\left(\mathrm{Tr}\left[\Phi\Delta_R\tilde{\Phi}^\dagger\Delta_L^\dagger\right]+\mathrm{Tr}\left[\Phi^\dagger\Delta_L\tilde{\Phi}\Delta_R^\dagger\right]\right), \qquad (6.9)
\end{aligned}
$$

where we include the complex parameters explicitly.

The $SU(2)_R$, $SU(2)_L$ and $U(1)_{B-L}$ gauge couplings in Eq. (6.7) are denoted by g_R, g_L and g_{B-L}. For the LRSM model to break down to the SM, the hierarchy of the vacuum expectation values (VEVs) must be, $v_R \gg (\kappa_1,\ \kappa_2) \gg v_L$, and $\sqrt{\kappa_1^2+\kappa_2^2} = v = 246$ GeV. Here the presence of non-zero VEV of Δ_R, v_R breaks the $SU(2)_R \otimes U(1)_{B-L}$ to $U(1)_Y$, while the presence of bi-doublet VEVs κ_1 and κ_2 break the electroweak symmetry, at the same time inducing a VEV for Δ_L denoted by v_L. The third component of the $SU(2)_R$ gauge boson and the gauge boson corresponding to $U(1)_{B-L}$ mix to give the mass eigenstate Z_R and the

gauge boson corresponding to the $U(1)_Y$, B^μ. Denoting the mixing angle as ϕ,

$$\begin{pmatrix} Z_R^\mu \\ B^\mu \end{pmatrix} = \begin{pmatrix} \cos\phi & -\sin\phi \\ \sin\phi & \cos\phi \end{pmatrix} \begin{pmatrix} W_R^{3\mu} \\ V^\mu \end{pmatrix} \tag{6.10}$$

Denoting the weak mixing angle as θ_W, the three neutral gauge bosons further mix to give the mass eigenstates Z_L^μ, Z_R^μ and the photon, A^μ:

$$\begin{pmatrix} Z_L^\mu \\ B^\mu \\ Z_R^\mu \end{pmatrix} = \begin{pmatrix} \cos\theta_W & -\sin\theta_W\sin\phi & -\sin\theta_W\cos\phi \\ \sin\theta_W & \cos\theta_W\sin\phi & \cos\theta_W\cos\phi \\ 0 & \cos\phi & -\sin\phi \end{pmatrix} \begin{pmatrix} W_L^{3\mu} \\ W_R^{3\mu} \\ V^\mu \end{pmatrix} \tag{6.11}$$

yielding

$$\begin{aligned} M_A &= 0 \\ M^2_{Z_{1,2}} &= \frac{1}{4}\Big[\left[g_L^2 v^2 + 2v_R^2(g_R^2 + g_{B-L}^2)\right] \\ &\mp \sqrt{\left[g_L^2 v^2 + 2v_R^2(g_R^2 + g_{B-L}^2)\right]^2 - 4g_L^2(g_R^2 + 2g_{B-L}^2)v^2 v_R^2}\Big] . \end{aligned} \tag{6.12}$$

In the charged sector, the left and right gauge bosons mix to give the mass eigenstates, W_1 and W_2;

$$\begin{pmatrix} W_1 \\ W_2 \end{pmatrix} = \begin{pmatrix} \cos\xi & -\sin\xi \\ \sin\xi & \cos\xi \end{pmatrix} \begin{pmatrix} W_L \\ W_R \end{pmatrix} , \tag{6.13}$$

where the mixing angle ξ and the mass eigenvalues are given by

$$\tan 2\xi = \frac{4g_R g_L \kappa_1\kappa_2}{2g_R^2 v_R^2 + (g_R^2 - g_L^2)v^2} \approx \frac{2g_L\kappa_1\kappa_2}{g_R v_R^2} \tag{6.14}$$

$$\begin{aligned} M^2_{W_1} &= \frac{1}{4}\left[g_L^2 v^2\cos^2\xi + g_R^2(2v_R^2 + v^2)\sin^2\xi - 2g_R g_L\kappa_1\kappa_2\cos\xi\sin\xi\right] \\ M^2_{W_2} &= \frac{1}{4}\left[g_L^2 v^2\sin^2\xi + g_R^2(2v_R^2 + v^2)\cos^2\xi + 2g_R g_L\kappa_1\kappa_2\cos\xi\sin\xi\right] . \end{aligned} \tag{6.15}$$

In the limit of $(\kappa_1, \kappa_2) \ll v_R$ and $g_R \sim g_L$ we have $\sin\xi \approx \frac{\kappa_1\kappa_2}{v_R^2}$, $\sin^2\xi \approx 0$, $\cos\xi \approx 1$, leading to

$$M^2_{W_1} = \frac{1}{4}g_L^2 v^2 , \qquad M^2_{W_2} = \frac{1}{4}\left[2g_R^2 v_R^2 + g_R^2 v^2 + 2g_R g_L \frac{\kappa_1^2\kappa_2^2}{v_R^2}\right] . \tag{6.16}$$

The $SU(2)_R$ breaking scale v_R, and mixing angle ξ are restricted from low energy observables,

such as $K_L - K_S$, ϵ_K, $B^0 - \bar{B}^0$ mixings and $b \to s\gamma$ processes, which constrain the right scale through the charged right handed W_R boson mass as well as the triplet Higgs masses. Taking into account the smallness of the mixing angle ξ, in what follows we shall refer to W_1 as W_L and W_2 as W_R, as to be able to compare with experimental results and nomenclature[2].

6.3 Mass Bounds on right-handed gauge, Higgs bosons, and neutrinos from colliders

The choice of the parameter space of the model would affect masses in the right-handed sector, and thus below, we summarize collider limits imposed on these.

6.3.1 Right-handed charged gauge boson

The W_R boson can decay into jets and, if the $SU(2)_{\rm R}$ gauge coupling equals the $SU(2)_L$ one ($g_L = g_R$), limits on sequential W' bosons can be reinterpreted straightforwardly. ATLAS and CMS have obtained bounds of 3.6 TeV [18] and 3.3 TeV [154], on such a sequential extra gauge boson, respectively. LHC has analyzed possible signatures of the additional gauge bosons in LRSM, which for the charged gauge boson translate into three main search channels, (i) $W_R \to t\bar{b}$ [20, 247], (ii) $W_R \to 2j$ [18] and (iii) $W_R \to \ell\nu_R \to \ell\ell W_R^* \to 2\ell 2j$ [22], the third one being relevant only in the kinematic regions with $M_{\nu_R} < M_{W_R}$. The Majorana nature of the right-handed neutrino allows for probing both the same-sign and opposite-sign dilepton channels [248]. Both ATLAS and CMS, in their latest analyses with 37 fb^{-1} and 35.9 fb^{-1} luminosities, respectively, at $\sqrt{s} = 13$ TeV, have provided stringent limits on M_{W_R}, in the 3.5-4.4 TeV region. CMS [249] considered both scenarios of (i) $M_{\nu_R} \geq M_{W_R}$ and (ii) $M_{\nu_R} < M_{W_R}$, where in the second case, in addition to the hadronic decay, W_R can decay to $\nu_R\ell$. The branching fraction of $W_R \to t\bar{b}$ is quoted as (0.32 - 0.33) in the first scenario and (0.24 - 0.25) in the second scenario, for a W_R mass range of 500 GeV to 5 TeV, where the 1% difference is due the phase space effects coming from the top quark mass (as compared to the vanishing light quark mass). The ATLAS analysis [21] also considered both scenarios. However, they searched for W_R gauge bosons in final states with two charged leptons and two jets. Both CMS and ATLAS assumed strict LR symmetry setting $g_R = g_L$ and $V_{\rm CKM}^L = V_{\rm CKM}^R$ in their analyses.

[2]Note however that they both contain a non-zero left and right $SU(2)$ gauge component.

6.3.2 Doubly-charged Higgs bosons

Mass bounds on the doubly-charged Higgs bosons must satisfy consistency with the various LHC limits. The restrictions on the mass of the left-handed doubly charged Higgs boson δ_L^{++} are considerably weakened as these can decay into both same sign lepton pairs and same sign W_L pairs. The latter decay mode is not available to the right-handed doubly-charged Higgs boson δ_R^{++}, so the restrictions coming from the doubly-charged Higgs bosons decaying into two same-sign leptons, which are very strong, apply. The exception is the case in which the doubly-charged Higgs boson decays into a di-tau final-state [250, 251]. Without any significant excess of events, the LHC analyses mentioned presently provide stringent constraints from direct searches, which require the masses of the doubly charged scalars to be above ~ 600 GeV (~ 500 GeV for decays into di-taus only).

Not all constraints coming from (first and second family) dilepton decays can be evaded, as the right-handed triplet Higgs field are needed to generate masses for the right-handed neutrinos. In our scenario, W_R production and decays are not affected by the doubly-charged triplet Higgs bosons, and thus the latter can be heavy, $\mathcal{O}(v_R)$.

6.3.3 Right-handed neutrinos

Generic searches for right-handed neutrinos were performed at LEP [252], leading to bounds on right-handed Majorana neutrino masses of at most 90.7 GeV. In our model the right-handed neutrino mass matrix reads

$$M_{\nu_R}^{ij} = h_R^{ij} v_R \ , \tag{6.17}$$

where h_R^{ij} also dictates the different doubly-charged Higgs branching ratios. If we enforce that the $SU(2)_R$ doubly-charged Higgs boson decays mainly into taus, the right-handed tau neutrino turns out to be significantly heavier than the others. The mass of right-handed neutrinos are determined by the choices of v_R and h_R and can be chosen to be either $M_{\nu_R} \geq M_{W_R}$ or $M_{\nu_R} \leq M_{W_R}$, for the two scenarios that we investigate. We now proceed to analyze the parameter space of the model, and subject it to constraints from phenomenology.

6.4 Model Implementation and Constraints

In most analyses, W_R bosons are expected to be heavy. However all of the analyses assume that the model is manifestly left-right symmetric, that is, the coupling constants are the same for the left and right gauge sectors, $g_L = g_R$ *and* that the quark mass mixing in the right-handed sector V^R_{CKM} is either diagonal, or equal to the one in the left-handed sector (the Cabibbo-Kobayashi-Maskawa matrix, V^L_{CKM}). This does not have to be the case, and analyses of a more general model, the so-called asymmetric left-right model exist [243, 245].

We take this general approach here. We calculate the production cross section and decays of the W_R bosons in the LRSM with $g_L \neq g_R$ and allowing for general entries in the mixing matrix for the right-handed quarks, V^R_{CKM}, parametrized as the left-handed matrix, but allowing the elements to vary independently:

$$V^R_{\rm CKM} = \begin{bmatrix} c^R_{12}c^R_{13} & s^R_{12}c^R_{13} & s^R_{13}e^{i\delta_R} \\ -s^R_{12}c^R_{23} - c^R_{12}s^R_{23}s_{13}e^{i\delta_R} & c^R_{12}c^R_{23} - s^R_{12}s^R_{23}s^R_{13}e^{i\delta_R} & s^R_{23}c^R_{13} \\ s^R_{12}s^R_{23} - c^R_{12}c^R_{23}s^R_{13}e^{i\delta_R} & -c^R_{12}c^R_{23} - s^R_{12}c^R_{23}s^R_{13}e^{i\delta_R} & c^R_{23}c^R_{13} \end{bmatrix} \tag{6.18}$$

We then proceed as follows.

- We first choose one value for M_{W_R}. Then we vary the parameters c^R_{12}, c^R_{13} and c^R_{23} in the range $[-1, 1]$. The phase δ_R is set to zero (as we are not concerned with CP violation), and we impose matrix unitary condition. For each set of the randomly chosen V^R_{CKM} parameters as above, we impose the theoretical and experimental constraints including the mass bounds and flavor constraints from K and B mesons, as listed in Table 6.1. This ensures, for instance, that the non-SM neutral bidoublet Higgs boson is very heavy (> 10 TeV), as required to suppress flavor-violating effects.

- For each value of M_{W_R} we obtain many solutions for V^R_{CKM} consistent with all bounds. Of these solutions, we choose the one yielding the smallest branching ratio for $W_R \to t\bar{b}$ [3].

- Noting that the flavor bounds are very sensitive to these elements, we fit them carefully for each solution. The V^R_{CKM} elements thus obtained are restricted to a viable ranges of values. We distinguish between two possibilities: one when the W_R mass is lighter than that of the right-handed neutrinos ν_R, and the case where the right-handed neutrino

[3] We have also tried to minimize $BR(W_R \to jj)$ but found that this choice yields a more restrictive lower mass bound for W_R.

Observable	Constraints	Ref.	Observable	Constraints	Ref.
ΔB_s	[10.2-26.4]	[253]	ΔB_d	[0.294-0.762]	[253]
ΔM_K	$< 5.00 \times 10^{-15}$	[254]	$\frac{\Delta M_K}{\Delta M_K^{SM}}$	[0.7-1.3]	[254]
ϵ_K	$< 3.00 \times 10^{-3}$	[254]	$\frac{\epsilon_K}{\epsilon_K^{SM}}$	[0.7-1.3]	[254]
$\mathrm{BR}(B^0 \to X_s\gamma)$	$[2.99, 3.87] \times 10^{-4}$	[90]	$\frac{BR(B^0 \to X_s\gamma)}{BR(B^0 \to X_s\gamma)_{SM}}$	[0.7-1.3]	[90]
M_h	[124, 126] GeV	[29]	$M_{H^{\pm\pm}_{1,2}}$	> 535 GeV	[255, 256]
$M_{H_4, A_2, H_2^{\pm}}$	$> 4.75 \times M_{W_R}$	[257]			-

Table 6.1: Current experimental bounds imposed for consistent solutions.

is lighter. In the second case, the right-handed gauge boson can decay also into $\nu_R \ell$, modifying its branching ratio to top and bottom quarks. For the case of $M_{\nu_R} < M_{W_R}$, these ranges of elements in the right-handed CKM matrix are

$$V^R_{\mathrm{CKM}} = \begin{bmatrix} [3.63 \times 10^{-3} - 0.736] & [0.650 - 0.999] & [3.18 \times 10^{-2} - 0.754] \\ [0.671 - 0.999] & [1.93 \times 10^{-3} - 0.550] & [2.24 \times 10^{-2} - 0.501] \\ [2.05 \times 10^{-4} - 0.439] & [3.01 \times 10^{-2} - 0.619] & [0.781 - 0.996] \end{bmatrix}, \tag{6.19}$$

while in case of $M_{\nu_R} > M_{W_R}$ the ranges of elements in the right-handed CKM matrix are:

$$V^R_{\mathrm{CKM}} = \begin{bmatrix} [1.28 \times 10^{-3} - 9.91 \times 10^{-2}] & [0.858 - 0.996] & [5.25 \times 10^{-2} - 0.504] \\ [0.805 - 0.997] & [8.68 \times 10^{-5} - 5.22 \times 10^{-2}] & [4.16 \times 10^{-4} - 0.585] \\ [9.30 \times 10^{-3} - 0.589] & [2.62 \times 10^{-2} - 0.511] & [0.807 - 0.998] \end{bmatrix}. \tag{6.20}$$

- When $M_{\nu_R} > M_{W_R}$, solutions emerge allowing for low values of $BR(W_R \to t\bar{b})$, which vary from about 23.3% for high M_{W_R}, to about 29% for low M_{W_R}, while when $M_{\nu_R} < M_{W_R}$, this ratio changes from 15.7% for high M_{W_R}, to about 24.7% for low M_{W_R} .

For this analysis, a version of an LRSM model produced with SARAH 4.13.0 [78, 79, 141] was implemented in SPHENO 4.0.3 package [76, 77]. We use HiggsBounds [94] and HiggsSignals [95] to test out the signal strengths of the SM-like Higgs state and check the consistency of the Higgs sector for each solution. The relevant cross sections were

Parameter	Scanned range	Parameter	Scanned range
v_R	[2.2, 20] TeV	diag(h_R^{ij})	[0.001, 1]
$V_{\rm CKM}^R$: c_{12}^R, c_{13}^R, c_{23}^R	[−1, 1]		

Table 6.2: Scanned parameter space.

calculated by MG5_aMC@NLO v2.6.3.2 [112, 258] using the NNPDF2.3 [224] parton distribution function (PDF) set. In order to get cross sections at the next-to-leading order (NLO) accuracy, a version of an LRSM model was produced with FeynRules [259]. An UFO [111] file obtained from FeynRules is implemented in MG5_aMC@NLO [260] and then used for the numerical evaluation of the hard-scattering matrix elements. We use pySLHA 3.2.2 package [145] for manipulating SUSY Les Houches Accord (SLHA) files during the numerical analysis performed in this work.

We performed random scans over the parameter space, as illustrated in Table 7.2, and imposed the mass bounds on all the particles, as well as other constraints as given in Table 6.1. In scanning the parameter space, we used the interface which employs the Metropolis-Hasting algorithm. In what follows, we shall distinguish between two cases, Scenario I, $M_{\nu_R} > M_{W_R}$, and Scenario II, $M_{\nu_R} < M_{W_R}$.

6.5 $M_{\rm W_R}$ Mass Bounds: the analysis

In a general left-right model, the masses of the Z_R and W_R gauge bosons are related, but the mass ratios depend sensitively on the values of the coupling constants g_R and g_{B-L}. While the mass of W_R is proportional to g_R, the mass of the Z_R boson is proportional to $\sqrt{g_R^2 + g_{B-L}^2}$. Breaking the symmetry to $U(1)_{\rm em}$ imposes that couplings constants are related through

$$\frac{1}{e^2} = \frac{1}{g_L^2} + \frac{1}{g_R^2} + \frac{1}{g_{B-L}^2}\,, \tag{6.21}$$

and therefore decreasing g_R results in increasing g_{B-L}. Note also that these couplings are related, through $SU(2)_R \otimes U(1)_{B-L} \to U(1)_Y$ symmetry breaking to the coupling of the hypercharge group, g_Y, through

$$\frac{1}{g_Y^2} = \frac{1}{g_R^2} + \frac{1}{g_{B-L}^2}\,. \tag{6.22}$$

This means that, setting $\sin\phi = \dfrac{g_{B-L}}{\sqrt{g_R^2 + g_{B-L}^2}}$, and with the usual definition of $\sin\theta_W = \dfrac{g_Y}{\sqrt{g_L^2 + g_Y^2}}$, we obtain

$$\tan\theta_W = \frac{g_R \sin\phi}{g_L} \leq \frac{g_R}{g_L}\,, \tag{6.23}$$

showing clearly that we cannot lower g_R below its minimum value, $g_L \tan\theta_W$. Lowering g_R will decrease the production cross section for W_R, while having no effect on its branching ratios. We analyze the case where $g_R = g_L$, as well as when $g_L \neq g_R = 0.37$, its allowed minimal value.

In the top left panel of Fig. 6.1 we plot the relationship between the two gauge boson masses, W_R and Z_R, for the two cases ($g_R = g_L$ and $g_L \neq g_R = 0.37$). As seen from the figure, the Z_R mass is much closer to W_R mass when $g_R = g_L$, and in that case the Z_R mass bounds (especially coming from production, followed by decays into dileptons) may have an effect on the W_R mass bounds. While for $g_L \neq g_R = 0.37$, Z_R is expected to be much heavier than W_R, making the latter more likely to be much lighter and more likely to be the first observed.

6.5.1 Scenario I: $M_{\nu_R} > M_{W_R}$

We now proceed to investigate the case where the right handed neutrino is heavier than W_R, (so the on-shell decay $W_R \to \nu_R \ell$ is disallowed) and where the possible decay channels for W_R are:

$$W_R \to jj(q\bar{q}'),\ W_R \to W_L h,\ W_R \to W_L Z \text{ and } W_R \to W_L hh\,,$$

all the other Higgs states being very heavy. Of these, the three-body decay $W_L hh$ is very weak with $\frac{\Gamma(W_R \to W_L h)}{\Gamma(W_R \to W_L hh)} \sim 1/v$, while the decay $W_R \to W_L h$ depends on $\tan\beta$. Most analyses assume $\tan\beta$ to be very small (~ 0.01), yielding $BR(W_R \to W_L h)$ to be negligible. Perturbativity bounds alone require $\tan\beta < 0.8$, however the mass of the SM-like Higgs boson h also depends on $\tan\beta$, and values of $\tan\beta > 0.6$ result in the instability of the h mass. To keep our analysis general, we investigated the production and decays of the W_R mass for two cases: small $\tan\beta = 0.01$, and large $\tan\beta = 0.5$. In addition, we allow for two values of g_R, viz. $g_R = g_L$, and $g_L \neq g_R = 0.37$, as well as vary matrix elements of $V^R_{\rm CKM}$ to show how the results are affected. The resulting plots for $\sigma(pp \to W_R) \times BR(W_R \to t\bar{b})$ are given in the top right plane of Fig. 6.1, where we compare our four different cases (different colour-coded,

as indicated in the panel insertion) with the CMS result [249] using collision data collected at $\sqrt{s}$ =13 TeV with $\mathcal{L}$=35.9 fb^{-1}. We show the observed and expected limit curves for the combined electron and muon final states. For $g_L = g_R$, $V^L_{\rm CKM} = V^R_{\rm CKM}$ and $\tan\beta = 0.01$, we note that the branching ratio W_R into $t\bar{b}$ ranges from 32% to 33%, as W_R decays into $q\bar{q}'$ pairs democratically. We confirm the CMS result [249] and exclude W_R boson mass up to 3.6 TeV. For the case where $g_R \neq g_L$ and $V^L_{\rm CKM} = V^R_{\rm CKM}$, represented by the blue line, we set $g_R \simeq 0.37$ and $\tan\beta = 0.01$. The W_R production cross section decreases due to relatively small g_R, and the exclusion limit for W_R masses can be reduced to 2.7 TeV in that scenario. Increasing $\tan\beta$ to 0.5 and $g_R \simeq 0.37$, enhances the branching ratios of $W_R \to W_L h$ to about $\sim 1.95\%$ and the branching ratio of $W_R \to W_L Z_L$ to about $\sim 2.0\%$. In this case, the branching ratio of $W_R \to t\bar{b}$ is reduced slightly, to 31.0% - 31.8%, as shown by the pink line. As can be read from the plot, this reduces the W_R mass limits only slightly, to 2675 GeV. However, when we allow $V^L_{\rm CKM} \neq V^R_{\rm CKM}$, $\tan\beta$= 0.5 and $g_R \simeq 0.37$, this maximizes decays of W_R into other final states, and the branching ratio of $W_R \to t\bar{b}$ is reduced substantially: from about 20% for high M_{W_R} (4 TeV) to about 29% for low M_{W_R} (1.5 TeV). The orange line in the top right plane of Fig. 6.1 represents our result for this scenario, and the exclusion limit is reduced to 2360 GeV with respect to observed limit, whereas it can be estimated at 1940 GeV based on the expected limit.

In the left bottom panel of Fig. 6.1 we plot the cross section of $pp \to W_R \to jj$ vs W_R mass, and compare it to the ATLAS result [18] at $\sqrt{s}$ =13 TeV for $\mathcal{L}$=37 fb^{-1}. (For comparison, we included their acceptance factor A). The red curve represents the exclusion limit for W_R mass when the gauge couplings $g_L = g_R$, and $\tan\beta = 0.01$. The branching fraction of $W_R \to jj$ varies slightly with mass. We keep the same color coding for curves as in the previous panel. The mass restrictions are comparable, but slightly weaker than those for the $W_R \to t\bar{b}$ decay, ranging from $M_{W_R} \geq 3625$ GeV when $g_L = g_R$, $\tan\beta = 0.01$ and $V^R_{\rm CKM} = V^L_{\rm CKM}$, to $M_{W_R} \geq 2.0$ TeV when $g_R = 0.37$, $\tan\beta = 0.5$ and $V^R_{\rm CKM} \neq V^L_{\rm CKM}$. Neither results are particularly sensitive to values of $\tan\beta$, but depend on choices for g_R and $V^R_{\rm CKM}$.

The right bottom plane of Fig. 6.1 represents comparison with the CMS result [19] which searches for decay $W_R \to W_L Z$ in the $\nu\nu q\bar{q}'$ final state using the pp collision data collected at $\sqrt{s}$ =13 TeV at $\mathcal{L}$=35.9 fb^{-1}. Since the branching ratio of $W_R \to W_L Z$ is negligible ($< 10^{-4}$) for small $\tan\beta$ values, we show our result in this channel only for large $\tan\beta$ values (i.e. $\tan\beta = 0.5$), when the branching ratio of $W_R \to W_L Z$ is at about 2 %. As seen from the graph, our curves are always below the experimental curves and thus W_R

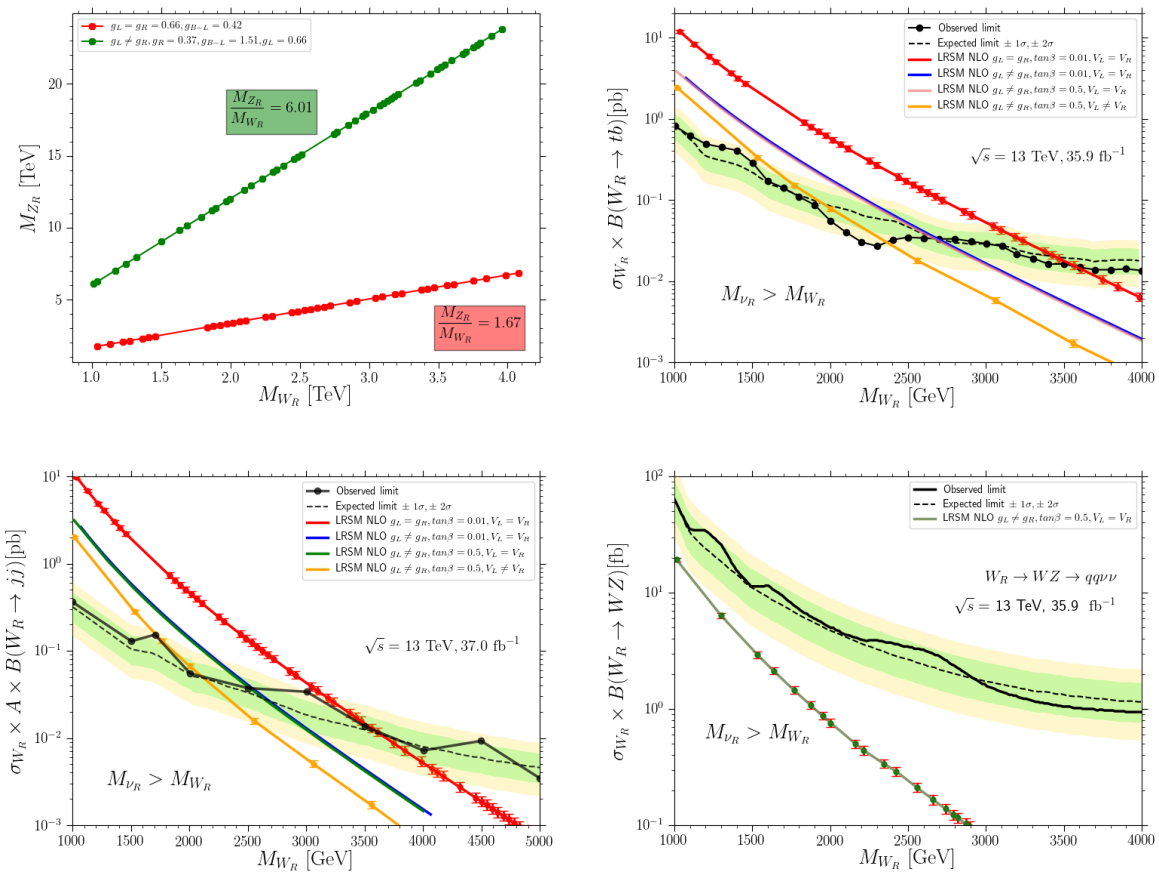

Figure 6.1: (Top left): The comparison of W_R and Z_R masses for $g_L = g_R$ and $g_L \neq g_R = 0.36$; (top right) The cross section of $W_R \to tb$ vs W_R mass for different values of $\tan\beta$ and g_R; (bottom left) The cross section of $W_R \to jj$ vs W_R mass, for different values of $\tan\beta$ and g_R, compared to ATLAS data [18]; (bottom right) The cross section of $W_R \to W_L Z$ vs W_R mass, where the experimental data shown for comparison is from CMS [19]. The last three plots are for the case when $M_{\nu_R} > M_{W_R}$.

masses cannot be excluded using the $W_R \to W_L Z \to q\bar{q}'\nu\nu$ channel.

6.5.2 Scenario II: $M_{\nu_R} < M_{W_R}$

The case where the W_R is heavier than the right-handed neutrino opens the possibility of $W_R \to \nu_R \ell$, followed by decay of $\nu_R \to \ell W_R^* \to \ell jj$ giving rise to an $\ell\ell jj$ signature. The Majorana nature of the right-handed neutrino allows for probing both the same-sign and opposite-sign dilepton channels [248]. Both the ATLAS [21] and CMS [22] collaborations have looked for such a W_R signal, excluding W_R masses up to about 4.7 TeV for right-handed (muon or electron) neutrino masses up to 3.1 TeV [22]. For lower right-handed neutrino masses (below 200 GeV), the bound is less restrictive than the one originating from dijet searches. For the tau channel, it is even much weaker, with M_{W_R} constrained to be only smaller than 2.9 TeV [261].

In Fig. 6.3, we plot our results and compare it with the current experimental results. Throughout our analysis we assign one right-handed neutrino mass to be half of the mass of W_R, for comparison with the experimental analysis. (The results obtained though are typical for large gaps between ν_R, W_R masses.) The top left plane of Fig. 6.3 shows the exclusion based on $W_R \to t\bar{b}$ channel. The red line shows the result for $g_L = g_R$, $\tan\beta = 0.01$ and $V^L_{\rm CKM} = V^R_{\rm CKM}$. In addition to the decays into hadrons, W_R also decays into $\nu_R\ell$, about 5.8% for each lepton flavor. We note that the branching ratio of W_R into $t\bar{b}$ ranges from 26.5% to 27.3%. We confirmed the CMS result [249] and find out that the observed (expected) 95% confidence level (CL) lower limit for W_R mass bounds is 3450 (3320) GeV. We also study the effect of $g_R \neq g_L$ by setting $g_R \simeq 0.37$ and $\tan\beta = 0.01$. In this scenario the leptonic decay rates ($W_R \to \nu_R\ell$) increase to about 6.7% for each lepton flavor, and the branching ratio of $W_R \to t\bar{b}$ ranges from 25.7% to 26.5%. The estimated observed (expected) bound on W_R masses is 2575 (2375) GeV at 95% CL, as seen from the blue line. In order to see the effect of large $\tan\beta$ and $g_R \neq g_L$, we set $g_R \simeq 0.37$ and $\tan\beta = 0.5$. In addition to W_R decays into $t\bar{b}$, $q\bar{q}'$ and $\nu_R\ell$, the decays of $W_R \to hW_L$ and $W_R \to W_L Z$ are non-negligible, with each one at about 2% BR. Therefore, the branching ratio of W_R into $t\bar{b}$ is reduced slightly further, and now ranges between 24.8% and 25.6%. The green line shows our result, and the estimated observed (expected) limit at 95% CL is 2565 (2350) GeV. Finally, setting $g_R \simeq 0.37$, $\tan\beta = 0.5$, and varying the matrix elements of $V^R_{\rm CKM}$, the branching ratio of $W_R \to t\bar{b}$ varies from about 15.7% for high M_{W_R} (4 TeV), to about 24.7% for low M_{W_R} (1.5 TeV). The pink line shows our result, and the estimated observed (expected) limit at 95% CL is 2320 (1850)

GeV.

The top right plane of Fig. 6.3 shows the W_R mass exclusion based on $W_R \to jj$ channel. The estimated exclusion limits vary from 3.5 TeV for the scenario where $g_L = g_R$, $\tan\beta = 0.01$ and $V^L_{\rm CKM} = V^R_{\rm CKM}$, to 2.0 TeV for the scenario which we set $g_L \neq g_R = 0.37$, $\tan\beta = 0.5$ and $V^L_{\rm CKM} \neq V^R_{\rm CKM}$ as can be read in detail from Table 6.4.

In addition to $W_R \to t\bar{b}$ and $W_R \to jj$ channels, the most stringent bounds come from the channel in which the W_R boson decays to a first or second generation charged lepton and a heavy neutrino of the same lepton flavor. Both ATLAS [21] and CMS [22] assume that the heavy neutrino further decays to another charged lepton of the same flavor and a virtual $W^\star_R$ with a 100% rate. The virtual $W^\star_R$ then decays into two light quarks, producing the decay chain

$$W_R \to \ell\nu_R \to \ell\ell W^\star_R \to \ell\ell qq', \quad \ell = e \text{ or } \mu\,. \tag{6.24}$$

However, this is true only for small $\tan\beta$ values, where the corresponding mixing angle ξ between the two charged gauge bosons is extremely small. In the large $\tan\beta$ case, the mixing between W_L and W_R, although small enough to satisfy flavor and CP bounds, becomes important, inducing a W_L contribution to the above channel, producing the decay chain

$$W_R \to \ell\nu_R \to \ell\ell W_L \to \ell\ell qq', \quad \ell = e \text{ or } \mu\,. \tag{6.25}$$

This can be traced to the interaction of right-handed neutrino field with $W^{+\mu}_L\ell$ and $W^{+\mu}_R\ell$ [260]:

$$\overline{\nu}W^{+\mu}_L\ell \;\longrightarrow\; \frac{i}{\sqrt{2}}\gamma^\mu\left(g_L P_L K_L \cos\xi - g_R P_R K_R \sin\xi\right) \tag{6.26}$$

$$\overline{\nu}W^{+\mu}_R\ell \;\longrightarrow\; \frac{i}{\sqrt{2}}\gamma^\mu\left(g_R P_R K_R \cos\xi - g_L P_L K_L \sin\xi\right) \tag{6.27}$$

where K_L and K_R are PMNS mixing matrices in the left and right leptonic sectors, defined as

$$K_L = V^{\nu\dagger}_L V^\ell_L, \qquad\qquad K_R = V^{\nu\dagger}_R V^\ell_R. \tag{6.28}$$

Remember that, while we denote the gauge bosons by $W_{R,L}$, in the presence of mixing, each physical eigenstate is a mixture of the the left- and right-handed gauge bosons. For the case of no mixing between charged gauge bosons, W_L is purely left-handed, and consequently, ν_R will not decay to this state. However, the second term in Eq. (6.26) is important as the mixing ξ increases, and M_{ν_R} decreases. Contributions to $\ell\ell jj$ final states through $W_R^\star$ and W_L are illustrated in the Fig. 6.2, where we set $M_{W_R} = 3.5$ TeV both in the left and right plane. The green line shows the branching ratio of $\nu_R \to \ell qq'$, namely, the contribution to $\ell\ell jj$ final states through virtual $W_R^\star$ boson, Eq. (6.27), while the red curve represents the branching ratio of $\nu_R \to W_L\ell$, namely, the contribution to $\ell\ell jj$ final state through an W_L boson Eq. (6.26). The lower x-axis and the top x-axis represent the mixing angle ξ between the charged gauge bosons and $\tan\beta$, respectively, thus showing the correlation between them. In the left plot, we show this correlation for the case of $g_L = g_R$, while the right plot depicts the same correlation, but for the case $g_L \neq g_R = 0.37$. The plots indicate that, when both $\tan\beta$ and ξ are small, all contributions proceed through a virtual $W_R^\star$ boson. As an increase in $\tan\beta$ induces an increase in ξ, the contributions to $\ell\ell jj$ final states receive contributions through both virtual $W_R^\star$ and real W_L bosons. When $g_L = g_R$, $\tan\beta = 0.01$ and $M_{W_R} = 3.5$ TeV, approximately 98% of the total contribution to $\ell\ell jj$ final state comes through the virtual $W_R^\star$ boson, with W_L boson contribution to about 2%. The mixing between two charged gauge bosons become more important in case of $g_L \neq g_R$. When $g_L \neq g_R = 0.37$, $\tan\beta = 0.5$ and $M_{W_R} = 3.5$ TeV, the contribution to $\ell\ell jj$ final state through W_L boson increases to 30%, meaning that the contribution through a virtual $W_R^\star$ boson has been reduced to 70%[4]. Since we increased the ratio of g_L/g_R from 1.0 to 1.79 by setting $g_R \simeq 0.37$, the vacuum expectation value v_R needs to be increased approximately by 1.8 times to obtain the the same W_R boson mass as in the $g_L = g_R$ case, the corresponding ξ value decreasing slightly compared to the case where $g_L \neq g_R$. The decrease in g_R and increase in $\tan\beta$ increases the contribution through W_L into $\ell\ell jj$ final state. In case of small ξ, which also corresponds to small $\tan\beta$, the branching ratio of $\nu_R \to W_L\ell$ is negligible ($< 10^{-4}$). As the mixing ξ between charged gauge bosons increases (concurrently with $\tan\beta$), the second term in Eq. (6.26) starts to give non-negligible contributions, and as a result, the branching ratio of $\nu_R \to W_L\ell$ becomes larger. In case of $g_R = g_L$ and small $\tan\beta$, the main contribution to $W_R \to \nu_R\ell$ comes from the first term in Eq. (6.27). Increasing $\tan\beta$ and decreasing g_R slightly reduces the contribution of this term since it is proportional to $g_R\cos\xi$. Therefore, the branching ratio of $W_R \to \nu_R\ell$ slightly decreases in the case of $g_L \neq g_R$, and the contribution to $\ell\ell jj$ final

[4]The values chosen for $\tan\beta$ and mixing angle ξ satisfy all flavor constraints in Table 6.1.

state is compensated through W_L contributions, slightly more so compared to the $g_L = g_R$ case.

The bottom planes of Fig. 6.3 show the result of the analysis of the $\ell\ell jj$ final states. The bottom left panel plots the result for decays into $\ell\ell = ee$ channel whereas the bottom right one is for the $\ell\ell = \mu\mu$ channel. For the scenarios where $\tan\beta = 0.01$, the contribution through W_L bosons is suppressed. Therefore, the main contribution to $\ell\ell jj$ final states comes via the virtual $W_R^\star$ boson. However, for consistency we sum up the contributions through the virtual $W_R^\star$ and real W_L boson, and our graphs for large $\tan\beta$ values in the bottom planes represent the combined contribution. The most stringent bounds occur for $g_L = g_R$, $\tan\beta = 0.01$ and $V_{\rm CKM}^L = V_{\rm CKM}^R$. We confirmed in that case the CMS result [22] and find out that the observed (expected) 95 % CL lower limit on W_R masses is 4420 (4420) GeV in the ee channel and 4420 (4500) GeV in the $\mu\mu$ channel.

The observed (expected) limit is reduced to 3800 (3800) GeV in the ee channel and 3800 (3950) GeV in the $\mu\mu$ channel when $g_L \neq g_R$, $\tan\beta = 0.01$ and $V_{\rm CKM}^L = V_{\rm CKM}^R$. In the scenarios where $\tan\beta = 0.5$, contributions to $\ell\ell jj$ final states proceed through both virtual $W_R^\star$ and W_L bosons. When the W_R mass is about 1 TeV, approximately 90.5% of the combined contribution is obtained through W_L bosons, limiting the virtual $W_R^\star$ boson contribution to 9.5%. However, this relation is flipped when W_R mass is about 4 TeV, where 77.5% of the combined contribution to $\ell\ell jj$ final states is obtained through the virtual $W_R^\star$ boson, leaving the W_L boson to contribute at 20.6%. In the scenario where we $g_L \neq g_R = 0.37$, $\tan\beta = 0.5$, and $V_{\rm CKM}^L = V_{\rm CKM}^R$, we improve the bounds to where the observed (expected) 95% CL lower limit is 3725 (3720) GeV in the ee channel, and 3750 (3900) GeV in the $\mu\mu$ channel. In addition to lowering g_R and increasing $\tan\beta$, we verified the effect of different CKM matrices, allowing $V_{\rm CKM}^L \neq V_{\rm CKM}^R$ in our final scenario. The partial contributions through virtual $W_R^\star$ and W_L in this scenario are very close to the one where $V_{\rm CKM}^L = V_{\rm CKM}^R$ and $g_R \neq g_L$, and $\tan\beta = 0.5$. In this case the results are least constraining and we find that the observed (expected) 95% CL lower limit is 3100 (3300) GeV in the ee channel and 3350 (3400) GeV in the $\mu\mu$ channel.

We now proceed to explore constraints on the W_R and related ν_R masses and compare these to the CMS and ATLAS analyses.

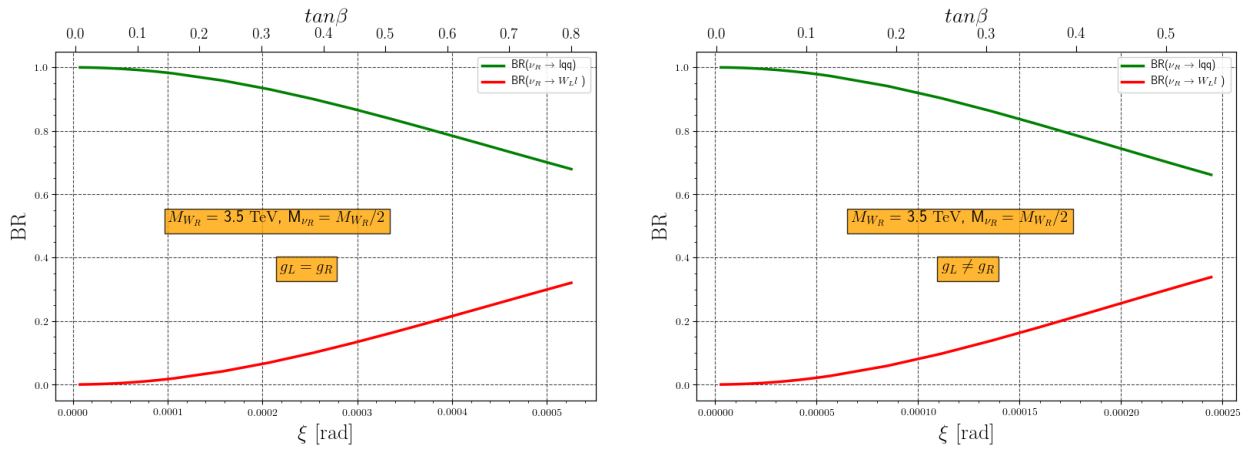

Figure 6.2: Branching ratios of $\nu_R \to lqq'$ and $\nu_R \to W_L\ell$ versus mixing angle ξ between W_L and W_R (bottom x-axis), changing with tan β (upper x-axis) when $g_L = g_R$ (left) and when $g_L \neq g_R = 0.37$ (right). We set $V^L_{\text{CKM}} = V^R_{\text{CKM}}$ for this analysis.

6.5.3 Correlating W_R and ν_R mass bounds

In Fig. 6.4, we analyze the correlations in the two dimensional $M_{W_R} - M_{\nu_R}$ mass plane, covering a range of neutrino masses both below and above the W_R boson mass. Contrary to the CMS analysis [22], which assumes that only one heavy neutrino flavor ν_R contributes significantly to the W_R decay width, in our analysis all three heavy right-handed neutrino flavors contribute democratically. The W_R production cross section is calculated for each solution in this 2D plane using MG5_aMC@NLO, and the observed (expected) 95% CL limits obtained from our analysis are applied to explore excluded regions. The expected and observed upper limits on the cross section for different W_R and ν_R mass hypotheses are compared with the latest CMS results [22] @ $\mathcal{L} = 35.9$ fb^{-1} and ATLAS results [21] @ $\mathcal{L} = 36.1$ fb^{-1}, as seen in Fig. 6.4. Note that we generate our results using the CMS [22] data, as this is available. The ATLAS analysis, although more recent and at a slightly higher luminosity, is able to rule out a small subset of parameter points in the $M_{W_R} < M_{\nu_R}$ region. However they do not share their observed (expected) cross section plots publicly. Because of that, when we extrapolate our results for slightly higher luminosity in that region, our cross sections are very small, and we do not obtain any restrictions. Thus, we decided it safer to compare our analysis with the existing data points provided by CMS, while indicating restrictions from both experimental analyses on the plots.

In the $M_{\nu_R} < M_{W_R}$ case, we assume that the contribution comes through the following

decay chain:

$$W_R \to \ell\nu_R \to \ell\ell W_R^\star \to \ell\ell qq', \quad \ell = e \text{ or } \mu\,, \tag{6.29}$$

while in the $M_{\nu_R} > M_{W_R}$ case, we assume that the contribution comes through the following decay chain:

$$W_R^\star \to \ell\nu_R \to \ell\ell W_R \to \ell\ell qq', \quad \ell = e \text{ or } \mu\,. \tag{6.30}$$

In our analysis, there is no excluded region in the $M_{\nu_R} > M_{W_R}$ region since the corresponding cross section in that region is below the experimental limits, as can be read from the color bars in Fig. 6.4. This is understood from our previous analysis, as the production cross section of $\nu_R\ell$ through W_R bosons dominates the one obtained through the virtual $W_R^\star$ bosons. The top planes of Fig. 6.4 represent the results of the exclusion in the two dimensional $M_{W_R} - M_{\nu_R}$ mass plane based on the scenario where $g_L = g_R$, $\tan\beta = 0.01$ and $V_{\rm CKM}^L = V_{\rm CKM}^R$, whereas middle and bottom planes show the same exclusion for the scenario where $g_L \neq g_R = 0.37$, $\tan\beta = 0.5$, $V_{\rm CKM}^L = V_{\rm CKM}^R$ and $g_L \neq g_R = 0.37$, $\tan\beta = 0.5$, $V_{\rm CKM}^L \neq V_{\rm CKM}^R$, respectively. For the scenario where $g_L \neq g_R$, $\tan\beta = 0.5$ and $V_{\rm CKM}^L = V_{\rm CKM}^R$, W_R bosons with masses up to 3.7 (3.7) TeV in the ee channel and up to 3.7 (3.9) TeV in the $\mu\mu$ channel are excluded at 95% CL, for M_{ν_R} up to 2.8 (2.9) TeV in the ee channel and 3.1 (3.0) TeV in the $\mu\mu$ channel. The 2D exclusion limits are less stringent in the ee channel, where W_R boson masses are excluded up to 3.0 TeV for ν_R masses close to the $M_{W_R} = M_{\nu_R}$ degeneracy line. On the other hand, we exclude less parameter space in the two dimensional $M_{W_R} - M_{\nu_R}$ mass plane when $g_L \neq g_R = 0.37$, $\tan\beta = 0.5$ and $V_{\rm CKM}^L \neq V_{\rm CKM}^R$. As seen from the bottom planes of Fig. 6.4, W_R bosons with masses up to 3.1 (3.3) TeV are excluded at 95% CL, for M_{ν_R} up to 2.1 TeV, in the ee channel whereas W_R bosons with masses up to 3.3 (3.4) TeV are excluded at 95% CL, for M_{ν_R} up to 2.6 (2.5) TeV in the $\mu\mu$ channel. Here again, the 2D exclusion limits are less stringent in the ee channel, where W_R boson masses are excluded up to 2.0 TeV for M_{ν_R} masses close to the $M_{W_R} = M_{\nu_R}$ degeneracy line.

In Table 6.3 we show explicitly the limits for different values of g_L, g_R, $\tan\beta$ and $V_{\rm CKM}^L$ versus $V_{\rm CKM}^R$ values for $M_{\nu_R} > M_{W_R}$ case. The second column gives the expected limits, while the third the observed limits[5]. The last column indicates the dominant constraining channel. For this scenario, the most stringent limits come from $W_R \to jj$, for the case when $g_L = g_R$, $\tan\beta = 0.01$ and $V_{\rm CKM}^L = V_{\rm CKM}^R$, where $M_{W_R} \geq 3.60$ (3.625) TeV for the observed (expected) mass limits, while the least constraining case is the decay $W_R \to t\bar{b}$, when $g_L \neq g_R = 0.37$,

[5]Our theoretically estimated observed and expected values are obtained for the points where our model curves intersect the respective observed and expected experimental curves.

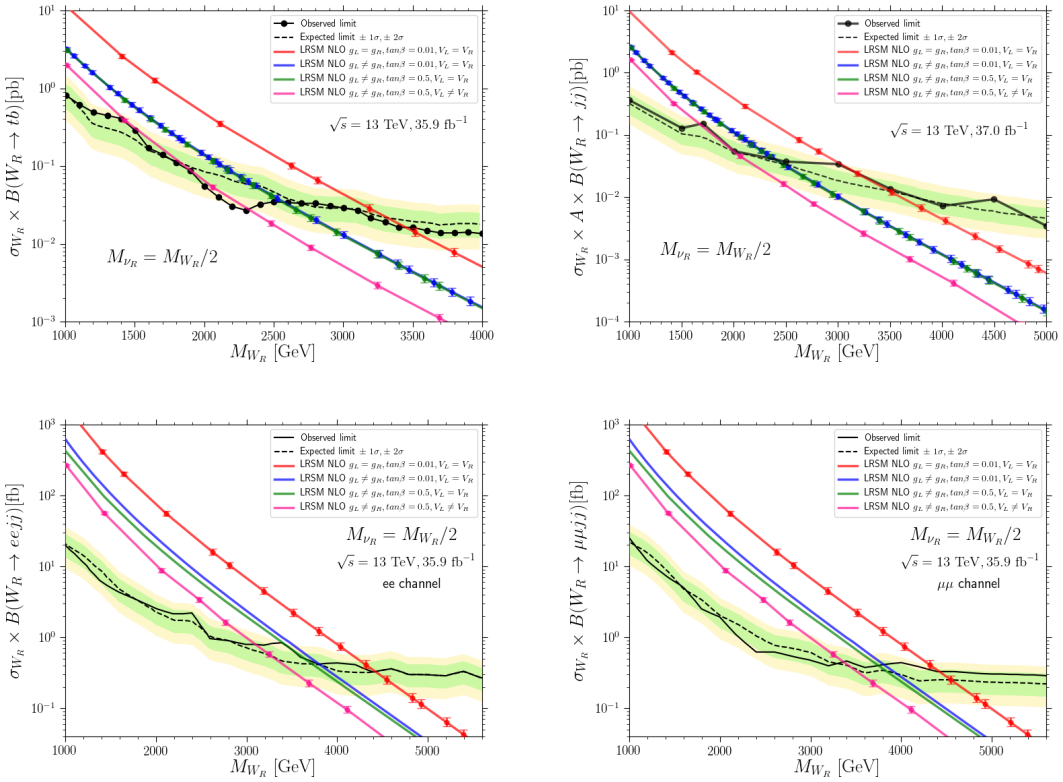

Figure 6.3: (Top left): The cross section of $W_R \to t\bar{b}$ vs W_R mass, compared to CMS data [20]; (top right) The cross section of $W_R \to jj$ vs W_R mass, compared to the ATLAS measurements [21]; (bottom left) The cross section of $W_R \to eejj$ vs W_R mass, for the case $M_{\nu_R} = M_{W_R}/2$, compared to the CMS data [22]; (bottom right) The cross section of $W_R \to \mu\mu jj$ vs W_R mass, for the case where $M_{\nu_R} = M_{W_R}/2$, compared to [22].

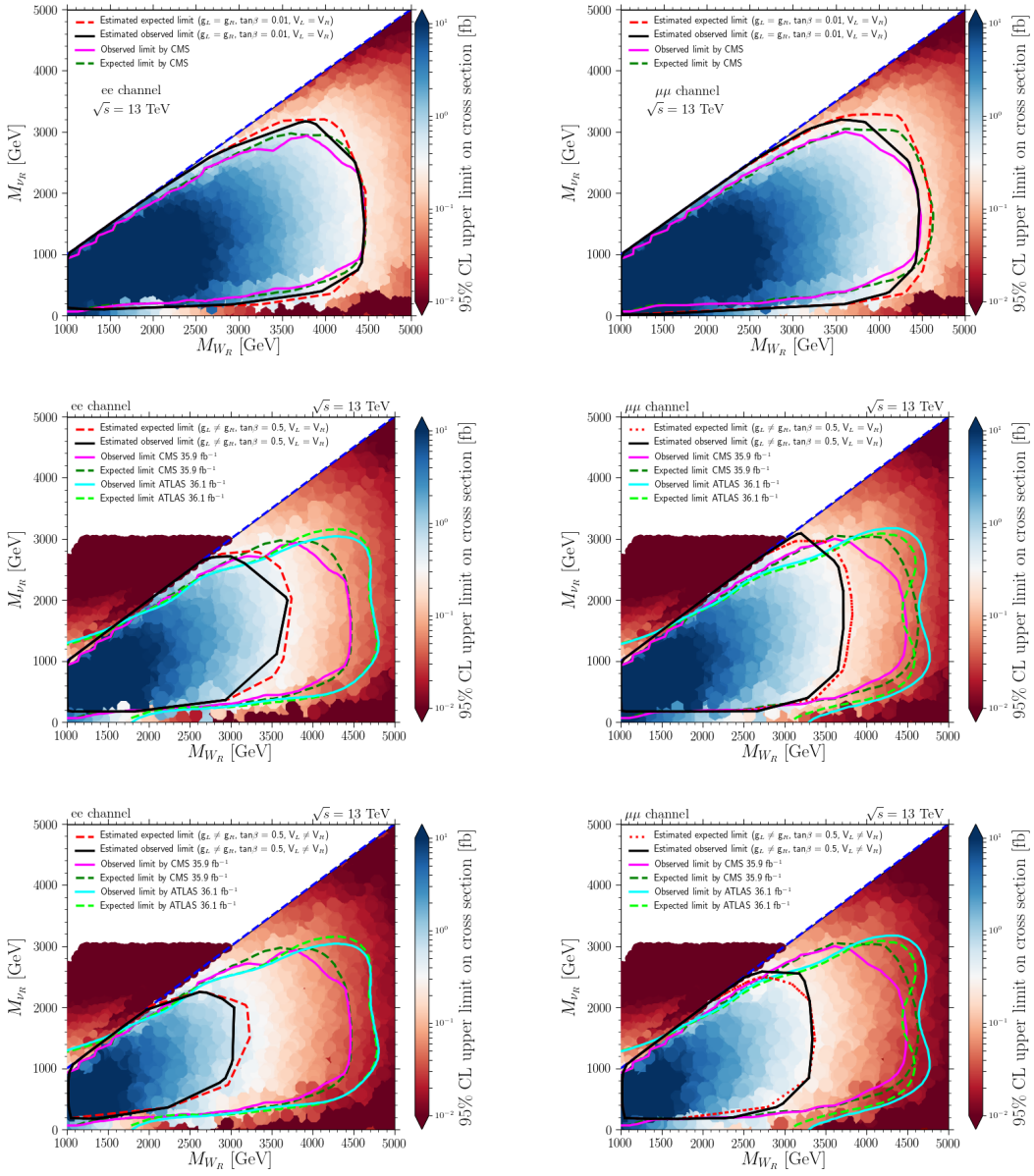

Figure 6.4: Observed (continuous lines) and expected (dashed lines) 95% CL exclusion contours in the $M_{W_R} - M_{\nu_R}$ plane in the ee (left columns) and $\mu\mu$ (right columns) channels for Majorana ν_R neutrinos. The dashed blue line in the each plane indicates the region where $M_{W_R} = M_{\nu_R}$. We also show observed and expected limits by ATLAS [21] @ $\mathcal{L} = 36.1$ fb^{-1}, and CMS [22] @ $\mathcal{L} = 35.9$ fb^{-1}, obtained assuming $g_L = g_R$, $\tan\beta = 0.01$ and $V^L_{\rm CKM} = V^R_{\rm CKM}$. The cross section values are indicated by the colors in the legend of the planes. In the top planes, the continuous (dashed) black (red) line shows the estimated observed (expected) limit for the scenario where $g_L = g_R$, $\tan\beta = 0.01$ and $V^L_{\rm CKM} = V^R_{\rm CKM}$. In the middle planes, $g_L \neq g_R = 0.37$, $\tan\beta = 0.5$ and $V^L_{\rm CKM} = V^R_{\rm CKM}$, whereas the same limits in the bottom planes are analyzed for the scenario where $g_L \neq g_R = 0.37$, $\tan\beta = 0.5$, and also $V^L_{\rm CKM} \neq V^R_{\rm CKM}$.

Scenario I: $M_{\nu_R} > M_{W_R}$	Lower limits for M_{W_R} (GeV)		Exclusion channel
	Expected	Observed	
$g_L = g_R$, $\tan\beta = 0.01$, $V^L_{\rm CKM} = V^R_{\rm CKM}$	3450	3600	$W_R \to tb$
$g_L \neq g_R$, $\tan\beta = 0.01$, $V^L_{\rm CKM} = V^R_{\rm CKM}$	2700	2700	$W_R \to tb$
$g_L \neq g_R$, $\tan\beta = 0.5$, $V^L_{\rm CKM} = V^R_{\rm CKM}$	2675	2675	$W_R \to tb$
$g_L \neq g_R$, $\tan\beta = 0.5$, $V^L_{\rm CKM} \neq V^R_{\rm CKM}$	1940	2360	$W_R \to tb$
$g_L = g_R$, $\tan\beta = 0.01$, $V^L_{\rm CKM} = V^R_{\rm CKM}$	3625	3620	$W_R \to jj$
$g_L \neq g_R$, $\tan\beta = 0.01$, $V^L_{\rm CKM} = V^R_{\rm CKM}$	2700	2555	$W_R \to jj$
$g_L \neq g_R$, $\tan\beta = 0.5$, $V^L_{\rm CKM} = V^R_{\rm CKM}$	2650	2500	$W_R \to jj$
$g_L \neq g_R$, $\tan\beta = 0.5$, $V^L_{\rm CKM} \neq V^R_{\rm CKM}$	2010	2000	$W_R \to jj$

Table 6.3: Lower limits for M_{W_R} in GeV, when $M_{\nu_R} > M_{W_R}$.

$\tan\beta = 0.5$ and $V^L_{\rm CKM} \neq V^R_{\rm CKM}$, where $M_{W_R} \geq 2.36$ (1.94) TeV for the observed (expected) mass limits.

We repeat the analysis in Table 6.4 for the case where $M_{\nu_R} < M_{W_R}$, using the same column notations as in Table 6.3. For this second scenario, the most stringent limits come from $W_R \to \mu\mu jj$, for the case when $g_L = g_R$, $\tan\beta = 0.01$ and $V^L_{\rm CKM} = V^R_{\rm CKM}$, where $M_{W_R} \geq 4.42$ (4.5) TeV for the observed (expected) mass limits, while the least constraining case is the case $W_R \to t\bar{b}$, when $g_L \neq g_R = 0.37$, $\tan\beta = 0.5$ and $V^L_{\rm CKM} \neq V^R_{\rm CKM}$, where $M_{W_R} \geq 2.32$ (1.85) TeV for the observed (expected) mass limits.

To assess properties and differences between the two scenarios, in Table 6.5 we give the complete set of parameters for two representative benchmarks, one for the first scenario, $M_{\nu_R} > M_{W_R}$ and one for the second scenario, $M_{\nu_R} < M_{W_R}$, with the W_R masses, cross sections and branching ratios given in Table 6.6, for LHC at $\sqrt{s} = 13$ and 27 TeV.

While there are no discerning differences in the parameters of scalar potential, Eq. (6.9), or $\tan\beta$ (chosen to maximize $W_R \to W_L h$), the Yukawa coupling generating the Majorana masses is an order of magnitude larger in Scenario I, needed to generate $M_{\nu_R} > M_{W_R}$; while in Scenario II v_R is about 50% larger, to generate an M_{W_R} larger by about 50% than in Scenario I. The main contributions to the cross sections come from the off-diagonal element $(12) = (us)$ and $(21) = cd$ in $V^R_{\rm CKM}$. For **BM I**, the largest partonic contribution to the cross section ($u\bar{s} \to W_R$) decreases by 8.2% from 13 TeV to 27 TeV while the contribution from the same channel decreases by 10.4% for **BM II**. For **BM I**, the second largest partonic

Scenario II: $M_{\nu_R} < M_{W_R}$	Lower limits for M_{W_R} (GeV)		Exclusion channel
	Expected	Observed	
$g_L = g_R$, $\tan\beta = 0.01$, $V^L_{\rm CKM} = V^R_{\rm CKM}$	4420	4420	$W_R \to qqee$
$g_L \neq g_R$, $\tan\beta = 0.01$, $V^L_{\rm CKM} = V^R_{\rm CKM}$	3800	3800	$W_R \to qqee$
$g_L \neq g_R$, $\tan\beta = 0.5$, $V^L_{\rm CKM} = V^R_{\rm CKM}$	3720	3725	$W_R \to qqee$
$g_L \neq g_R$, $\tan\beta = 0.5$, $V^L_{\rm CKM} \neq V^R_{\rm CKM}$	3300	3100	$W_R \to qqee$
$g_L = g_R$, $\tan\beta = 0.01$, $V^L_{\rm CKM} = V^R_{\rm CKM}$	4500	4420	$W_R \to qq\mu\mu$
$g_L \neq g_R$, $\tan\beta = 0.01$, $V^L_{\rm CKM} = V^R_{\rm CKM}$	3950	3800	$W_R \to qq\mu\mu$
$g_L \neq g_R$, $\tan\beta = 0.5$, $V^L_{\rm CKM} = V^R_{\rm CKM}$	3900	3750	$W_R \to qq\mu\mu$
$g_L \neq g_R$, $\tan\beta = 0.5$, $V^L_{\rm CKM} \neq V^R_{\rm CKM}$	3400	3350	$W_R \to qq\mu\mu$
$g_L = g_R$, $\tan\beta = 0.01$, $V^L_{\rm CKM} = V^R_{\rm CKM}$	3320	3450	$W_R \to tb$
$g_L \neq g_R$, $\tan\beta = 0.01$, $V^L_{\rm CKM} = V^R_{\rm CKM}$	2375	2575	$W_R \to tb$
$g_L \neq g_R$, $\tan\beta = 0.5$, $V^L_{\rm CKM} = V^R_{\rm CKM}$	2350	2565	$\mathrm{W}_R \to tb$
$g_L \neq g_R$, $\tan\beta = 0.5$, $V^L_{\rm CKM} \neq V^R_{\rm CKM}$	1850	2320	$\mathrm{W}_R \to tb$
$g_L = g_R$, $\tan\beta = 0.01$, $V^L_{\rm CKM} = V^R_{\rm CKM}$	3500	3500	$W_R \to jj$
$g_L \neq g_R$, $\tan\beta = 0.01$, $V^L_{\rm CKM} = V^R_{\rm CKM}$	2500	2430	$W_R \to jj$
$g_L \neq g_R$, $\tan\beta = 0.5$, $V^L_{\rm CKM} = V^R_{\rm CKM}$	2460	2400	$W_R \to jj$
$g_L \neq g_R$, $\tan\beta = 0.5$, $V^L_{\rm CKM} \neq V^R_{\rm CKM}$	2000	2000	$W_R \to jj$

Table 6.4: Lower limits for M_{W_R} in GeV when $M_{\nu_R} < M_{W_R}$.

	v_R	g_R	$\tan\beta$	$\text{diag}(\text{h}_R^{ij})$	α_1	α_2	α_3
BM I :	9.8 TeV	0.36	0.55	0.9	0.6	0.6	2.0
BM II :	14.1 TeV	0.37	0.55	7.5×10^{-2}	0.6	0.6	2.0
	λ_1	λ_2	λ_3	ρ_1	ρ_2	ρ_3	$\rho_4 = \lambda_4$
BM I :	0.15	0.14	0.142	2.12×10^{-3}	3.4×10^{-3}	5.5×10^{-3}	0.0
BM II :	0.16	0.16	0.162	1.79×10^{-3}	4.0×10^{-3}	4.0×10^{-3}	0.0

Table 6.5: Parameter values for **BM I** and **BM II**.

	BM I : $M_{\nu_R} > M_{W_R}$	**BM II** : $M_{\nu_R} < M_{W_R}$
m_{W_R} [GeV]	2557	3689
m_{ν_R} [GeV]	16797	1838
$\sigma(\text{pp} \to W_R)$ [fb] @13 TeV	48.7	3.98
$\sigma(\text{pp} \to W_R)$ [fb] @27 TeV	478.0	77.3
$\text{BR}(W_R \to t\bar{b})$ [%]	26.3	19.9
$\text{BR}(W_R \to jj)$ [%]	58.6	45.8
$\text{BR}(W_R \to \nu_R \ell)$ [%]	-	6.5 (each family)
$\text{BR}(W_R \to h_1 W_L)$ [%]	1.8	1.5
$\text{BR}(W_R \to W_L Z)$ [%]	2.0	1.6
$\text{BR}(\nu_R \to \ell q q')$ [%]	-	65.3
$\text{BR}(\nu_R \to W_L \ell)$ [%]	1.1×10^{-4}	33.1
$\text{BR}(\nu_R \to W_R \ell)$ [%]	99.9	-

Table 6.6: Related Branching Ratios and Cross Sections for **BM I** and **BM II**.

contribution, $d\bar{c} \to W_R$ increases by 3.1% from 13 TeV to 27 TeV, while the contribution from the same channel increases by 5.6% for **BM II**. Because of the highly non-diagonal V_{CKM}^R for both benchmarks, the dominant decay is into $jj = q\bar{q}' \neq t\bar{b}$, followed by $t\bar{b}$ in **BMI**, while in **BM II** the decay into leptons and neutrinos (combined for three families) is of the same strength as $t\bar{b}$.

Chapter 7

Natural dark matter and light bosons with an alternative left-right symmetry

7.1 Introduction

The nature of dark matter and its interactions is one of the most puzzling conceptual issues of the Standard Model of particle physics and points clearly towards the existence of new physics. So far, the most popular extensions of the Standard Model (SM) that contain natural dark matter (DM) candidates have been either supersymmetric, so that R-parity conservation enforces a stable supersymmetric state behaving as a weakly-interacting massive particle (WIMP) [262], or featuring axion-like particles that could additionally shed light on a potential solution to the strong CP problem [263, 264]. While experimental DM searches are on-going and put stronger and stronger constraints on the phenomenological viability of the models, several new *ad-hoc* mechanisms have been recently designed to supplement the SM with a DM candidate. In the latter, the observed properties of DM [12] can be successfully reproduced by an appropriate tuning of the particle masses and properties. For instance, new force carriers could be introduced to mediate the interactions of the dark sector with the SM one, as within the dark photon or vector portal models [265–269]. Differently, the connection between the dark and visible sector could be realised through interactions with vector-like fermions [270–275]. Whilst appealing from a phenomenological point of view by virtue of their simplicity, such DM setups are however quite unnatural. In this work, we

therefore go back to natural dark matter models and focus on a less studied class of scenarios that emerges from the grand unification of the SM gauge interactions.

Grand unification models based on the breaking of the exceptional group E_6 [276, 277] have been popular for awhile, at the beginning as a result of developments in string theories [178], then later as generators of models with additional $U(1)$ symmetries [210]. These so-called $U(1)'$ models arise from considering the $SO(10) \times U(1)$ subgroup of E_6. However, the E_6 group has also an $SU(3) \times SU(3) \times SU(3)$ subgroup. One of these $SU(3)$ remains unbroken and is associated with the SM strong interaction group $SU(3)_c$, while the two others further break into the $SU(2)_L \times SU(2)_H \times U(1)_X$ group that embeds the $SU(2)_L \times U(1)_Y$ electroweak symmetry. In the so-called left-right symmetric model (LRSM), that naturally accounts for non-vanishing neutrino masses [231, 232, 234, 241], $SU(2)_H$ is identified with $SU(2)_R$ and $U(1)_X$ with $U(1)_{B-L}$. In such a configuration, the right-handed SM fermions and the right-handed neutrino ν_R are collected into $SU(2)_R$ doublets. The structure of the Higgs sector could however lead to non-acceptable tree-level flavour-violating interactions that would conflict with the observed properties of kaon and B-meson systems. Consequently, the $SU(2)_R \times U(1)_{B-L}$ symmetry has to be broken at a very high energy scale to mass-suppress any potential flavour-violating effect. This additionally pushes the masses of the extra Higgs and gauge bosons of the model to the high scale, making them unlikely to detect at the LHC. Furthermore, in its minimal incarnation, the LRSM lacks any viable DM candidate [278].

It is nevertheless possible to associate the $SU(2)_H$ symmetry with a different $SU(2)_{R'}$ group in which the assignments of the SM fermions into doublets are different [279, 280]. This model is called the alternative left-right symmetric model (ALRSM) [281, 282]. In this case, the $SU(2)_{R'}$ partner of the right-handed up-quark u_R is an exotic down-type quark d'_R (instead of the SM right-handed down-type quark d_R), and the $SU(2)_{R'}$ partner of the right-handed charged lepton e_R is a new neutral lepton, the scotino n_R (instead of the more standard right-handed neutrino ν_R). The right-handed neutrino ν_R and down-type quark d_R therefore remain singlets under both the $SU(2)_L$ and $SU(2)_{R'}$ groups. In addition, the model field content also includes $SU(2)_L$ singlet counterparts to the new states, *i.e.* an n_L scotino and a d'_L down-type quark. Consequently, one generation of quarks is described by one $SU(2)_L$ doublet $Q_L = (u_L, d_L)$, one $SU(2)_{R'}$ doublet $Q_R = (u_R, d'_R)$ and two $SU(2)_L \times SU(2)_{R'}$ singlets d'_L and d_R. Similarly, one generation of leptons is described by one $SU(2)_L$ doublet $L_L = (\nu_L, e_L)$, one $SU(2)_{R'}$ doublet $L_R = (n_R, e_R)$ and two $SU(2)_L \times SU(2)_{R'}$ singlets n_L and ν_R. Moreover, the right-handed neutrino ν_R and the n_L scotino being singlets under

$U(1)_{B-L}$, are unlikely to be viable DM candidates, as their too weak interactions with the SM particles would make them over-abundant. On the contrary, the n_R scotino may fulfill the role.

In this work, we will show that this is indeed the case. The n_R scotino can be an acceptable DM candidate satisfying requirements from imposing agreement with the observed relic density and the non-violation of the DM direct and indirect detection bounds. This however yields very stringent constraints on the model parameter space. In contrast with the usual LRSM, the charged right-handed gauge boson W' couples right-handed up-type quarks and charged leptons to their exotic quarks and scotino partners. Therefore, the limits on the W'-boson mass (originating mainly from the properties of the $K^0 - \bar{K}^0$ mixing in the LRSM case [244]) do not apply. Similarly, the different couplings of the Higgs states to fermions forbid most dangerous flavour-violating effects, so that the mass limits on the Higgs states can also be relaxed. As will be demonstrated in the rest of this paper, these considerations lead to a quite predictable lower-energy spectrum with signatures potentially observable at the high-luminosity LHC.

The aim of this work is therefore to provide a comprehensive analysis of the ALRSM setup, emphasising for the first time the complementarity between cosmological, low-energy and collider constraints in this class of extensions of the SM. We update and extent previous recent works that have focused on the dark matter [283] and collider [284] phenomenology independently. In section 7.2, we provide a brief description of the ALRSM and detail the technical setup underlying our analysis in section 7.3. Our results are presented in the next sections. In section 7.4, we analyse the constraints on the model parameter space originating from LHC searches for new gauge bosons, performed in a similar way as for the LRSM [4]. Section 7.5 is dedicated to cosmological considerations and their impact on the parameter space. In section 7.6 we focus on determining promising signals of the model at the future high-luminosity upgrade of the LHC. In appendices B.1 and B.2, we include further details on the diagonalisation of the model Higgs and fermionic sector respectively, and document our implementation of the ALRSM in FeynRules [259] in appendix B.3.

7.2 The alternative left-right symmetric model

The alternative left-right symmetric model [279–282] is a variant of the more usual minimal left-right symmetric model. It is based on the $SU(3)_c \times SU(2)_L \times SU(2)_{R'} \times U(1)_{B-L}$

gauge group, to which we supplement a global $U(1)_S$ symmetry. The spontaneous breaking of $SU(2)_{R'} \times U(1)_S$ is implemented so that the $L = S + T_{3R}$ charge, that can be seen as a generalised lepton number, remains unbroken (with T_{3R} being the third generator of $SU(2)_{R'}$).

The quantum numbers and representations chosen for the fermionic field content of the ALRSM are motivated by heterotic superstring models in which all SM matter multiplets are collected into a **27**-plet of E_6. Under the E_6 maximal subgroup $SU(3)_c \times SU(3)_L \times SU(3)_H$, the **27** representation is decomposed as

$$\mathbf{27} = (\mathbf{3}, \mathbf{3}, 1) + (\bar{\mathbf{3}}, 1, \bar{\mathbf{3}}) + (1, \bar{\mathbf{3}}, \mathbf{3}) \qquad \equiv \quad q \quad + \quad \bar{q} \quad + \quad l \; . \tag{7.1}$$

Explicitly, the particle content for this decomposition can be written, ignoring the sign structure for clarity, as

$$q = \begin{pmatrix} u_L \\ d_L \\ d'_L \end{pmatrix} \; , \qquad \bar{q} = \begin{pmatrix} u^c_R & d^c_R & d'^c_R \end{pmatrix} \; , \qquad l = \begin{pmatrix} E^c_R & N_L & \nu_L \\ N^c_R & E_L & e_L \\ e^c_R & \nu^c_R & n^c_R \end{pmatrix} \; , \tag{7.2}$$

where d', E, N and n are exotic fermions and u, d, e and ν are the usual up-type quarks, down-type quarks, charged leptons and neutrinos. In this setup, $SU(3)_L$ operates vertically and $SU(3)_H$ horizontally. There are three different ways to embed $SU(2)_H$ into $SU(3)_H$ [279]. The most common one consists in imposing the first and second column of the above multiplets to form $SU(2)_H$ doublets, which corresponds to the usual LRSM ($SU(2)_H = SU(2)_R$) [231, 232, 234, 241]. The second option requires in contrast that the first and third columns of the above multiplets form an $SU(2)_H$ doublet, which corresponds to the ALRSM ($SU(2)_H = SU(2)_{R'}$) [279–282] . Finally, the third and last option corresponds to doublets formed from the second and third columns of the above multiplets, which corresponds to the Inert Doublet Model ($SU(2)_H = SU(2)_I$) [285–287].

We are interested here in the second option. In the rest of this section, we present a summary of the model description, leaving computational details for the appendix. While previous descriptions of the ALRSM exist, we provide extensive details to properly and consistently define our notations, which is relevant for the model implementation in the high-energy physics tools depicted in section 7.3.

Fields	Repr.	$U(1)_S$
$Q_L = \begin{pmatrix} u_L \\ d_L \end{pmatrix}$	$(\mathbf{3}, \mathbf{2}, \mathbf{1}, \frac{1}{6})$	0
$Q_R = \begin{pmatrix} u_R \\ d'_R \end{pmatrix}$	$(\mathbf{3}, \mathbf{1}, \mathbf{2}, \frac{1}{6})$	$-\frac{1}{2}$
d'_L	$(\mathbf{3}, \mathbf{1}, \mathbf{1}, -\frac{1}{3})$	-1
d_R	$(\mathbf{3}, \mathbf{1}, \mathbf{1}, -\frac{1}{3})$	0
$L_L = \begin{pmatrix} \nu_L \\ e_L \end{pmatrix}$	$(\mathbf{1}, \mathbf{2}, \mathbf{1}, -\frac{1}{2})$	1
$L_R = \begin{pmatrix} n_R \\ e_R \end{pmatrix}$	$(\mathbf{1}, \mathbf{1}, \mathbf{2}, -\frac{1}{2})$	$\frac{3}{2}$
n_L	$(\mathbf{1}, \mathbf{1}, \mathbf{1}, 0)$	2
ν_R	$(\mathbf{1}, \mathbf{1}, \mathbf{1}, 0)$	1

Fields	Repr.	$U(1)_S$
$\phi = \begin{pmatrix} \phi_1^0 & \phi_2^+ \\ \phi_1^- & \phi_2^0 \end{pmatrix}$	$(\mathbf{1}, \mathbf{2}, \mathbf{2}^*, 0)$	$-\frac{1}{2}$
$\chi_L = \begin{pmatrix} \chi_L^+ \\ \chi_L^0 \end{pmatrix}$	$(\mathbf{1}, \mathbf{2}, \mathbf{1}, \frac{1}{2})$	0
$\chi_R = \begin{pmatrix} \chi_R^+ \\ \chi_R^0 \end{pmatrix}$	$(\mathbf{1}, \mathbf{1}, \mathbf{2}, \frac{1}{2})$	$\frac{1}{2}$
G_μ	$(\mathbf{8}, \mathbf{1}, \mathbf{1}, 0)$	0
$W_{L\mu}$	$(\mathbf{1}, \mathbf{3}, \mathbf{1}, 0)$	0
$W_{R\mu}$	$(\mathbf{1}, \mathbf{1}, \mathbf{3}, 0)$	0
B_μ	$(\mathbf{1}, \mathbf{1}, \mathbf{1}, 0)$	0

Table 7.1: ALRSM particle content, given together with the representation of each field under $SU(3)_c \times SU(2)_L \times SU(2)_{R'} \times U(1)_{B-L}$ (second column) and the $U(1)_S$ quantum numbers (third column). We consider the matter sector (left panel), the gauge sector (lower right panel) and the Higgs sector (upper right panel) separately.

Pairing the fields presented in eq. (7.2) into $SU(3)_c \times SU(2)_L \times SU(2)_{R'} \times U(1)_{B-L}$ multiplets yields phenomenological issues for the neutrino sector, as the lightest neutrinos get masses of the order of the up quark mass [288]. This can be cured by adding an E_6 singlet scotino n_L to the field content, together with a pair of (heavy) $\mathbf{27} + \overline{\mathbf{27}}$ Higgs fields. As a consequence, the exotic E and N fermions become much heavier and can be phenomenologically ignored. The resulting fermionic content of the model is presented in the left panel of table 7.1, together with the representations under the model gauge group and the associated $U(1)_S$ quantum numbers. The electric charge of the different fields can be obtained through a generalised Gell-Mann-Nishijima relation $Q = T_{3R} + T_{3L} + Y_{B-L}$, which subsequently explains the unconventional $B - L$ charges.

In order to recover the electroweak symmetry group, the gauge and global symmetry $SU(2)_{R'} \times U(1)_{B-L} \times U(1)_S$ is first broken down to the hypercharge $U(1)_Y$ while preserving the generalised lepton number L. This is achieved through an $SU(2)_{R'}$ doublet of scalar fields χ_R charged under $U(1)_S$. While we introduce an $SU(2)_L$ counterpart χ_L to maintain the left-right symmetry, the latter is in contrast blind to the global $U(1)_S$ symmetry. The electroweak symmetry is then broken down to electromagnetism by means of a bidoublet of Higgs fields charged under both $SU(2)_L$ and $SU(2)_{R'}$, but with no $B - L$ quantum numbers. We refer to the right panel of table 7.1 for details on the gauge and Higgs sector of the ALRSM.

The model Lagrangian includes, on top of standard gauge-invariant kinetic terms for all fields, a Yukawa interaction Lagrangian $\mathcal{L}_{\mathrm{Y}}$ and a scalar potential V_{H}. The most general Yukawa Lagrangian allowed by the gauge and the global $U(1)_S$ symmetries is given by

$$\mathcal{L}_{\mathrm{Y}} = \bar{Q}_L \hat{\mathbf{Y}}^u \hat{\phi}^\dagger Q_R - \bar{Q}_L \hat{\mathbf{Y}}^d \chi_L d_R - \bar{Q}_R \hat{\mathbf{Y}}^{d'} \chi_R d'_L - \bar{L}_L \hat{\mathbf{Y}}^e \phi L_R + \bar{L}_L \hat{\mathbf{Y}}^\nu \hat{\chi}_L^\dagger \nu_R + \bar{L}_R \hat{\mathbf{Y}}^n \hat{\chi}_R^\dagger n_L + \mathrm{h.c.}\,, \tag{7.3}$$

where all flavour indices have been omitted for clarity so that the Yukawa couplings $\hat{\mathbf{Y}}$ are 3×3 matrices in the flavour space, and where the hatted quantities refer to the duals of the scalar fields $\hat{\phi} = \sigma_2 \phi \sigma_2$ and $\hat{\chi}_{L,R} = i\sigma_2 \chi_{L,R}$ (with σ_2 being the second Pauli matrix). The most general Higgs potential V_{H} preserving the left-right symmetry is given, following

standard conventions [289], by

$$
\begin{aligned}
V_{\rm H} = &- \mu_1^2 {\rm Tr}\left[\phi^\dagger\phi\right] - \mu_2^2\left[\chi_L^\dagger\chi_L + \chi_R^\dagger\chi_R\right] + \lambda_1\left({\rm Tr}\left[\phi^\dagger\phi\right]\right)^2 + \lambda_2\,\left(\phi\cdot\hat{\phi}\right)\,\left(\hat{\phi}^\dagger\cdot\phi^\dagger\right) \\
&+ \lambda_3\left[\left(\chi_L^\dagger\chi_L\right)^2 + \left(\chi_R^\dagger\chi_R\right)^2\right] + 2\lambda_4\,\left(\chi_L^\dagger\chi_L\right)\,\left(\chi_R^\dagger\chi_R\right) + 2\alpha_1 {\rm Tr}\left[\phi^\dagger\phi\right]\left[\chi_L^\dagger\chi_L + \chi_R^\dagger\chi_R\right] \\
&+ 2\alpha_2\left[\left(\chi_L^\dagger\phi\right)\left(\chi_L\phi^\dagger\right) + \left(\phi^\dagger\chi_R^\dagger\right)\,\left(\phi\chi_R\right)\right] + 2\alpha_3\left[\left(\chi_L^\dagger\hat{\phi}^\dagger\right)\,\left(\chi_L\hat{\phi}\right) + \left(\hat{\phi}\chi_R^\dagger\right)\,\left(\hat{\phi}^\dagger\chi_R\right)\right] \\
&+ \kappa\left[\chi_L^\dagger\phi\chi_R + \chi_R^\dagger\phi^\dagger\chi_L\right]\,,
\end{aligned}
\tag{7.4}
$$

and contains bilinear (μ), trilinear (κ) and quartic (λ, α) contributions. In the above expression, the dot to the $SU(2)$-invariant product.

After the breaking of the left-right symmetry down to electromagnetism, the neutral components of the scalar fields acquire non-vanishing vacuum expectation values (vevs),

$$
\langle\phi\rangle = \frac{1}{\sqrt{2}}\begin{pmatrix} 0 & 0 \\ 0 & k \end{pmatrix}\,, \qquad \langle\chi_L\rangle = \frac{1}{\sqrt{2}}\begin{pmatrix} 0 \\ v_{_L} \end{pmatrix}\,, \qquad \langle\chi_R\rangle = \frac{1}{\sqrt{2}}\begin{pmatrix} 0 \\ v_{_R} \end{pmatrix}\,, \tag{7.5}
$$

with the exception of ϕ_1^0, which is protected by the conservation of the generalised lepton number that also forbids mixing between the SM d and exotic d' quarks. Moreover, all scalar fields with the same electric charge mix. Expressing the complex neutral scalar fields in terms of their real degrees of freedom,

$$
\begin{aligned}
\phi_1^0 &= \frac{1}{\sqrt{2}}\Big[\Re\{\phi_1^0\} + i\,\Im\{\phi_1^0\}\Big]\,, \\
\phi_2^0 &= \frac{1}{\sqrt{2}}\Big[k + \Re\{\phi_2^0\} + i\,\Im\{\phi_2^0\}\Big]\,, \\
\chi_{L,R}^0 &= \frac{1}{\sqrt{2}}\Big[v_{_{L,R}} + \Re\{\chi_{L,R}^0\} + i\,\Im\{\chi_{L,R}^0\}\Big]\,,
\end{aligned}
\tag{7.6}
$$

we can write the mixing relations involving the massive CP-even Higgs bosons H_i^0 (with $i = 0, 1, 2, 3$), the massive CP-odd Higgs bosons A_i^0 (with $i = 1, 2$) and the two massless Goldstone bosons G_1^0 and G_2^0 that give rise to the longitudinal degrees of freedom of the Z and Z' bosons, as

$$
\begin{pmatrix} \Im\{\phi_1^0\} \\ \Im\{\phi_2^0\} \\ \Im\{\chi_L^0\} \\ \Im\{\chi_R^0\} \end{pmatrix} = \begin{pmatrix} 1 & 0 & 0 & 0 \\ 0 & & & \\ 0 & & U_{3\times3}^{\rm A} & \\ 0 & & & \end{pmatrix}\begin{pmatrix} A_1^0 \\ G_1^0 \\ G_2^0 \\ A_2^0 \end{pmatrix} \qquad \text{and} \qquad \begin{pmatrix} \Re\{\phi_1^0\} \\ \Re\{\phi_2^0\} \\ \Re\{\chi_L^0\} \\ \Re\{\chi_R^0\} \end{pmatrix} = \begin{pmatrix} 1 & 0 & 0 & 0 \\ 0 & & & \\ 0 & & U_{3\times3}^{\rm H} & \\ 0 & & & \end{pmatrix}\begin{pmatrix} H_1^0 \\ H_0^0 \\ H_2^0 \\ H_3^0 \end{pmatrix}\,. \tag{7.7}
$$

The ϕ_1^0 field has been prevented from any mixing by virtue of the conservation of the generalised lepton number, and we refer to appendix B.1 for the expressions of the 3×3 Higgs mixing matrices $U^{\rm A}_{3\times3}$ and $U^{\rm H}_{3\times3}$, as well as for those of the six Higgs-boson masses. In the charged sector, the $\phi_1^\pm$, $\phi_2^\pm$, $\chi_L^\pm$ and $\chi_R^\pm$ fields mix into two physical massive charged Higgs bosons $H_1^\pm$ and $H_2^\pm$, as well as two massless Goldstone bosons $G_1^\pm$ and $G_2^\pm$ that are absorbed by the W and W' gauge bosons,

$$\begin{pmatrix} \phi_2^\pm \\ \chi_L^\pm \end{pmatrix} = \begin{pmatrix} \cos\beta & \sin\beta \\ -\sin\beta & \cos\beta \end{pmatrix} \begin{pmatrix} H_1^\pm \\ G_1^\pm \end{pmatrix} \ , \quad \begin{pmatrix} \phi_1^\pm \\ \chi_R^\pm \end{pmatrix} = \begin{pmatrix} \cos\zeta & \sin\zeta \\ -\sin\zeta & \cos\zeta \end{pmatrix} \begin{pmatrix} H_2^\pm \\ G_2^\pm \end{pmatrix} \ , \tag{7.8}$$

with

$$\tan\beta = \frac{k}{v_{\scriptscriptstyle L}} \qquad \text{and} \qquad \tan\zeta = \frac{k}{v_{\scriptscriptstyle R}} \ . \tag{7.9}$$

We refer again to appendix B.1 for the explicit expressions of the masses of the physical states in terms of other model parameters.

By definition, the breaking of the left-right symmetry generates masses for the model gauge bosons and induces their mixing (from the Higgs-boson kinetic terms). The charged $W = W_L$ and $W' = W_R$ bosons do not mix as $\langle \phi_1^0 \rangle = 0$, and their masses are given by

$$M_W = \frac{1}{2} g_{\scriptscriptstyle L} \sqrt{k^2 + v_{\scriptscriptstyle L}^2} \equiv \frac{1}{2} g_{\scriptscriptstyle L} v \qquad \text{and} \qquad M_{W'} = \frac{1}{2} g_{\scriptscriptstyle R} \sqrt{k^2 + v_{\scriptscriptstyle R}^2} \equiv \frac{1}{2} g_{\scriptscriptstyle R} v' \ . \tag{7.10}$$

In the neutral sector, the gauge boson squared mass matrix is written, in the $(B_\mu, W^3_{L\mu}, W^3_{R\mu})$ basis, as

$$(\mathcal{M}_V^0)^2 = \frac{1}{4} \begin{pmatrix} g_{B-L}^2 \, (v_{\scriptscriptstyle L}^2 + v_{\scriptscriptstyle R}^2) & -g_{B-L} \, g_{\scriptscriptstyle L} \, v_{\scriptscriptstyle L}^2 & -g_{B-L} \, g_{\scriptscriptstyle R} \, v_{\scriptscriptstyle R}^2 \\ -g_{B-L} \, g_{\scriptscriptstyle L} \, v_{\scriptscriptstyle L}^2 & g_{\scriptscriptstyle L}^2 \, v^2 & -g_{\scriptscriptstyle L} \, g_{\scriptscriptstyle R} \, k^2 \\ -g_{B-L} \, g_{\scriptscriptstyle R} \, v_{\scriptscriptstyle R}^2 & -g_{\scriptscriptstyle L} \, g_{\scriptscriptstyle R} \, k^2 & g_{\scriptscriptstyle R}^2 \, v'^2 \end{pmatrix} \ . \tag{7.11}$$

It can be diagonalised through three rotations that mix the B, W_L^3 and W_R^3 bosons into the massless photon A and massive Z and Z' states,

$$\begin{pmatrix} B_\mu \\ W^3_{L\mu} \\ W^3_{R\mu} \end{pmatrix} = \begin{pmatrix} c_{\varphi_W} & 0 & -s_{\varphi_W} \\ 0 & 1 & 0 \\ s_{\varphi_W} & 0 & c_{\varphi_W} \end{pmatrix} \begin{pmatrix} c_{\theta_W} & -s_{\theta_W} & 0 \\ s_{\theta_W} & c_{\theta_W} & 0 \\ 0 & 0 & 1 \end{pmatrix} \begin{pmatrix} 1 & 0 & 0 \\ 0 & c_{\vartheta_W} & -s_{\vartheta_W} \\ 0 & s_{\vartheta_W} & c_{\vartheta_W} \end{pmatrix} \begin{pmatrix} A_\mu \\ Z_\mu \\ Z'_\mu \end{pmatrix} \ , \tag{7.12}$$

where s_i and c_i respectively denote the sine and cosine of the angle i. The φ_W-rotation mixes the B and W_R^3 bosons into the hypercharge boson B' as generated by the breaking of $SU(2)_{R'} \times U_{B-L}$ into to the hypercharge group $U(1)_Y$. The θ_W-rotation denotes the usual

electroweak mixing, and the ϑ_W-rotation is related to the strongly constrained Z/Z' mixing. The various mixing angles are defined by

$$\begin{aligned} s_{\varphi_W} &= \frac{g_{B-L}}{\sqrt{g_{B-L}^2 + g_R^2}} = \frac{g_Y}{g_R} \qquad \text{and} \qquad s_{\theta_W} = \frac{g_Y}{\sqrt{g_L^2 + g_Y^2}} = \frac{e}{g_L} \ , \\ \tan(2\vartheta_W) &= \frac{2c_{\varphi_W} c_{\theta_W} g_L g_R (c_{\varphi_W}^2 k^2 - s_{\varphi_W}^2 v_L^2)}{-(g_L^2 - c_{\varphi_W}^2 c_{\theta_W}^2 g_R^2) c_{\varphi_W}^2 k^2 - (g_L^2 - c_{\theta_W}^2 g_{B-L}^2 s_{\varphi_W}^2) c_{\varphi_W}^2 v_L^2 + c_{\theta_W}^2 g_R^2 v_R^2} \ , \end{aligned} \tag{7.13}$$

where g_Y and e denote the hypercharge and electromagnetic coupling constant respectively. Neglecting the Z/Z' mixing, the Z and Z' boson masses are given by

$$M_Z = \frac{g_L}{2c_{\theta_W}} \, v \qquad \text{and} \qquad M_{Z'} = \frac{1}{2} \sqrt{g_{B-L}^2 s_{\varphi_W}^2 v_L^2 + \frac{g_R^2 (c_{\varphi_W}^4 k^2 + v_R^2)}{c_{\varphi_W}^2}} \ . \tag{7.14}$$

The breaking of the gauge symmetry furthermore generates masses and mixings in the fermion sector. The masses of the up-type quark and charged leptons are controlled by the vev k of the Higgs bidoublet, whereas the masses of the neutrinos and the down-type quarks arise from the vev v_L of the χ_L Higgs triplet. The scale of the exotic fermion masses is in contrast solely induced by the vev v_R of the χ_R triplet. Similarly to what is achieved in the LRSM, all fermion mixing are conveniently absorbed into two CKM (V_{CKM} and $V_{\text{CKM}'}$) and two PMNS (V_{PMNS} and $V_{\text{PMNS}'}$) rotations,

$$d_L \to V_{\text{CKM}} d_L \ , \quad \nu_L \to V_{\text{PMNS}} d_L \ , \quad d'_R \to V_{\text{CKM}'} d'_R \ , \quad n_R \to V_{\text{PMNS}'} n_R \ . \tag{7.15}$$

We refer to appendix B.2 for additional details on the generation of the fermion masses, and their explicit expression in terms of the other model free parameters.

Finally, we supplement the model Lagrangian by the effective couplings a_{H}^g and a_{H}^a of the SM Higgs boson to gluons and photons,

$$\mathcal{L}_{\text{eff}} = -\frac{1}{4} a_{\text{H}}^g H_0^0 G_{\mu\nu}^a G_a^{\mu\nu} - \frac{1}{4} a_{\text{H}}^a H_0^0 F_{\mu\nu} F^{\mu\nu} \ , \tag{7.16}$$

where $G_{\mu\nu}^a$ and $F_{\mu\nu}$ respectively denote the gluon and photon field strength tensors.

7.3 Computational setup

To perform our analysis of the cosmology and collider phenomenology of the ALRSM, we have implemented the model presented in section 7.2 into FeynRules (version 2.3.35) [259]. Whereas an implementation was already publicly available for many years [284, 290], we found several issues with the latter that justified the development of a new implementation from scratch. First, the Goldstone sector is incorrectly implemented in the existing implementation, which could yield wrong predictions when jointly used with a tool handling computations in Feynman gauge by default (like MicrOMEGAs [220]). Secondly, all scalar fields are doubly-declared (*i.e.* both under their standard and dual form), the implementation is only partly relying on FeynRules built-in functions to treat index contractions and covariant derivatives, and the declaration of the model parameters relies particularly heavily on the existence of an unnecessary large amount of temporary intermediate abbreviations. This consequently renders the implementation hard to verify and understand. Moreover, the electroweak sector is defined by five independent parameters instead of three. Thirdly, the existing implementation enforces the unnecessary equality $g_L = g_R$, that is justified neither theoretically nor phenomenologically. Relaxing this constraint would have required to modify all relations relevant for the gauge and Higgs boson masses and mixings (see section 7.2 and appendix B.1), which would have been quite a complex task given the heavy handling of the model parameters. Finally, the original implementation has also the $V_{\text{CKM}} = V_{\text{CKM}'}$ and $V_{\text{PMNS}} = V_{\text{PMNS}'}$ equalities built in, which is again not justified (see appendix B.2). For all those reasons, we decided on designing a fresh, more general, implementation, that is also publicly released on the FeynRules model database[1]. In order to facilitate the usage of our FeynRules implementation, we document it further in appendix B.3, where we provide information on the new physics mass-eigenstates supplementing the SM field content, the free model parameters and their relation to all the other (internal) parameters.

We have then made use of FeynRules to generate CalcHep [142] model files and a UFO [111] version of the model [143], so that we could employ MicrOMEGAs (version 5.0.8) [220] for the computation of the predictions relevant for our dark matter study, and MG5_aMC (version 2.6.4) [112] for generating the hard-scattering event samples necessary for our collider study. These events, obtained by convoluting the hard-scattering matrix elements with the leading-order set of NNPDF 2.3 parton densities [224], are subsequently matched with the Pythia 8 (version 8.243) [167] parton showering and hadroni-

[1] See http://feynrules.irmp.ucl.ac.be/wiki/ALRM_general.

Parameter	Scanned range	Parameter	Scanned range
$\tan\beta$	$[0.7, 50]$	m_{n_1}	$[10, 2000]$ GeV
g_R	$[0.37, 0.768]$	m_{n_2}	$[10, 2000]$ GeV
v'	$[6.5, 13]$ TeV	m_{n_3}	$[10, 2000]$ GeV
λ_2	0.	$m_{d'}$	$[500, 2000]$ GeV
λ_3	$[0.01, 0.09]$	$m_{s'}$	$[m_{d'}, 2500]$ GeV
κ	$[-50, -1]$ GeV	$m_{b'}$	$[m_{s'}, 3000]$ GeV
$\alpha_1 = \alpha_2 = \alpha_3$	$[0.01, 0.5]$		

Table 7.2: Ranges where the new parameters defining the new physics sector of the model are allowed to vary.

sation algorithms, and we simulate the typical response of an LHC detector by means of the DELPHES 3 [168] programme (version 3.4.2) that internally relies on the anti-k_T algorithm [171] as implemented into FASTJET [172] (version 3.3.2) for event reconstruction. We have employed MADANALYSIS 5 [173] (version 1.8.23) for the collider analysis of section 7.6. Moreover, we have additionally used the generated UFO model with MADDM [291] to independently verify the results obtained with MICROMEGAS , in particular for what concerns gauge invariance.

In addition, we have relied on HIGGSBOUNDS (version 4.3.1) [292] and HIGGSSIGNALS (version 1.4.0) [95] to verify the compatibility of the ALRSM Higgs sector with data, with the H_0^0 field being associated with the SM Higgs boson. We have used the PYSLHA package [145] to read the input values for the model parameters that we encode under the SLHA format [146], and to integrate the various employed programmes into a single framework. Using our interfacing, we performed a random scan of the model parameter space following the Metropolis-Hastings technique. We have fixed the SM parameters to their Particle Data Group (PDG) values [153], chosen the $V_{\text{CKM}'}$ and $V_{\text{PMNS}'}$ matrices to be equal to their SM counterparts, and varied the remaining 15 parameters as described in table 7.2.

The $SU(2)_{R'}$ coupling g_R is allowed to vary within the $[0.37, 0.768]$ window. The lower bound originates from the g_R/g_L ratio that is theoretically constrained to be larger than $\tan\theta_W$ [293], whereas the upper bound is phenomenological. In practice, g_R can indeed vary all up to the perturbative limit of $g_R = \sqrt{4\pi}$. However, imposing an upper bound on g_R that is 4–5 times smaller guarantees scenarios that are viable with respect to LHC limits [18, 294–296] and that feature at least one light extra gauge boson (see section 7.4). The same light-spectrum considerations has lead to our choices for the values of the $\tan\beta$

and v' parameters, with the additional constrains stemming from the expectation that the $SU(2)_{R'}$ symmetry has to be broken in the multi-TeV regime and that the Z/Z' mixing must be negligibly small.

The ranges and configuration adopted for the parameters of the Higgs sector are driven by the Higgs potential minimisation conditions of eqs. (B.2) and (B.3), as well as by the above-mentioned LHC constraints on the Z'-boson mass, and by the requirement that the lightest charged Higgs boson is not tachyonic. It turns out that all phenomenologically acceptable scenarios feature $\alpha_1 \sim \alpha_2 = \alpha_3$ and $\lambda_2 = 0$, so that we set for simplicity

$$\lambda_2 = 0 \quad \text{and} \quad \alpha_1 = \alpha_2 = \alpha_3 \ . \tag{7.17}$$

Moreover, λ_3 has to be small and we recall that κ has to be negative (see appendix B.1). Finally, the exotic quarks and scotino masses are not restricted and we allow them to vary mostly freely, with a phenomenological upper bound allowing them to be not too heavy.

7.4 Gauge boson mass constraints

Following the methodolgy described in the previous section, we scan the parameter space imposing constraints on the properties of the Higgs sector so that the H_0^0 scalar boson is SM-like and has features agreeing with experimental data. In this section, we analyse the properties of the gauge sector for all scenarios accepted in our scanning procedure.

In the upper left and right panels of figure 7.1, we depict the relations between the masses of the extra gauge bosons $M_{Z'}$ and $M_{W'}$ and the ALRSM coupling constants g_L, g_{B-L} and g_R. We observe, in the upper left panel of the figure, that in the ALRSM the ratio of the neutral to the charged extra boson masses ranges from about 1.20 for a maximal g_R value of 0.768 (light green line) to about 3.05 for a minimal setup defined by $g_R = 0.37$ (purple line). The left-right symmetric case $g_L = g_R \approx 0.64$ is also indicated (dark blue line). This shows that a large variety of splittings can be realised for gauge boson masses lying in the 1–5 TeV range. Equivalently, both compressed spectra in which the Z'-boson is only 20% heavier than the W'-boson and more split spectra in which the Z'-boson is more than about 3 times heavier than the W'-boson are allowed by Higgs data, and this for a large set of W'-boson masses lying in the 1–4 TeV range. We compare those findings with predictions relevant for the usual LRSM for similar g_R values (dark green and orange lines for $g_L = g_R$ and $g_R = 0.37$

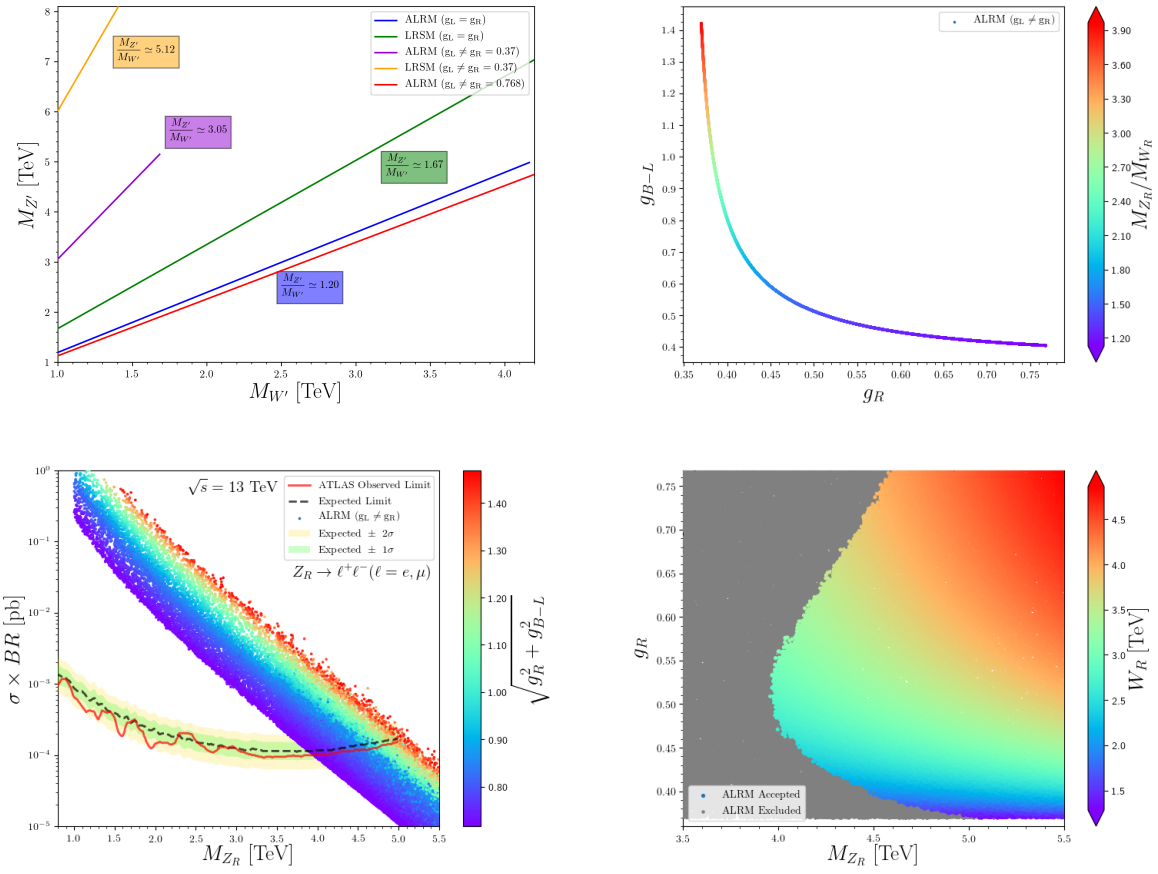

Figure 7.1: Properties of the gauge sector for the ALRSM scenarios featuring a Higgs sector compatible with data. We emphasise the relations between the W' and Z' boson masses with the gauge couplings and also investigate the LHC constraints on the mass of the Z' boson.

respectively). It turns out that the $M_{Z'}/M_{W'}$ ratio is lower in the ALRSM than in the LRSM for a given g_R value, *i.e.* the ALRSM gauge boson spectrum is more compressed than in the standard LRSM for a given $SU(2)_R$ coupling constant value. In the upper right panel of figure 7.1, we study the dependence of this mass ratio on the g_{B-L} an g_R coupling constants. The latter two couplings are related to the hypercharge coupling,

$$\frac{1}{g_Y^2} = \frac{1}{g_R^2} + \frac{1}{g_{B-L}^2} \, , \tag{7.18}$$

so that large g_R values are always associated with low g_{B-L} values and *vice versa*. In typical scenarios, the hierarchy $v_L \ll k \ll v_R$ is fulfilled as v_L is small (which is also favoured by constraints originating from the ρ parameter [297]), k drives the electroweak vacuum and is of $\mathcal{O}(100)$ GeV, and v_R is related to the breaking of the $SU(2)_{R'}$ symmetry and is thus larger. Therefore, eqs. (7.10), (7.13) and (7.14) yield

$$\frac{M_{Z'}}{M_{W'}} \approx \frac{1}{c_{\varphi_W}} = \frac{g_{B-L}}{g_Y} \, . \tag{7.19}$$

When g_R is larger, g_{B-L} is smaller and c_{φ_W} is consequently larger. Smaller $M_{Z'}/M_{W'}$ ratios are thus expected. Conversely, with increasing values of g_{B-L}, c_{φ_W} and g_R become smaller so that the $M_{Z'}/M_{W'}$ ratio increases. In those case, the W' boson can become up to about three times lighter than the Z'-boson (see the upper left panel of the figure). This feature has profound consequences on the possible existence of light ALRSM W' bosons allowed by data.

The W'-boson does not indeed couple to pairs of ordinary SM fermions, but instead couples to a SM up-type quark and an exotic down-type quark d', or an electron and a scotino. It can consequently not be directly produced at colliders and all LHC bounds on an additional W' boson originating from dijet and dileptonic resonance searches are automatically evaded [18, 294–296]. Only the neutral ALRSM Z'-boson can potentially be searched for through standard extra gauge boson LHC analyses, as it is allowed to couple to pairs of SM fermions. We evaluate the resulting bounds in the lower left panel of figure 7.1 in which we consider the most constraining limits originating from the cleaner searches in the dilepton mode. For each benchmark scenario selected by our scanning procedure, we evaluate the Z'-boson production cross section, including the branching ratio associated with a $Z' \to e^+e^-$ or $\mu^+\mu^-$ decay, and compare our predictions to the bounds arising from the ATLAS search of ref. [296]. The spread in cross section obtained for a given Z' mass stems from the different

values of the strength of the Z'-boson fermionic couplings, which we estimate by $\sqrt{g_R^2 + g_{B-L}^2}$ and which is represented through the colour map in the figure. For the smallest coupling values, Z' bosons as light as 4 TeV are allowed by data, whilst when the coupling strength gets larger, the limits can be pushed up to 5 TeV[2].

As previously mentioned and visible from the upper left panel of figure 7.1, the W'- and Z'-bosons can feature a very split spectrum so that a 4-5 TeV Z' boson can coexist with a 1–2 TeV W'-boson. This feature is illustrated in the lower right panel of the figure in which we present, for each scenario satisfying the LHC Z' bounds (the excluded benchmarks being shown in grey), the corresponding value of the g_R coupling. The latter dictates the W'-boson mass value, as given by eq. (7.10) which we also represent through the colour map. For the lowest g_R values allowed in the scan, the additional gauge boson splitting is expected to be the largest (see the upper left panel of figure 7.1), so that viable scenarios featuring a W' boson as light as 1–2 TeV and a Z'-boson not excluded by present searches are found. The considered Z' bounds are expected to slightly improve by about 20% during the high-luminosity operation phase of the LHC [298], which does not challenge the existence of light W' bosons (see the lower right panel of figure 7.1). The lightest options for the W' boson correspond to scenarios featuring the smallest g_R value theoretically allowed ($g_R \sim 0.37$), the Z'-boson being in this case constrained to lie above roughly 5 TeV. Viable scenarios in which the Z'-boson is lighter, with $M_{Z'} \approx 4$ TeV, are also allowed by data. In that configuration, the $U(1)_{B-L}$ and $SU(2)_{R'}$ coupling constant are of a similar magnitude, $g_R \approx g_{B-L} \sim 0.5$ (see the upper right panel of figure 7.1), and the W'/Z' boson splitting is smaller ($M_{W'} \approx 3$ TeV). Our results also show that the largest g_R values correspond to the heaviest scenarios, being thus disfavoured to be observed at current colliders. This motivates the upper bound set on g_R in our scan (see section 7.3).

7.5 Dark matter

In this section, we investigate the constraints on the model arising from imposing the lightest scotino as a viable DM candidate with properties compatible with current cosmological data. First, we require that the predicted relic density agrees within 20% (to conservatively allow for uncertainties on the predictions) with the recent Planck results, $\Omega_{\rm DM}h^2 = 0.12$ [11]. We

[2]Whilst in the large coupling case, the Z' width over mass ratio can reach 10%, we have verified that our approximation in which we neglect the interferences of the signal with the SM dilepton continuum was reasonably satisfactory.

calculate, for all points returned by our scanning procedure that are in addition compatible with the LHC Z'-boson bounds (see section 7.4), the associated DM relic density. We present our results in figure 7.2. In all the subfigures, the relic density is given as a function of the mass of the lightest scotino that we denote by $m_{n_{\rm DM}}$. Two classes of solutions emerge from the results. In a first set of allowed masses, the lightest scotino is quite light, with a mass lying in the $[700, 1050]$ GeV window. The relic density as observed by the Planck collaboration can however also be accommodated when the spectrum is heavier, *i.e.* with a lightest scotino featuring $m_{n_{\rm DM}} \in [1.7, 2]$ TeV. This last case is naturally less appealing from a collider search point of view. For this reason, we did not increase the scanned scotino mass range (see section 7.3), although potentially viable scenarios could be obtained for even heavier scotinos, and we mostly ignore this regime in the following discussion. In this case, the right value obtained for the relic density prediction stems from enhanced annihilations into fermions through Z'-boson s-channel exchanges (see the lower right panel of the figure).

In the different panels of figure 7.2, we analyse the properties of those ALRSM scenarios for which a relic density compatible with Planck data has been found. A first remarkable feature is that when the DM scotino state is light (*i.e.* when $m_{n_{\rm DM}} \in [700, 1050]$ GeV), several Higgs bosons are also light (upper left panel of the figure). The degenerate H_1^0 and A_1^0 neutral states, as well as the charged $H_2^\pm$ boson, hence have masses of 100–200 GeV. The heavier the lightest scotino, the lighter these scalar and pseudoscalar bosons turn out to be. More precisely, for a scotino mass of about 750 GeV, the (pseudo)scalar masses are about 200 GeV, whilst for a scotino mass of 800–1000 GeV, they turn out to be about 100 GeV. Moreover, the second scalar states H_2^0 and A_2^0 are only slightly heavier (upper right panel of figure 7.2), with masses found to lie around 400 GeV. As a consequence of the presence of all those light states, scotino annihilations into pairs of Higgs bosons contribute significantly to the total annihilation cross section, as illustrated in the central right panel of figure 7.2. This figure shows that on the contrary to any other regime probed in our scan, channels where DM annihilates into Higgs bosons contribute about 30–65% to the total relic density when $m_{n_{\rm DM}} \in [700, 1050]$ GeV. Such an enhancement (by comparison with heavier DM scenarios where those channels are usually negligible) arises from the heaviest scalar state H_3^0 that can mediate several DM annihilation modes. This scalar boson is found to have a mass roughly equal to twice the DM mass $M_{H_3^0} \approx 2m_{n_{\rm DM}}$ (see the central left panel of figure 7.2). There hence exists a new funnel allowing for efficient DM annihilations into Higgs bosons, preventing DM from being over-abundant. In addition, the H_3^0 funnel also mediates annihilations into $W'^\mp H_2^\pm$ systems, that turn to be dominant for a DM mass of about 900 GeV (lower left

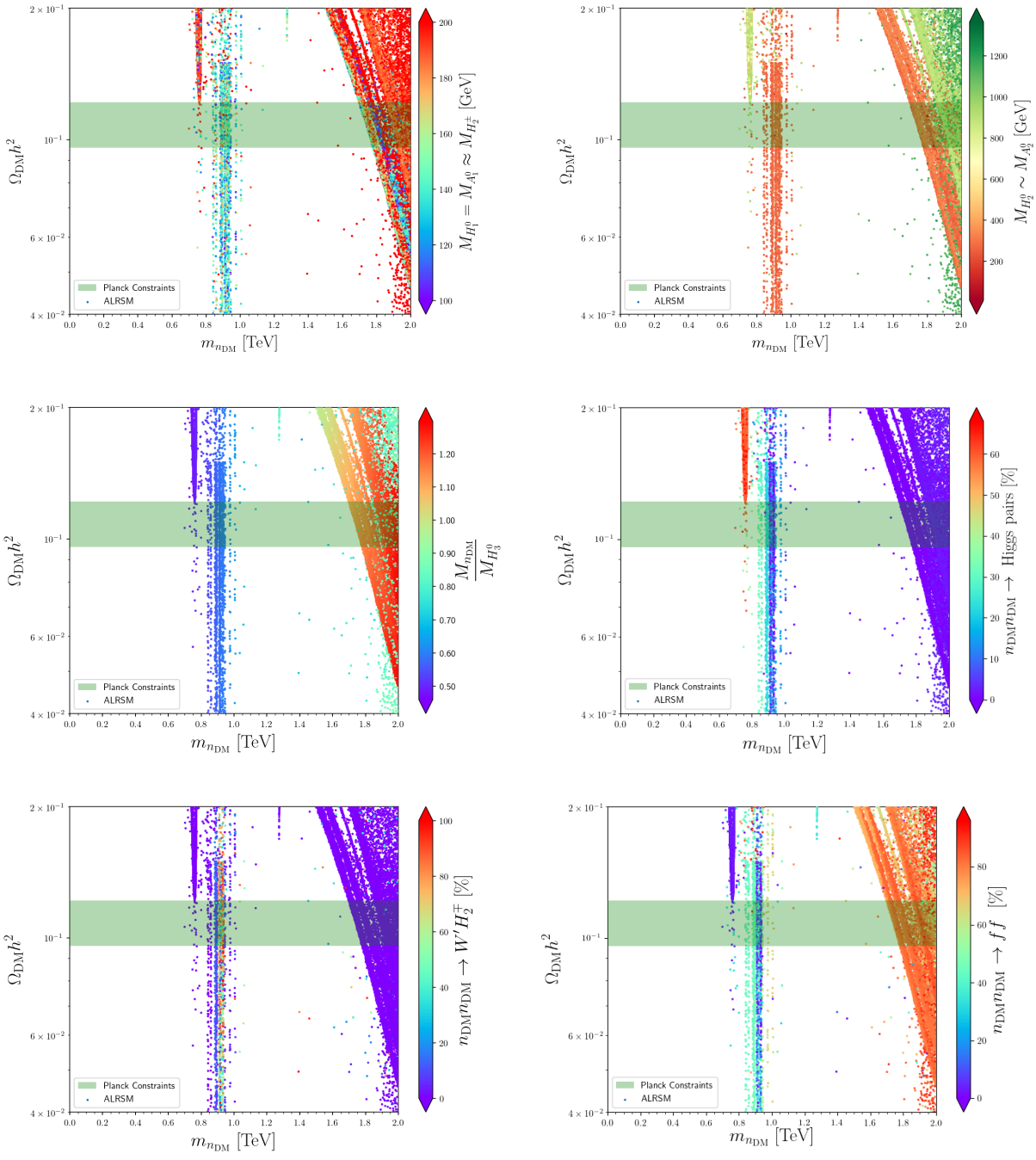

Figure 7.2: Relic density predictions for all ALRSM scenarios satisfying the Higgs constraints imposed during our scan and compatible with LHC Z' bounds, and its dependence on the mass of the lightest scotino. In each panel of the figure, we depict a specific property of all those scenarios. In the upper left panel, we represent by a colour code the mass of the H_1^0, A_1^0 and $H_2^\pm$ Higgs states, whilst in the upper right panel, we focus on the one of the H_2^0 and A_2^0 Higgs bosons. The mass of the scalar Higgs boson H_3^0 is presented relatively to the scotino mass in the central left panel, and the fractions of the DM annihilation cross section associated with annihilations in Higgs bosons, $W'^\pm H_2^\mp$ systems and fermions pairs are given in the central right, lower left and lower right panels respectively.

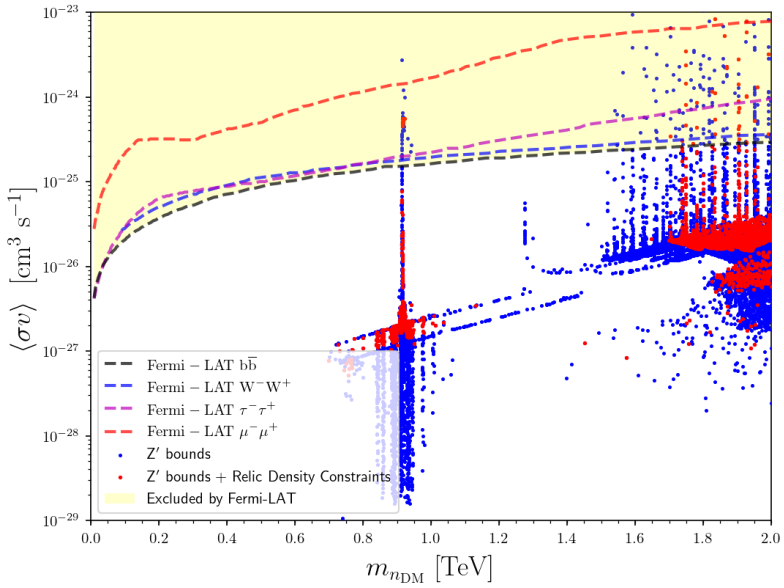

Figure 7.3: Predictions for the total DM annihilation cross section as a function of the mass of the lightest scotino. We show all points returned by the scan and that are compatible with LHC Z' bounds. Scenarios for which the predictions for the relic density agree with Planck data are shown in red, whilst scenarios for which DM is over-abundant or under-abundant are shown in blue. We superimpose to our predictions constraints from Fermi-LAT [23], the yellow area being excluded.

panel of figure 7.2).

Whilst we have demonstrated that the lightest scotino could be a viable DM candidate from the point of view of the relic density, it is important to verify that dark matter indirect and direct detection bounds are at the same time satisfied. In figure 7.3, we present the value of the total DM annihilation cross section at zero velocity as a function of the scotino mass for all scanned scenarios satisfying the Z'-boson LHC limits. Configurations for which the relic density is found in agreement with Planck data are shown in red, whilst any other setup returned by the scan is shown in blue. In our predictions, we have moreover rescaled the DM annihilation cross section to its present-day density. We compare our predictions to the latest bounds derived from the Fermi satellite mission data [23]. We depict, as a yellow area, the parameter space region that is found out to be excluded. Most scanned scenarios naturally feature an annihilation cross section that is 1 or 2 orders of magnitude too small to leave any potentially visible signals in Fermi-LAT data, with a few exceptions where the annihilation cross section at present time is enhanced. In general, such an enhancement simultaneously leads to a reduction of the relic density so that Planck data is at the same time accommodated.

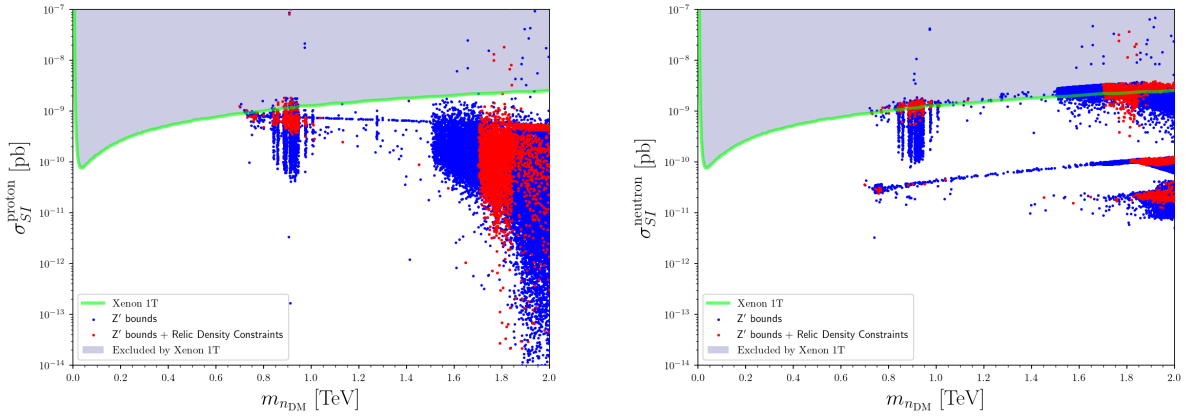

Figure 7.4: DM-proton (left) and DM-neutron (right) spin-independent scattering cross section as a function of the mass of the lightest scotino $m_{n_{\text{DM}}}$. Red points represent the scenarios featuring a relic density consistent with Planck data, and blue point any other scenario returned by the scan. We restrict the results to scenarios satisfying the LHC Z' bounds.

Equivalently, a significant fraction of the scenarios that are excluded by indirect detection bounds turn out to feature a relic density agreeing with cosmological data (the red points lying within the yellow contour). Fortunately, most potentially viable parameter regions from the relic density standpoint are unaffected by current indirect detection limits and will potentially stay so for some time by virtue of their correspondingly small annihilation cross sections.

In figure 7.4, we focus on DM direct detection bounds and represent the DM-proton (left panel) and DM-neutron (right panel) spin-independent scattering cross section $\sigma_{\text{SI}}^{\text{proton}}$ and $\sigma_{\text{SI}}^{\text{neutron}}$ as a function of the of the mass of the lightest scotino. Once again, our results are normalised to the present-day relic density and points compatible (incompatible) with Plank data are shown in red (blue). Our predictions are then compared with the results of the Xenon 1T experiment [155]. In the ALRSM, neutron-scotino scattering cross sections are naturally larger than proton-scotino scattering ones by virtue of the differences between the Z and Z' couplings to the up-type and down-type quarks, so that stronger constraints arise from the former process. Moreover, the distribution of points in three clusters, as visible in the right panel of figure 7.4, stem from two features. First, these clusters are associated with different Z' mass ranges, lighter Z'-bosons being associated with smaller neutron-DM scattering rates. Second, down-type quarks play a special role in the ALRSM as they do not couple to the Z'-boson. This impacts the DM-neutron scattering cross section (consequently due to the larger down-quark content of the neutron) whilst leading to a more 'continuous' behaviour for

the DM-proton scattering cross section. A large fraction of all scenarios accommodating the correct relic density are consequently excluded by the Xenon 1T limits on the neutron-DM scattering cross section. Few options featuring a scotino mass in the 700–1050 GeV range survive, made possible by a suppression of the Z'-boson exchange diagrams due to a larger Z' boson mass in those scenarios.

In conclusion, we were able to obtain scenarios satisfying DM relic density and direct and indirect detection constraints. The existence of those scenarios is however pretty constrained, in particular due to direct detection bounds that put severe requirements on the model spectrum, rendering it very predictable. In the surviving scenarios, the lightest scotino (*i.e.* our DM candidate) has a mass in the 750–1000 GeV window and a set of non-SM-like Higgs bosons are light. In particular, the lightest H_1^0 and A_1^0 bosons, as well as the $H_2^\pm$ boson, have masses in the 100–200 GeV window. Moreover, the next scalar state H_2^0 and pseudoscalar state A_2^0 are only mildly heavier, with masses in general around 400 GeV. The heaviest scalar H_3^0 is in contrast much heavier, with a mass roughly equal to twice the lightest scotino mass. As a consequence of the presence of the funnel topology, the DM annihilation cross section is predicted to be in the right range of values to accommodate Planck data. A small fraction of scenarios are moreover compatible with DM direct and indirect detection bounds. Another general feature is that those scenarios feature a potentially light W' boson, with a mass lying in the 1–2 TeV range, not excluded by the results of the LHC.

7.6 Scotino DM signal at colliders

In this section we explore the implications at the LHC of the cosmology-favoured scenarios that have emerged from our dark matter analysis. We choose three benchmark scenarios consistent with the constraints previously studied and provide their definition in terms of the model free parameters in the upper panel of table 7.3. As detailed in section 7.3, the scalar potential parameter $\lambda_2 = 0$ for all scenarios. Moreover, the small λ_3 value, together with the equality of all α_i parameters and the moderate κ value, implies that the A_1^0, H_1^0 and $H_2^\pm$ Higgs bosons are quite light (as derived from the relations presented in appendix B.1). We have also chosen scenarios with a small g_R value close to the theoretically allowed limit, which guarantees a light W'-boson (see section 7.4) and induces $v' \approx v_R \sim 7-8$ TeV. The breaking of the $SU(2)_{R'} \times U(1)_{B-L}$ symmetry at such a scale naturally leads to a Z'-boson mass of about 5 TeV for all benchmark scenarios and a W'-boson mass of about 1.5 TeV. This is more

	$\tan\beta$	g_R	v' [GeV]	λ_3	κ [GeV]	$\alpha_1 = \alpha_2 = \alpha_3$
BM I	4.58	0.374	7799	0.0196	-31.08	0.0144
BM II	1.78	0.370	6963	0.0237	-2.43	0.110
BM III	4.55	0.374	7799	0.0196	-30.38	0.0144

[GeV]	$M_{H_1^0}$	$M_{H_2^0}$	$M_{H_3^0}$	$M_{A_1^0}$	$M_{A_2^0}$	$M_{H_1^\pm}$	$M_{H_2^\pm}$
BM I	193	907	1546	193	907	907	194
BM II	82	213	1578	82	167	167	82
BM III	192	894	1546	192	894	894	192

[GeV]	$M_{Z'}$	$M_{W'}$	M_{n_1}	M_{n_2}	M_{n_3}	$M_{d'}$	$M_{s'}$	$M_{b'}$
BM I	4992	1460	756	971	1202	1500	1800	2000
BM II	5113	1288	909	1134	1223	1400	1822	2200
BM III	4992	1460	902	1023	1312	1500	1936	2821

Table 7.3: Values of the free ALRSM parameters defining our three benchmark scenarios **BM I**, **BM II** and **BM III** (upper panel) and resulting mass spectrum (middle and lower panels). All masses are given in GeV.

precisely shown in the lower and middle panels of table 7.3 in which we present the masses of all new physics fields. In the selection of our benchmark points, we impose the lightest scotino to have a mass in the [700–1050] GeV mass window, the **BM I** scenario focusing on a lighter DM option ($m_{n_{\rm DM}} \approx 750$ GeV) and the two other scenarios on a heavier setup ($m_{n_{\rm DM}} \approx 900$ GeV). As discussed in section 7.5, many Higgs states are quite light, with masses of about 200 GeV (**BM I** and **BM III** scenarios) or 100 GeV (**BM II** scenario). In addition, our benchmark points choice is LHC-driven, so that we target spectra in which the exotic down-type quarks are heavier than the W'-boson so that a typical model signature could consist of W'-boson pairs produced in association with jets through the $pp \to d'd' \to W'jW'j$ process, for instance.

An interesting feature of the model concerns the lightest charged Higgs boson $H_2^\pm$, that, from the LHC perspective, is long-lived, so that previous studies [284] are inapplicable. As seen in table 7.4, the $H_2^\pm$ decay width is indeed of about 2×10^{-18} GeV for the **BM I** and **BM III** scenarios, and of 2×10^{-20} GeV for the **BM II** case, so that those scenarios could be probed by searches for heavy stable charged particles (HSCP), the $H_2^\pm$ bosons being pair-produced via the Drell-Yan mechanism. The corresponding cross sections are given in table 7.4, for proton-proton collisions at centre-of-mass energies of 7, 8 and 13 TeV and

for electron-positron collisions at a centre-of-mass energy of 183 GeV. As the $H_2^\pm$ boson is lighter in the **BM II** scenario than in the other two scenarios, the associated predictions are larger in the **BM II** case. For instance, for proton-proton collisions at 13 TeV, the total production rate hence reaches about 414 fb, compared to about 18 fb for the **BM I** and **BM III** cases.

The related searches in 13 TeV LHC collisions exclude signal cross sections ranging from 10 to 100 fb, the exact limit value depending on the model [299–304]. The cross sections associated with **BM I** and **BM III** $H_2^\pm$-boson pair production lie at the border of the stau exclusion limits, so that it is possible that two those benchmark scenarios are excluded. However, a direct transposition of the limits is not straightforward as a consequence of the modeling of various detector effects, which renders any conclusive statement complicated. Similar conclusions hold for 7 and 8 TeV LHC search results [305–307]. On the other hand, all those searches specifically target HSCP with masses larger than 100 GeV, so that they are unsensitive to the **BM II** scenario. For the latter, one must thus rely on LEP results, covering the [45.9, 89.5] GeV mass range [308]. Upper limits on typical HSCP signal cross sections of 0.05–0.19 pb have been extracted from data, but again for models different from the one investigated in this work. Such a model dependence in the results once again prevents us from reinterpreting the results in the ALRSM framework. As HSCP search results may consist in a very general smoking gun on the model, we strongly encourage the LHC experimental collaborations to provide information allowing one to recast of their search precisely enough, as to be able to provide limits for the model considered in this work. In the meantime, we focus on other probes for the model.

The heavier charged Higgs state $H_1^\pm$ could in principle be constrained by more standard searches for additional Higgs states, such as the one of ref. [309]. Those searches are however always targeting a specific production mode and a given decay channel which are not relevant in the cosmology-favoured ALRSM case. For example, the CMS [309] and ATLAS [310] collaborations have investigated the LHC sensitivity to a charged Higgs boson decaying in the $H^\pm \to \tau^\pm \nu_\tau$ mode. In the heavy $H_1^\pm$ case (scenarios **BM I** and **BM III**), cross sections of a few fbs are excluded whilst in the light case (**BM II** scenario), the analysis targets charged Higgs boson production from the rare decay of a top quark. For heavier charged Higgs bosons, analyses of charged Higgs boson production and decay in a tb final state or heavy Higgs boson production in association with a tb pair or a Wbb system have also been carried on (see, *e.g.*, refs. [311, 312]).

Benchmarks	**BM I**	**BM II**	**BM III**
$\Gamma(H_1^\pm)$[GeV]	3.07	1.9×10^{-3}	3.07
$\sigma(pp \to H_1^\pm)$ @ 13 TeV [pb]	6.503×10^{-5}	0.04352	6.901×10^{-5}
$\sigma(pp \to H_1^\pm W^\mp b\bar{b})$ @ 13 TeV [pb]	2.723×10^{-3}	2.44	2.919×10^{-3}
$\sigma(pp \to H_1^\pm t\bar{b} + \text{h.c.})$ @ 13 TeV [pb]	2.664×10^{-3}	2.374	2.859×10^{-3}
$\Gamma(H_2^\pm)$[GeV]	1.93×10^{-18}	2.62×10^{-20}	1.85×10^{-18}
$\sigma(pp \to H_2^\pm H_2^\mp)$ @ 7 TeV [fb]	5.412	163.3	5.588
$\sigma(pp \to H_2^\pm H_2^\mp)$ @ 8 TeV [fb]	7.153	199.8	7.392
$\sigma(pp \to H_2^\pm H_2^\mp)$ @ 13 TeV [fb]	18.18	414.7	18.71
$\sigma(ee \to H_2^\pm H_2^\mp)$ @ 183 GeV [fb]	-	161.1	-
$BR(H_1^\pm \to t\bar{b})$	99.6 %	–	99.6 %
$BR(H_1^\pm \to Wb\bar{b})$	–	80.5 %	–
$BR(H_1^\pm \to c\bar{s})$	–	8.9 %	–
$BR(H_1^\pm \to \tau\nu)$	–	4.83 %	–
$BR(H_1^\pm \to c\bar{b})$	–	2.1 %	–

Table 7.4: Properties of the light charged Higgs states for the **BM I**, **BM II** and **BM III** benchmark scenarios.

We have compared, for all the experimentally relevant signatures, the corresponding predictions (reported in table 7.4) in the considered ALRSM scenarios with the most recent bounds. The cross sections excluded at the 95% confidence level have been found to be orders of magnitude larger than our model predictions. Similarly, we have verified that the corresponding mass ranges (for the heavy stable H_2 state) are not excluded by LEP [313].

The light neutral states H_1^0 and A_1^0 are also long-lived, and can therefore leads to a missing-energy signatures (as they cannot decay into lepton or quark pairs). However, in the corresponding considered spectrum, they can only be produced from rare decays of exotic quarks, so that this gives rise to signatures potentially worth investigating in order to discover or exclude the model. In the following, we focus instead on more abundantly produced final states.

In table 7.5, we present, for each of the considered benchmark scenarios, predictions for the dark matter features studied in section 7.5. Each scenario leads to predictions compatible with the cosmological experimental bounds by virtue of a different dynamics. In the first **BM I** scenario, the DM annihilation cross section is dominated by annihilations into Higgs-boson pairs ($\sim 60\%$) as well as into pairs of SM gauge bosons ($\sim 35\%$), and fermions to a smaller

	$\Omega_{\rm DM}h^2$	$\sigma_{\rm SI}^{\rm proton}$ [pb]	$\sigma_{\rm SI}^{\rm neutron}$ [pb]	$\langle\sigma v\rangle$ [cm^{3}s^{-1}]
BM I	0.118	8.08×10^{-10}	2.88×10^{-11}	7.81×10^{-28}
BM II	0.120	8.09×10^{-10}	8.37×10^{-10}	3.29×10^{-27}
BM III	0.119	7.72×10^{-10}	3.67×10^{-11}	1.17×10^{-27}

Table 7.5: Predictions, for the **BM I**, **BM II** and **BM III** scenarios, of the observables discussed in our dark matter analysis of the previous section.

	$\sigma(pp \to Z')$ [fb]	$\sigma(pp \to W'W')$ [fb]	$\sigma(pp \to W'd')$ [fb]	$\sigma(pp \to d'd')$ [fb]
BM I	0.821	0.0458	0.574	1.65
BM II	0.871	0.0672	1.080	2.72
BM III	0.810	0.0465	0.564	1.61

	BR($Z' \to \ell\ell$)	BR($W' \to e\ n_{\rm DM}$)	BR($W' \to \mu\ n_{\rm DM}$)	BR($W' \to \tau\ n_{\rm DM}$)
BM I	0.166	0.203	0.054	0.020
BM II	0.167	0.158	0.056	0.016
BM III	0.171	0.178	0.063	0.018

	BR($d' \to W'\ u$)	BR($d' \to W'\ c$)	BR($d' \to H_2^\pm\ u$)	BR($d' \to H_2^\pm\ t$)
BM I	0.764	0.041	0.089	0.047
BM II	0.919	0.049	0.014	≈ 0
BM III	0.764	0.041	0.089	0.048

Table 7.6: Predictions, for the **BM I**, **BM II** and **BM III** scenarios, of various quantities relevant for the associated LHC phenomenology at a centre-of-mass energy of 13 TeV. In our notation, ℓ equivalently denotes an electron or a muon.

extent. Such an annihilation pattern is typical of light scotino DM setups, as illustrated in the figure 7.2. In the **BM II** scenario, DM annihilates essentially in $W'^{\mp}H_2^\pm$ systems, whilst in the **BM III** scenario, it dominantly annihilates into pairs of SM charged leptons ($\sim 50\%$), quarks ($\sim 30\%$) and neutrinos ($\sim 15\%$). The **BM II** and **BM III** scenarios hence illustrate the two classes of viable scenarios emerging from more moderately heavy scotino dark matter ($m_{n_{\rm DM}} \in [800, 1000]$ GeV).

In table 7.6, we show predictions relevant for the LHC phenomenology at a centre-of-mass energy of 13 TeV for our three benchmark scenarios. Production cross sections for various processes involving new physics states are presented in the upper panel, whilst the middle and lower panels include the dominant branching ratios of the extra gauge bosons and exotic down-type quarks. We ignore monojet production via the associated production of a

scotino pair with a hard jet as this process occurs at a too small rate ($\mathcal{O}(1)$ fb for an optimistic 100 GeV requirement on the leading jet). Other new physics processes generally occur at a larger rate, as shown in the table. For all three scenarios, Z'-boson production is small enough relatively to the LHC limits (by construction of our benchmarks). The rate is hence of about 0.15 fb after accounting for the Z'-boson branching ratio into electron and muon pairs, $\text{BR}(Z' \to \ell\ell) \sim 17\%$ for ℓ equivalently denoting an electron or a muon. Consequently this makes the Z' signal difficult to observe, even with more luminosity. As the W'-boson only couples to SM up-type quarks and exotic down-type quarks, it cannot be singly produced. We therefore focus on other processes typical of the ALRSM that instead involve pairs of W' bosons and exotic d' quarks. The production of a pair of W'-bosons leads to the production of multileptonic systems in association with missing transverse energy carried away by scotinos, as illustrated by the branching ratio information of the middle panel of table 7.6. The total W'-boson branching ratio into leptons and scotinos $\text{BR}(W' \to \ell n_{\text{DM}})$ reaches 20–30% in all three scenarios, after including the subdominant tau-lepton contribution. The resulting signal cross section (including the branching ratio into a lepton-scotino pair) is then about 0.010 fb. Such a rate is far beyond the reach of typical multileptons plus missing energy searches at the LHC, as confirmed by reinterpreting [314, 315] and extrapolating [316] the results of the CMS search of ref. [317] targeting electroweak superpartner production and decay in the leptons plus missing energy mode to 3 ab^{-1} with MadAnalysis 5[3]. This signal, featuring a production times decay rate observable in the 10 ab range at the LHC (for a centre-of-mass energy of 13 TeV), could however become visible at future colliders.

The upper panel of table 7.6 also includes cross sections relevant for $d'd'$ and $d'W'$ production. Such processes yield production cross sections in the 1 fb range, which makes them potentially more appealing as a door to observing ALRSM at the LHC. Taking into account the large $d' \to W'j$ branching fraction, a key signature of those processes is comprised of two leptons, jets and missing transverse energy carried away by the scotinos emerging from the W'-boson decays. This signature is also typically expected from supersymmetric squark production and decay, so that the results of supersymmetry searches in the opposite-sign dilepton, jets and missing energy mode could be reinterpreted to constrain the ALRSM. We therefore recast the results of the CMS stop search of Ref. [24] with MadAnalysis 5[4], and extrapolate our findings to 3 ab^{-1}. We present our results in figure 7.5. The LHC significance

[3]Details on the reimplementation of the CMS electroweak superpartner search of ref. [317] in MadAnalysis 5 can be found in refs. [318, 319].

[4]Details on the reimplementation of the CMS stop search of ref. [24] in MadAnalysis 5 can be found in refs. [320, 321].

is evaluated according to two measures, labelled by s and Z_A, that are given by

$$s = \frac{S}{\sqrt{B+\sigma_B^2}} \quad \text{and} \quad Z_A = \sqrt{2\left[(S+B)\ln\left[\frac{(S+B)(S+\sigma_B^2)}{B^2+(S+B)\sigma_B^2}\right] - \frac{B^2}{\sigma_B^2}\ln\left[1+\frac{\sigma_B^2 S}{B(B+\sigma_B^2)}\right]\right]}, \tag{7.20}$$

where the number of selected signal and background events are denoted by S and $B \pm \sigma_{\mathrm{B}}$ respectively. The first method (s) is rather standard, whereas the second one (Z_A) is more adapted to small numbers of background events [322]. Moreover we consider a signal where both the $W'd'$ and the $d'd'$ channels contribute. It turns out that while the LHC has currently very little sensitivity to the signal (*i.e.* with 36 fb^{-1}), sensitivity levels of about 3σ (for the **BM I** and **BM III** scenarios) to 5σ (**BM II** scenario) could be reached at its high-luminosity operation phase (*i.e.* with 3000 fb^{-1}) with a conservative level of systematical uncertainties of 20%. In the figure, we also show how a better understanding of the background (corresponding to reduced uncertainties) could guarantee a discovery with luminosities as low as about 750 fb^{-1} (5% of systematics) or 1500 fb^{-1} (10% of systematics) for the most optimistic **BM II** scenario. For the two other more difficult to observe scenarios, the signal is suppressed so that luminosities of about 1500-2000 fb^{-1} should be necessary for a discovery with a level of 5% systematics.

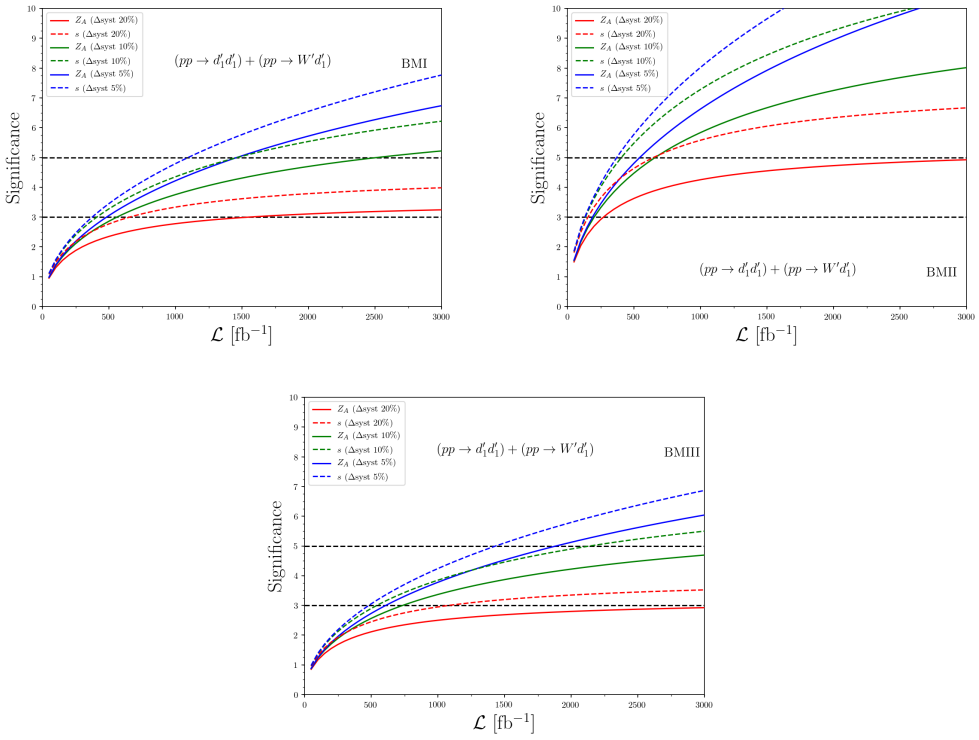

Figure 7.5: LHC sensitivity to a signature comprised of a dilepton, jets and missing energy in the context of the **BM I** (upper left), **BM II** (upper right) and **BM III** (lower) scenarios. We present our results as a function of the luminosity and recast the CMS stop search of ref. [24], and plot the two significance measures of eq. (7.20).

Chapter 8

Conclusion

In chapter 3, we analyzed the predictions of the mass spectrum in the BLRSSM framework with universal boundary condition, highlighting the solutions consistent with the DM restrictions (relic density and spin independent cross sections with nucleons) for both neutralino and sneutrino LSP scenarios. We found that the stop and sbottom masses are between 2-3 TeV, and the chargino can be degenerate with the LSP neutralino between 300-500 GeV. In addition, the relic density constraint can be satisfied for masses in the range $300 \lesssim m_{\widetilde{\chi}_1^0} \lesssim 800$ GeV. $\widetilde{H}$ dominated or mixed LSP neutralino solution can be obtained below 300 GeV, however these solutions are ruled out by the XENON1T spin independent cross section exclusion curve. When all DM constraints are taken into account, the model favours LSP neutralinos with masses between $500 \lesssim m_{\widetilde{\chi}_1^0} \lesssim 800$ GeV, bino-dominated, and with composition 60% $\widetilde{B}_R$ - 40% $\tilde{B}$. We also showed that, when the LSP is neutralino, A_1 and h_3 are funnel channels for pair-producing them.

In addition, the model allows in principle a sneutrino LSP where its content can be either right-handed dominated or mixed, $\widetilde{\nu}_R$ and $\widetilde{S}$, with masses between 250-1300 GeV. In this sense, sneutrino LSP solutions can be lighter than the neutralino LSP ones. Purely right-handed dominated sneutrino LSP solutions have difficulty to satisfy the relic density constraint and only mixed ones survive. Also, most of the sneutrino LSP solutions are consistent with the XENON 1T spin independent cross section exclusion curve. However, strict imposition of the Z' mass bounds basically rule out the sneutrino solutions, while not having any effect on the neutralino LSP parameter space. This is one of the most important predictions of the model.

The parameter spaces corresponding to neutralino and sneutrino are quite different.

If allowed, sneutrino LSP solutions favor low singlet higgsino mass parameter, μ_R, and the second lightest neutral Higgs boson as singlet, while neutralino LSP favor larger μ_R parameters. Sneutrino LSP solutions are spread out over the whole range of $\tan\beta$, while neutralino solutions are restricted in the $40 \lesssim \tan\beta \lesssim 60$. Neutralino LSP solutions allow for degenerate masses of the two lightest neutral Higgs bosons, while the sneutrino LSP, although favoring a light m_{h_2}, does not. The anomaly in the anomalous magnetic moment of the muon favors neutralino LSP contributions, where for a large range of scalar masses, and a more restricted one for gauginos and higgsinos, the corrections are within 2σ of the experimental result, while sneutrino LSP solutions can at best produce results within 3σ of the desired values.

We analyzed collider signatures of this proposed scenario, including all constraints, and they are not promising, even at the high-luminosity LHC. The largest cross sections are obtained for chargino/neutralino production, and they are at most of $\mathcal{O}(1)$ fb, without including cascade decays into leptons which would reduce them further. In the future, collider signals could be enhanced by relaxing some of the severe constraints on the model, such as the universality conditions, and finding suitable cuts to enhance signal versus background. This may extend the parameter space, allowing sneutrino LSP back into the consideration. Work in these directions is underway.

However, under the present scenario, the Z' mass lies just below the sensitivity of LHC at 36 fb^{-1}, and would be seen during the LHC Run 2, with a modest increase in luminosity. For dark matter detection, direct searches remain the most promising. Projected sensitivities of XENONnT and particularly of DARWIN(200t $\times$ y) would observe or rule out the most promising region of neutralino LSP candidates (500-800 GeV). These features are hopeful indicators for the accessibility of the BLRSSM model in the near future.

In chapter 4, we have presented an analysis of the secluded UMSSM, a non-minimal SUSY scenario wherein the gauge symmetry of the MSSM is augmented by a $U(1)'$ group and where a secluded sector is also added in the form of three additional scalar superfields. Their role is to separate the SUSY-breaking scale from the mass of the Z', the gauge boson introduced by the additional gauge symmetry following its spontaneous breaking, so that the latter can have a value well within the LHC reach irrespectively of the SUSY mass scale.

Our analysis here has highlighted, in particular, some novel phenomenological features pertaining to this BSM scenario, which would make it distinguishable from the MSSM or $E6$ motivated UMSSM scenarios. For a start, the Z' can be leptophobic without invoking gauge kinetic mixing. Thus one can naturally lower the experimentally imposed limits on its mass

coming from its LHC hadroproduction followed by di-lepton and di-jet decays. In addition, and setting it apart from that of $U(1)'$ scenarios with gauge kinetic mixing, the Z' is also d-quark-phobic, allowing one to reduce its mass constraints event further.

Then, we have shown that the model predicts the existence of very light charginos and neutralinos, the lightest of the latter being a singlino-like DM candidate satisfying relic density constraints as well as direct and indirect detection bounds. In fact, alongside this new singlino state, an LSP with mass $M_{\tilde{\chi}_1^0} \lesssim 50$ GeV, our BSM scenario also accommodates a similarly light lightest chargino companion, with $M_{\tilde{\chi}_1^\pm} \lesssim 350$ GeV, both of which are respecting collider constraints. Furthermore, the next-to-LSP and next-to-next-to-LSP are higgsinos and, together with the lightest chargino, they are largely responsible (once appropriately combined with the lightest sleptons in one-loop Feynman diagrams) for obtaining a value for the muon anomalous moment consistent with experimental measurements at 1σ.

Finally, armed with such specific model setup, we have investigated the prospects of detecting such a light Z' boson in its SUSY cascade decays via the aforementioned lightest charginos and neutralinos, eventually yielding a di-lepton final state in presence of significant missing transverse energy. The fact that the model is d-quark phobic, useful to reduce the mass constraints, has an adverse effect on the production cross section for Z', rendering it smaller than in the $E6$ motivated UMSSM. In addition, the S, T, U parameters impose conditions on the $U(1)'$ associated charges, constraining them to be small. The secluded UMSSM is a good model for loosening Z' mass bounds, but no so promising for signal observability.

Requiring the parameter space to satisfy all experimental conditions, including the DM and $(g-2)_\mu$ ones simultaneously, or just the relic density, we have devised most favourable benchmark points with $M_{Z'} \approx 3.3$ TeV. Relaxing the $(g-2)_\mu$ requirement, our second benchmark allows $M_{Z'} \approx 2.3$ TeV. Of the two benchmarks, the latter one shows more promise to be observed at the HE-LHC at 3σ or better, as proved from a prototypical MC analysis performed, while the former would be observed only assuming small systematic errors. Our analysis should justify dedicated searches with real data from ATLAS and/or CMS.

In chapter 5, we have explored the low scale and DM implications of an E_6 based UMSSM, with generic mixing between the two ensuing Abelian groups, mapped in terms of the standard angle θ_{E_6}. Within this scenario, we have restricted the parameter space such that the LSP is always the lightest neutralino $\tilde{\chi}_1^0$, thus serving as the DM candidate. We have then applied all current collider and DM bounds onto the parameter space of this construct,

including a refined treatment of Z' mass and coupling limits from LHC direct searches via $pp \to ll$ and $pp \to WW$ processes, allowing for interference effects between their Z' and γ, Z components. We have done so as compliance of such a generic E_6 inspired UMSSM with all other experimental constraints necessarily requires a gauge kinetic mixing between the Z and Z' states (predicted from RGE evolution from the GUT to the EW scale), which in turn onsets a significant $Z'WW$ coupling. So that, for Z' masses in the TeV range, the $Z' \to WW$ decay channel overwhelm the $Z' \to ll$ one, thus producing a wide (yet, still perturbative) Z' state and so that it is the former and not the latter search channel that sets the limit on $M_{Z'}$, at 4 TeV, significantly below what would be obtained in a NWA treatment of the Z'. To achieve this large Z' width scenario, the fundamental parameters responsible for it, i.e., the gauge kinetic mixing coefficient and the aforementioned E_6 mixing angle, are found to be $0.2 \lesssim \kappa \lesssim 0.4$ and $-1 \lesssim \theta_{E6} \lesssim -0.8$ radians, respectively. Curiously, the values of θ_{E_6} that survive our analysis are not those of currently studied models, known as ψ, N, I, S, χ and η types. As for the DM sector, solutions consistent with all current experimental bounds coming from relic density and direct detection experiments were found for two specific LSP compositions: a higgsino-like LSP neutralino with 0.9 TeV $\lesssim m_{\tilde{\chi}_1^0} \lesssim$ 1.2 TeV and a singlino-like LSP neutralino with 0.9 TeV $\lesssim m_{\tilde{\chi}_1^0} \lesssim$ 1.6 TeV. In this respect, we have been able to identify chargino-neutralino coannihilation and A (the pseudoscalar Higgs state) mediated resonant annihilation as the main channels rendering our DM scenario consistent with WMAP and Planck measurements, with the LSP state being more predominantly singlino-like than higgsino-like. Further, as for SI and SD $\tilde{\chi}_1^0$ - n scattering cross section bounds from DM direct detection experiments, we have seen that both DM scenarios are currently viable (i.e., compliant with present limits) yet they could be detected by the next generation of such experiments (though we did not dwell on how the two different DM compositions could be separated herein). In fact, other than in the DM sector, further evidence of the emerging E_6 scenario may be found also in collider experiments, in both the Z' and SUSY sectors. In the former case, in the light of the above discussion, it is clear that direct searches at the LHC Run 3 for heavy neutral resonances in WW final states may yield evidence of the Z' state, though such experimental analyses should be adapted to the case of a wide resonance. In the latter case, since our set up yields a rather heavy sparticle spectrum for third generation sfermions ($m_{\tilde{t},\tilde{b}} \gtrsim 4$ TeV and $m_{\tilde{\tau}} \gtrsim 5$ TeV) as well as the gluino ($m_{\tilde{g}} \gtrsim 4$ TeV), chances of detection may stem solely from the EW -ino sector, where some relevant masses can be around or just below the 1 TeV ballpark, with $pp \to \tilde{\chi}_2^0 \tilde{\chi}_3^0 \to (h/Z)(h/Z)\tilde{\chi}_1^0 \tilde{\chi}_1^0$ being a potential discovery channel at the HL-LHC. Addressing quantitatively these three

future probes of our E_6 based UMSSM was beyond the scope of this paper, but this will be the subject of forthcoming publications.

In chapter 6, we performed a comprehensive analysis of mass bounds on W_R gauge boson in a LRSM with general gauge couplings, VEVs, mixing angles and right-handed quark mixing matrix. We reinterpret the CMS and ATLAS analyses using this scenario, and find considerably relaxed bounds on W_R masses. We divide the parameter space into two cases, one for $M_{W_R} < M_{\nu_R}$, and another for $M_{W_R} > M_{\nu_R}$, as this ordering has implications on W_R decay channels.

When $M_{\nu_R} > M_{W_R}$, decays of right-handed W-boson into a top quark and a bottom quark or into two jets are dominant. We compare our predictions with the results of CMS and ATLAS at $\sqrt{s} = 13$ TeV, integrated luminosity of 35.9 fb^{-1} and 37.0 fb^{-1}, respectively. 95% CL upper limits on the product of the W_R boson production cross section with its branching fraction to a top and a bottom quark ($t\bar{b}$) or with the branching fraction to two jets (jj) are calculated as a function of the W_R boson mass. These analyses recover the excluded ranges obtained by CMS and ATLAS ranging from 55.4% for the two jets channel to 65.5% for a top and bottom quark channel in the limit of exact left-right symmetry and small $\tan\beta$, while when relaxing these limits, much less stringent constraints are obtained on the production of W_R bosons decaying to a top and a bottom quark and on W_R bosons decaying into two jets. Note that increasing $\tan\beta$ only serves to enhance the non-fermionic decays $W_R \to W_L h$ and $W_R \to W_L Z_L$, whose branching ratios are small for allowed values of $\tan\beta$, 2% at most. While the results are not particularly sensitive to $\tan\beta$, they depend crucially on g_R and $V^R_{\rm CKM}$. The least constrained choice for this scenario is setting $g_L \neq g_R = 0.37$, $\tan\beta = 0.5$ and $V^L_{\rm CKM} \neq V^R_{\rm CKM}$, when the observed (expected) lower limit on W_R mass at 95% CL is 2360 (1940) GeV for the tb channel and 2000 (2010) GeV for the jj channel.

When $M_{\nu_R} < M_{W_R}$, we investigate exclusion bounds for W_R bosons and heavy right-handed Majorana neutrinos masses, using the final states containing a pair of charged leptons (electrons or muons), and two jets ($\ell\ell jj$), with $\ell = e, \mu$. We compare our result with the results obtained by CMS (ATLAS) with $\mathcal{L} = 35.9$ fb^{-1} (36.1 fb^{-1}) at $\sqrt{s} = 13$ TeV at the LHC. We again reproduce the CMS and ATLAS results for $g_L = g_R$, $\tan\beta = 0.01$ and $V^L_{\rm CKM} = V^R_{\rm CKM}$, and find three different parameter choices which relax the current W_R and ν_R mass exclusion limits. Assuming that gauge couplings and CKM matrices in the right-handed sector are different from those of the SM, a region in the two-dimensional plane $(M_{W_R} - M_{\nu_R})$ excluding a smaller range of right-handed neutrino masses is found at 95%

CL. Based on the scenario where we allow $g_L \neq g_R = 0.37$, $\tan\beta = 0.5$ and $V^L_{\rm CKM} \neq V^R_{\rm CKM}$, a W_R boson decaying into a right-handed heavy neutrino is excluded at 95% CL up to a mass of 3100 GeV in the ee channel, and 3350 GeV in the $\mu\mu$ channel, providing less stringent limits on this parameter space. The excluded region for M_{W_R} extends to about $M_{W_R} \simeq$ 3.1 TeV, for $M_{\nu_R} \simeq 2.0$ TeV in the electron channel and about $M_{W_R} \simeq 3.3$ TeV, for M_{ν_R} $\simeq 2.0$ TeV in the muon channel. Conversely, the M_{ν_R} limits reach about 2.2 TeV for M_{W_R} $= 2.6$ TeV in the electron channel and 2.6 TeV for $M_{W_R} = 2.8$ TeV in the muon channel. We also analyze the region where $M_{\nu_R} > M_{W_R}$ in the $M_{W_R} - M_{\nu_R}$ contour plot, but find no excluded solutions in this region. These results also recover the experimentally excluded ranges, further relaxing the limits obtained by CMS and ATLAS, ranging from 66% for BR's in the $eejj$ channel to 71% for $\mu\mu jj$ channel. Overall our results yield weaker limits on W_R mass from the production of W_R bosons decaying into $\ell\ell jj$, yielding hope that W_R could be discovered at HL-HE LHC.

Finally, allowing $g_L \neq g_R = 0.37$ and $V^L_{\rm CKM} \neq V^R_{\rm CKM}$ will not have significant consequences on other sectors of the model. Both the singly charged and doubly charged Higgs bosons δ^+_R and δ^{++}_R are expected to be heavy. Even so, their production mechanism is dominated by photon-mediated Drell Yan, or $\gamma\gamma$ fusion, and their branching ratios are independent of g_R. This leads further support to W_R production and decay as being most promising signal to test this scenario.

The Standard Model is plagued by several theoretical inconsistencies, while being confirmed by experiments to a high degree of accuracy. Still, there are at least two outstanding experimental facts which the SM does not explain: neutrino masses and dark matter. The standard left-right symmetric model (LRSM) naturally incorporates neutrino masses. However, without *ad hoc* additional particles it does not include any viable dark matter candidate. In chapter 7 ,we have considered in this work an alternative realisation of the left-right symmetric model, the so-called ALRSM, that can also be obtained from the breaking of an E_6 Grand Unified setup. Such a class of models has the advantage to offer naturally solutions for *both* neutrino masses and dark matter problems of the SM. Unlike in the LRSM, in ALRSM the $SU(2)_{R'}$ doublets of right-handed fermions contain exotic states, namely down-type-like quarks d' in the quark sector, and neutrino-like scotinos n in the lepton sector. The latter, being part of a doublet, couples to the extra W' and Z' bosons. In this work, we have shown that this property of the scotino is sufficient to promote it as a *bona fide* dark matter candidate. Its gauge couplings indeed allow for a sufficient increase in the DM annihilation cross section so that the relic density, as measured by the Planck collaboration, can be

accommodated.

Imposing various constraints on the model, such as requiring a cosmology compatible with data (relic density, DM direct and indirect detection) and extra gauge bosons not excluded by the LHC results, we have shown that scotino DM must have a mass in a relatively narrow range of 750–1000 GeV (while ignoring heavier options less appealing from the point of view of new physics at current collider experiments). In addition, this restriction imposes strict mass bounds on several of the Higgs bosons of the model. In particular, at least one scalar, one pseudoscalar and one charged Higgs boson have to be light, in the 100–400 GeV mass regime. Moreover, the W' gauge boson does not couple to pairs of ordinary fermions so that its mass is mostly unconstrained, unlike the one of the W_R boson of the usual LRSM. The only existing bounds arise indirectly, from limits on the Z'-boson mass derived from its non-observation in LHC data. This however still allows the W' boson to be light, with a mass of $\mathcal{O}(1)$ TeV. The model also predicts additional light Higgs states. Given the structure of the model, they however evade all present collider bounds. Of these, a light charged Higgs boson is expected to be long lived, while neutral states would manifest themselves as missing transverse energy at colliders.

We have devised three benchmark scenarios and studied the possibility of observing those DM-favoured ALRSM realisations at the LHC. We have tested the relevance of the ALRSM signatures arising from the $pp \to W'W'$, $W'd'$ and $d'd'$ processes. For our choice of spectra, we have shown that the latter two processes have similar cross sections, so that they could both provide an opportunity for the discovery of the ALRSM at the LHC. Out of the three benchmarks, the most promising one can indeed yield a 5σ discovery within the future high-luminosity run of the HL-LHC, the exactly luminosity needed depending on assumptions made on the systematic errors. The two other scenarios, associated with smaller cross sections, are harder to probe but good prospects are foreseen provided one gets a better control of the background. On the other hand, HSCP searches could possibly consist in smoking guns on the model, provided that future results are either directly interpreted in the ALRSM framework or are released together with enough information for a proper recasting.

In summary, the ALRSM analysed here has numerous attractive features once we impose that its cosmological properties accommodate data: light Higgs bosons, a light charged gauge boson, neutrino masses, and a viable dark matter candidate. The latter in particular renders the spectrum well-defined. In addition, such ALRSM scenarios emerge naturally

from a grand unified E_6 theory, a promising UV completion of the SM, and they offer the promise of being detectable at the high-luminosity LHC.

Last but not least, we studied the predictions of the mass spectrum in the BLRSSM framework with universal boundary condition. However, there are some of the advantages of considering non-universal masses and /or boundary conditions. Resolution of the little hierarchy problem, describing the tension between the observed Higgs boson mass and the prediction of the MSSM. Also, the ATLAS result on direct SUSY searches reinforces the exclusion of the low mass part of the stau co-annihilation region. Constraints from B meson decays lead support for the supersymmetric parameter space for $\tan\beta \geq 30$, where the resonant annihilation region of the SUSY dark matter relic density is also effective, reinforcing the exclusion of the low mass part of the latter. The direct DM detection experiments strengthen incompatibility between the SUSY explanations of the observed muon $g-2$ anomaly and DM relic density with the 125 GeV Higgs boson mass, unless scalar masses are non-universal.

It is also crucial to relate W′ and Z′ signal at the collider since they are completely independent searches at the LHC. One can investigate the LHC phenomenology of a class of realistic theories beyond the SM with the electroweak gauge group extended to include an additional $SU(2)'$ gauge group, which predicts the existence of both W' and Z' bosons. One way to take into account the correlations between W' and Z' is to work in a general framework, that is to parameterize the interaction of new heavy resonances in a model independent manner. In this scenario, the Lagrangian describing the interactions includes many free parameters. Alternatively, it may desirable to restrict this freedom and chose a simple specific model. For example, in the Sequential Standard Model (SSM) [323, 324], the boson couplings are assumed to be SM-like and the only free parameter is their mass, possibly together with a global normalization factor for the coupling strength. As a future study, I try to provide a framework enabling one to cross reference W′ & Z′ searches. Meaning, these objects can come together in BSM scenarios, so any information experimentally obtained (exclusion, evidence, etc.) on one such particle can be transferred (under some theoretical assumption) onto the other. For example, this can avoid W' results being interpreted in parameter spaces of BSM scenarios which may have already been excluded by Z' results interpreted in the same framework, and vice versa. Or, more interestingly, if an anomaly is seen in one case, this would point to where the correlated anomaly must be seen in the other case, if the underlying model is correct. In doing so, I use both cross section and asymmetry (charge and spin) observables, the latter being particularly useful for broad W′ & Z′. I try to parametrise this correlation in a form that can capture many models at once.

Appendix A

Renormalization Group Equations for BLRSSM

We gather below some of the relevant equation referred to in the paper.

$$\beta_{\mu}^{(1)} = \mu\Big(-3g_L^2 + 3\mathrm{Tr}\Big(Y_d Y_d^{\dagger}\Big) + 3\mathrm{Tr}\Big(Y_u Y_u^{\dagger}\Big) - g_R^2 - g_{RB}^2 + \mathrm{Tr}\Big(Y_e Y_e^{\dagger}\Big) + \mathrm{Tr}\Big(Y_v Y_v^{\dagger}\Big)\Big)\,. \quad \text{(A.1)}$$

$$\beta_{\mu_R}^{(1)} = -\frac{1}{2}\mu_R\Big(2g_R^2 + 2g_{RB}^2 - 2\sqrt{6}g_{BL}g_{RB} - 2\sqrt{6}g_{BR}g_R + 3g_{BL}^2 + 3g_{BR}^2 - 2\mathrm{Tr}\Big(Y_s Y_s^{\dagger}\Big)\Big)\,. \quad \text{(A.2)}$$

$$\begin{aligned}\beta_{B_\mu}^{(1)} = \quad & +B_\mu\Big(-3g_L^2 + 3\mathrm{Tr}\Big(Y_d Y_d^{\dagger}\Big) + 3\mathrm{Tr}\Big(Y_u Y_u^{\dagger}\Big) - g_R^2 - g_{RB}^2 + \mathrm{Tr}\Big(Y_e Y_e^{\dagger}\Big) + \mathrm{Tr}\Big(Y_v Y_v^{\dagger}\Big)\Big) \\ + \quad & 2\mu\Big(2g_R g_{RB} M_{BR} + 3g_L^2 M_2 + 3\mathrm{Tr}\Big(Y_d^{\dagger} T_d\Big) + 3\mathrm{Tr}\Big(Y_u^{\dagger} T_u\Big) + g_R^2 M_4 + g_{RB}^2 M_1 + \mathrm{Tr}\Big(Y_e^{\dagger} T_e\Big) \\ + \quad & \mathrm{Tr}\Big(Y_v^{\dagger} T_\nu\Big)\Big)\,. \end{aligned} \quad \text{(A.3)}$$

$$
\begin{aligned}
\beta^{(1)}_{B_{\mu_R}} = \quad & +B_{\mu_R}\Big(-\frac{3}{2}g^2_{BL} - \frac{3}{2}g^2_{BR} - g^2_R - g^2_{RB} + \sqrt{6}g_{BL}g_{RB} + \sqrt{6}g_{BR}g_R + \mathrm{Tr}\Big(Y_sY_s^\dagger\Big)\Big) \\
& + \mu_R\Big(3g^2_{BL}M_1 + 2g^2_{RB}M_1 - 2\sqrt{6}g_{BR}g_{RB}M_{BR} + 4g_Rg_{RB}M_{BR} \\
& - 2g_{BL}\Big(-3g_{BR}M_{BR} + \sqrt{6}g_{RB}M_1 + \sqrt{6}g_RM_{BR}\Big) \\
& + 3g^2_{BR}M_4 - 2\sqrt{6}g_{BR}g_RM_4 + 2g^2_RM_4 + 2\mathrm{Tr}\Big(Y_s^\dagger T_s\Big)\Big)\,.
\end{aligned}
\tag{A.4}
$$

$$
\begin{aligned}
\beta^{(1)}_{m^2_{H_u}} = \quad & -2g^2_R|M_4|^2 - 6g^2_L|M_2|^2 - 2g_{RB}\Big(g_{RB}M_1 + g_RM_{BR}\Big)M_1^* \\
& - 2\Big(g^2_RM_{BR} + g^2_{RB}M_{BR} + g_Rg_{RB}\Big(M_1 + M_4\Big)\Big)M^*_{BR} - 2g_Rg_{RB}M_{BR}M_4^* \\
& + g_{RB}\sigma_{1,1} + g_R\sigma_{1,3} + 6m^2_{H_u}\mathrm{Tr}\Big(Y_uY_u^\dagger\Big) + 2m^2_{H_u}\mathrm{Tr}\Big(Y_vY_v^\dagger\Big) + 6\mathrm{Tr}\Big(T^*_uT_u^T\Big) + 2\mathrm{Tr}\Big(T^*_\nu T_\nu^T\Big) \\
& + 2\mathrm{Tr}\Big(m^2_lY_v^\dagger Y_v\Big) + 6\mathrm{Tr}\Big(m^2_qY_u^\dagger Y_u\Big) + 6\mathrm{Tr}\Big(m^2_uY_uY_u^\dagger\Big) + 2\mathrm{Tr}\Big(m^2_\nu Y_vY_v^\dagger\Big)\,.
\end{aligned}
\tag{A.5}
$$

$$
\begin{aligned}
\beta^{(1)}_{m^2_\nu} = \quad & -3g^2_{BR}\mathbf{1}|M_4|^2 + 2\sqrt{6}g_{BR}g_R\mathbf{1}|M_4|^2 - 2g^2_R\mathbf{1}|M_4|^2 \\
& + \Big(-3g^2_{BL}M_1 + g_{BL}\Big(2\sqrt{6}g_{RB}M_1 - 3g_{BR}M_{BR} + \sqrt{6}g_RM_{BR}\Big) \\
& + g_{RB}\Big(-2g_{RB}M_1 - 2g_RM_{BR} + \sqrt{6}g_{BR}M_{BR}\Big)\Big)\mathbf{1}M_1^* \\
& + \Big(-3g^2_{BL}M_{BR} - 3g^2_{BR}M_{BR} + \sqrt{6}g_{BR}\Big(2g_RM_{BR} + g_{RB}\Big(M_1 + M_4\Big)\Big) \\
& - 2\Big(g^2_RM_{BR} + g^2_{RB}M_{BR} + g_Rg_{RB}\Big(M_1 + M_4\Big)\Big) + g_{BL}\Big(-3g_{BR}\Big(M_1 + M_4\Big) \\
& + \sqrt{6}\Big(2g_{RB}M_{BR} + g_R\Big(M_1 + M_4\Big)\Big)\Big)\Big)\mathbf{1}M^*_{BR} - 3g_{BL}g_{BR}M_{BR}\mathbf{1}M_4^* + \sqrt{6}g_{BL}g_RM_{BR}\mathbf{1}M_4^* \\
& + \sqrt{6}g_{BR}g_{RB}M_{BR}\mathbf{1}M_4^* - 2g_Rg_{RB}M_{BR}\mathbf{1}M_4^* + \sqrt{\frac{3}{2}}g_{BL}\mathbf{1}\sigma_{1,1} - g_{RB}\mathbf{1}\sigma_{1,1} + \sqrt{\frac{3}{2}}g_{BR}\mathbf{1}\sigma_{1,3} \\
& - g_R\mathbf{1}\sigma_{1,3} + 2m^2_\chi Y_sY_s^\dagger + 4m^2_{H_u}Y_vY_v^\dagger + 2T_sT_s^\dagger + 4T_\nu T_\nu^\dagger + m^2_\nu Y_sY_s^\dagger + 2m^2_\nu Y_vY_v^\dagger \\
& + 2Y_sm^2_SY_s^\dagger + Y_sY_s^\dagger m^2_\nu + 4Y_vm^2_lY_v^\dagger + 2Y_vY_v^\dagger m^2_\nu\,.
\end{aligned}
\tag{A.6}
$$

$$
\begin{aligned}
\beta^{(1)}_{m_l^2} = \quad & -3g_{BR}^2\mathbf{1}|M_4|^2 - 6g_L^2\mathbf{1}|M_2|^2 - 3g_{BL}\Big(g_{BL}M_1 + g_{BR}M_{BR}\Big)\mathbf{1}M_1^* \\
- \quad & 3\Big(g_{BL}^2 M_{BR} + g_{BL}g_{BR}\Big(M_1 + M_4\Big) + g_{BR}^2 M_{BR}\Big)\mathbf{1}M_{BR}^* \\
- \quad & 3g_{BL}g_{BR}M_{BR}\mathbf{1}M_4^* - \sqrt{\frac{3}{2}}g_{BL}\mathbf{1}\sigma_{1,1} - \sqrt{\frac{3}{2}}g_{BR}\mathbf{1}\sigma_{1,3} \\
+ \quad & 2m_{H_d}^2 Y_e^\dagger Y_e + 2m_{H_u}^2 Y_v^\dagger Y_v + 2T_e^\dagger T_e + 2T_\nu^\dagger T_\nu + m_l^2 Y_e^\dagger Y_e \\
+ \quad & m_l^2 Y_v^\dagger Y_v + 2Y_e^\dagger m_e^2 Y_e + Y_e^\dagger Y_e m_l^2 + 2Y_v^\dagger m_\nu^2 Y_v + Y_v^\dagger Y_v m_l^2 \,. \qquad \text{(A.7)}
\end{aligned}
$$

Appendix B

Alternative left-right symmetric model (ALRSM)

B.1 Diagonalisation of the scalar sector

The scalar potential V_{H} of eq. (7.4) is bounded from below if

$$\lambda_1 \geq 0\,, \quad \lambda_2 \leq 0\,, \quad \lambda_3 \geq 0\,, \quad \alpha_{12} \geq 0\,, \quad \alpha_{13} \geq 0 \quad \text{and} \quad \alpha_2 - \alpha_3 \geq 0\,, \tag{B.1}$$

where $\alpha_{ij} = \alpha_i + \alpha_j$, and if one of the following conditions is realised,

$$\Big[\lambda_{12} \geq 0\Big] \qquad \text{or} \qquad \Big[\lambda_{12} \leq 0\,, \quad \lambda_1 + \lambda_2 \geq 0 \quad \text{and} \quad \lambda_1^2 + 4\lambda_2^2 + 8\lambda_1\lambda_2 \leq 0\Big]\,, \tag{B.2}$$

with $\lambda_{12} = \lambda_1 + 2\lambda_2$. Moreover, its minimisation allows for the reduction of the number of degrees of freedom of the Higgs sector by three,

$$\mu_1^2 = \alpha_{12}\big(v_L^2 + v_R^2\big) + k^2\lambda_1 + \frac{\kappa v_L v_R}{\sqrt{2}k}\,, \qquad \mu_2^2 = \alpha_{12}k^2 + \lambda_3\big(v_L^2 + v_R^2\big)\,, \qquad \lambda_4 = \lambda_3 - \frac{\kappa k}{\sqrt{2}v_L v_R}\,. \tag{B.3}$$

Focusing first on the charged scalar sector, the squared mass matrix turns out to be block diagonal. The $\phi_1^\pm$ and $\chi_L^\pm$ fields therefore mix independently from the $\phi_2^\pm$ and $\chi_R^\pm$ fields, as shown by eq. (7.8). The corresponding 2×2 blocks of the mass matrix $(\mathcal{M}_L^\pm)^2$ and $(\mathcal{M}_R^\pm)^2$

are written, respectively, in the $(\phi_2^\pm, \chi_L^\pm)$ and $(\phi_1^\pm, \chi_R^\pm)$ bases, as

$$(\mathcal{M}^\pm_{L,R})^2 = \begin{pmatrix} -(\alpha_2-\alpha_3)v_{L,R}^2 - \frac{\kappa v_L v_R}{\sqrt{2}k} & (\alpha_2-\alpha_3)kv_{L,R} + \frac{\kappa v_{R,L}}{\sqrt{2}} \\ (\alpha_2-\alpha_3)k + \frac{\kappa v_{R,L}}{\sqrt{2}} & -(\alpha_2-\alpha_3)k^2 - \frac{\kappa k v_{R,L}}{\sqrt{2}v_{L,R}} \end{pmatrix} , \tag{B.4}$$

and are diagonalised by the rotations of eq. (7.8). The corresponding mass eigenvalues $M_{H_1^\pm}$ and $M_{H_2^\pm}$ are

$$M_{H_1^\pm} = \frac{k^2+v_L^2}{2kv_L}\Big[-2(\alpha_2-\alpha_3)kv_L - \sqrt{2}\kappa v_R\Big] \quad \text{and} \quad M_{H_2^\pm} = \frac{k^2+v_R^2}{2kv_R}\Big[-2(\alpha_2-\alpha_3)kv_R - \sqrt{2}\kappa v_L\Big] . \tag{B.5}$$

As $\alpha_2 - \alpha_3 \geq 0$ from eq. (B.1), forbidding tachyonic fields yields $\kappa < 0$. This further implies $\lambda_4 \geq 0$ by virtue of eq. (B.3). As shown by eq. (7.7), the pseudoscalar and scalar components of the ϕ_1^0 field do not mix and consist of the physical H_1^0 and A_1^0 eigenstates. They are mass-degenerate, with masses $M_{H_1^0}$ and $M_{A_1^0}$ reading

$$M^2_{H_1^0} = M^2_{A_1^0} = -(\alpha_2-\alpha_3)(v_L^2+v_R^2) - \frac{\kappa v_L v_R}{\sqrt{2}k} + 2k^2\lambda_2 . \tag{B.6}$$

The squared mass matrices $(\mathcal{M}^0_\Re)^2$ and $(\mathcal{M}^0_\Im)^2$ of the three remaining scalar and pseudoscalar fields are respectively given, in the $(\Re\{\phi_2^0\}, \Re\{\chi_L^0\}, \Re\{\chi_R^0\})$ and $(\Im\{\phi_2^0\}, \Im\{\chi_L^0\}, \Im\{\chi_R^0\})$ bases, by

$$\begin{aligned} (\mathcal{M}^0_\Re)^2 &= \begin{pmatrix} 2k^2\lambda_1 - \frac{\kappa v_L v_R}{\sqrt{2}k} & 2\alpha_{12}kv_L + \frac{\kappa v_R}{\sqrt{2}} & 2\alpha_{12}kv_R + \frac{\kappa v_L}{\sqrt{2}} \\ 2\alpha_{12}kv_L + \frac{\kappa v_R}{\sqrt{2}} & 2\lambda_3 v_L^2 - \frac{\kappa k v_R}{\sqrt{2}v_L} & 2\lambda_3 v_L v_R - \frac{\kappa k}{\sqrt{2}} \\ 2\alpha_{12}kv_R + \frac{\kappa v_L}{\sqrt{2}} & 2\lambda_3 v_L v_R - \frac{\kappa k}{\sqrt{2}} & 2\lambda_3 v_R^2 - \frac{\kappa k v_L}{\sqrt{2}v_R} \end{pmatrix} , \\ (\mathcal{M}^0_\Im)^2 &= \frac{\kappa}{\sqrt{2}} \begin{pmatrix} -\frac{v_L v_R}{k} & v_R & -v_L \\ v_R & -\frac{kv_R}{v_L} & k \\ -v_L & k & -\frac{kv_L}{v_R} \end{pmatrix} , \end{aligned} \tag{B.7}$$

and are diagonalised by the two $U^{\rm H}_{3\times3}$ and $U^{\rm A}_{3\times3}$ rotation matrices of eq. (7.7). These are explicitly given by

$$U^{\rm A}_{3\times3} = \frac{1}{\sqrt{2}} \begin{pmatrix} -\frac{k}{\sqrt{k^2+v_R^2}} & \frac{kv_R^2}{\sqrt{\left(k^2+v_R^2\right)\left(v_L^2v_R^2+k^2v_L^2+v_R^2k^2\right)}} & \frac{v_Rv_L}{\sqrt{v_L^2v_R^2+k^2v_L^2+v_R^2k^2}} \\ 0 & v_L\frac{\sqrt{k^2+v_R^2}}{\sqrt{v_L^2v_R^2+k^2v_L^2+v_R^2k^2}} & -\frac{kv_R}{\sqrt{v_L^2v_R^2+k^2v_L^2+v_R^2k^2}} \\ \frac{v_R}{\sqrt{v_R^2+k^2}} & \frac{k^2v_R}{\sqrt{\left(k^2+v_R^2\right)\left(v_L^2v_R^2+k^2v_L^2+v_R^2k^2\right)}} & \frac{kv_L}{\sqrt{v_L^2v_R^2+k^2v_L^2+v_R^2k^2}} \end{pmatrix} , \tag{B.8}$$

$$U^{\rm H}_{3\times3} = \frac{1}{\sqrt{2}} \begin{pmatrix} \frac{f_0}{\sqrt{\mathcal{D}_1}} & \frac{f_2(1+g_0^2)-f_0(1+g_0g_2)}{\sqrt{\mathcal{D}_1\mathcal{D}_2}} & \frac{\xi(g_2-g_0)}{\sqrt{\mathcal{D}_2}} \\ \frac{g_0}{\sqrt{\mathcal{D}_1}} & \frac{g_2(1+f_0^2)-g_0(1+f_0f_2)}{\sqrt{\mathcal{D}_1\mathcal{D}_2}} & \frac{\xi(f_0-f_2)}{\sqrt{\mathcal{D}_2}} \\ \frac{1}{\sqrt{\mathcal{D}_1}} & \frac{f_0^2+g_0^2-f_0f_2-g_0g_2}{\sqrt{\mathcal{D}_1\mathcal{D}_2}} & \frac{\xi(g_0f_2-g_2f_0)}{\sqrt{\mathcal{D}_2}} \end{pmatrix} ,$$

and depend on various functions of the Higgs mass eigenvalues $M_{H^0_i}$,

$$\begin{aligned} f_i &= \frac{2M^4_{H^0_i}v_Lv_R + M^2_{H^0_i}(v_L^2+v_R^2)(\sqrt{2}k\kappa - 4v_Lv_R\lambda_3) - 2\sqrt{2}k(v_L^2-v_R^2)^2\lambda_3\kappa}{v_R\Big[M^2_{H^0_i}(4kv_Lv_R\alpha_{12}+\sqrt{2}v_L^2\kappa) + 2\sqrt{2}(k^2\alpha_{12}+v_L^2\lambda_3)(v_R^2-v_L^2)\kappa\Big]} , \\ g_i &= \frac{v_L}{v_R}\,\frac{M^2_{H^0_i}(4kv_Lv_R\alpha_{12}+\sqrt{2}v_R^2\kappa) + 2\sqrt{2}(k^2\alpha_{12}+v_R^2\lambda_3)(v_L^2-v_R^2)\kappa}{M^2_{H^0_i}(4kv_Lv_R\alpha_{12}+\sqrt{2}v_L^2\kappa) + 2\sqrt{2}(k^2\alpha_{12}+v_L^2\lambda_3)(v_R^2-v_L^2)\kappa} , \\ \mathcal{D}_1 &= 1+f_0^2+g_0^2 , \\ \mathcal{D}_2 &= f_2^2(1+g_0^2)+(g_0-g_2)^2-2f_0f_2(1+g_0g_2)+f_0^2(1+g_2^2) , \\ \xi &= \mathrm{sgn}\big[g_0(f_2-f_3)+g_2(f_3-f_0)+g_3(f_0-f_2)\big] . \end{aligned} \tag{B.9}$$

In our conventions, we trade the λ_1 free parameter of the scalar potential for the mass of the lightest Higgs state H^0_0 (that can then be set freely and thus match the SM Higgs boson mass). λ_1 becomes thus a dependent parameter,

$$\lambda_1 = \frac{1}{2k^3}\,\frac{\sqrt{2}kv_Lv_RM^6_{H^0_0} + \mathfrak{a}^{(4)}M^4_{H^0_0} - 2\mathfrak{a}^{(2)}M^2_{H^0_0} - 4\alpha_{12}^2\kappa k^4(v_L^2-v_R^2)^2}{\sqrt{2}v_Lv_RM^4_{H^0_0} + (\kappa k - 2\sqrt{2}\lambda_3v_Lv_R)(v_L^2+v_R^2)M^2_{H^0_0} - 2\kappa k\lambda_3(v_L^2-v_R^2)^2} , \tag{B.10}$$

and the remaining scalar masses then read

$$M^2_{A^0_2} = -\frac{\kappa}{\sqrt{2}kv_Lv_R}\Big[v_L^2v_R^2 + k^2(v_L^2+v_R^2)\Big] \qquad \text{and} \qquad M^2_{H^0_{2,3}} = \frac{1}{2}\left[\mathfrak{a} \pm \sqrt{\mathfrak{a}^2 + 4(\mathfrak{b} + \mathfrak{a}M^2_{H^0_0})}\right] . \tag{B.11}$$

with

$$\begin{aligned}
\mathfrak{a}^{(4)} &= -2\sqrt{2}k\lambda_3 v_Lv_R(v_L^2+v_R^2) + \kappa\Big(v_L^2v_R^2 + k^2(v_L^2+v_R^2)\Big) ,\\
\mathfrak{a}^{(2)} &= 2\sqrt{2}\alpha_{12}^2k^3v_Lv_R(v_L^2+v_R^2) + \kappa\Big(\lambda_3v_L^2v_R^2(v_L^2+v_R^2) + k^2\big[4\alpha_{12}v_L^2v_R^2 + \lambda_3(v_L^2-v_R^2)^2\big]\Big) ,\\
\mathfrak{a} &= \frac{1}{\sqrt{2}kv_Lv_R}\Big[v_Lv_R\big(2\sqrt{2}k^3\lambda_1 - \kappa v_Lv_R\big) + k\big(2\sqrt{2}\lambda_3v_Lv_R - \kappa k\big)\big(v_L^2+v_R^2\big)\Big] - M^2_{H^0_0} ,\\
\mathfrak{b} &= \frac{1}{kv_Lv_R}\Big[\sqrt{2}\kappa k^2\Big(4\alpha_{12}v_L^2v_R^2 + \lambda_3(v_L^2-v_R^2)^2\Big)\\
&\qquad + \Big(4k^3(\alpha_{12}^2-\lambda_1\lambda_3)v_Lv_R + \sqrt{2}\kappa(k^4\lambda_1+\lambda_3v_L^2v_R^2)\Big)\Big(v_L^2+v_R^2\Big)\Big] .
\end{aligned} \tag{B.12}$$

B.2 The fermion sector

Fermion mass terms are generated from the Yukawa Lagrangian of eq. (7.3) after the breaking of the $SU(2)_L \times SU(2)_{R'} \times U(1)_{B-L}$ symmetry down to electromagnetism,

$$\mathcal{L}_{\rm F}^{\rm mass} = -\frac{k}{\sqrt{2}}\Big[\bar{e}_L\hat{\mathbf{Y}}^e e_R + \bar{u}_L\hat{\mathbf{Y}}^u u_R\Big] - \frac{v_L}{\sqrt{2}}\Big[\bar{d}_L\hat{\mathbf{Y}}^d d_R + \bar{\nu}_L\hat{\mathbf{Y}}^\nu \nu_R\Big] - \frac{v_R}{\sqrt{2}}\Big[\bar{d}'_R\hat{\mathbf{Y}}^{d'} d'_L + \bar{n}_R\hat{\mathbf{Y}}^n n_L\Big] + \text{h.c.} \tag{B.13}$$

The different mass matrices $\hat{\mathbf{Y}}$ can be diagonalised through 12 unitary rotations,

$$\frac{k}{\sqrt{2}}\hat{\mathbf{Y}}^u \to \frac{k}{\sqrt{2}}V_u\mathbf{Y}^u U_u^\dagger = \begin{pmatrix} M_u & 0 & 0 \\ 0 & M_c & 0 \\ 0 & 0 & M_t \end{pmatrix}, \frac{v_L}{\sqrt{2}}\hat{\mathbf{Y}}^d \to \frac{v_L}{\sqrt{2}}V_d\mathbf{Y}^d U_d^\dagger = \begin{pmatrix} M_d & 0 & 0 \\ 0 & M_s & 0 \\ 0 & 0 & M_b \end{pmatrix},$$
$$\frac{v_L}{\sqrt{2}}\hat{\mathbf{Y}}^\nu \to \frac{v_L}{\sqrt{2}}V_\nu\mathbf{Y}^\nu U_\nu^\dagger = \begin{pmatrix} M_{\nu_e} & 0 & 0 \\ 0 & M_{\nu_\mu} & 0 \\ 0 & 0 & M_{\nu_\tau} \end{pmatrix}, \frac{k}{\sqrt{2}}\hat{\mathbf{Y}}^e \to \frac{k}{\sqrt{2}}V_e\mathbf{Y}^e U_e^\dagger = \begin{pmatrix} M_e & 0 & 0 \\ 0 & M_\mu & 0 \\ 0 & 0 & M_\tau \end{pmatrix},$$
$$\frac{v_R}{\sqrt{2}}\hat{\mathbf{Y}}^{d'} \to \frac{v_R}{\sqrt{2}}U_{d'}\mathbf{Y}^{d'} V_{d'}^\dagger = \begin{pmatrix} M_{d'} & 0 & 0 \\ 0 & M_{s'} & 0 \\ 0 & 0 & M_{b'} \end{pmatrix}, \frac{v_R}{\sqrt{2}}\hat{\mathbf{Y}}^n \to \frac{v_R}{\sqrt{2}}U_n\mathbf{Y}^n V_n^\dagger = \begin{pmatrix} M_{n_e} & 0 & 0 \\ 0 & M_{n_\mu} & 0 \\ 0 & 0 & M_{n_\tau} \end{pmatrix}, \tag{B.14}$$

leading to diagonal and real $\mathbf{Y}$ matrices. These rotations equivalently correspond to replacing the fermion gauge eigenbasis by the physical one,

$$\begin{aligned} &u_L \to V_u u_L\ , \quad d_L \to V_d d_L\ , \quad \nu_L \to V_\nu \nu_L\ , \quad e_L \to V_e e_L\ , \quad d'_L \to V_{d'} d'_L\ , \quad n_L \to V_n n_L\ , \\ &u_R \to U_u u_R\ , \quad d_R \to U_d d_R\ , \quad \nu_R \to U_\nu \nu_R\ , \quad e_R \to U_e e_R\ , \quad d'_R \to U_{d'} d'_R\ , \quad n_R \to U_n n_R\ . \end{aligned} \tag{B.15}$$

As in the SM, conventionally we keep the left-handed up-type quark and charged lepton bases unchanged and absorb the $V_u - V_d$ and $V_\nu - V_e$ rotations in a redefinition of the down-type quark and neutrino states. Similarly, the $U_u - U_{d'}$ and $U_n - U_e$ rotations are conveniently absorbed in a redefinition of the d'_R and n_L bases, the right-handed up-type quark and charged lepton bases being kept unchanged,

$$\begin{aligned} d_L \to V_u^\dagger V_d d_L \equiv V_{\rm CKM} d_L\ , \quad \nu_L \to V_e^\dagger V_\nu \nu_L \equiv V_{\rm PMNS} d_L\ , \\ d'_R \to U_u^\dagger U_{d'} d'_R \equiv V_{\rm CKM'} d'_R\ , \quad n_R \to U_e^\dagger U_n n_R \equiv V_{\rm PMNS'} n_R\ . \end{aligned} \tag{B.16}$$

Omitting any potential Majorana phase, each of the four CKM/PMNS rotation matrices can be defined by three mixing angles θ_{ij} and a Dirac phase δ.

Field	Spin	Name	PDG
Z'	1	Zp	32
W'^{+}	1	Wp	34
n_i $(i=1,2,3)$	1/2	nl	6000012, 6000014, 6000016
d'_i $(i=1,2,3)$	1/2	dqp	6000001, 6000003, 6000005
H_i^0 $(i=0,1,2,3)$	0	h0	25, 25, 45, 55
A_i^0 $(i=1,2)$	0	A0	36, 46
H_i^+ $(i=1,2)$	0	Hp	37, 47

Table B.1: Mass eigenstates that supplement the SM, together with their spin quantum number (second column), the name used in the FeynRules implementation (third column) and the associated PDG identifier (last column).

Parameter	Name	LH block	LH counter
$\tan\beta$	tb	SMINPUTS	5
g_R	gR	SMINPUTS	6
v'	vevp	SMINPUTS	7
λ_2	lam2	HPOTINPUTS	1
λ_3	lam3	HPOTINPUTS	2
α_1	alp1	HPOTINPUTS	3
α_2	alp2	HPOTINPUTS	4
α_3	alp3	HPOTINPUTS	5
κ	kap	HPOTINPUTS	6
$a_{\rm H}^g$	Ghgg	EFFECTIVEHIGGS	1
$a_{\rm H}^a$	Ghaa	EFFECTIVEHIGGS	2

Parameter	Name	LH block	LH counter
M_{ν_e}	Mve	MASS	12
M_{ν_μ}	Mvm	MASS	14
M_{ν_τ}	Mvt	MASS	16
M_{n_e}	Mne	MASS	6000012
M_{n_μ}	Mnm	MASS	6000014
M_{n_τ}	Mnt	MASS	6000016
$M_{d'}$	MDP	MASS	6000001
$M_{s'}$	MSP	MASS	6000003
$M_{b'}$	MBP	MASS	6000005

Parameter	Name	LH block	LH counter
λ	CKMlam	CKMBLOCK	1
A	CKMA	CKMBLOCK	2
$\bar\rho$	CKMrho	CKMBLOCK	3
$\bar\eta$	CKMeta	CKMBLOCK	4
$s_{12}^{(\mathrm{CKM}')}$	CKMps12	CKMBLOCK	11
$s_{23}^{(\mathrm{CKM}')}$	CKMps23	CKMBLOCK	12
$s_{13}^{(\mathrm{CKM}')}$	CKMps13	CKMBLOCK	13
$\delta_{\mathrm{CKM}'}$	CKMpdel	CKMBLOCK	14

Parameter	Name	LH block	LH counter
$s_{12}^{(\mathrm{PMNS})}$	PMNSs12	PMNSBLOCK	1
$s_{23}^{(\mathrm{PMNS})}$	PMNSs23	PMNSBLOCK	2
$s_{13}^{(\mathrm{PMNS})}$	PMNSs13	PMNSBLOCK	3
δ_{PMNS}	PMNSdel	PMNSBLOCK	4
$s_{12}^{(\mathrm{PMNS}')}$	PMNSps12	PMNSBLOCK	11
$s_{23}^{(\mathrm{PMNS}')}$	PMNSps23	PMNSBLOCK	12
$s_{13}^{(\mathrm{PMNS}')}$	PMNSps13	PMNSBLOCK	13
$\delta_{\mathrm{PMNS}'}$	PMNSpdel	PMNSBLOCK	14

Table B.2: New physics external parameters of our ALRSM implementation, together with their name and the Les Houches (LH) block and counter information allowing to change its numerical value on run time. We recall that for consistency, $\kappa < 0$ and the conditions of eqs. (B.1) and (B.2) must be satisfied. Those parameters supplement the usual set of electroweak inputs given in the LEP scheme, as well as all SM fermion masses.

B.3 Technical details on our FeynRules implementation

We collect the properties of the new physics fields and external parameters associated with our FeynRules implementation of the ALRSM model in tables B.1 and B.2, where we additionally include properties useful for the user when running any programme relying on our implementation.

As can be noticed from the tables, the left-handed and right-handed scotinos are combined to form a Dirac fermion n_i (with $i = 1, 2, 3$ being a generation index) and the left-handed and right-handed exotic quarks are combined to form a Dirac fermion d'_i (with $i = 1, 2, 3$ being again a generation index). Whilst all fermion masses are free parameters of the model (see also appendix B.2), all boson masses are internal (*i.e.* are derived parameters), with the exception of the SM Higgs boson mass $M_{H_0^0}$ (see appendix B.1) and the Z-boson mass. As for the SM implementation included with FeynRules, our model defines the electroweak sector following the LEP scheme that is known to yield the minimal parametric uncertainty in the predictions. The three electroweak inputs are thus the Fermi coupling $G_{_F}$, the fine structure constant α and the Z-boson mass M_Z. The gauge and scalar sectors are then fully defined by fixing nine parameters, that we choose to be v', t_β, $g_{_R}$, λ_2, λ_3, α_1, α_2, α_3 and κ. We recall that the user must ensure that the conditions of eqs. (B.1) and (B.2) are satisfied when providing the numerical values of these parameters, and that $\kappa < 0$ to avoid tachyonic charged Higgs bosons.

All other parameters of the gauge and Higgs sectors are then derived as follows. The vacuum expectation values v, $v_{_L}$, $v_{_R}$ and k are obtained from $G_{_F}$, v' and t_β,

$$v^2 = \frac{1}{\sqrt{2}G_{_F}} \ , \qquad v_{_L} = v \ \cos\beta \ , \qquad k = v \ \sin\beta \qquad \text{and} \qquad v_{_R}^2 = v'^2 - k^2 \ . \tag{B.17}$$

As in the SM the W-boson mass is derived from the electroweak inputs,

$$M_W^2 = \frac{M_Z^2}{2}\left[1 + \sqrt{1 - 2\sqrt{2}\frac{\pi\alpha}{G_{_F}M_Z^2}}\right] , \tag{B.18}$$

so that eq. (7.10) can be used to derive the $SU(2)_L$ gauge coupling g_L. As $e = \sqrt{4\pi\alpha}$, one can then derive the hypercharge coupling $g_{_Y}$ and the sine and cosine of the electroweak mixing angle $\theta_{_W}$ from eq. (7.13), which further allows us to calculate the $B - L$ coupling constant $g_{_{B-L}}$, the cosine of the $\varphi_{_W}$ mixing angle and the so far neglected $Z - Z'$ mixing. It is up to the user to verify that his/her choice of input parameter yields $\tan(2\vartheta_{_W}) \lesssim 10^{-3}$.

Furthermore, the W'- and Z'-boson masses are obtained from eqs. (7.10) and (7.14), and the other parameters of the Higgs potential (*i.e.*, μ_1, μ_2, λ_1 and λ_4) are obtained from eq. (B.3) and eq. (B.10).

In the fermion sector, the various CKM and PNMS matrices are obtained from their standard expressions in terms of three mixing angles and a phase,

$$V = \begin{pmatrix} c_{12}c_{13} & s_{12}c_{13} & s_{13}e^{-i\delta} \\ -s_{12}c_{23} - c_{12}s_{23}s_{13}e^{i\delta} & c_{12}c_{23} - s_{12}s_{23}s_{13}e^{i\delta} & s_{23}c_{13} \\ s_{12}s_{23} - c_{12}c_{23}s_{13}e^{i\delta} & -c_{12}s_{23} - s_{12}c_{23}s_{13}e^{i\delta} & c_{23}c_{13} \end{pmatrix} , \tag{B.19}$$

where $s_{ij} \equiv \sin\theta_{ij}$ and $c_{ij} \equiv \cos\theta_{ij}$ denote the sine and cosine of the various mixing angles. Concerning the SM CKM matrix, we have however traded the input parameters by the usual Wolfenstein parameters A, λ, $\bar{\rho}$ and $\bar{\eta}$,

$$s_{12}^{(\mathrm{CKM})} = \lambda \ , \qquad s_{23}^{(\mathrm{CKM})} = A\lambda^2 \qquad \text{and} \qquad s_{13}^{(\mathrm{CKM})} e^{i\delta_{\mathrm{CKM}}} = \frac{A\lambda^3\sqrt{1-A^2\lambda^4}(\bar{\rho}+i\bar{\eta})}{\sqrt{1-\lambda^2}\big[1-A^2\lambda^4(\bar{\rho}+i\bar{\eta})\big]} \ . \tag{B.20}$$

Bibliography

[1] M. Frank and Ö. Özdal, *Exploring the supersymmetric $U(1)_{B-L}\times$ $U(1)_R$ model with dark matter, muon $g-2$ and Z' mass limits*, *Phys. Rev. D* **97** (2018) 015012, [1709.04012].

[2] M. Frank, Y. Hiçyılmaz, S. Moretti and Ö. Özdal, *Leptophobic Z' bosons in the secluded $U(1)'$ model*, 2005.08472.

[3] M. Frank, Y. Hiçyılmaz, S. Moretti and Ö. Özdal, *E_6 motivated UMSSM confronts experimental data*, *JHEP* **05** (2020) 123, [2004.01415].

[4] M. Frank, Ö. Özdal and P. Poulose, *Relaxing LHC constraints on the W_R mass*, *Phys. Rev.* **D99** (2019) 035001, [1812.05681].

[5] M. Frank, B. Fuks and Ö. Özdal, *Natural dark matter and light bosons with an alternative left-right symmetry*, *JHEP* **04** (2020) 116, [1911.12883].

[6] ATLAS collaboration, T. A. collaboration, *Search for new high-mass phenomena in the dilepton final state using 36.1 fb^{-1} of proton-proton collision data at $\sqrt{s} = 13$ TeV with the ATLAS detector*, ATLAS-CONF-2017-027.

[7] CMS collaboration, A. M. Sirunyan et al., *Search for dijet resonances in proton?proton collisions at $\sqrt{s} = 13$ TeV and constraints on dark matter and other models*, *Phys. Lett.* **B769** (2017) 520–542, [1611.03568].

[8] Fermi-LAT collaboration, M. Ackermann et al., *The Fermi Galactic Center GeV Excess and Implications for Dark Matter*, *Astrophys. J.* **840** (2017) 43, [1704.03910].

[9] ATLAS collaboration, G. Aad et al., *Search for high-mass dilepton resonances using 139 fb^{-1} of pp collision data collected at $\sqrt{s}$ =13 TeV with the ATLAS detector*, *Phys. Lett.* **B796** (2019) 68–87, [1903.06248].

[10] CMS collaboration, A. M. Sirunyan et al., *Search for high mass dijet resonances with a new background prediction method in proton-proton collisions at* $\sqrt{s} = 13$ *TeV*, 1911.03947.

[11] Planck collaboration, P. A. R. Ade et al., *Planck 2013 results. XVI. Cosmological parameters*, *Astron. Astrophys.* **571** (2014) A16, [1303.5076].

[12] Planck collaboration, N. Aghanim et al., *Planck 2018 results. VI. Cosmological parameters*, 1807.06209.

[13] ATLAS collaboration, G. Aad et al., *Search for direct production of electroweakinos in final states with one lepton, missing transverse momentum and a Higgs boson decaying into two b-jets in (pp) collisions at* $\sqrt{s} = 13$ *TeV with the ATLAS detector*, 1909.09226.

[14] ATLAS collaboration, G. Aad et al., *Search for electroweak production of charginos and sleptons decaying into final states with two leptons and missing transverse momentum in* $\sqrt{s} = 13$ *TeV pp collisions using the ATLAS detector*, *Eur. Phys. J.* **C80** (2020) 123, [1908.08215].

[15] ATLAS collaboration, M. Aaboud et al., *Search for* WW/WZ *resonance production in* $\ell\nu qq$ *final states in pp collisions at* $\sqrt{s} = 13$ *TeV with the ATLAS detector*, *JHEP* **03** (2018) 042, [1710.07235].

[16] CMS collaboration, A. M. Sirunyan et al., *Search for massive resonances decaying into* WW, WZ, ZZ, qW, *and* qZ *with dijet final states at* $\sqrt{s} = 13$ TeV, *Phys. Rev.* **D97** (2018) 072006, [1708.05379].

[17] CMS collaboration, A. M. Sirunyan et al., *Search for a heavy resonance decaying to a pair of vector bosons in the lepton plus merged jet final state at* $\sqrt{s} = 13$ *TeV*, *JHEP* **05** (2018) 088, [1802.09407].

[18] ATLAS collaboration, M. Aaboud et al., *Search for new phenomena in dijet events using 37* fb^{-1} *of pp collision data collected at* $\sqrt{s}$ *=13 TeV with the ATLAS detector*, *Phys. Rev.* **D96** (2017) 052004, [1703.09127].

[19] CMS collaboration, A. M. Sirunyan et al., *Search for a heavy resonance decaying into a Z boson and a vector boson in the* $\nu\bar{\nu}\mathrm{q}\bar{\mathrm{q}}$ *final state*, *JHEP* **07** (2018) 075, [1803.03838].

[20] CMS collaboration, A. M. Sirunyan et al., *Searches for W? bosons decaying to a top quark and a bottom quark in proton-proton collisions at 13 TeV*, *JHEP* **08** (2017) 029, [1706.04260].

[21] ATLAS collaboration, M. Aaboud et al., *Search for heavy Majorana or Dirac neutrinos and right-handed W gauge bosons in final states with two charged leptons and two jets at $\sqrt{s}$=13 TeV with the ATLAS detector*, 1809.11105.

[22] CMS collaboration, A. M. Sirunyan et al., *Search for a heavy right-handed W boson and a heavy neutrino in events with two same-flavor leptons and two jets at $\sqrt{s} = 13$ TeV*, *JHEP* **05** (2018) 148, [1803.11116].

[23] MAGIC, Fermi-LAT collaboration, M. L. Ahnen et al., *Limits to Dark Matter Annihilation Cross-Section from a Combined Analysis of MAGIC and Fermi-LAT Observations of Dwarf Satellite Galaxies*, *JCAP* **1602** (2016) 039, [1601.06590].

[24] CMS collaboration, A. M. Sirunyan et al., *Search for top squarks and dark matter particles in opposite-charge dilepton final states at $\sqrt{s} = 13$ TeV*, *Phys. Rev.* **D97** (2018) 032009, [1711.00752].

[25] L. Ryder, *QUANTUM FIELD THEORY*. Cambridge University Press, 6, 1996.

[26] P. Langacker, *Introduction to the Standard Model and Electroweak Physics*, in *Theoretical Advanced Study Institute in Elementary Particle Physics: The Dawn of the LHC Era*, pp. 3–48, 2010. 0901.0241. DOI.

[27] S. Novaes, *Standard model: An Introduction*, in *10th Jorge Andre Swieca Summer School: Particle and Fields*, pp. 5–102, 1, 1999. hep-ph/0001283.

[28] ATLAS collaboration, G. Aad et al., *Observation of a new particle in the search for the Standard Model Higgs boson with the ATLAS detector at the LHC*, *Phys. Lett.* **B716** (2012) 1–29, [1207.7214].

[29] CMS collaboration, S. Chatrchyan et al., *Observation of a new boson at a mass of 125 GeV with the CMS experiment at the LHC*, *Phys. Lett.* **B716** (2012) 30–61, [1207.7235].

[30] O. Ozdal, *The Higgs boson and right-handed neutrinos in supersymmetric models*, Master's thesis, Izmir Inst. Tech., 2017.

[31] C. S. Un and O. Ozdal, *Mass Spectrum and Higgs Profile in BLSSM*, *Phys. Rev.* **D93** (2016) 055024, [1601.02494].

[32] S. P. Martin, *A Supersymmetry primer*, vol. 21, pp. 1–153. 2010. hep-ph/9709356. 10.1142/9789812839657_0001.

[33] J. Wess and J. Bagger, *Supersymmetry and supergravity*. Princeton University Press, Princeton, NJ, USA, 1992.

[34] P. Srivastava, *SUPERSYMMETRY, SUPERFIELDS AND SUPERGRAVITY: AN INTRODUCTION*. 1986.

[35] P. C. West, *INTRODUCTION TO SUPERSYMMETRY AND SUPERGRAVITY*. 1986.

[36] P. C. West, *Introduction to supersymmetry and supergravity*. 1990.

[37] S. Weinberg, *The quantum theory of fields. Vol. 3: Supersymmetry*. Cambridge University Press, 6, 2013.

[38] M. Drees, R. Godbole and P. Roy, *Theory and phenomenology of sparticles: An account of four-dimensional N=1 supersymmetry in high energy physics*. 2004.

[39] H. Baer and X. Tata, *Weak scale supersymmetry: From superfields to scattering events*. Cambridge University Press, 5, 2006.

[40] S. Gates, M. T. Grisaru, M. Rocek and W. Siegel, *Superspace Or One Thousand and One Lessons in Supersymmetry*, vol. 58. 1983.

[41] H. E. Haber, *Introductory low-energy supersymmetry*, in *Theoretical Advanced Study Institute (TASI 92): From Black Holes and Strings to Particles*, pp. 589–686, 4, 1993. hep-ph/9306207.

[42] M. E. Peskin, *Duality in supersymmetric Yang-Mills theory*, in *Theoretical Advanced Study Institute in Elementary Particle Physics (TASI 96): Fields, Strings, and Duality*, pp. 729–809, 2, 1997. hep-th/9702094.

[43] J. D. Lykken, *Introduction to supersymmetry*, in *Theoretical Advanced Study Institute in Elementary Particle Physics (TASI 96): Fields, Strings, and Duality*, pp. 85–153, 6, 1996. hep-th/9612114.

[44] M. A. Shifman, *Nonperturbative dynamics in supersymmetric gauge theories*, *Prog. Part. Nucl. Phys.* **39** (1997) 1–116, [hep-th/9704114].

[45] M. A. Luty, *2004 TASI lectures on supersymmetry breaking*, in *Theoretical Advanced Study Institute in Elementary Particle Physics: Physics in $D \geqq 4$*, pp. 495–582, 9, 2005. hep-th/0509029.

[46] I. J. Aitchison, *Supersymmetry and the MSSM: An Elementary introduction*, hep-ph/0505105.

[47] H. Murayama, *Supersymmetry phenomenology*, in *ICTP Summer School in Particle Physics*, pp. 296–335, 2, 2000. hep-ph/0002232.

[48] S. Moretti and S. Khalil, *Supersymmetry beyond minimality: from theory to experiment*. CRC Press, 2017.

[49] G. G. Ross, K. Schmidt-Hoberg and F. Staub, *Revisiting fine-tuning in the MSSM*, *JHEP* **03** (2017) 021, [1701.03480].

[50] J. Casas, J. Espinosa and I. Hidalgo, *The MSSM fine tuning problem: A Way out*, *JHEP* **01** (2004) 008, [hep-ph/0310137].

[51] Z. Altin, O. Ozdal and C. S. Un, *Muon g-2 in an Alternative Quasi-Yukawa Unification with Low Fine-Tuned Inverse SeeSaw Mechanism*, 1703.00229.

[52] A. Çiçi, Z. Kı rca and C. S. Ün, *Light Stops and Fine-Tuning in MSSM*, *Eur. Phys. J. C* **78** (2018) 60, [1611.05270].

[53] L. Delle Rose, S. Khalil, S. J. D. King, C. Marzo, S. Moretti and C. S. Un, *Naturalness and dark matter in the supersymmetric B-L extension of the standard model*, *Phys. Rev. D* **96** (2017) 055004, [1702.01808].

[54] Y. s. Hiçyı lmaz, M. Ceylan, A. Altas, L. Solmaz and C. S. Un, *Quasi Yukawa Unification and Fine-Tuning in U(1) Extended SSM*, *Phys. Rev. D* **94** (2016) 095001, [1604.06430].

[55] J. Casas, J. Espinosa and I. Hidalgo, *A Relief to the supersymmetric fine tuning problem*, in *2nd String Phenomenology 2003*, pp. 76–85, 2, 2004. hep-ph/0402017. DOI.

[56] J. Casas, J. Espinosa and I. Hidalgo, *Implications for new physics from fine-tuning arguments. 1. Application to SUSY and seesaw cases*, *JHEP* **11** (2004) 057, [hep-ph/0410298].

[57] G. W. Anderson and D. J. Castano, *Measures of fine tuning*, *Phys. Lett. B* **347** (1995) 300–308, [hep-ph/9409419].

[58] H. E. Haber and M. Sher, *Higgs Mass Bound in $E(6)$ Based Supersymmetric Theories*, *Phys. Rev.* **D35** (1987) 2206.

[59] M. Cvetic, D. A. Demir, J. R. Espinosa, L. L. Everett and P. Langacker, *Electroweak breaking and the mu problem in supergravity models with an additional U(1)*, *Phys. Rev.* **D56** (1997) 2861, [hep-ph/9703317].

[60] E. Ma, *Exceeding the MSSM Higgs Mass Bound in a Special Class of U(1) Gauge Models*, *Phys. Lett.* **B705** (2011) 320–323, [1108.4029].

[61] R. N. Mohapatra and A. Rasin, *Simple supersymmetric solution to the strong CP problem*, *Phys. Rev. Lett.* **76** (1996) 3490–3493, [hep-ph/9511391].

[62] R. N. Mohapatra and G. Senjanovic, *Neutrino Masses and Mixings in Gauge Models with Spontaneous Parity Violation*, *Phys. Rev.* **D23** (1981) 165.

[63] J. Schechter and J. W. F. Valle, *Neutrino Masses in SU(2) x U(1) Theories*, *Phys. Rev.* **D22** (1980) 2227.

[64] J. Schechter and J. W. F. Valle, *Neutrino Decay and Spontaneous Violation of Lepton Number*, *Phys. Rev.* **D25** (1982) 774.

[65] M. Malinsky, J. C. Romao and J. W. F. Valle, *Novel supersymmetric SO(10) seesaw mechanism*, *Phys. Rev. Lett.* **95** (2005) 161801, [hep-ph/0506296].

[66] V. De Romeri, M. Hirsch and M. Malinsky, *Soft masses in SUSY SO(10) GUTs with low intermediate scales*, *Phys. Rev.* **D84** (2011) 053012, [1107.3412].

[67] M. Hirsch, W. Porod, L. Reichert and F. Staub, *Phenomenology of the minimal supersymmetric $U(1)_{B-L} \times U(1)_R$ extension of the standard model*, *Phys. Rev.* **D86** (2012) 093018, [1206.3516].

[68] Muon g-2 collaboration, G. W. Bennett et al., *Final Report of the Muon E821 Anomalous Magnetic Moment Measurement at BNL*, *Phys. Rev.* **D73** (2006) 072003, [hep-ex/0602035].

[69] M. Hirsch, M. Malinsky, W. Porod, L. Reichert and F. Staub, *Hefty MSSM-like light Higgs in extended gauge models*, *JHEP* **02** (2012) 084, [1110.3037].

[70] R. N. Mohapatra and A. Rasin, *A Supersymmetric solution to CP problems*, *Phys. Rev.* **D54** (1996) 5835–5844, [hep-ph/9604445].

[71] L. Delle Rose, S. Khalil, S. J. D. King, C. Marzo, S. Moretti and C. S. Un, *Naturalness and Dark Matter Properties of the BLSSM*, in *25th International Workshop on Deep Inelastic Scattering and Related Topics (DIS 2017) Birmingham, UK, April 3-7, 2017*, 2017. 1706.01301.

[72] L. Basso, *The Higgs sector of the minimal SUSY $B-L$ model*, *Adv. High Energy Phys.* **2015** (2015) 980687, [1504.05328].

[73] W. Abdallah and S. Khalil, *Dark Matter in B-L supersymmetric Standard Model with inverse seesaw*, *JCAP* **1704** (2017) 016, [1701.04436].

[74] S. Khalil and C. S. Un, *Muon Anomalous Magnetic Moment in SUSY B-L Model with Inverse Seesaw*, *Phys. Lett.* **B763** (2016) 164–168, [1509.05391].

[75] S. Khalil and S. Moretti, *The $B-L$ Supersymmetric Standard Model with Inverse Seesaw at the Large Hadron Collider*, *Rept. Prog. Phys.* **80** (2017) 036201, [1503.08162].

[76] W. Porod, *SPheno, a program for calculating supersymmetric spectra, SUSY particle decays and SUSY particle production at e+ e- colliders*, *Comput. Phys. Commun.* **153** (2003) 275–315, [hep-ph/0301101].

[77] W. Porod and F. Staub, *SPheno 3.1: Extensions including flavour, CP-phases and models beyond the MSSM*, *Comput. Phys. Commun.* **183** (2012) 2458–2469, [1104.1573].

[78] F. Staub, *SARAH*, 0806.0538.

[79] F. Stub, *Automatic Calculation of supersymmetric Renormalization Group Equations and Self Energies*, *Comput. Phys. Commun.* **182** (2011) 808–833, [1002.0840].

[80] V. Lucas and S. Raby, *GUT scale threshold corrections in a complete supersymmetric SO(10) model: Alpha-s (m(z)) versus proton lifetime*, *Phys. Rev.* **D54** (1996) 2261–2272, [hep-ph/9601303].

[81] A. Kusenko, *Color and charge breaking minima in the MSSM*, *Nucl. Phys. Proc. Suppl.* **52A** (1997) 67–69, [hep-ph/9607287].

[82] U. Chattopadhyay and A. Dey, *Exploring MSSM for Charge and Color Breaking and Other Constraints in the Context of Higgs@125 GeV*, *JHEP* **11** (2014) 161, [1409.0611].

[83] CDF, D0 collaboration, T. E. W. Group, *Combination of CDF and D0 Results on the Mass of the Top Quark*, 0903.2503.

[84] I. Gogoladze, Q. Shafi and C. S. Un, *Higgs Boson Mass from t-b-τ Yukawa Unification*, *JHEP* **08** (2012) 028, [1112.2206].

[85] M. Adeel Ajaib, I. Gogoladze, Q. Shafi and C. S. Un, *A Predictive Yukawa Unified SO(10) Model: Higgs and Sparticle Masses*, *JHEP* **07** (2013) 139, [1303.6964].

[86] I. Gogoladze, R. Khalid, S. Raza and Q. Shafi, *Higgs and Sparticle Spectroscopy with Gauge-Yukawa Unification*, *JHEP* **06** (2011) 117, [1102.0013].

[87] Particle Data Group collaboration, C. Patrignani et al., *Review of Particle Physics*, *Chin. Phys.* **C40** (2016) 100001.

[88] LHCb collaboration, R. Aaij et al., *First Evidence for the Decay $B_s^0 \to \mu^+\mu^-$*, *Phys. Rev. Lett.* **110** (2013) 021801, [1211.2674].

[89] Heavy Flavor Averaging Group collaboration, D. Asner et al., *Averages of b-hadron, c-hadron, and τ-lepton properties*, 1010.1589.

[90] Heavy Flavor Averaging Group collaboration, Y. Amhis et al., *Averages of B-Hadron, C-Hadron, and tau-lepton properties as of early 2012*, 1207.1158.

[91] WMAP collaboration, E. Komatsu et al., *Seven-Year Wilkinson Microwave Anisotropy Probe (WMAP) Observations: Cosmological Interpretation*, *Astrophys. J. Suppl.* **192** (2011) 18, [1001.4538].

[92] WMAP collaboration, D. N. Spergel et al., *Wilkinson Microwave Anisotropy Probe (WMAP) three year results: implications for cosmology*, *Astrophys. J. Suppl.* **170** (2007) 377, [astro-ph/0603449].

[93] G. Belanger, F. Boudjema, A. Pukhov and R. K. Singh, *Constraining the MSSM with universal gaugino masses and implication for searches at the LHC*, *JHEP* **11** (2009) 026, [0906.5048].

[94] P. Bechtle, O. Brein, S. Heinemeyer, O. Stål, T. Stefaniak, G. Weiglein et al., HiggsBounds – 4*: Improved Tests of Extended Higgs Sectors against Exclusion Bounds from LEP, the Tevatron and the LHC*, *Eur. Phys. J.* **C74** (2014) 2693, [1311.0055].

[95] P. Bechtle, S. Heinemeyer, O. Stål, T. Stefaniak and G. Weiglein, *HiggsSignals: Confronting arbitrary Higgs sectors with measurements at the Tevatron and the LHC*, *Eur. Phys. J.* **C74** (2014) 2711, [1305.1933].

[96] G. BÃ©langer, F. Boudjema, A. Pukhov and A. Semenov, *micrOMEGAs4.1: two dark matter candidates*, *Comput. Phys. Commun.* **192** (2015) 322–329, [1407.6129].

[97] L. Calibbi, J. M. Lindert, T. Ota and Y. Takanishi, *Cornering light Neutralino Dark Matter at the LHC*, *JHEP* **10** (2013) 132, [1307.4119].

[98] ATLAS collaboration, T. A. collaboration, *Search for squarks and gluinos in final states with jets and missing transverse momentum using 36 fb^{-1} of $\sqrt{s} = 13$ TeV pp collision data with the ATLAS detector*, *ATLAS-CONF-2017-022* .

[99] XENON collaboration, E. Aprile et al., *First Dark Matter Search Results from the XENON1T Experiment*, 1705.06655.

[100] XENON collaboration, E. Aprile et al., *Physics reach of the XENON1T dark matter experiment*, *JCAP* **1604** (2016) 027, [1512.07501].

[101] DARWIN collaboration, J. Aalbers et al., *DARWIN: towards the ultimate dark matter detector*, *JCAP* **1611** (2016) 017, [1606.07001].

[102] Muon g-2 Collaboration collaboration, G. W. Bennett, B. Bousquet, H. N. Brown, G. Bunce, R. M. Carey, P. Cushman et al., *Final report of the e821 muon anomalous magnetic moment measurement at bnl*, *Phys. Rev. D* **73** (Apr, 2006) 072003.

[103] Muon (g-2) Collaboration collaboration, G. W. Bennett, B. Bousquet, H. N. Brown, G. Bunce, R. M. Carey, P. Cushman et al., *Improved limit on the muon electric dipole moment*, *Phys. Rev. D* **80** (Sep, 2009) 052008.

[104] Muon g-2 collaboration, J. Grange et al., *Muon (g-2) Technical Design Report*, 1501.06858.

[105] J-PARC g-'2/EDM collaboration, N. Saito, *A novel precision measurement of muon g-2 and EDM at J-PARC*, *AIP Conf. Proc.* **1467** (2012) 45–56.

[106] M. Davier, A. Hoecker, B. Malaescu and Z. Zhang, *Reevaluation of the Hadronic Contributions to the Muon g-2 and to alpha(MZ)*, *Eur. Phys. J.* **C71** (2011) 1515, [1010.4180].

[107] J. Y. Araz, M. Frank and B. Fuks, *Differentiating $U(1)'$ supersymmetric models with right sneutrino and neutralino dark matter*, *Phys. Rev.* **D96** (2017) 015017, [1705.01063].

[108] AMS collaboration, L. Accardo et al., *High Statistics Measurement of the Positron Fraction in Primary Cosmic Rays of 0.5?500 GeV with the Alpha Magnetic Spectrometer on the International Space Station*, *Phys. Rev. Lett.* **113** (2014) 121101.

[109] V. Balkanov et al., *An upper limit on the diffuse flux of high energy neutrinos obtained with the Baikal detector NT-96*, *Astropart. Phys.* **14** (2000) 61–66.

[110] IceCube collaboration, M. G. Aartsen et al., *Evidence for High-Energy Extraterrestrial Neutrinos at the IceCube Detector*, *Science* **342** (2013) 1242856, [1311.5238].

[111] C. Degrande, C. Duhr, B. Fuks, D. Grellscheid, O. Mattelaer and T. Reiter, *UFO - The Universal FeynRules Output*, *Comput. Phys. Commun.* **183** (2012) 1201–1214, [1108.2040].

[112] J. Alwall, R. Frederix, S. Frixione, V. Hirschi, F. Maltoni, O. Mattelaer et al., *The automated computation of tree-level and next-to-leading order differential cross sections, and their matching to parton shower simulations*, *JHEP* **07** (2014) 079, [1405.0301].

[113] IceCube collaboration, R. Abbasi et al., *The IceCube Data Acquisition System: Signal Capture, Digitization, and Timestamping*, *Nucl. Instrum. Meth.* **A601** (2009) 294–316, [0810.4930].

[114] H. Baer, V. Barger, J. S. Gainer, P. Huang, M. Savoy, H. Serce et al., *What hadron collider is required to discover or falsify natural supersymmetry?*, 1702.06588.

[115] H. Baer, V. Barger, J. S. Gainer, P. Huang, M. Savoy, D. Sengupta et al., *Gluino reach and mass extraction at the LHC in radiatively-driven natural SUSY*, *Eur. Phys. J.* **C77** (2017) 499, [1612.00795].

[116] M. Cvetic and P. Langacker, *New gauge bosons from string models*, *Mod. Phys. Lett.* **A11** (1996) 1247–1262, [hep-ph/9602424].

[117] D. Suematsu and Y. Yamagishi, *Radiative symmetry breaking in a supersymmetric model with an extra U(1)*, *Int. J. Mod. Phys.* **A10** (1995) 4521–4536, [hep-ph/9411239].

[118] H.-S. Lee, K. T. Matchev and T. T. Wang, *A U(1) -prime solution to the μ^- problem and the proton decay problem in supersymmetry without R-parity*, *Phys. Rev.* **D77** (2008) 015016, [0709.0763].

[119] D. A. Demir, *Two Higgs doublet models from TeV scale supersymmetric extra U(1) models*, *Phys. Rev.* **D59** (1999) 015002, [hep-ph/9809358].

[120] D. A. Demir and Y. Farzan, *Correlating mu parameter and right-handed neutrino masses in N=1 supergravity*, *JHEP* **03** (2006) 010, [hep-ph/0601096].

[121] D. A. Demir, L. L. Everett and P. Langacker, *Dirac Neutrino Masses from Generalized Supersymmetry Breaking*, *Phys. Rev. Lett.* **100** (2008) 091804, [0712.1341].

[122] P. Langacker, *The Physics of Heavy Z' Gauge Bosons*, *Rev. Mod. Phys.* **81** (2009) 1199–1228, [0801.1345].

[123] J. Erler, P. Langacker, S. Munir and E. Rojas, *Improved Constraints on Z-prime Bosons from Electroweak Precision Data*, *JHEP* **08** (2009) 017, [0906.2435].

[124] O. C. Anoka, K. S. Babu and I. Gogoladze, *Constraining Z-prime from supersymmetry breaking*, *Nucl. Phys.* **B687** (2004) 3–30, [hep-ph/0401133].

[125] J. Y. Araz, G. Corcella, M. Frank and B. Fuks, *Loopholes in Z' searches at the LHC: exploring supersymmetric and leptophobic scenarios*, *JHEP* **02** (2018) 092, [1711.06302].

[126] B. Coleppa, S. Kumar and A. Sarkar, *Fermiophobic gauge boson phenomenology in 221 Models*, *Phys. Rev. D* **98** (2018) 095009, [1808.09728].

[127] T. G. Rizzo, *Gauge kinetic mixing and leptophobic Z' in E(6) and SO(10)*, *Phys. Rev.* **D59** (1998) 015020, [hep-ph/9806397].

[128] K. S. Babu, C. F. Kolda and J. March-Russell, *Leptophobic U(1) s and the R(b) - R(c) crisis*, *Phys. Rev.* **D54** (1996) 4635–4647, [hep-ph/9603212].

[129] C.-W. Chiang, T. Nomura and K. Yagyu, *Phenomenology of E_6-Inspired Leptophobic Z' Boson at the LHC*, *JHEP* **05** (2014) 106, [1402.5579].

[130] A. Celis, J. Fuentes-Martin, M. Jung and H. Serodio, *Family nonuniversal Z' models with protected flavor-changing interactions*, *Phys. Rev. D* **92** (2015) 015007, [1505.03079].

[131] B. Allanach, J. Butterworth and T. Corbett, *Collider constraints on Z' models for neutral current B-anomalies*, *JHEP* **08** (2019) 106, [1904.10954].

[132] J. Alvarado, C. E. Diaz and R. Martinez, *A $U(1)_X$ extension to the MSSM with three families*, in *Meeting of the Division of Particles and Fields of the American Physical Society*, 9, 2019. 1909.02891.

[133] S. Mantilla, R. Martinez and F. Ochoa, *Neutrino and CP-even Higgs boson masses in a nonuniversal* $\mathrm{U}(1)'$ *extension*, *Phys. Rev. D* **95** (2017) 095037, [1612.02081].

[134] Y. Tang and Y.-L. Wu, *Flavor non-universal gauge interactions and anomalies in B-meson decays*, *Chin. Phys. C* **42** (2018) 033104, [1705.05643].

[135] J. F. Kamenik, Y. Soreq and J. Zupan, *Lepton flavor universality violation without new sources of quark flavor violation*, *Phys. Rev. D* **97** (2018) 035002, [1704.06005].

[136] A. Alves, S. Profumo and F. S. Queiroz, *The dark Z' portal: direct, indirect and collider searches*, *JHEP* **04** (2014) 063, [1312.5281].

[137] J. Erler, P. Langacker and T.-j. Li, *The Z - Z′ mass hierarchy in a supersymmetric model with a secluded U(1) -prime breaking sector*, *Phys. Rev.* **D66** (2002) 015002, [hep-ph/0205001].

[138] C.-W. Chiang and E. Senaha, *Electroweak phase transitions in the secluded U(1)-prime-extended MSSM*, *JHEP* **06** (2010) 030, [0912.5069].

[139] D. A. Demir, M. Frank, L. Selbuz and I. Turan, *Scalar Neutrinos at the LHC*, *Phys. Rev.* **D83** (2011) 095001, [1012.5105].

[140] J. Kang, P. Langacker and B. D. Nelson, *Theory and Phenomenology of Exotic Isosinglet Quarks and Squarks*, *Phys. Rev.* **D77** (2008) 035003, [0708.2701].

[141] F. Staub, *Exploring new models in all detail with SARAH*, *Adv. High Energy Phys.* **2015** (2015) 840780, [1503.04200].

[142] A. Belyaev, N. D. Christensen and A. Pukhov, *CalcHEP 3.4 for collider physics within and beyond the Standard Model*, *Comput. Phys. Commun.* **184** (2013) 1729–1769, [1207.6082].

[143] N. D. Christensen, P. de Aquino, C. Degrande, C. Duhr, B. Fuks, M. Herquet et al., *A Comprehensive approach to new physics simulations*, *Eur. Phys. J. C* **71** (2011) 1541, [0906.2474].

[144] G. Bélanger, F. Boudjema, A. Goudelis, A. Pukhov and B. Zaldivar, *micrOMEGAs5.0 : Freeze-in*, *Comput. Phys. Commun.* **231** (2018) 173–186, [1801.03509].

[145] A. Buckley, *PySLHA: a Pythonic interface to SUSY Les Houches Accord data*, *Eur. Phys. J. C* **75** (2015) 467, [1305.4194].

[146] P. Z. Skands et al., *SUSY Les Houches accord: Interfacing SUSY spectrum calculators, decay packages, and event generators*, *JHEP* **07** (2004) 036, [hep-ph/0311123].

[147] G. Cacciapaglia, C. Csaki, G. Marandella and A. Strumia, *The Minimal Set of Electroweak Precision Parameters*, *Phys. Rev.* **D74** (2006) 033011, [hep-ph/0604111].

[148] G. Altarelli and R. Barbieri, *Vacuum polarization effects of new physics on electroweak processes*, *Phys. Lett.* **B253** (1991) 161–167.

[149] M. E. Peskin and T. Takeuchi, *A New constraint on a strongly interacting Higgs sector*, *Phys. Rev. Lett.* **65** (1990) 964–967.

[150] M. E. Peskin and T. Takeuchi, *Estimation of oblique electroweak corrections*, *Phys. Rev.* **D46** (1992) 381–409.

[151] I. Maksymyk, C. P. Burgess and D. London, *Beyond S, T and U*, *Phys. Rev.* **D50** (1994) 529–535, [hep-ph/9306267].

[152] Gfitter Group collaboration, M. Baak, J. Cúth, J. Haller, A. Hoecker, R. Kogler, K. Mönig et al., *The global electroweak fit at NNLO and prospects for the LHC and ILC*, *Eur. Phys. J.* **C74** (2014) 3046, [1407.3792].

[153] Particle Data Group collaboration, M. Tanabashi et al., *Review of Particle Physics*, *Phys. Rev.* **D98** (2018) 030001.

[154] CMS collaboration, A. M. Sirunyan et al., *Search for narrow and broad dijet resonances in proton-proton collisions at* $\sqrt{s} = 13$ *TeV and constraints on dark matter mediators and other new particles*, *JHEP* **08** (2018) 130, [1806.00843].

[155] XENON collaboration, E. Aprile et al., *Dark matter search results from a one ton-year exposure of xenon1t*, *Phys.Rev.Lett.* **121** (2018) 111302, [1805.12562].

[156] Fermi-LAT collaboration, M. Ackermann et al., *Searching for Dark Matter Annihilation from Milky Way Dwarf Spheroidal Galaxies with Six Years of Fermi Large Area Telescope Data*, *Phys. Rev. Lett.* **115** (2015) 231301, [1503.02641].

[157] R. H. Parker, C. Yu, W. Zhong, B. Estey and H. Muller, *Measurement of the fine-structure constant as a test of the standard model*, *Science* **360** (Apr, 2018) 191?195.

[158] F. Ambrogi, S. Kraml, S. Kulkarni, U. Laa, A. Lessa, V. Magerl et al., *SModelS v1.1 user manual: Improving simplified model constraints with efficiency maps*, *Comput. Phys. Commun.* **227** (2018) 72–98, [1701.06586].

[159] F. Ambrogi et al., *SModelS v1.2: long-lived particles, combination of signal regions, and other novelties*, *Comput. Phys. Commun.* **251** (2020) 106848, [1811.10624].

[160] J. Dutta, S. Kraml, A. Lessa and W. Waltenberger, *SModelS extension with the CMS supersymmetry search results from Run 2*, *LHEP* **1** (2018) 5–12, [1803.02204].

[161] C. K. Khosa, S. Kraml, A. Lessa, P. Neuhuber and W. Waltenberger, *SModelS database update v1.2.3*, 2005.00555.

[162] ATLAS collaboration, M. Aaboud et al., *Search for squarks and gluinos in final states with jets and missing transverse momentum at $\sqrt{s} = 13$ TeV with the ATLAS detector*, *Eur. Phys. J. C* **76** (2016) 392, [1605.03814].

[163] ATLAS collaboration, M. Aaboud et al., *Search for squarks and gluinos in final states with jets and missing transverse momentum using 36 fb^{-1} of $\sqrt{s} = 13$ TeV pp collision data with the ATLAS detector*, *Phys. Rev. D* **97** (2018) 112001, [1712.02332].

[164] CMS collaboration, A. M. Sirunyan et al., *Search for supersymmetry in multijet events with missing transverse momentum in proton-proton collisions at 13 TeV*, *Phys. Rev. D* **96** (2017) 032003, [1704.07781].

[165] ATLAS collaboration, *Search for squarks and gluinos in final states with jets and missing transverse momentum using 139 fb^{-1} of $\sqrt{s}$ =13 TeV pp collision data with the ATLAS detector*, .

[166] NNPDF collaboration, R. D. Ball et al., *Parton distributions from high-precision collider data*, *Eur. Phys. J. C* **77** (2017) 663, [1706.00428].

[167] T. Sjöstrand, S. Ask, J. R. Christiansen, R. Corke, N. Desai, P. Ilten et al., *An Introduction to PYTHIA 8.2*, *Comput. Phys. Commun.* **191** (2015) 159–177, [1410.3012].

[168] DELPHES 3 collaboration, J. de Favereau, C. Delaere, P. Demin, A. Giammanco, V. Lemaître, A. Mertens et al., *DELPHES 3, A modular framework for fast simulation of a generic collider experiment*, *JHEP* **02** (2014) 057, [1307.6346].

[169] J. Anderson et al., *Snowmass Energy Frontier Simulations*, 1309.1057.

[170] A. Avetisyan et al., *Methods and Results for Standard Model Event Generation at $\sqrt{s}$ = 14 TeV, 33 TeV and 100 TeV Proton Colliders (A Snowmass Whitepaper)*, in *Community Summer Study 2013: Snowmass on the Mississippi*, 8, 2013. 1308.1636.

[171] M. Cacciari, G. P. Salam and G. Soyez, *The anti-k_t jet clustering algorithm*, *JHEP* **04** (2008) 063, [0802.1189].

[172] M. Cacciari, G. P. Salam and G. Soyez, *FastJet User Manual*, *Eur. Phys. J. C* **72** (2012) 1896, [1111.6097].

[173] E. Conte, B. Fuks and G. Serret, *MadAnalysis 5, A User-Friendly Framework for Collider Phenomenology*, *Comput. Phys. Commun.* **184** (2013) 222–256, [1206.1599].

[174] L. Roszkowski, E. M. Sessolo and A. J. Williams, *Prospects for dark matter searches in the pMSSM*, *JHEP* **02** (2015) 014, [1411.5214].

[175] W. Abdallah and S. Khalil, *MSSM Dark Matter in Light of Higgs and LUX Results*, *Adv. High Energy Phys.* **2016** (2016) 5687463, [1509.07031].

[176] D. A. Demir, G. L. Kane and T. T. Wang, *The Minimal U(1)' extension of the MSSM*, *Phys. Rev.* **D72** (2005) 015012, [hep-ph/0503290].

[177] S. M. Barr, *Effects of Extra Light Z Bosons in Unified and Superstring Models*, *Phys. Rev. Lett.* **55** (1985) 2778.

[178] J. L. Hewett and T. G. Rizzo, *Low-Energy Phenomenology of Superstring Inspired E(6) Models*, *Phys. Rept.* **183** (1989) 193.

[179] M. Cvetic and P. Langacker, *Implications of Abelian extended gauge structures from string models*, *Phys. Rev.* **D54** (1996) 3570–3579, [hep-ph/9511378].

[180] G. Cleaver, M. Cvetic, J. R. Espinosa, L. L. Everett and P. Langacker, *Intermediate scales, mu parameter, and fermion masses from string models*, *Phys. Rev.* **D57** (1998) 2701–2715, [hep-ph/9705391].

[181] G. Cleaver, M. Cvetic, J. R. Espinosa, L. L. Everett and P. Langacker, *Classification of flat directions in perturbative heterotic superstring vacua with anomalous U(1)*, *Nucl. Phys.* **B525** (1998) 3–26, [hep-th/9711178].

[182] D. M. Ghilencea, L. E. Ibanez, N. Irges and F. Quevedo, *TeV scale Z-prime bosons from D-branes*, *JHEP* **08** (2002) 016, [hep-ph/0205083].

[183] S. F. King, S. Moretti and R. Nevzorov, *Theory and phenomenology of an exceptional supersymmetric standard model*, *Phys. Rev.* **D73** (2006) 035009, [hep-ph/0510419].

[184] R. Diener, S. Godfrey and T. A. W. Martin, *Discovery and Identification of Extra Neutral Gauge Bosons at the LHC*, in *Particles and fields. Proceedings, Meeting of the*

Division of the American Physical Society, DPF 2009, Detroit, USA, July 26-31, 2009, 2009. 0910.1334.

[185] M. Frank, L. Selbuz, L. Solmaz and I. Turan, *Higgs bosons in supersymmetric U(1)′ models with CP violation*, *Phys. Rev.* **D87** (2013) 075007, [1302.3427].

[186] M. Frank, L. Selbuz and I. Turan, *Neutralino and Chargino Production in U(1)' at the LHC*, *Eur. Phys. J.* **C73** (2013) 2656, [1212.4428].

[187] P. Athron, D. Harries and A. G. Williams, *Z' mass limits and the naturalness of supersymmetry*, *Phys. Rev.* **D91** (2015) 115024, [1503.08929].

[188] P. Athron, S. F. King, D. J. Miller, S. Moretti and R. Nevzorov, *The Constrained Exceptional Supersymmetric Standard Model*, *Phys. Rev.* **D80** (2009) 035009, [0904.2169].

[189] P. Athron, S. F. King, D. J. Miller, S. Moretti and R. Nevzorov, *Predictions of the Constrained Exceptional Supersymmetric Standard Model*, *Phys. Lett.* **B681** (2009) 448–456, [0901.1192].

[190] P. Athron, S. F. King, D. J. Miller, S. Moretti and R. Nevzorov, *Constrained Exceptional Supersymmetric Standard Model with a Higgs Near 125 GeV*, *Phys. Rev.* **D86** (2012) 095003, [1206.5028].

[191] P. Athron, D. Stockinger and A. Voigt, *Threshold Corrections in the Exceptional Supersymmetric Standard Model*, *Phys. Rev.* **D86** (2012) 095012, [1209.1470].

[192] P. Athron, M. Mühlleitner, R. Nevzorov and A. G. Williams, *Non-Standard Higgs Decays in U(1) Extensions of the MSSM*, *JHEP* **01** (2015) 153, [1410.6288].

[193] P. Athron, D. Harries, R. Nevzorov and A. G. Williams, *E_6 Inspired SUSY benchmarks, dark matter relic density and a 125 GeV Higgs*, *Phys. Lett.* **B760** (2016) 19–25, [1512.07040].

[194] P. Athron, D. Harries, R. Nevzorov and A. G. Williams, *Dark matter in a constrained E_6 inspired SUSY model*, *JHEP* **12** (2016) 128, [1610.03374].

[195] P. Athron, A. W. Thomas, S. J. Underwood and M. J. White, *Dark matter candidates in the constrained Exceptional Supersymmetric Standard Model*, *Phys. Rev.* **D95** (2017) 035023, [1611.05966].

[196] P. Athron, J.-h. Park, T. Steudtner, D. Stöckinger and A. Voigt, *Precise Higgs mass calculations in (non-)minimal supersymmetry at both high and low scales*, *JHEP* **01** (2017) 079, [1609.00371].

[197] V. Jain and R. Shrock, *U(1)-A models of fermion masses without a mu problem*, hep-ph/9507238.

[198] Y. Nir, *Gauge unification, Yukawa hierarchy and the mu problem*, *Phys. Lett.* **B354** (1995) 107–110, [hep-ph/9504312].

[199] N. Okada and O. Seto, *Higgs portal dark matter in the minimal gauged $U(1)_{B-L}$ model*, *Phys. Rev. D* **82** (2010) 023507, [1002.2525].

[200] N. Okada and S. Okada, *Z'-portal right-handed neutrino dark matter in the minimal $U(1)_X$ extended Standard Model*, *Phys. Rev. D* **95** (2017) 035025, [1611.02672].

[201] N. Okada and S. Okada, *Z'_{BL} portal dark matter and LHC Run-2 results*, *Phys. Rev. D* **93** (2016) 075003, [1601.07526].

[202] P. Agrawal, N. Kitajima, M. Reece, T. Sekiguchi and F. Takahashi, *Relic Abundance of Dark Photon Dark Matter*, *Phys. Lett. B* **801** (2020) 135136, [1810.07188].

[203] B. Allanach, F. S. Queiroz, A. Strumia and S. Sun, *Z' models for the LHCb and $g-2$ muon anomalies*, *Phys. Rev. D* **93** (2016) 055045, [1511.07447].

[204] M.-C. Chen, J. Huang and W. Shepherd, *Dirac Leptogenesis with a Non-anomalous $U(1)'$ Family Symmetry*, *JHEP* **11** (2012) 059, [1111.5018].

[205] J. Heeck and W. Rodejohann, *Gauged L_μ - L_τ Symmetry at the Electroweak Scale*, *Phys. Rev.* **D84** (2011) 075007, [1107.5238].

[206] E. Keith and E. Ma, *Efficacious extra U(1) factor for the supersymmetric standard model*, *Phys. Rev.* **D54** (1996) 3587–3593, [hep-ph/9603353].

[207] E. Accomando, F. Coradeschi, T. Cridge, J. Fiaschi, F. Hautmann, S. Moretti et al., *Production of Z'-boson resonances with large width at the LHC*, *Phys. Lett.* **B803** (2020) 135293, [1910.13759].

[208] E. Accomando, A. Belyaev, J. Fiaschi, K. Mimasu, S. Moretti and C. Shepherd-Themistocleous, *Forward-backward asymmetry as a discovery tool for Z' bosons at the LHC*, *JHEP* **01** (2016) 127, [1503.02672].

[209] J. Kang and P. Langacker, *Z ' discovery limits for supersymmetric E(6) models*, *Phys. Rev.* **D71** (2005) 035014, [hep-ph/0412190].

[210] P. Langacker and J. Wang, *U(1)-prime symmetry breaking in supersymmetric E(6) models*, *Phys. Rev.* **D58** (1998) 115010, [hep-ph/9804428].

[211] J. P. Hall, S. F. King, R. Nevzorov, S. Pakvasa, M. Sher, R. Nevzorov et al., *Novel Higgs Decays and Dark Matter in the E(6)SSM*, *Phys. Rev.* **D83** (2011) 075013, [1012.5114].

[212] M. Cvetic, J. Halverson and P. Langacker, *Implications of String Constraints for Exotic Matter and Z' s Beyond the Standard Model*, *JHEP* **11** (2011) 058, [1108.5187].

[213] Y. Hiçyılmaz, L. Solmaz, S. H. Tanyıldızı and C. S. Ün, *Least fine-tuned U (1) extended SSM*, *Nucl. Phys.* **B933** (2018) 275–298, [1706.04561].

[214] B. Holdom, *Two U(1)'s and Epsilon Charge Shifts*, *Phys. Lett.* **166B** (1986) 196–198.

[215] K. S. Babu, C. F. Kolda and J. March-Russell, *Implications of generalized Z - Z-prime mixing*, *Phys. Rev.* **D57** (1998) 6788–6792, [hep-ph/9710441].

[216] H. Tran, *Kinetic mixing in models with an extra abelian gauge symmetry*, *Communications in Physics* **28** (2018) 41.

[217] G. Bélanger, J. Da Silva and H. M. Tran, *Dark matter in U(1) extensions of the MSSM with gauge kinetic mixing*, *Phys. Rev.* **D95** (2017) 115017, [1703.03275].

[218] J. Hisano, H. Murayama and T. Yanagida, *Nucleon decay in the minimal supersymmetric SU(5) grand unification*, *Nucl. Phys.* **B402** (1993) 46–84, [hep-ph/9207279].

[219] WMAP collaboration, G. Hinshaw et al., *Nine-Year Wilkinson Microwave Anisotropy Probe (WMAP) Observations: Cosmological Parameter Results*, *Astrophys. J. Suppl.* **208** (2013) 19, [1212.5226].

[220] G. Bélanger, F. Boudjema, A. Goudelis, A. Pukhov and B. Zaldivar, *micrOMEGAs5.0 : Freeze-in*, *Comput. Phys. Commun.* **231** (2018) 173–186, [1801.03509].

[221] P. A. Grassi, B. A. Kniehl and A. Sirlin, *Width and partial widths of unstable particles in the light of the Nielsen identities*, *Phys. Rev.* **D65** (2002) 085001, [hep-ph/0109228].

[222] E. Accomando, D. Becciolini, A. Belyaev, S. Moretti and C. Shepherd-Themistocleous, *Z' at the LHC: Interference and Finite Width Effects in Drell-Yan*, *JHEP* **10** (2013) 153, [1304.6700].

[223] E. Accomando, D. Becciolini, A. Belyaev, S. De Curtis, D. Dominici, S. F. King et al., *W' and Z' searches at the LHC*, *PoS* **DIS2013** (2013) 125.

[224] R. D. Ball et al., *Parton distributions with LHC data*, *Nucl. Phys.* **B867** (2013) 244–289, [1207.1303].

[225] T. Bandyopadhyay, G. Bhattacharyya, D. Das and A. Raychaudhuri, *Reappraisal of constraints on Z' models from unitarity and direct searches at the LHC*, *Phys. Rev.* **D98** (2018) 035027, [1803.07989].

[226] PandaX-II collaboration, X. Cui et al., *Dark Matter Results From 54-Ton-Day Exposure of PandaX-II Experiment*, *Phys. Rev. Lett.* **119** (2017) 181302, [1708.06917].

[227] LUX collaboration, D. S. Akerib et al., *Results from a search for dark matter in the complete LUX exposure*, *Phys. Rev. Lett.* **118** (2017) 021303, [1608.07648].

[228] XENON collaboration, E. Aprile et al., *Constraining the spin-dependent WIMP-nucleon cross sections with XENON1T*, *Phys. Rev. Lett.* **122** (2019) 141301, [1902.03234].

[229] PandaX-II collaboration, J. Xia et al., *PandaX-II Constraints on Spin-Dependent WIMP-Nucleon Effective Interactions*, *Phys. Lett.* **B792** (2019) 193–198, [1807.01936].

[230] LUX collaboration, D. S. Akerib et al., *Limits on spin-dependent WIMP-nucleon cross section obtained from the complete LUX exposure*, *Phys. Rev. Lett.* **118** (2017) 251302, [1705.03380].

[231] J. C. Pati and A. Salam, *Lepton Number as the Fourth Color*, *Phys. Rev.* **D10** (1974) 275–289.

[232] R. N. Mohapatra and J. C. Pati, *A Natural Left-Right Symmetry*, *Phys. Rev.* **D11** (1975) 2558.

[233] R. N. Mohapatra and J. C. Pati, *Left-Right Gauge Symmetry and an Isoconjugate Model of CP Violation*, *Phys. Rev.* **D11** (1975) 566–571.

[234] G. Senjanovic and R. N. Mohapatra, *Exact Left-Right Symmetry and Spontaneous Violation of Parity*, *Phys. Rev.* **D12** (1975) 1502.

[235] R. N. Mohapatra and G. Senjanovic, *Neutrino Mass and Spontaneous Parity Violation*, *Phys. Rev. Lett.* **44** (1980) 912.

[236] R. N. Mohapatra, *UNIFICATION AND SUPERSYMMETRY. THE FRONTIERS OF QUARK - LEPTON PHYSICS*. Springer, Berlin, 1986, 10.1007/978-1-4757-1928-4.

[237] R. N. Mohapatra and G. Senjanovic, *Cabibbo Angle, CP Violation and Quark Masses*, *Phys. Lett.* **73B** (1978) 176–180.

[238] M. A. B. Beg and H. S. Tsao, *Strong P, T Noninvariances in a Superweak Theory*, *Phys. Rev. Lett.* **41** (1978) 278.

[239] M. A. B. Beg, R. V. Budny, R. N. Mohapatra and A. Sirlin, *Manifest Left-Right Symmetry and Its Experimental Consequences*, *Phys. Rev. Lett.* **38** (1977) 1252.

[240] G. Senjanovic, *Spontaneous Breakdown of Parity in a Class of Gauge Theories*, *Nucl. Phys.* **B153** (1979) 334–364.

[241] R. N. Mohapatra, F. E. Paige and D. P. Sidhu, *Symmetry Breaking and Naturalness of Parity Conservation in Weak Neutral Currents in Left-Right Symmetric Gauge Theories*, *Phys. Rev.* **D17** (1978) 2462.

[242] G. C. Branco, J. M. Frere and J. M. Gerard, *The Value of ϵ'/ϵ in Models Based on SU(2)-l X SU(2)-r X U(1)*, *Nucl. Phys.* **B221** (1983) 317–330.

[243] P. Langacker and S. U. Sankar, *Bounds on the Mass of W(R) and the W(L)-W(R) Mixing Angle xi in General SU(2)-L x SU(2)-R x U(1) Models*, *Phys. Rev.* **D40** (1989) 1569–1585.

[244] G. Barenboim, J. Bernabeu, J. Prades and M. Raidal, *Constraints on the W_R mass and CP violation in left-right models*, *Phys. Rev.* **D55** (1997) 4213–4221, [hep-ph/9611347].

[245] M. Frank, A. Hayreter and I. Turan, *Production and Decays of W_R bosons at the LHC*, *Phys. Rev.* **D83** (2011) 035001, [1010.5809].

[246] Y. Zhang, H. An, X. Ji and R. N. Mohapatra, *General CP Violation in Minimal Left-Right Symmetric Model and Constraints on the Right-Handed Scale*, *Nucl. Phys.* **B802** (2008) 247–279, [0712.4218].

[247] A. Sirunyan, A. Tumasyan, W. Adam, F. Ambrogi, E. Asilar, T. Bergauer et al., *Search for heavy resonances decaying to a top quark and a bottom quark in the lepton+jets final state in proton-proton collisions at 13 tev*, *Physics Letters B* **777** (2018) 39 – 63.

[248] W.-Y. Keung and G. Senjanovic, *Majorana Neutrinos and the Production of the Right-handed Charged Gauge Boson*, *Phys. Rev. Lett.* **50** (1983) 1427.

[249] CMS collaboration, A. M. Sirunyan et al., *Search for heavy resonances decaying to a top quark and a bottom quark in the lepton+jets final state in proton-proton collisions at 13 TeV*, *Phys. Lett.* **B777** (2018) 39–63, [1708.08539].

[250] CMS collaboration, S. Chatrchyan et al., *A search for a doubly-charged Higgs boson in pp collisions at $\sqrt{s} = 7$ TeV*, *Eur. Phys. J.* **C72** (2012) 2189, [1207.2666].

[251] CMS collaboration, C. Collaboration, *Search for a doubly-charged Higgs boson with $\sqrt{s} = 8$ TeV pp collisions at the CMS experiment*, .

[252] L3 collaboration, P. Achard et al., *Search for heavy neutral and charged leptons in e^+e^- annihilation at LEP*, *Phys. Lett.* **B517** (2001) 75–85, [hep-ex/0107015].

[253] T. Jubb, M. Kirk, A. Lenz and G. Tetlalmatzi-Xolocotzi, *On the ultimate precision of meson mixing observables*, *Nucl. Phys.* **B915** (2017) 431–453, [1603.07770].

[254] K. Blum, Y. Grossman, Y. Nir and G. Perez, *Combining K^0–$\overline{k}^0$ mixing and D^0–$\overline{d}^0$ mixing to constrain the flavor structure of new physics*, *Phys. Rev. Lett.* **102** (May, 2009) 211802.

[255] ATLAS collaboration, M. Aaboud et al., *Search for doubly charged scalar bosons decaying into same-sign W boson pairs with the ATLAS detector*, *Submitted to: Eur. Phys. J.* (2018) , [1808.01899].

[256] CMS collaboration, C. Collaboration, *A search for doubly-charged Higgs boson production in three and four lepton final states at* $\sqrt{s} = 13$ TeV, .

[257] C. Bonilla, M. E. Krauss, T. Opferkuch and W. Porod, *Perspectives for Detecting Lepton Flavour Violation in Left-Right Symmetric Models*, *JHEP* **03** (2017) 027, [1611.07025].

[258] J. Alwall, M. Herquet, F. Maltoni, O. Mattelaer and T. Stelzer, *MadGraph 5 : Going Beyond*, *JHEP* **06** (2011) 128, [1106.0522].

[259] A. Alloul, N. D. Christensen, C. Degrande, C. Duhr and B. Fuks, *FeynRules 2.0 - A complete toolbox for tree-level phenomenology*, *Comput. Phys. Commun.* **185** (2014) 2250–2300, [1310.1921].

[260] A. Roitgrund, G. Eilam and S. Bar-Shalom, *Implementation of the left-right symmetric model in FeynRules*, *Comput. Phys. Commun.* **203** (2016) 18–44, [1401.3345].

[261] CMS collaboration, A. M. Sirunyan et al., *Search for third-generation scalar leptoquarks and heavy right-handed neutrinos in final states with two tau leptons and two jets in proton-proton collisions at* $\sqrt{s} = 13$ *TeV*, *JHEP* **07** (2017) 121, [1703.03995].

[262] G. Arcadi, M. Dutra, P. Ghosh, M. Lindner, Y. Mambrini, M. Pierre et al., *The waning of the WIMP? A review of models, searches, and constraints*, *Eur. Phys. J.* **C78** (2018) 203, [1703.07364].

[263] M. Kawasaki and K. Nakayama, *Axions: Theory and Cosmological Role*, *Ann. Rev. Nucl. Part. Sci.* **63** (2013) 69–95, [1301.1123].

[264] P. W. Graham, I. G. Irastorza, S. K. Lamoreaux, A. Lindner and K. A. van Bibber, *Experimental Searches for the Axion and Axion-Like Particles*, *Ann. Rev. Nucl. Part. Sci.* **65** (2015) 485–514, [1602.00039].

[265] D. Feldman, B. Kors and P. Nath, *Extra-weakly Interacting Dark Matter*, *Phys. Rev.* **D75** (2007) 023503, [hep-ph/0610133].

[266] E. Izaguirre, G. Krnjaic, P. Schuster and N. Toro, *Analyzing the Discovery Potential for Light Dark Matter*, *Phys. Rev. Lett.* **115** (2015) 251301, [1505.00011].

[267] D. Curtin, R. Essig, S. Gori and J. Shelton, *Illuminating Dark Photons with High-Energy Colliders*, *JHEP* **02** (2015) 157, [1412.0018].

[268] R. Essig et al., *Working Group Report: New Light Weakly Coupled Particles*, in *Proceedings, 2013 Community Summer Study on the Future of U.S. Particle Physics: Snowmass on the Mississippi (CSS2013): Minneapolis, MN, USA, July 29-August 6, 2013*, 2013. 1311.0029.

[269] H. Davoudiasl, H.-S. Lee and W. J. Marciano, *'Dark' Z implications for Parity Violation, Rare Meson Decays, and Higgs Physics*, *Phys. Rev.* **D85** (2012) 115019, [1203.2947].

[270] T. Toma, *Internal Bremsstrahlung Signature of Real Scalar Dark Matter and Consistency with Thermal Relic Density*, *Phys. Rev. Lett.* **111** (2013) 091301, [1307.6181].

[271] F. Giacchino, L. Lopez-Honorez and M. H. G. Tytgat, *Scalar Dark Matter Models with Significant Internal Bremsstrahlung*, *JCAP* **1310** (2013) 025, [1307.6480].

[272] F. Giacchino, L. Lopez-Honorez and M. H. G. Tytgat, *Bremsstrahlung and Gamma Ray Lines in 3 Scenarios of Dark Matter Annihilation*, *JCAP* **1408** (2014) 046, [1405.6921].

[273] A. Ibarra, T. Toma, M. Totzauer and S. Wild, *Sharp Gamma-ray Spectral Features from Scalar Dark Matter Annihilations*, *Phys. Rev.* **D90** (2014) 043526, [1405.6917].

[274] F. Giacchino, A. Ibarra, L. Lopez Honorez, M. H. G. Tytgat and S. Wild, *Signatures from Scalar Dark Matter with a Vector-like Quark Mediator*, *JCAP* **1602** (2016) 002, [1511.04452].

[275] S. Colucci, B. Fuks, F. Giacchino, L. Lopez Honorez, M. H. G. Tytgat and J. Vandecasteele, *Top-philic Vector-Like Portal to Scalar Dark Matter*, *Phys. Rev.* **D98** (2018) 035002, [1804.05068].

[276] F. Gursey, P. Ramond and P. Sikivie, *A Universal Gauge Theory Model Based on E6*, *Phys. Lett.* **60B** (1976) 177–180.

[277] Y. Achiman and B. Stech, *Quark Lepton Symmetry and Mass Scales in an E6 Unified Gauge Model*, *Phys. Lett.* **77B** (1978) 389–393.

[278] S. Bahrami, M. Frank, D. K. Ghosh, N. Ghosh and I. Saha, *Dark matter and collider studies in the left-right symmetric model with vectorlike leptons*, *Phys. Rev.* **D95** (2017) 095024, [1612.06334].

[279] E. Ma, *Particle Dichotomy and Left-Right Decomposition of E(6) Superstring Models*, *Phys. Rev.* **D36** (1987) 274.

[280] M. Frank, I. Turan and M. Sher, *Neutrino masses in the effective rank-5 subgroups of E(6): Supersymmetric case*, *Phys. Rev.* **D71** (2005) 113002, [hep-ph/0503084].

[281] K. Babu, X.-G. He and E. Ma, *New Supersymmetric Left-Right Gauge Model: Higgs Boson Structure and Neutral Current Analysis*, *Phys.Rev.* **D36** (1987) 878.

[282] E. Ma, *Dark Left-Right Model: CDMS, LHC, etc*, *J.Phys.Conf.Ser.* **315** (2011) 012006, [1006.3804].

[283] S. Khalil, H.-S. Lee and E. Ma, *Bound on Z' Mass from CDMS II in the Dark Left-Right Gauge Model II*, *Phys. Rev.* **D81** (2010) 051702, [1002.0692].

[284] M. Ashry and S. Khalil, *Phenomenological aspects of a TeV-scale alternative left-right model*, *Phys. Rev.* **D91** (2015) 015009, [1310.3315].

[285] N. G. Deshpande and E. Ma, *Pattern of Symmetry Breaking with Two Higgs Doublets*, *Phys. Rev.* **D18** (1978) 2574.

[286] E. Ma, *Verifiable radiative seesaw mechanism of neutrino mass and dark matter*, *Phys. Rev.* **D73** (2006) 077301, [hep-ph/0601225].

[287] R. Barbieri, L. J. Hall and V. S. Rychkov, *Improved naturalness with a heavy Higgs: An Alternative road to LHC physics*, *Phys. Rev.* **D74** (2006) 015007, [hep-ph/0603188].

[288] M. Frank, I. Turan and M. Sher, *Neutrino masses in effective rank-5 subgroups of e(6) I: Non-SUSY case*, *Phys. Rev.* **D71** (2005) 113001, [hep-ph/0412090].

[289] D. Borah, S. Patra and U. Sarkar, *TeV scale Left Right Symmetry with spontaneous D-parity breaking*, *Phys. Rev.* **D83** (2011) 035007, [1006.2245].

[290] M. Ashry, *TeV scale left-right symmetric model with minimal Higgs sector*, M.Sc. thesis, U. Cairo, 2015.

[291] F. Ambrogi, C. Arina, M. Backovic, J. Heisig, F. Maltoni, L. Mantani et al., *MadDM v.3.0: a Comprehensive Tool for Dark Matter Studies*, *Phys. Dark Univ.* **24** (2019) 100249, [1804.00044].

[292] P. Bechtle, O. Brein, S. Heinemeyer, G. Weiglein and K. E. Williams, *HiggsBounds: Confronting Arbitrary Higgs Sectors with Exclusion Bounds from LEP and the Tevatron*, *Comput. Phys. Commun.* **181** (2010) 138–167, [0811.4169].

[293] P. S. B. Dev, R. N. Mohapatra and Y. Zhang, *Probing the Higgs Sector of the Minimal Left-Right Symmetric Model at Future Hadron Colliders*, *JHEP* **05** (2016) 174, [1602.05947].

[294] CMS collaboration, A. M. Sirunyan et al., *Search for pair-produced resonances decaying to quark pairs in proton-proton collisions at $\sqrt{s} = 13$ TeV*, *Phys. Rev.* **D98** (2018) 112014, [1808.03124].

[295] CMS collaboration, A. M. Sirunyan et al., *Search for high-mass resonances in dilepton final states in proton-proton collisions at $\sqrt{s} = 13$ TeV*, *JHEP* **06** (2018) 120, [1803.06292].

[296] ATLAS collaboration, M. Aaboud et al., *Search for new high-mass phenomena in the dilepton final state using 36 fb^{-1} of proton-proton collision data at $\sqrt{s} = 13$ TeV with the ATLAS detector*, *JHEP* **10** (2017) 182, [1707.02424].

[297] A. Arhrib, R. Benbrik, M. Chabab, G. Moultaka, M. C. Peyranere, L. Rahili et al., *The Higgs Potential in the Type II Seesaw Model*, *Phys. Rev.* **D84** (2011) 095005, [1105.1925].

[298] ATLAS Collaboration, *Prospects for searches for heavy Z' and W' bosons in fermionic final states with the ATLAS experiment at the HL-LHC*, ATL-PHYS-PUB-2018-044.

[299] CMS collaboration, C. Collaboration, *Search for heavy stable charged particles with* 12.9 fb^{-1} *of 2016 data*, .

[300] CMS collaboration, V. Khachatryan et al., *Search for long-lived charged particles in proton-proton collisions at $\sqrt{s} = 13$ TeV*, *Phys. Rev.* **D94** (2016) 112004, [1609.08382].

[301] ATLAS collaboration, G. Aad et al., *Search for long-lived, massive particles in events with a displaced vertex and a muon with large impact parameter in pp collisions at* $\sqrt{s} = 13$ *TeV with the ATLAS detector*, 2003.11956.

[302] ATLAS collaboration, M. Aaboud et al., *Search for heavy charged long-lived particles in the ATLAS detector in 36.1* fb^{-1} *of proton-proton collision data at* $\sqrt{s} = 13$ *TeV*, *Phys. Rev.* **D99** (2019) 092007, [1902.01636].

[303] ATLAS collaboration, M. Aaboud et al., *Search for long-lived, massive particles in events with displaced vertices and missing transverse momentum in* $\sqrt{s} = 13$ *TeV pp collisions with the ATLAS detector*, *Phys. Rev.* **D97** (2018) 052012, [1710.04901].

[304] J. Alimena et al., *Searching for Long-Lived Particles beyond the Standard Model at the Large Hadron Collider*, 1903.04497.

[305] CMS collaboration, S. Chatrchyan et al., *Searches for Long-Lived Charged Particles in pp Collisions at* $\sqrt{s}$*=7 and 8 TeV*, *JHEP* **07** (2013) 122, [1305.0491].

[306] CMS collaboration, V. Khachatryan et al., *Search for Heavy Stable Charged Particles in pp collisions at* $\sqrt{s} = 7$ *TeV*, *JHEP* **03** (2011) 024, [1101.1645].

[307] ATLAS collaboration, G. Aad et al., *Search for heavy long-lived charged particles with the ATLAS detector in pp collisions at* $\sqrt{s} = 7$ *TeV*, *Phys. Lett.* **B703** (2011) 428–446, [1106.4495].

[308] OPAL collaboration, K. Ackerstaff et al., *Search for stable and longlived massive charged particles in e+ e- collisions at s**(1/2) = 130-GeV - 183-GeV*, *Phys. Lett.* **B433** (1998) 195–208, [hep-ex/9803026].

[309] CMS collaboration, A. M. Sirunyan et al., *Search for charged Higgs bosons in the* $H^{\pm} \to \tau^{\pm}\nu_{\tau}$ *decay channel in proton-proton collisions at* $\sqrt{s} = 13$ *TeV*, *JHEP* **07** (2019) 142, [1903.04560].

[310] ATLAS collaboration, M. Aaboud et al., *Search for charged Higgs bosons produced in association with a top quark and decaying via* $H^{\pm} \to \tau\nu$ *using pp collision data recorded at* $\sqrt{s} = 13$ *TeV by the ATLAS detector*, *Phys. Lett.* **B759** (2016) 555–574, [1603.09203].

[311] CMS collaboration, A. M. Sirunyan et al., *Search for charged Higgs bosons decaying into a top and a bottom quark in the all-jet final state of pp collisions at $\sqrt{s} = 13$ TeV*, 2001.07763.

[312] ATLAS collaboration, M. Aaboud et al., *Search for charged Higgs bosons decaying into top and bottom quarks at $\sqrt{s} = 13$ TeV with the ATLAS detector*, *JHEP* **11** (2018) 085, [1808.03599].

[313] ALEPH, DELPHI, L3, OPAL, LEP collaboration, G. Abbiendi et al., *Search for Charged Higgs bosons: Combined Results Using LEP Data*, *Eur. Phys. J.* **C73** (2013) 2463, [1301.6065].

[314] B. Dumont, B. Fuks, S. Kraml, S. Bein, G. Chalons, E. Conte et al., *Toward a public analysis database for LHC new physics searches using MADANALYSIS 5*, *Eur. Phys. J.* **C75** (2015) 56, [1407.3278].

[315] E. Conte and B. Fuks, *Confronting new physics theories to LHC data with MADANALYSIS 5*, *Int. J. Mod. Phys.* **A33** (2018) 1830027, [1808.00480].

[316] J. Y. Araz, M. Frank and B. Fuks, *Reinterpreting the results of the LHC with MadAnalysis 5: uncertainties and higher-luminosity estimates*, 1910.11418.

[317] CMS collaboration, A. M. Sirunyan et al., *Search for electroweak production of charginos and neutralinos in multilepton final states in proton-proton collisions at $\sqrt{s} = 13$ TeV*, *JHEP* **03** (2018) 166, [1709.05406].

[318] A. Chatterjee, M. Frank, B. Fuks, K. Huitu, S. Mondal, S. K. Rai et al., *Multileptonic signals of co-annihilating left-right supersymmetric dark matter*, *Phys. Rev.* **D99** (2019) 035017, [1810.03891].

[319] B. Fuks and S. Mondal, *MadAnalysis 5 implementation of the CMS search for supersymmetry in the multilepton channel with 35.9 fb-1 of 13 TeV LHC data (CMS-SUS-16-039)*, 10.7484/INSPIREHEP.DATA.HE48.D9HD.1.

[320] B. Fuks *et al.*, *Proceedings of the first MadAnalysis 5 workshop on LHC recasting in Korea*, 1806.02537.

[321] S. Bein, S.-M. Choi, B. Fuks, S. Jeong, D. W. Kang, J. Li et al., *Madanalysis5 implementation of CMS-SUS-17-001*, 10.7484/INSPIREHEP.DATA.MMM1.876Z.

[322] G. Cowan, K. Cranmer, E. Gross and O. Vitells, *Asymptotic formulae for likelihood-based tests of new physics*, *Eur. Phys. J.* **C71** (2011) 1554, [1007.1727].

[323] S. Gopalakrishna, T. Han, I. Lewis, Z.-g. Si and Y.-F. Zhou, *Chiral Couplings of W' and Top Quark Polarization at the LHC*, *Phys. Rev. D* **82** (2010) 115020, [1008.3508].

[324] T. Han, I. Lewis, R. Ruiz and Z.-g. Si, *Lepton Number Violation and W′ Chiral Couplings at the LHC*, *Phys. Rev. D* **87** (2013) 035011, [1211.6447].